Petrogenesis of the Swartruggens and Star Group II kimberlite dyke swarms, South Africa

Nancy Coe

Thesis submitted in fulfilment of the requirements
for the degree of Master of Science

University of Cape Town
March, 2004

Declaration

I hereby declare that the work presented in this thesis is my own, except where otherwise stated in the text.

Nancy Coe
March, 2004

Abstract

The Swartruggens (156 Ma) and Star (128 Ma) kimberlites are two Group II, diamondiferous, hypabyssal kimberlite dyke swarms, situated in the Northern Province and the Free State respectively, South Africa. Representative samples from all dykes exposed in the mining operations, the Main and Changehouse Dykes, South Fissure and the barren Muil Dyke at Swartruggens, and the Wynandsfontein, East Star, Clewer, Byrnes and Barren dykes at Star, have been analysed for their major and trace element contents and Sr, Nd and Hf isotope compositions. Primary kimberlite magma chemistry is subjected to considerable modification due to the incorporation of both mantle and crustal material during ascent to the surface, crystal fractionation, and post-emplacement alteration by deuteric fluids. This study aims to constrain the effects of these processes, and thus to identify least-modified, close-to-primary, parental magma compositions, with the view to understanding the source region characteristics of, and the petrogenetic processes giving rise to, these kimberlites.

Petrographically the kimberlites at both localities are similar to other South African micaceous kimberlites, containing rounded, anhedral, macrocrystic olivine (variably altered to serpentine and replaced by calcite) and kink-banded macrocrystic phlogopite in a fine-grained groundmass of phlogopite, olivine, and carbonate with or without diopside and minor apatite, perovskite and Fe-Ti oxides. Occasional rounded eclogitic garnets are present in some samples. The Muil (barren) dyke at Swartruggens is a lamprophyre and differs petrographically from the kimberlite dykes in that it consists of euhedral olivine macrocrysts in a groundmass of phlogopite, diopside and sanidine.

Major and trace element variations are considerable at each locality. The Swartruggens kimberlite has MgO = 12.0 – 25.4 wt%, SiO_2 = 25.1 – 41.6 wt% and K_2O = 2.44 – 5.77 wt%. In contrast, for similar MgO and K_2O contents (5.5-36.7 wt % and 0.64 – 4.22 wt % respectively), the Star kimberlite is less enriched in SiO_2 (22.7 – 43.7 wt %). Trace element abundances are equally variable; the Swartruggens kimberlite dykes have La = 124-300 ppm, Zr = 264-1145 ppm and Nb = 80.1 - 351 ppm, and the Star kimberlite dykes have 131 – 285 ppm La, 31.3-410 ppm Zr and 68 - 189 ppm Nb. Compatible element abundances are also variable, with the Swartruggens kimberlite having Ni = 617 – 1814 ppm, Cr = 1270 – 1845 ppm, and Star Ni = 684 – 1988 ppm and Cr = 1800 – 2733ppm. In contrast incompatible trace element ratios are more restricted and are similar between the two dykes swarms (Swartruggens: Zr/Hf = 45.0 ± 3.9, La/Th = 8.3 ± 0.9, Ce/Pb = 9.1 ± 2.3, K/Rb = 202 ± 9.7; Star Zr/Hf = 40.6 ± 5.6, La/Th = 7.0 ± 1.2, Ce/Pb = 15 ± 4.0, K/Rb = 196 ± 15).

Chondrite normalised rare earth element (REE) patterns define steep, sub-parallel arrays, which are strongly enriched in the light REE relative to heavy REE, with average La/Yb_n of 97 for the Swartruggens kimberlite and 205 for the Star kimberlite dykes. Normalised heavy REE abundances are 3 – 15 times chondrite for the Swartruggens kimberlite and 2 - 6 times chondrite for the Star kimberlite. Primitive mantle normalised incompatible trace element patterns show strong negative Ti and Sr anomalies, subdued negative K, Rb, Nb and Ta and positive Pb anomalies for both localities. In addition, the majority of samples

from Swartruggens and Star show slight negative Zr and Hf anomalies. The Muil dyke at Swartruggens is considerably less enriched than any of the other dykes and shows no Ti anomaly.

The isotopic compositions of the two kimberlites show some variation, both between and within individual dykes (Swartruggens kimberlites: $^{87}Sr/^{86}Sr_i$ = 0.707711 to 0.710447, $^{143}Nd/^{144}Nd_i$ = 0.511825 to 0.511855, $^{176}Hf/^{177}Hf_i$ = 0.282160 to 0.282244; Star diamondiferous kimberlites: $^{87}Sr/^{86}Sr_i$ = 0.707304 to 0.708724, $^{143}Nd/^{144}Nd_i$ = 0.511997 to 0.512040, $^{176}Hf/^{177}Hf_i$ = 0.282472 to 0.282485; Star Barren Dyke: $^{87}Sr/^{86}Sr_i$ = 0.707183 to 0.707407, $^{143}Nd/^{144}Nd_i$ 0.512073 to 0.512077, $^{176}Hf/^{177}Hf_i$ = 0.282560 to 0.282564). Much of the variation in Sr isotope composition is argued to be due to interaction with groundwater and minor crustal contamination, with crustal contamination and peridotite entrainment accounting for the range in Hf and Nd isotope compositions. Despite having a similar Sr isotope composition to the Star diamondiferous kimberlite dykes, the Barren Dyke has considerably more radiogenic Nd and Hf isotope compositions and must originate from an isotopically distinct source region. The Swartruggens Muil Dyke has similar $^{87}Sr/^{86}Sr$ to the Swartruggens kimberlite dykes ($^{87}Sr/^{86}Sr_i$ = 0.708230 to 0.709797), but has much higher initial $^{143}Nd/^{144}Nd$ (0.511971 to 0.511990). Together with major and trace element evidence, this implies that the Muil lamprophyre is unrelated to the Swartruggens kimberlite dykes.

Following the isolation of the geochemical effects of alteration and crustal contamination, the geochemical variation within and between the Swartruggens kimberlite dykes is consistent with up to 50% entrainment of peridotite (dominant in the Changehouse Dyke) and minor amounts of olivine and phlogopite fractionation (dominant within the South Fissure). The primary kimberlite magma is inferred to have a composition between the trends of peridotite entrainment and olivine and phlogopite fractionation. The major element variation within and between the Star diamondiferous kimberlite dykes is consistent with up to 40% dilution by peridotite (dominant in the East Star Dyke) and small degrees of fractionation of olivine and phlogopite (dominant within the Byrnes Dyke), and the primary kimberlite magma is similarly inferred to have a composition between these two trends. However, the variable La/Yb_n between the different dykes requires further explanation, and is interpreted to reflect a continuum of small degrees of partial melting, with the Wynandsfontein and East Star Dykes being slightly lower degree partial melts than the Bymes and Clewer Dykes.

The Swartruggens close-to-primary kimberlite magma contains ~38 wt % SiO_2, ~21 wt % MgO, ~8.5 wt % CaO and ~6.6 wt % K_2O, and is best represented by the Main Dyke. For a similar MgO content (~22 wt %), the Star close-to-primary kimberlite magma is less enriched in SiO_2 (~36 wt %) and K_2O (3.3 wt %) and more enriched in CaO (~10.5 wt %) than that at Swartruggens, and is best represented by the Wynandsfontein Dyke. The close-to-primary magmas at both Swartruggens and Star are strongly enriched in both the compatible and incompatible trace elements, with greater enrichment in the more, relative to the less, incompatible trace elements relative to primitive mantle. Superimposed on relatively smooth enrichment patterns, both close-to-primary kimberlite magmas display strong negative K, Ti and Sr anomalies, subdued negative Nb, Ta and Hf, and strong positive Pb anomalies, when normalised to primitive mantle values. The primary magmas at both localities have steep chondrite normalised REE

patterns, with greater enrichment in the light REE than the heavy REE. The Swartruggens close-to-primary kimberlite magma is more enriched in the heavy REE (Gd/Yb_n = 6.9) than that at Star (Gd/Yb_n = 11.0).

Integration of major and trace element and isotopic data allows the nature of the likely source region of the primary kimberlite magmas to be inferred. Trace element concentrations in source regions of the Swartruggens and Star kimberlites have been calculated using simple partial melting modelling assuming low degrees of partial melting of a garnet lherzolite source. For both these Group II kimberlites, the calculated source regions are strongly enriched in incompatible trace elements, and, importantly, depleted in HREE relative to primitive mantle values. Superimposed on relatively smooth enrichment patterns, the calculated source regions of the Swartruggens and Star kimberlites show similarly sized strong negative Ti, K and Sr anomalies when normalised to primitive mantle. Although the negative Ti and K anomalies present in the kimberlite magmas could be created by residual accessory phases such as phlogopite, K-richterite and titanates, these phases are argued not to have been residual after the partial melting events giving rise to these two kimberlites. The inferred depletion in the heavy REE relative to primitive mantle suggests that the respective source regions of the Star and Swartruggens kimberlites were located within the lithospheric mantle, rather than within a convecting asthenospheric or plume mantle, and both sources had experienced a melt depletion event prior to strong metasomatic enrichment preceding kimberlite genesis. Ce/Pb and Nb/U ratios of the Swartruggens and Star kimberlites are similar to those of Karoo and Etendeka flood basalts, considered by some authors to be of lithospheric origin, but are much lower than those of asthenosphere derived mid-ocean ridge basalts (MORB) and plume derived ocean island basalts (OIB). The Sr and Nd isotope compositions of the close-to-primary kimberlite magmas at each locality require a source region that has been separated from the convecting mantle for some time and thus support a lithospheric origin for the two kimberlites. Model Nd enrichment ages, calculated relative to depleted mantle and using the Sm/Nd of the calculated kimberlite source regions, suggest the enrichment event occurred at a minimum of 1 Ga. The source regions of the Swartruggens and Star kimberlites are therefore inferred to be located within the sub-Gondwana lithospheric mantle. Their geochemical composition does not require a contribution from Mesozoic plume material prior to or during the break-up of the supercontinent.

Acknowledgements

First and foremost, my sincere thanks to my supervisor, Anton le Roex, for the opportunity to undertake this study and for his considerable guidance, support, enthusiasm and patience. Thank you also to John Gurney, for help in the field and for his advice as my co-supervisor.

Thanks to Jim Davidson and Helam and Star Diamond Mines, for organising two trips underground and allowing me to freely sample the kimberlite dykes.

Geoff Nowell and Graham Pearson at the Department of Earth Sciences, Durham University, who sparked my interest in kimberlites: thank you for the use of the Arthur Holmes Isotope Geosciences Laboratory and for all your help with obtaining Sr, Nd and the most precise Hf isotope data ever recorded. Thank you especially to Geoff for his continued support and innumerable long distance phone calls.

At the University of Cape Town, I would like to thank Andreas Späth for help with the electron microprobe and ICP-MS analyses. Also thank you to all the support staff, who have helped me out so much over the course of this project; in particular, David Wilson, Ernest Stout, Fayrooza Rawoort, and Shireen Govinder for your help with sample preparations and analyses. To all the post-grads at UCT – thank you for a great time! A special thank you to Kalle Westerlund and Megan Coetzee for your support, proof reading and (usually constructive) criticism.

Last, not least, my family and friends: without your love and encouragement I would never have finished – thank you!

Contents

Chapter 1

Introduction

1.1 Kimberlites

Kimberlites are extremely rare, volatile-rich, alkaline igneous rocks. Despite their small total volume, they have attracted large interest not only because of their economic importance as the main primary host for diamonds, but also because they are geologically significant for a number of reasons. They are believed to originate from deeper in the mantle than any other magma type and they carry xenoliths of both upper and lower mantle that give an important insight into mantle processes (e.g. Wagner, 1914; Boyd, 1987; Finnerty and Boyd, 1987). The kimberlite magmas themselves are also unusual, being extremely enriched in certain incompatible trace elements despite their low SiO_2 and high MgO contents. As hybrid rocks, with widely diverse petrography, major element geochemistry and texture even within individual intrusions, kimberlites are difficult to unambiguously define (e.g. Mitchell, 1995). The commonly accepted definition of Clement *et al.* (1984), is quoted below:

> *"Kimberlite is a volatile rich, potassic, ultrabasic, igneous rock which occurs as small volcanic pipes and sills. It has a distinctively inequigranular texture resulting from the presence of macrocrysts set in a finer-grained matrix. This matrix contains, as prominent primary phenocrystal and/ or groundmass constituents, olivine and several of the following minerals: phlogopite, carbonate (commonly calcite), serpentine, clinopyroxene (commonly diopside), monticellite, apatite, spinels, perovskite and ilmenite. The macrocrysts are anhedral, mantle-derived, ferromagnesian minerals which include olivine, phlogopite, picroilmenite, chromian spinel, magnesian garnet, clinopyroxene (commonly diopside), and orthopyroxene (commonly enstatite). Olivine is extremely abundant relative to the other macrocrysts, all of which are not necessarily present. The macrocrysts and relatively early-formed matrix minerals are commonly altered by deuteric processes, mainly serpentinisation and carbonitisation. Kimberlite commonly contains inclusions of upper mantle-derived ultramafic rocks. Variable quantities of crustal xenoliths and xenocrysts may also be present. Kimberlite may contain diamond but only as a very rare constituent."*

Kimberlites occur world-wide, but are generally confined to Archean / Proterozoic cratons or Proterozoic stable platforms, with diamonds usually only occurring in on-craton kimberlites (Clifford, 1966; Dawson, 1970). Unlike other kimberlite provinces worldwide, two distinct groups of kimberlites exist in southern Africa. First identified as petrologically different by Wagner (1914), who termed them "basaltic" and "micaceous" kimberlites based on the abundance of phlogopite in the latter relative to the former, these two

groups were later discovered to be isotopically distinct (Smith, 1983a). Smith (1983a) termed "Group I kimberlites" those with $^{87}Sr/^{86}Sr_i = 0.7033 - 0.7049$, $^{143}Nd/^{144}Nd_i = 0.51271 - 0.51277$, $^{206}Pb/^{204}Pb_i = 18.45 - 20.05$ and "Group II kimberlites" those with $^{87}Sr/^{86}Sr_i = 0.7074 - 0.7109$, $^{143}Nd/^{144}Nd_i = 0.51208 - 0.51228$, $^{206}Pb/^{204}Pb_i = 17.2 - 17.7$. Group I kimberlites broadly correspond to Wagner's "basaltic kimberlites" and are similar to those found world-wide, whereas Group II kimberlites correspond to Wagner's "micaceous kimberlites" and appear to be unique to southern Africa. Mitchell (1994) claims that Group II kimberlites are in fact not true kimberlites and suggested that they be renamed "orangeites". The IUGS now recommend a characterisation, rather than a definition, of both Group I and Group II kimberlites based on their characteristic mineral assemblages (Le Maitre, 2002), following the earlier work of Dawson (1980), Clement *et al.* (1984) and Mitchell (1994, 1995). A third group of kimberlites "transitional kimberlites", with mineralogy and isotope geochemistry intermediate between Group I and Group II kimberlites, have also been recognised (Skinner, 1989; Skinner *et al.*, 1992).

Kimberlite intrusions most commonly form pipes or "diatremes", with vertical axes and steep (75 – 85°) margins, consisting primarily of diatreme facies kimberlite or tuffistic kimberlite breccia (Clement, 1982). These are thought to arise due to build up of pressure as vapour phases segregate from the kimberlite magma at depth (e.g. Wyllie, 1980) or due to interaction of the kimberlite magma with groundwater in the crust, leading to rupturing of the country rock and explosive phreatomagmatic emplacement (Lorenz *et al.*, 1999). Kimberlite diatremes commonly contain abundant xenolithic and xenocrystic material, including bodies of country rock, and are often pervasively altered by low temperature deuteric and weathering processes (Clement, 1982). However, kimberlites also occur as hypabyssal dykes and sills, which may be associated with root zones of diatremes (as precursor, contemporaneous, or crosscutting intrusions; Clement, 1982), but are also emplaced in settings apparently unrelated to major pipes. Dyke systems such as these may represent volumes of magma either too small, or with volatile contents too low, for explosive emplacement, or intrusion into host rock structures that are not conducive to pipe formation (e.g. Gurney and Kirkley, 1996). Alternatively, these dyke systems may be feeders to pipes that have now been eroded away (Gurney and Kirkley, 1996).

1.2 Models of kimberlite petrogenesis

Over the last thirty years, kimberlites have been studied from many angles, from their mantle xenoliths, diamonds and their inclusions, megacrysts and using experimental petrology, as well as the bulk rock major and trace element geochemistry and radiogenic isotope systematics of the kimberlite magmas themselves. Kaapvaal craton mantle xenolith geothermobarometry (e.g. Finnerty and Boyd, 1987) has yielded geotherms that approximately correspond to the 40mW/m^2 conductive model geotherm of Pollack and Chapman (1977). Therefore, using the graphite-diamond phase boundary of Kennedy and Kennedy (1976), the origins of diamond-bearing kimberlites of the Kaapvaal craton are constrained to pressures greater than approximately 5GPa. Kimberlites are commonly thought to have equilibrated against residual garnet, due to the depletion in heavy rare earth elements (REE) relative to basaltic magmas and the low Al_2O_3 contents of

the magmas (e.g. Tainton and McKenzie, 1994). On this basis, their major element abundances constrain their origin to pressures greater than 6GPa, using phase petrology known to date (Sweeney and Winter, 1999). A deeper origin has been proposed for some kimberlites due to the presence of high pressure minerals such as majorite and ferropericlase included in diamond (e.g. Moore and Gurney, 1985, 1989; Hart and Harris, 1994). Although supported by the experimental data of Ringwood *et al.* (1992) and Kesson *et al.* (1994), this is in conflict with the study of Canil and Scarfe (1990), who reported that although protokimberlitic magmas may exist at depths greater than 7 GPa, such magmas are not erupted on the Earth's surface.

The high degree of enrichment of the incompatible elements in kimberlites indicates that they formed from small degrees of partial melting (e.g. Tainton and McKenzie, 1994; le Roex *et al.*, 2003). Experimental work has confirmed that kimberlite-like magmas can be produced by small degrees (1-2%) of melting of carbonated garnet lherzolite at pressures between 5 and 7 GPa (Eggler and Wendlandt, 1979; Wyllie, 1980; Canil and Scarfe, 1990; Girnis *et al.*, 1995; Dalton and Presnall, 1998; Ulmer and Sweeney, 2002), with a number of these experiments illustrating the importance of CO_2 and H_2O in the starting composition. The experimental data of Ringwood *et al.* (1992), suggested a transition zone origin (14 GPa) although on later revision these workers conceded that they could not preclude melting at around 300 km depth (Kesson *et al.*, 1994).

There is much evidence for a relationship between kimberlites and mantle plumes or hotspots (Crough *et al.*, 1980, le Roex, 1986) and the backtracking of hotspots and plate motions world wide reveals a correlation that is significant at the above the 90 % level (Crough *et al.*, 1980). South African Group I kimberlites have trace element ratios (e.g. Nb/U and Ce/Pb) similar to those of ocean island basalts (le Roex *et al.*, 2003) and, together with other kimberlites world wide, have Sr, Nd, Pb and Os isotope systematics consistent with an asthenospheric origin (Smith, 1983a; Pearson *et al.*, 1995, 2003a). However, the theory of protokimberlitic magmatism beginning at the core-mantle boundary, based on the timing correlation between periods of kimberlite eruption and perturbation of the geomagnetic field, interpreted to reflect disruption of the D" layer and the beginning of a mantle plume (Haggerty, 1994), has recently been rejected based on whole rock W isotope systematics of kimberlites (Schersten *et al.*, 2004). The recent work of le Roex *et al.* (2003), and Harris *et al.* (2004) suggests the relationship between Group I kimberlites and hotspots, is rather one of metasomatism of a lithospheric source by sub-lithospheric, plume derived melts or fluids, than of an entirely sub-lithospheric origin.

Although a sub-lithospheric contribution to the source region of Group I kimberlites remains undisputed, there is considerable evidence this may not be the case for the source region of Group II kimberlites. Smith (1983a) proposed that the isotopic systematics of Group II kimberlites require a source in enriched mantle that has been separated from the convecting mantle for some time. Using inversion modelling of trace element data, Tainton and McKenzie (1994) illustrated that the source region of Group II kimberlites had suffered a depletion event, with subsequent strong enrichment, prior to kimberlite genesis. The source region of these kimberlites must be separated from the convecting mantle for this depleted signature to be

preserved. Experimental evidence neither confirms nor refutes this theory, as those studies suggesting a deeper origin for kimberlites (Ringwood *et al.*, 1992) were carried out on kimberlites of Group I composition. In an experimental study on Group II kimberlites, Ulmer and Sweeney (2002) constrain their origins merely to pressures greater than 6GPa.

Several lines of evidence, however, have been proposed to suggest that a sub-lithospheric origin for Group II kimberlites cannot, as yet, be completely rejected. le Roex (1986) suggested that the isotopic systematics of Group II kimberlites do not preclude an sub-lithospheric origin. He noted that Group II kimberlites have similar isotopic systematics and trace element ratios to those of Dupal ocean island basalts (OIB), generally considered to be related to mantle plumes containing a proportion of subducted oceanic crust, whereas Group I kimberlites have isotopic systematics similar to non-Dupal OIB. In addition the most radiogenic Os isotope compositions of Group II kimberlites are similar to those of Group I kimberlites, supporting an origin for both in the convecting asthenoshere (Pearson *et al.*, 2003a). Hf isotope systematics have also been used to argue for a common source for Group I and Group II kimberlites, as the continuum in Hf isotope compositions between the two groups is not considered supportive of entirely separate source regions (Nowell *et al.*, 1999, 2004; Dowall *et al.*, 2003a). However, unlike Group I kimberlites as discussed below, the Hf isotope systematics of Group II kimberlites are not widely different from those of other mantle melts and thus Hf isotope evidence cannot refute a lithospheric origin for Group II kimberlites (Nowell *et al.*, 2004).

Another important aspect to consider in the petrogenesis of kimberlite magmas is the role of subducted slabs. Following the ideas of Sharp (1974) and Helmstaedt and Gurney (1984, 1997), McCandless (1999) proposed that kimberlite magmatism is triggered by the presence of deep-seated subducted oceanic slabs. He proposed that spatial-temporal trends in kimberlite magmatism in southern Africa and North America are correlated with reductions in plate convergence over the last approximately 200 Ma, and that the quantity of water held by a slab is enough to trigger significant melting. The transition zone origin theory of Ringwood *et al.* (1992) also favours that this boundary layer was refertilised by partial melts from a subducted slab. Nowell *et al.* (1999, 2004) report that the deviation in Hf isotope systematics from the well defined mantle array in Hf-Nd space, particularly apparent in Group I kimberlites, cannot be accounted for by a source region consisting of lithospheric or entirely asthenospheric mantle. These authors proposed that the signature reflects a contribution to the source region from a subducted slab within the sub-lithospheric mantle. Support for this hypothesis can be acquired from the high pressure melting experiments of Edgar *et al.* (1988), and Edgar and Charbonneau (1993) on the Wesselton Group I kimberlite. These experiments demonstrated that the composition of this kimberlite does not require derivation from a source containing either orthopyroxene or olivine, and that the primary magma may have been derived by partial melting of a garnetitic or eclogitic assemblage from a subduction-related process. However, on the basis that Os isotopic compositions of kimberlites are not more radiogenic than OIB (Pearson *et al.*, 2003a), these authors concluded that kimberlites cannot be derived solely from subducted slabs.

1.3 Purpose and scope of this study

Due to their hybrid nature and susceptibility to alteration, the bulk-rock geochemistry of kimberlites has commonly been thought to be far removed from that of the primary kimberlite magmas (e.g. Mitchell, 1995). Therefore, relatively little work has been done to date using the bulk-rock geochemistry of kimberlites to quantitatively evaluate their source region characteristics and the petrogenetic processes giving rise to kimberlites. Major and trace element analyses of kimberlites have been frequently reported, but generally on a more regional basis and without attempt to identify primary magma compositions (e.g. Dawson, 1971, 1980; Fesq *et al.*, 1975; Kable *et al.*, 1975; Clement, 1982; Shee, 1985). So far only one major study, that of Tainton and McKenzie (2004), has provided a combined major and trace element and isotopic approach to modelling the source regions of Group II kimberlites. The recent work of Price *et al.*, (2000) on the Jericho pipe in Canada, le Roex *et al.* (2003) on Group I kimberlites from Kimberley, and Harris *et al.* (2004) on the off-craton Group I Uintjiesberg kimberlite, has demonstrated the use of a suite of samples from one locality in quantifying the effects of secondary processes on a kimberlite magma, allowing isolation of the close-to-primary magmas compositions, which can then be used to model source region characteristics. This has been shown to yield valuable information about the source regions of, and the petrogenetic processes giving rise to, these kimberlites.

This study is focussed on two Group II kimberlite dyke swarms, Swartruggens and Star, located on the Kaapvaal craton in South Africa. Both dyke swarms are currently being mined to considerable depths, giving access to relatively fresh kimberlite samples. Sample suites from each of the exposed dykes at Swartruggens and Star have been petrographically described and analysed for a range of major and trace element abundances, and Sr, Nd and Hf isotopes, with the following objectives in mind:

- To document and describe the major and trace element and Sr, Nd and Hf isotope compositions of the Swartruggens and Star kimberlite dykes, to evaluate the variation within and between individual dykes at each locality, and to compare the two localities to each other and to other South African Group II and Group I kimberlites.
- To use the sets of data from each locality to assess the effects of alteration, crustal assimilation, peridotite entrainment and crystal fractionation on the bulk rock geochemistry of the samples studied, and so to isolate the major and trace element and isotopic characteristics of the primary kimberlite magmas.
- Using the close-to-primary kimberlite magma compositions, to quantitatively model the source region trace element characteristics at each locality, and to thus constrain the petrogenetic processes giving rise to the Swartruggens and Star kimberlite magmas.
- To assess the lithospheric versus asthenospheric contributions to, and evolution of, the source regions at each locality.

Chapter 2

Geological Setting and Sampling

2.1 Introduction

Southern Africa is peppered with occurrences of both Group I and Group II kimberlites, occurring both on and off the Kaapvaal craton, a stable Archean shield with a surface area of 1.2 x 10^6 Km^2 (de Wit *et al.*, 1992) and roots that are at least 3.3Ga (Richardson *et al.*, 1984). The distinction between on- and off-craton kimberlites is important principally from an economic perspective, as those that occur on-craton may be diamond bearing, whereas those that occur off-craton are generally not (Clifford, 1966). The locations of some major kimberlite provinces in South Africa relative to the Kaapvaal craton are illustrated in Figure 2.1.

2.2 Location of the Swartruggens and Star kimberlite dyke swarms

Both the Swartruggens and Star kimberlite dyke swarms are both located on the Kaapvaal craton in South Africa (Figure 2.1). The Swartruggens kimberlite is situated in the centre of the craton, approximately 60km West of Rustenberg, in the Northwest Province (McKenna, 2001; Figure 2.1). The Star kimberlite is located in the centre of the southern extent of the craton, 10km North of Theunissen (Hill, 1989; Figure 2.1).

2.3 Nature and geological setting of the Swartruggens kimberlite dyke swarm

The Swartruggens kimberlite is a Group II micaceous kimberlite (e.g. Smith, 1983a and b) consisting of a series of *en echelon* kimberlite dykes, which trend East-West for a minimum strike length of 7km (Gurney and Kirkley, 1996). Two principal parallel dykes occur at Swartruggens, the Main Dyke, which represents the first intrusive phase (Klump, 1995) and has the highest diamond grade of any kimberlite in South Africa (Gurney and Kirkley, 1996), and the crosscutting sub-economic Changehouse Dyke. The estimated diamond grade of the Changehouse Dyke is up to 90% lower than that of the Main Dyke (McKenna, 2001). The Main Dyke reaches up to 60cm in width, whereas the Changehouse dyke is typically only 20-40cm wide (Gurney and Kirkley, 1996; McKenna, 2001). In addition, the North and South Fissures are encountered to the eastern extent of the dyke swarm, in the Third Lease section of the mine. A fifth dyke, the barren Muil Dyke, occurs in the western 2-3km of the dyke system. This dyke contains neither diamonds nor other indicator minerals (Gurney and Kirkley, 1996) and is argued by some to be a lamprophyre rather than a true kimberlite (e.g. Skinner and Scott, 1979). The Muil Dyke crosscuts the kimberlite dykes (Klump, 1995), but

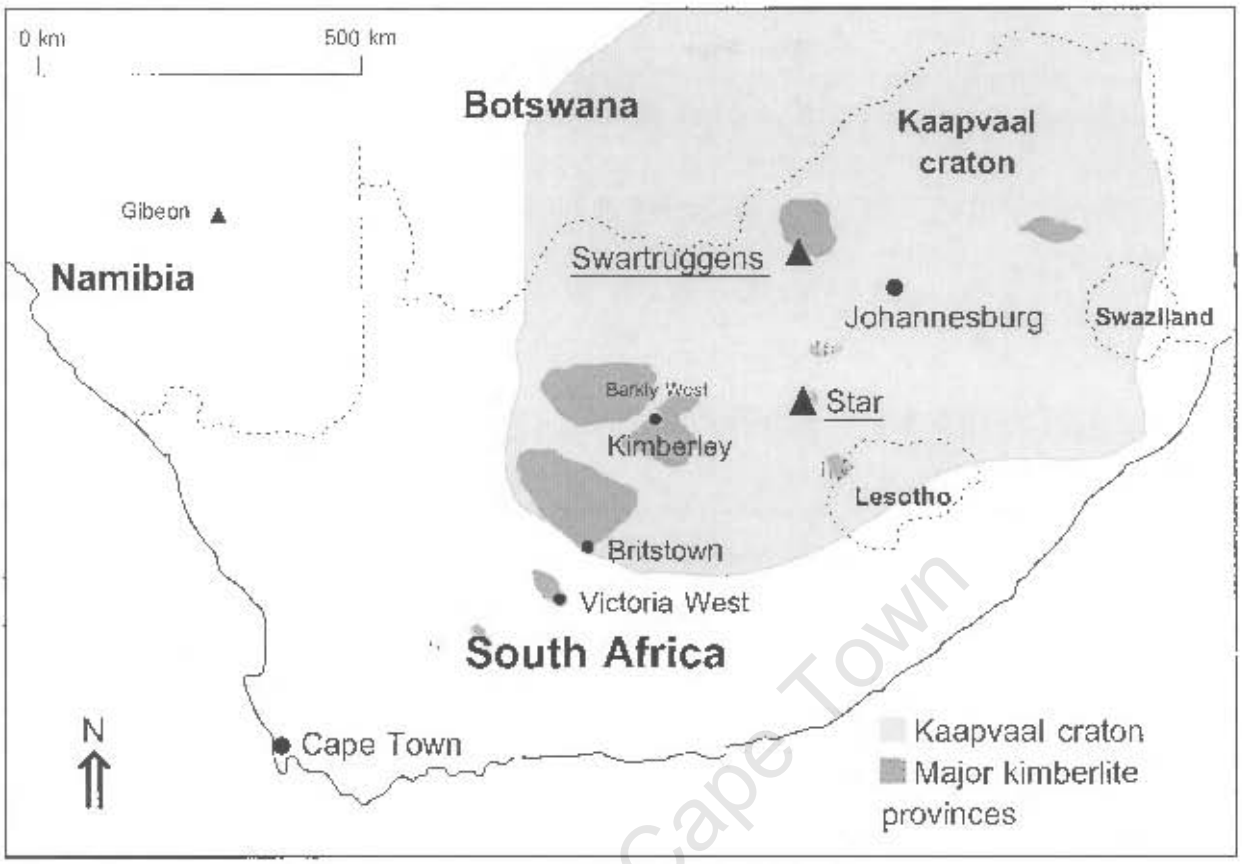

Figure 2.1 Map of Southern Africa illustrating the location of the Swartruggens and Star kimberlite dyke swarms, the extent of the Kaapvaal craton, and other major kimberlite provinces, after Mitchell (1995).

contacts are gradational indicating that it was emplaced at a similar time (Gurney and Kirkley, 1996). However, the genetic relationship of the Muil Dyke to the kimberlite dykes has not previously been established. Using Rb-Sr dating of phlogopite macrocrysts, Smith *et al.* (1985a) acquired an age of 156 ± 13 Ma for the kimberlite dykes. Although one Muil Dyke sample was included in the study of Smith *et al.* (1985a), and it appeared to plot on the isochron of the kimberlite dykes, it cannot be concluded that the Muil dyke is related to the kimberlite dykes.

The Precambrian Transvaal Sequence of andesitic lavas and metasediments host the Swartruggens kimberlite (McKenna, 2001). At the surface, the kimberlite dykes intrude lavas and shales to approximately 1km depth, below which is a layer of shale and slate approximately 1.5km thick (Gurney and Kirkley, 1996). A thick sequence of Chuniespoort dolomite is encountered at approximately 2km depth (Gurney and Kirkley, 1996; Kirkley, 1987). The incompetent, fractured nature of the host shales causes a wide range in thickness of the dykes along strike, lenses sometimes pinch or end abruptly, and intertwining of the dykes is common (Gurney and Kirkley, 1996). The Swartruggens kimberlite occurs in close proximity to the Bushveld complex, and it exploits Bushveld related structures during emplacement (McKenna, 2001). Unfortunately, a detailed map of the outcrop of the Swartruggens kimberlite dykes is not available.

2.4 Nature and geological setting of the Star kimberlite dyke swarm

The Star micaceous kimberlite consists of a series of East-West trending *en echelon* dykes with a strike length of 5 km and is part of a larger (15km long) system of dykes and a number of associated small blows (Hill, 1989; Figure 2.2). It has been dated using the K-Ar method at 124 Ma (McIntyre and Dawson, 1976). From East to West, the Star dyke swarm consists of the Wynandsfontein, East Star, Byrnes, Micaceous or Barren, Clewer and South Fissure Dykes (Figure 2.2). The diamond grade of the Star kimberlite dykes varies from zero in the Barren Micaceous Dyke to as high as 150ct/100 tonne for the East Star Dyke (Campbell, 1975). The Byrnes Dyke yields an average grade of approximately 40 ct/100 tonne (Gurney and Hatton, 1989). The South Fissure intersects the Clewer Dyke and extends further to the East (Figure 2.2). This dyke has a widely variable diamond grade, and possibly represents a mixture of the Barren Micaceous Dyke and the economic Clewer Dyke (Gurney and Kirkley, 1996). The Phoenix Pipe, a small blow located at the western end of the dyke system postdates the kimberlite dykes (Hill; 1989; Figure 2.2). At the surface the dykes consist of multiple thin stringers rather than single discrete intrusions, but at depth the stringers consolidate into fewer, wider intrusions with dyke widths commonly 45 - 60 cm, although widths of 90 - 100cm are sustained over short distances (Gurney and Kirkley, 1996).

The country rocks hosting the Star kimberlite dyke swarm are Late Permian to Early Triassic shales, sandstones and dolerites of the Beaufort Series of the Karoo System (Hill, 1989), which overly Precambrian basement gneisses (Kirkley, 1987).

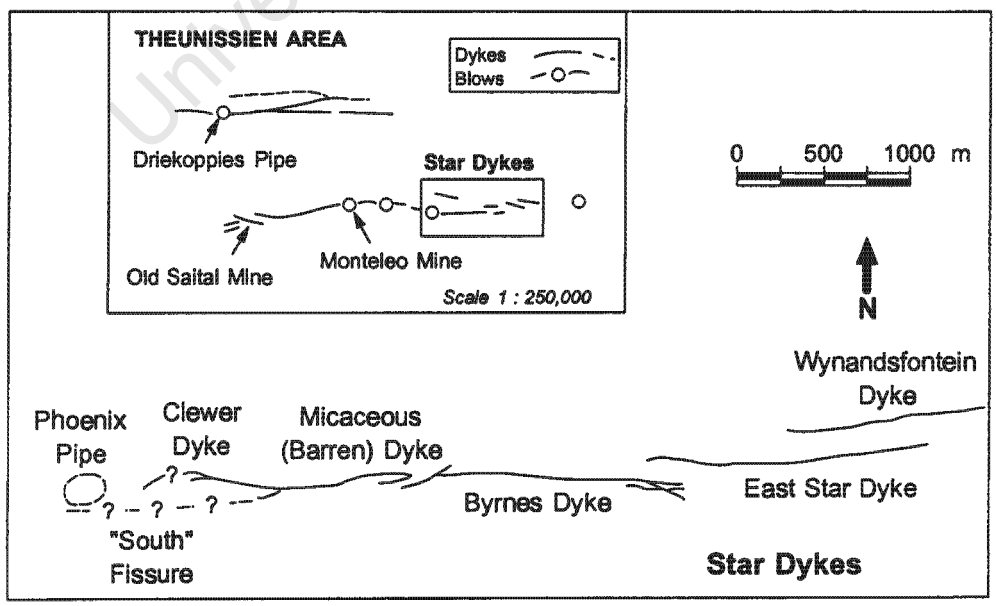

Figure 2.2 Schematic map showing the outcrop of the Star kimberlite dykes in the Theunissen area. After Hill (1989) and Gurney and Kirkley (1996).

2.5 Sampling

Samples, numbered NC 004 - 014, were collected from each of the exposed dykes at Swartruggens (the Main, Changehouse, South Fissure and Muil Dykes) for this project during a visit to the Helam mine in January 2002. Samples NC 001 to NC 003 were collected during the same visit from the Third Lease mining dump. Since both the North and South Fissures had been mined in this area and it is uncertain to which dyke the samples belong, these samples are referred to as "Third Lease samples" throughout this work. It will be demonstrated, however, that these samples are geochemically distinct from those obtained from the South Fissure, and thus they are more likely to represent the North Fissure. A further collection of samples was taken from the University of Cape Town mantle room collection, collected by John Gurney and Jens Klump. A full list of samples from the Swartruggens kimberlite analysed in this work and their localities is reported in Appendix 1, together with individual petrographic descriptions and photomicrographs.

The majority of the Star samples analysed in this work are from the University of Cape Town mantle room collection, and were collected by John Gurney and Stuart Hill. Samples NC 050 - 054 were collected for this project during a visit to the Star mine in July 2002. Samples taken from the Barren Micaceous Dyke have widely differing abundances of mica, and this dyke is hereafter referred to simply as the "Barren Dyke". A full list of samples from the Star kimberlite analysed in this work and their localities is reported in Appendix 2, together with individual petrographic descriptions and photomicrographs.

Chapter 3

Petrography

3.1 Introduction

Petrographically kimberlites are diverse rocks, and consequently definitions based on their mineralogy are complex and often confusing. Their mineralogy is complicated by the presence of xenoliths and xenocrysts of both mantle and crustal material entrained by the magma *en route* to the surface, and by the alteration of primary phases by late stage deuteric fluids. In addition, kimberlites are permeable and porous, and so are susceptible to large quantities of groundwater infiltration, which further alters the primary minerals as well as crystallising secondary minerals such as calcite. Consequently the IUGS (Le Maitre, 2002) recommend a mineralogical characterisation, rather than a definition, of Group II kimberlites, as quoted below:

"[Group II kimberlites] *are characterised by phlogopite macrocrysts and microphenocrysts, together with groundmass micas which vary in composition from "tetraferriphlogopite" to phlogopite. Rounded macrocrysts of olivine and euhedral primary crystals of olivine are common but are not invariably major constituents.*

Characteristic primary phases in the groundmass include: diopside, commonly zoned to, and mantled by, titanian aegirine; spinels ranging in composition from Mg-bearing chromite to Ti-bearing magnetite; Sr- and REE-rich perovskite; Sr-rich apatite; REE-rich phosphates (monazite, daqingshanite); potassian barian titanites belonging to the hollandite group; potassium triskaidecatitanites ($K_2Ti_{13}O_{27}$); Nb-bearing rutile and Mn-bearing ilmenite. These are set in a mesostasis that may contain calcite, dolomite, ancylite and other rare-earth carbonates, witherite, northesite and serpentine.

Evolved members of the group contain groundmass sanidine and potassium richterite. Zirconium silicates (wadeite, zircon, kimzeyitic garnet, Ca-Zr-silicate) may occur as groundmass minerals. Barite is a common deuteric secondary mineral."

Both the Swartruggens and Star kimberlites have been previously identified as micaceous Group II kimberlites. The petrography of the Swartruggens kimberlites has previously been studied by Skinner and Scott (1979), Allen (1990), and Hammond and Mitchell (2002). The petrography of the Star kimberlite has previously been described by Skinner (1976). However, detailed petrographic examination of the samples studied in this work is important, not only to document petrographic similarities and differences between individual dykes at each locality and between the two localities, but also to assess the degree of alteration,

crustal contamination and peridotite assimilation, all of which may have affected the whole-rock geochemistry of the analysed samples. In this chapter the petrography of each of the kimberlites is summarised, and modal proportions (in volume %) of each of the dykes at Swartruggens and Star, based on visual estimates, are given in Tables 3.1 and 3.2, respectively. However, it should be recognised that many of the samples are heterogeneous on a hand-specimen scale, particularly with respect to the abundance of macrocrysts and the degree of alteration. Thin sections are thus not necessarily representative of the entire sample. The individual dykes are then further classified according to the scheme of Skinner and Clement (1979) who proposed that prefixes should be added in order of increasing mineral abundances. Detailed petrographic descriptions and photomicrographs of each individual sample are given in Appendices 1 (Swartruggens) and 2 (Star). In the following descriptions, the term *macrocryst* is used for crystals larger than 2mm in size (Mitchell 1995). Minerals belonging to the macrocryst suite have previously been attributed to disaggregated mantle peridotite assimilated by the kimberlite *en route* to the surface (e.g. Clement, 1982, Shee, 1985, le Roex *et al.*, 2003). However, in accord with previous kimberlite studies, the term macrocryst is preferred to xenocryst, as it is free from genetic inferences (Mitchell, 1995). Many of the macrocrysts at both localities are fragmented, and anhedral fragments smaller than 2mm are also classed with the macrocryst suite, with the term *phenocryst* being reserved for euhedral or subhedral crystals between 0.5mm and 2mm which are believed to have crystallised from the kimberlite magma. The term *microphenocryst* is used to describe subhedral to euhedral crystal less than 0.5mm in size, set in a finer grained or interstitial groundmass.

3.2 Petrography of the Swartruggens kimberlite dykes

The petrography of the Swartruggens kimberlite dykes has been determined optically from nineteen thin sections (3 from the Third Lease, 7 from the Main Dyke, 4 from the Changehouse Dyke and 4 from the South Fissure). Individual petrographic descriptions of the samples are reported in Appendix 1, with photomicrographs of each sample. Petrographically, the Swartruggens Muil Dyke differs in many ways from the Swartruggens kimberlite dykes and it will be discussed separately in Section 3.3.

3.2.1 Texture

The Swartruggens kimberlite dykes typically have a macrocrystic texture, containing between 10 and 50 volume % macrocrysts in a fine-grained groundmass, although macrocrysts are widely variable in abundance within individual dykes (Table 3.1). The most macrocrystic samples are from the Changehouse Dyke (Plate 3.1a), which contains at least 25 volume %, and up to 50 volume % macrocrysts, whereas some macrocryst-poor and aphanitic samples, with less than 10 volume % macrocrysts, are found within the Main Dyke and Third Lease (Plate 3.1b; Table 3.1). The South Fissure samples contain between 20 and 35 volume % macrocrysts. The macrocryst suite is composed dominantly of olivine with subordinate phlogopite in these samples, with olivine comprising almost the entire macrocryst suite of the Changehouse Dyke (Table 3.1). Phenocryst proportions in the Swartruggens kimberlites range up to 40 volume % and are most abundant in the Changehouse Dyke, where they comprise 20 to 40 volume % of the rock (Table 3.1). The

Third Lease samples contain between 10% and 30% phenocrysts, and the Main Dyke and South Fissure contain between 10 and 20 volume % phenocrysts. Phlogopite is the most abundant phenocryst phase in all the Swartruggens kimberlites, although diopside phenocrysts are also present in the Changehouse Dyke and present in minor amounts (up to 2 volume %) in the other dykes, and olivine phenocrysts are present in some Changehouse Dyke samples. The groundmass of the Swartruggens kimberlite dykes is fine-grained with equigranular microphenocrysts approximately 0.1 to 0.2 mm in size of phlogopite and calcite, and an interstitial matrix of carbonate and serpentine. Diopside is present in small amounts throughout the groundmass of the Changehouse Dyke, South Fissure and Third Lease samples, but only occasionally present in minor amounts in the Main Dyke groundmass (Table 3.1).

Flow features are evident in all the Swartruggens kimberlite dykes, with macrocrysts, phenocrysts and groundmass minerals commonly aligned parallel to the dyke margins. The macrocrysts are sometimes separated into bands parallel to the fabric of the rock, and the groundmass minerals are commonly bent around the macrocrysts (Plate 3.1c).

Table 3.1 Modal proportions (volume %), based on visual estimates, of the main macrocryst, phenocryst and groundmass phases in the Swartruggens kimberlite dykes and the Muil lamprophyric dyke. Other = serpentine, chlorite, opaque oxides, apatite, perovskite.

Dyke	Third Lease	Main dyke	Changehouse Dyke	South Fissure	Muil Dyke
Macrocrysts	**10 – 25**	**10 – 30**	**25 – 50**	**20 – 35**	**5 - 25**
Olivine	5 – 20	5 – 20	20 – 45	10 – 30	5 - 25
Phlogopite	< 5 – 10	< 5 – 15	< 5 – 10	<5 – 10	-
Phenocrysts	**10 – 30**	**10 – 20**	**20 – 40**	**10 – 20**	**10 - 20**
Phlogopite	10 – 30	10 – 20	15 – 30	10 – 20	0 – 5
Diopside	< 2	< 1	5 – 10	< 1	< 2
Olivine	-	-	0 – 5	-	5 - 10
Groundmass	**45 – 80**	**50 – 80**	**20 – 40**	**40 – 70**	**50 - 85**
Phlogopite	30 – 40	40 – 70	15 – 30	30 – 60	25 – 40
Calcite	10 – 30	< 5 – 10	< 5	5 – 10	0 – 20
Diopside	< 5	< 1	< 5	< 2	5 – 20
Olivine	-	-	< 3	-	5 – 10
Sanidine	-	-	-	-	10 - 30
Other	5 – 10	1 – 10	1	<1	2 - 5

3.2.2 Macrocryst Phases

Olivine is the most abundant macrocryst phase in the Swartruggens kimberlite dykes, and constitutes up to 95% of the macrocryst suite. As well as having a generally higher proportion of macrocrysts, the Changehouse dyke contains a higher proportion of olivine relative to phlogopite in the macrocryst suite, with

olivine macrocrysts constituting 20 to 45 volume % of the samples (Table 3.1). Olivine macrocrysts constitute similar proportions of the Main Dyke and Third Lease samples (5 – 20 vol. %; Table 3.1) and are slightly more abundant (10 - 30 vol. %; Table 3.1) in the South Fissure. In all the Swartruggens kimberlite dykes the olivine macrocrysts are rounded, anhedral and many are strained (Plate 3.1a, c and d). They range up to 8mm in size although larger macrocrysts are frequently fractured and many smaller (approximately 1mm diameter) fragments are present throughout the groundmass. The olivine macrocrysts are variably altered and very little or no fresh olivine remains; they are commonly completely serpentinised, and often further partially or completely replaced to calcite (Plate 3.1 c, d and f). Where replacement by calcite occurs, it is usually around the edge of the crystals and along fractures first. Some olivine macrocrysts are also partially replaced by phlogopite, especially around the edges of the crystals (Plate 3.1d). Opaque Fe-Ti oxides, up to 0.1mm in size, are common around the rims of, and sometimes within, relic olivine macrocrysts and are inferred to have formed during the breakdown of the olivine.

Phlogopite forms the remainder of the macrocryst suite in the Swartruggens kimberlite dykes. Phlogopite macrocrysts are most abundant in the Main Dyke, constituting less than 5 to 15 volume % of the samples and up to 50% of the macrocryst suite (Table 3.1). In the other Swartruggens kimberlite dykes phlogopite macrocrysts are less abundant (up to 10 vol. %; Table 3.1) and constitute only approximately 20 % of the macrocryst suite. The phlogopite macrocrysts tend to be smaller than the olivine macrocrysts but range up to 6mm in size. They are anhedral and rounded, and commonly elongate. Many phlogopite macrocrysts are extremely strained, with undulose extinction, and show extensive fracturing and kink banding. Some of the macrocrysts are torn apart along cleavage planes and infilled with calcite (Plate 3.1e and f). Many phlogopite macrocrysts are optically zoned, usually with darker cores than rims. In some samples the phlogopite has thin rims of tetraferriphlogopite. Some phlogopite macrocrysts are partially altered to chlorite, particularly within the Third Lease samples, although this is not pervasive within individual thin sections.

Representative major element analyses of phlogopite macrocrysts in the Main and Changehouse Dykes are reported in Table 3.2. The phlogopite macrocryst cores have compositions typical of mantle phlogopite (e.g. Gregoire *et al.*, 2002), with FeO* contents ranging from 4.27 – 5.19 wt % and Al_2O_3 contents ranging from 12.0 – 14.4 wt % (Table 3.2). The macrocryst rims have major element abundances consistent with the petrographic observation of tetraferriphlogopite rims, with higher FeO* (up to 10.5 wt %; Table 3.2) and suppressed Al_2O_3 contents (8.19 – 11.5 wt %). TiO_2 contents are also slightly higher in the rims than the cores of the phlogopite macrocrysts (rims TiO_2 = 1.88 – 2.06 wt %; cores TiO_2 = 1.43 – 1.88 wt %; Table 3.2).

Although only olivine and phlogopite macrocrysts were observed in the thin sections of samples used in this study, McKenna (2001) and Klump (1995) report garnet macrocrysts in the Main and Changehouse Dykes. In both dykes the garnets are of harzburgitic, lherzolitic and eclogitic origin, with considerably fewer eclogitic garnets in the Changehouse Dyke than the Main Dyke (McKenna, 2001).

Table 3.2 Representative major element analyses of phlogopites from the Swartruggens kimberlite dykes and the Muil lamprophyre. Mac = macrocryst; g'mass = groundmass; FeO* = total iron as FeO; Mg# = atomic Mg/(Mg + Fe^{2+}) with Fe_2O_3 /FeO = 0.2. Atomic proportions for these analyses have been calculated and are reported in Appendix 1.

Dyke	Main dyke							
Sample	NC 006	NC 006	NC 006	NC 006	NC 006	NC 010	NC 010	NC 010
Description	Phlog mac	Phlog mac	Phlog mac	Phlog g'mass	Phlog g'mass	Phlog mac	Phlog mac	Phlog mac rim
SiO_2	42.3	42.3	41.2	43.1	42.4	42.2	41.8	41.0
TiO_2	1.65	1.64	1.57	1.76	1.54	1.43	1.88	2.06
Al_2O_3	13.0	12.0	12.4	11.1	7.97	12.6	12.4	8.19
FeO*	4.76	5.19	4.94	4.80	9.24	4.90	4.46	10.5
MnO	0.02	0.02	0.05	0.02	0.07	0.04	0.06	0.08
MgO	24.7	23.9	25.1	24.8	24.2	24.4	23.9	24.6
CaO	0.02	0.01	0.02	0.03	0.09	0.01	0.02	0.12
Na_2O	0.23	0.30	0.19	0.20	0.12	0.19	0.24	0.25
K_2O	10.8	10.2	10.2	9.81	9.06	10.4	10.1	10.2
Total	97.5	95.6	95.8	95.6	94.7	96.2	94.8	96.9
Mg#	0.91	0.90	0.91	0.91	0.84	0.91	0.91	0.82

Dyke	Main Dyke					Changehouse Dyke		
Sample	NC 010	NC 010	NC 010	NC 010	NC 010	NC 009	NC 009	NC 009
Description	Phlog mac rim	Phlog g'mass	Phlog g'mass	Phlog g'mass	Phlog g'mass	Phlog mac	Phlog g'mass	Phlog g'mass
SiO_2	38.2	42.2	42.1	41.5	41.6	40.1	42.5	40.5
TiO_2	1.88	1.60	1.79	1.65	1.69	1.63	2.05	1.82
Al_2O_3	11.5	12.2	12.5	12.3	11.3	14.4	10.2	12.1
FeO*	8.13	4.95	4.33	5.53	6.57	4.27	5.58	4.57
MnO	0.06	0.01	0.03	0.06	0.04	0.02	0.08	0.00
MgO	24.1	25.1	24.2	25.3	25.5	25.3	24.5	24.5
CaO	0.00	0.08	0.03	0.03	0.03	0.08	0.14	0.05
Na_2O	0.21	0.18	0.12	0.13	0.13	0.25	0.24	0.15
K_2O	11.8	10.7	10.5	10.8	10.5	11.1	8.72	9.62
Total	95.9	97.1	95.6	97.3	97.4	97.2	94.0	93.3
Mg#	0.86	0.91	0.92	0.90	0.89	0.92	0.90	0.91

Dyke	Changehouse Dyke		Muil Dyke					
Sample	NC 009	NC 005	NC 012	NC 012	NC 012	NC 012	NC 012	NC 012
Description	Phlog g'mass	Phlog g'mass	Phlog g'mass	Phlog g'mass	Phlog g'mass	Phlog g'mass	Phlog g'mass	Phlog g'mass
SiO_2	41.0	39.4	38.3	37.8	39.8	39.6	39.3	40.1
TiO_2	1.92	1.47	3.87	3.74	3.33	3.75	3.41	3.05
Al_2O_3	12.9	11.8	11.9	12.0	11.9	12.7	11.3	10.2
FeO*	4.45	5.65	7.42	8.25	7.76	7.06	7.14	9.67
MnO	0.06	0.04	0.05	0.07	0.04	0.05	0.09	0.09
MgO	24.6	23.0	22.0	21.5	23.6	22.6	23.9	21.6
CaO	0.02	0.09	0.10	0.04	0.02	0.12	0.10	4.06
Na_2O	0.24	0.11	0.15	0.14	0.21	0.16	0.16	0.66
K_2O	9.94	10.9	8.96	9.06	8.59	9.57	8.55	5.85
Total	95.1	92.5	92.7	92.6	95.2	95.6	93.9	95.3
Mg#	0.92	0.89	0.85	0.84	0.86	0.86	0.87	0.82

3.2.3 Phenocryst phases

By far the most abundant phenocryst phase in the Swartruggens kimberlite dykes is phlogopite, which is usually euhedral or subhedral but often occurs as lath-shaped crystals up to 2mm in length. The phlogopite phenocrysts are usually pale brown in thin section, displaying weak pleochroism, and are commonly optically zoned. Most of the phlogopite phenocrysts are rimmed to variable extents by tetraferriphlogopite.

Phlogopite phenocrysts constitute between 10 and 20 volume % of the Main Dyke and the South Fissure, and between 10 and 30 volume % of the Third Lease samples (Table 3.1). In the Changehouse Dyke, phlogopite phenocrysts are slightly more abundant and constitute 15 to 30 volume % of the dyke (Table 3.1). In some samples, particularly those from the Third Lease, some of the phlogopite phenocrysts are severely altered to chlorite, but this is not pervasive throughout individual thin sections and, in general, the phlogopite phenocrysts are fresher than the phlogopite macrocrysts.

Diopside phenocrysts usually occur as subhedral laths up to 2mm in length, although they are generally smaller and thinner than phlogopite phenocrysts. They are most abundant in the Changehouse Dyke, where they constitute 5 to 10 volume % of the rock. In the Third Lease and South Fissure dykes, diopside phenocrysts are present in small amounts (<2 volume % in the Third Lease samples and <1 volume % in the South Fissure), but they are absent from the majority of the Main Dyke samples and are only present in small amounts (<1 volume %) in samples NC 006 and NC 010 (Table 3.1). Most of the diopside phenocrysts are fairly fresh, although they are occasionally slightly altered around the crystal edges.

Euhedral olivine phenocrysts up to 1mm in length are present in the Changehouse Dyke samples NC 007 and SR 7, but are absent from the other Swartruggens kimberlite samples (Table 3.1). Where present in the Changehouse Dyke, these olivine phenocrysts are completely altered to serpentine or replaced by calcite. The rarity of olivine phenocrysts in the Swartruggens kimberlite dykes has been attributed to replacement of olivine by phlogopite (Skinner and Scott, 1979, Allen, 1990), but may also be a consequence of extensive serpentine and calcite in the groundmass of some samples, coupled with the subhedral nature of some olivine macrocrysts, which makes the identification of true relic olivine phenocrysts extremely difficult.

3.2.4 Groundmass mineralogy

The groundmass of all the Swartruggens kimberlite dykes is fine-grained and fairly equigranular, and contains abundant phlogopite. The groundmass phlogopite occurs primarily as euhedral or subhedral stubby laths, up to 0.2mm in size, although microphenocrysts of phlogopite up to 0.5mm in size are common in all the dykes. Groundmass phlogopite constitutes between 40 and 70 volume % of the Main Dyke, between 20 and 60 volume % of the South Fissure, and 30 to 40 volume % in the Third Lease samples. In the Changehouse Dyke groundmass phlogopite is less abundant than in the other dykes, and constitutes between 15 and 30 volume % of the dyke (Table 3.1). The groundmass phlogopite is pale brown in thin section, showing weak pleochroism and is usually rimmed by tetraferriphlogopite (Plate 3.1g). In some samples from all the dykes, but particularly in the Third Lease samples, the groundmass phlogopite is partially chloritised. This is not pervasive throughout individual thin sections and usually occurs in patches, with parts of the sample unaltered (Plate 3.1h).

Diopside occurs as euhedral or subhedral microphenocrysts up to 0.5mm in size in the groundmass of the Swartruggens kimberlite dykes. It constitutes up to 20% of the groundmass of the Changehouse Dyke, but only 5 to 10 volume % of the groundmass of the Third Lease and South Fissure samples. As with diopside phenocrysts, groundmass diopside is present only in minor amounts in the Main Dyke (Table 3.1). Minor

amounts (< 3 volume %; Table 3.1) of groundmass olivine are present in the Changehouse Dyke. This has all been altered completely to calcite. Groundmass olivine was not observed in the samples from the other Swartruggens kimberlite dykes. However, it should be noted that the abundance of groundmass serpentine and calcite in many samples (see below) might, to some extent, mask the presence of relic groundmass olivine in these samples.

The remainder of the groundmass of the Swartruggens kimberlite dykes is predominantly calcite, which is considerably more abundant in the groundmass of the Third Lease samples than in the other dykes (Table 3.1). Calcite occurs as euhedral crystals up to 0.2mm in size, but is more commonly present as an interstitial phase. Thin (<1mm) veins of secondary calcite cut through some samples. Interstitial serpentine is present in subordinate amounts, and minor apatite and perovskite occur in all the dykes. Disseminated opaque oxides less than 0.1mm in size are abundant and occur throughout the groundmass of all the kimberlite dykes in addition to being associated with relic olivine macrocrysts. The accessory phases barite, zircon and wadeite have been identified in the groundmass of samples from the Main Dyke (Hammond and Mitchell, 2002) although these were not observed in the samples used for this project. Allan (1990) also reported minor amounts of possible sanidine in the groundmass of the South Fissure, but again this was not observed in these samples.

3.2.5 Classification of the Swartruggens kimberlite dykes

Based on the classification system of Skinner and Clement (1979) and using the modal mineral abundances reported in Table 3.1, the Swartruggens kimberlite dykes are classified as reported in Table 3.3.

Table 3.3 Classification of the Swartruggens kimberlite dykes (after Skinner and Clement, 1979).

Main Dyke	Phlogopite kimberlite
Third Lease South Fissure	Diopside – bearing phlogopite kimberlite
Changehouse Dyke	Diopside phlogopite kimberlite

3.3 Petrography of the Swartruggens Muil Dyke

3.3.1 Texture

The Swartruggens Muil Dyke consists of large (up to 6mm in size), euhedral or subhedral olivine macrocrysts and phenocrysts set in a groundmass of needle-like phlogopite, diopside and sanidine. The olivine macrocrysts and phenocrysts form a continuum of size variations, and may be genetically related. However, as they are now altered to serpentine and cannot be analysed chemically, for the purposes of this study they have been separated on the grounds of size as stated in section 3.1. The texture of the Muil Dyke ranges from coarsely macrocrystic, containing up to 25 volume % macrocrysts, to aphanitic, with

sample JJG 3141 containing only 5 volume % macrocrysts (Table 3.1). Phenocryst proportions range from 10 – 20 volume %, with olivine being the predominant phenocryst phase and subordinate phlogopite and diopside occurring in similar proportions (Table 3.1), in a groundmass consisting primarily of phlogopite, diopside and sanidine needles. The groundmass needles are commonly aligned and flow around the macrocrysts and some of the olivine phenocrysts.

3.3.2 Macrocryst phases

All the macrocrysts in the Muil Dyke are olivine, which occurs as euhedral to subhedral crystals up to 6mm in size (Plate 3.1i and j), very different in appearance to the rounded anhedral olivine macrocrysts of the Swartruggens kimberlite dykes. Some of the macrocrysts form complex shapes and they sometimes occur as twins. The olivine is completely altered to serpentine, often with associated opaque oxides (<0.1mm in size), with no fresh olivine remaining in these samples. Partial replacement by phlogopite is common, particularly around the edges of the olivine macrocrysts and along fractures (Plate 3.1k). In the most altered sample (JJG 3141) the olivine macrocrysts are replaced by calcite. Olivine macrocryst proportions in the Muil dyke range from 5 volume % in sample JJG 3141, to 25 volume % in the more macrocrystic samples (Table 3.1).

3.3.3 Phenocryst phases

Phenocryst phases are present in all the Muil Dyke samples, and range in abundance from 10 – 20 volume %. 5 - 10 volume % of the phenocrysts are olivine, which occurs as euhedral or subhedral crystals up to 2mm in size. The olivine phenocrysts are completely altered to serpentine, often with associated opaque oxides, and some have been partially replaced by phlogopite. In sample JJG 3141, the olivine phenocrysts are completely replaced by calcite. Phlogopite and diopside phenocrysts range from 0 – 5 and 0 – 2 volume % of the Muil Dyke respectively. Both these minerals occur as needle or lath-shaped crystals, up to approximately 1.5mm in size. The phlogopite phenocrysts are different in appearance to those of the Swartruggens kimberlites, being a much darker red-brown in colour and showing strong pleochroism. These differences correspond to different mineral chemistry, as reported by Skinner and Scott (1979) and Mitchell (1995), and confirmed by this study for groundmass phlogopites (see below and Table 3.2).

3.3.4 Groundmass mineralogy

The groundmass minerals of the Muil Dyke are commonly acicular and vary in size from an average of 0.5mm in length in the finer-grained samples (e.g. NC 012 and SR 9) to 0.5 – 1mm in the coarser-grained samples (e.g. NC 015). Phlogopite is the most abundant groundmass mineral, constituting between 25 and 40 volume % of the dyke. Similarly to the phlogopite phenocrysts described above, the groundmass phlogopite is different in appearance to that of the Swartruggens kimberlites, being much darker red-brown in colour and strongly pleochroic. Representative major element analyses of groundmass phlogopite from the Muil Dyke are reported together with analyses from the Swartruggens kimberlites in Table 3.2. The Muil Dyke groundmass phlogopites have higher TiO_2 contents, slightly higher FeO* contents and lower MgO than the kimberlite phlogopites, in agreement with the studies of Skinner and Scott (1979) and Mitchell (1995). Diopside is common in the groundmass of the Muil Dyke, ranging from 5 to 30 volume % of the dyke. The

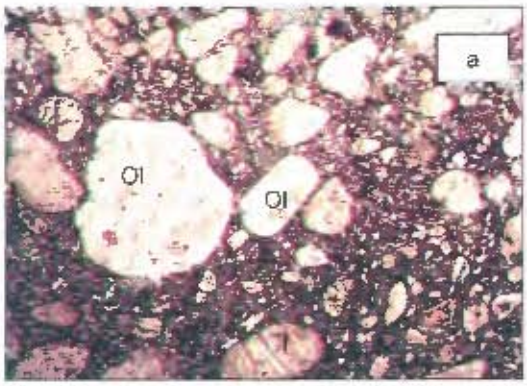

a) Macrocrystic texture in the Changchouse Dyke (sample NC 009). FOV approx. 15mm.

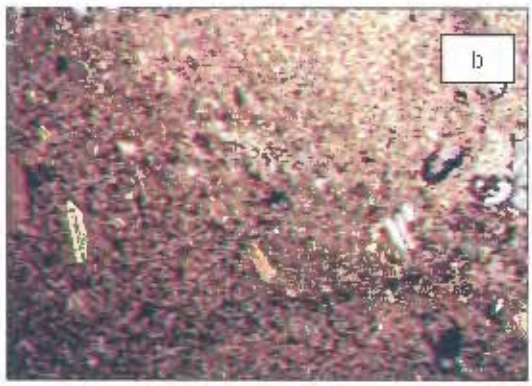

b) Aphanitic texture in the Main Dyke (sample NC 006). FOV approx. 20mm.

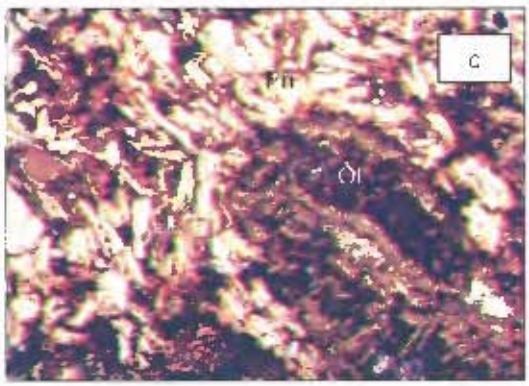

c) Groundmass phlogopite bent around serpentinised olivine macrocryst in the Changchouse Dyke (NC 005). FOV approx. 3mm.

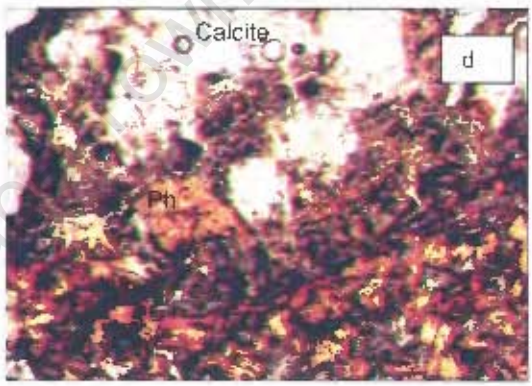

d) Relic olivine macrocryst replaced partially by calcite and partially replaced by phlogopite in the South Fissure (JJG 3148). FOV approx. 3mm.

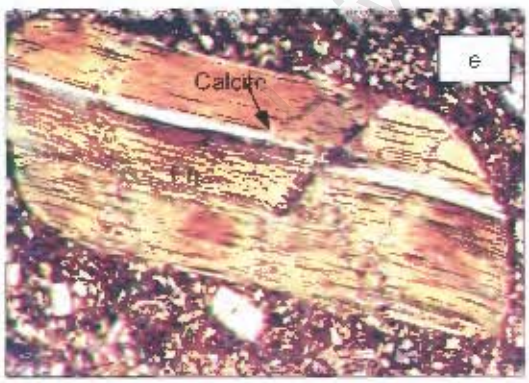

e) Phlogopite macrocryst in the Main Dyke (NC 010) with a calcite vein along a cleavage plane. FOV approx. 3mm

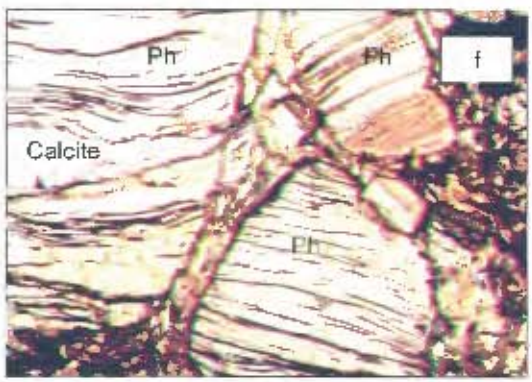

f) Bent and fractured phlogopite macrocrysts in the Main Dyke (NC 011) FOV approx. 2mm

Plate 3. 1 Photomicrographs of selected features of the Swartruggens kimberlite dykes and the Muil lamprophyre. FOV = field of view; Ol = olivine; Ph = phlogopite, S = sanidine.

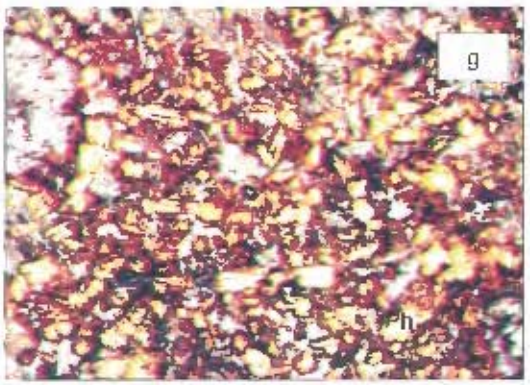

g) Groundmass phlogopite of the South Fissure (JJG 3145) rimmed by darker, red brown tetraferriphlogopite. FOV approx. 3mm.

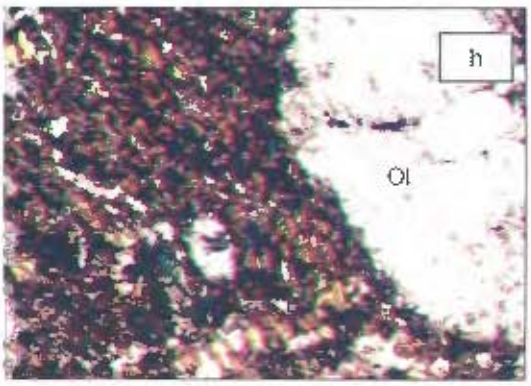

h) Typical appearance of the Third Lease samples, showing an anhedral olivine macrocryst completely replaced by calcite, and some groundmass phlogopite partially altered to chlorite. FOV approx. 3mm.

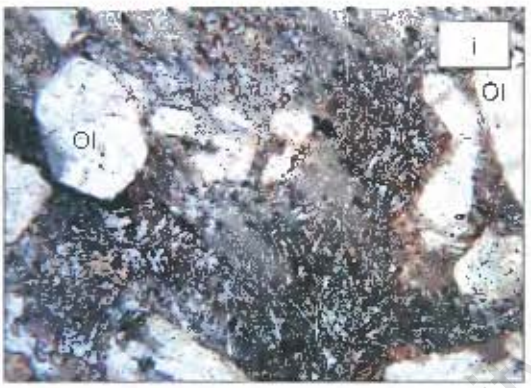

i) Typical appearance of the Mull dyke, showing euhedral or subhedral altered olivine macrocrysts and phenocrysts in a groundmass of needle-like phlogopite and diopside. FOV approx. 30mm.

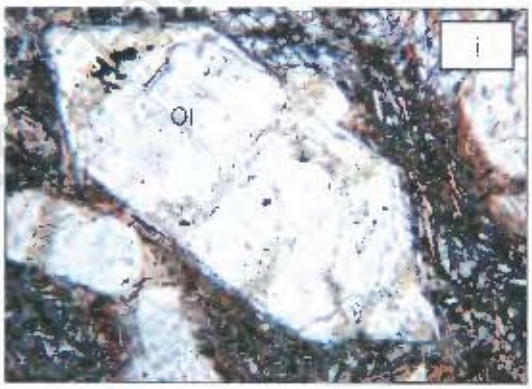

j) Euhedral serpentinised and calcitised olivine macrocryst in the Mull dyke with associated opaque oxides. FOV approx. 2mm.

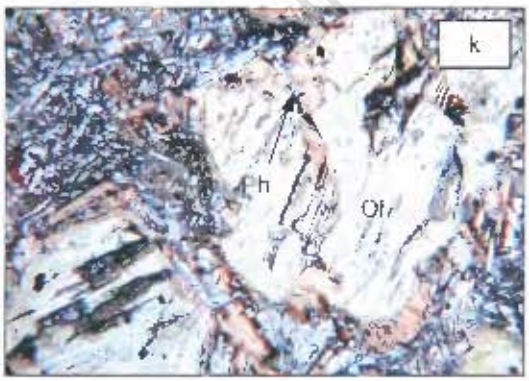

k) Fractured serpentinised olivine macrocrysts in the Mull Dyke, which have been partially replaced by phlogopite around the crystal edges and along fracrures. FOV approx. 2mm

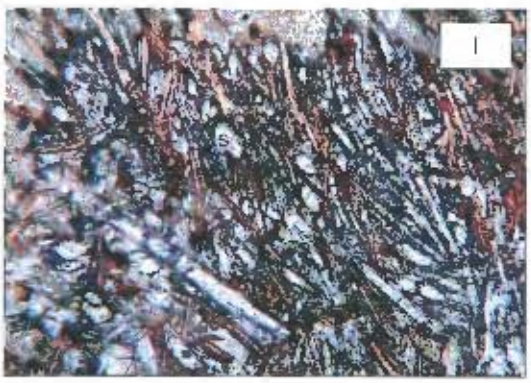

l) Close-up view of the Mull Dyke groundmass, showing the aligned needles of phlogopite (red-brown) and diopside (colourless). Many of the smaller, anhedral, colourless crystals are sanidine. FOV approx .1.5mm.

Plate 3.1 Continued

diopside is usually acicular, ranging up to 0.5mm in length but also occurs as smaller, euhedral crystals. Groundmass olivine ranges up to 15 volume %, and occurs as euhedral or subhedral crystals up to 0.5mm in size, which are completely altered to serpentine. In sample JJG 3141 the groundmass olivine has been replaced by calcite, although this is not pervasive throughout the dyke. Sanidine occurs in the groundmass of all the Muil dyke samples, both as acicular and euhedral crystals, and constitutes up to 30 volume % of the dyke. Groundmass calcite is absent from the Muil Dyke in all samples except JJG 3141, where it is abundant, constituting approximately 30 volume % of the sample. Opaque oxides up to 0.3mm in size are abundant throughout the groundmass of the Muil Dyke, in addition to being associated with relic olivine macrocrysts and phenocrysts, and euhedral apatite approximately 0.1mm in size is present in minor amounts (~1 volume %). Skinner and Scott (1979) reported nepheline in the groundmass of the Muil Dyke as well as possible altered leucite and a variety of secondary minerals that were not observed in these samples.

3.3.5 Classification of the Swartruggens Muil Dyke

The Swartruggens Muil dyke has two petrographic features that are typical of lamprophyres and atypical of kimberlites:

1) The euhedral nature of the olivine macrocrysts does not fit the definition of Clement *et al.* (1984), given on page 10. Macrocrysts in kimberlites are typically anhedral and rounded, whereas euhedral macrocrysts are typical of lamprophyres (Rock, 1981).
2) Abundant sanidine is present in the groundmass. Alkali feldspar does not occur in kimberlites but may be present in lamprophyres (Mitchell, 1995; Rock, 1981).

It is therefore concluded that the Muil Dyke was correctly identified as a lamprophyre by Skinner and Scott (1979). Although the lamprophyre branch to which it should be assigned is still uncertain, the presence of nepheline (Skinner and Scott, 1979) constrains the Muil Dyke to either the ultramafic lamprophyres or the alkaline lamprophyres.

3.4 Petrography of the Star kimberlite Dykes

The petrography of the Star kimberlite Dykes has been determined optically from twenty-two thin sections (2 from the Clewer Dyke, 7 from the Wynandsfontein Dyke, 5 from the East Star Dyke, 4 from the Byrnes Dyke and 4 from the Barren Dyke). One of the Barren Dyke samples (NC 054) was observed in hand specimen to be considerably less micaceous than the other three samples, and is referred to as the "less-micaceous" Barren Dyke sample in the following descriptions. Individual sample descriptions are given in Appendix 2, together with photomicrographs of each sample.

3.4.1 Texture

The Star kimberlite dykes are typically macrocrystic, containing between 15 and 40 volume % macrocrysts in a fine-grained groundmass, although macrocryst proportions vary widely within individual dykes (Table 3.4). In hand specimen there is clear evidence for flow differentiation, with more macrocryst-poor material

close to the margins of the dyke, and bands of macrocrysts aligned parallel to the dyke margins. The macrocryst suite of the Star kimberlites is composed primarily of olivine, with subordinate phlogopite and rare eclogitic garnets. The most macrocrystic samples are from the East Star Dyke and the less-micaceous Barren Dyke, which contain up to 40 volume % macrocrysts (Table 3.4; Plate 3.2a and b). Sample SJH 77 from the Byrnes Dyke is less macrocrystic than the other Star samples (Plate 3.2c), containing only 15 volume % macrocrysts, although macrocrysts in this dyke range up to 30 volume %. The micaceous Barren Dyke samples contain approximately 30 volume % macrocrysts, whereas macrocryst proportions in the

Table 3.4 Modal mineralogy (volume %) of the Star kimberlite dykes based on visual estimates. mic = micaceous; l. mic = less micaceous; other = serpentine, chlorite, opaque oxides, perovskite.

Dyke	Clewer Dyke	Wynandsfontein Dyke	East Star Dyke	Byrnes Dyke	Barren Dyke	
					mic	l. mic
Macrocrysts	**20 – 30**	**20 – 40**	**20 – 40**	**15 – 30**	**30**	**40**
Olivine	15 – 30	15 – 30	15 – 35	15 – 30	25	35
Phlogopite	< 5	< 5 - 10	< 5	< 5	< 5	< 5
Phenocrysts	**20**	**5 – 10**	**5 – 10**	**5 – 20**	**5**	**3**
Phlogopite	15 – 20	5 – 10	5 – 10	5 – 20	3 - 5	-
Diopside	< 2	-	-	-	-	-
Olivine	0 - 2	0 - 3	-	-	<2	3
Groundmass	**50 – 60**	**35 – 75**	**50 – 75**	**60 – 70**	**65**	**60**
Phlogopite	35 – 50	30 – 50	35 – 50	30 – 55	45	25
Calcite	5 – 15	15 – 35	10 – 30	10 – 25	5 - 10	5
Diopside	6	-	-	-	-	-
Other	2	< 5	<5 – 15	<5 – 15	10 - 15	30

Clewer and Wynandsfontein Dykes range from 20 - 30 volume % macrocrysts (Table 3.4). Phenocrysts constitute approximately 5 volume % of the micaceous Barren Dyke and approximately 3 volume % of the less micaceous sample (Table 3.4). In the Byrnes and Clewer Dykes phenocryst proportions range up to 20 volume %, whereas the East Star and Wynandsfontein Dykes contain between 5 and 10 volume % phenocrysts. Phlogopite is the main phenocryst phase in the Star kimberlite dykes, with olivine phenocrysts only present in the Clewer, Wynandsfontein and Barren Dykes at <3 volume % (Table 3.4). Diopside phenocrysts are present only in the Clewer Dyke at up to 2 volume % (Table 3.4). All the Star kimberlite dykes have a fine-grained groundmass, consisting of up to 80 volume % equigranular phlogopite, with minor amounts of diopside in the Clewer Dyke, in a matrix predominantly of calcite and serpentine. The groundmass phlogopite is commonly aligned parallel to the macrocrysts and the dyke margins.

3.4.2 Macrocryst phases

The Barren Dyke samples have high proportions of olivine macrocrysts (25 and 35 vol. % of the micaceous samples and non-micaceous samples respectively), whereas all the other dykes have similar, wide ranges in abundance of olivine macrocrysts from 15 to 35 volume %. The olivine macrocrysts are rounded and anhedral, ranging up to 10mm in size (Plate 3.2a and b). They are frequently strained, showing undulose extinction and some are recrystalised. Many olivine macrocrysts are fragmented, and many small (approximately 1mm diameter) fragments are scattered throughout the groundmass, particularly of the Byrnes Dyke and less-micaceous Barren dyke (Plate 3.2c). The olivine macrocrysts are frequently partially altered to serpentine around the edges and along fractures (Plate 3.2d), and sometimes pervasively. In more altered samples, such as JJG 6361 from the Wynandsfontein Dyke, the olivine macrocrysts are replaced partially or wholly by calcite (Plate 3.2h), often with associated abundant opaque oxides (<0.1mm in size). Some macrocrysts are also partially replaced by phlogopite. However many of the samples (e.g. JJG 2833, Clewer Dyke; JJG 4570, SJH 38, East Star Dyke; JJG 6360, NC 050, Wynandsfontein Dyke; and the Barren Dyke samples) do have very fresh olivine macrocrysts or fresh olivine cores (Plate 3.2e). Representative major element analyses of fresh olivine macrocrysts from the Clewer, East Star, Wynandsfontein and Barren Dykes are reported in Table 3.5. The macrocrysts do not vary significantly in composition between cores and rims, or between the different dykes, and range in composition from Fo_{90} to Fo_{94}. Olivine macrocryst 4 (from the Clewer Dyke) has a lower NiO content (NiO = 0.02 wt %; Table 3.5) than the other analysed olivine macrocrysts from the Star diamondiferous kimberlite dykes (NiO = 0.38 – 0.49 wt %; Table 3.5) and may represent a large phenocryst rather than olivine of xenocrystic origin. The olivine macrocrysts from the Barren Dyke typically have higher CaO contents (CaO = 0.03 – 0.07 wt %; Table 3.5) than those from the Star diamondiferous kimberlite dykes (CaO = 0.01 – 0.05 wt %), perhaps signifying lower pressures of crystallisation.

Phlogopite macrocrysts are present in all the dykes, although they far less abundant than olivine macrocrysts, constituting only between 10 and 20 % of the macrocryst suite and constituting less than 5 to 10 volume % of the samples (Table 3.4). The Barren, Byrnes, Clewer and East Star Dykes contain up to 5 volume % phlogopite macrocrysts whereas in the Wynandsfontein Dyke phlogopite macrocrysts are slightly more abundant, constituting up to 10 volume % of the dyke (Table 3.4). The phlogopite macrocrysts occur as anhedral or subhedral elongate crystals, which reach up to 4mm, but are more commonly 1 to 2 mm, in length. The phlogopite macrocrysts are often extremely strained, with undulose extinction, and commonly show kink banding. Many of the phlogopite macrocrysts are extensively fractured, particularly along cleavage planes, with fractures usually infilled with calcite (Plate 3.2f). Zoning is common, with most of the macrocrysts having darker cores than rims (Plate 3.2g), and some of the phlogopite macrocrysts are mantled by tetraferriphlogopite. Representative major element analyses of phlogopite macrocrysts from the Clewer, East Star and Byrnes Dykes are reported in Table 3.6. FeO* contents in the phlogopite typically ranges between 4.07 and 5.58, with macrocryst 6 (East Star Dyke) having 7.10 wt % FeO*, although the rim of macrocryst 11 (Byrnes Dyke) has 15.4 wt % FeO* which, together with the very low Al_2O_3 content, is more typical of tetraferriphlogopite. In areas of some more altered samples (e.g. JJG 6361A, JJG 6361C,

Table 3.5 Representative major element analyses of olivine macrocrysts in the Star kimberlite dykes, acquired using the electron microprobe, University of Cape Town. Ol = olivine; mac = macrocryst; co = core; FeO* = total iron as FeO; Fo cont. = Mg/ (Mg + Fe^{2+}). Atomic proportions for these analyses have been calculated and are reported in Appendix 2.

Dyke	Clewer Dyke			East Star Dyke				
Sample	JJG 2833	JJG 2833	JJG 2833	JJG 4570	JJG 4570	JJG 4570	JJG 4570	JJG 4570
Description	Ol mac 1 co	Ol ma 4 co	Ol mac 8 co	Ol mac 1 co	Ol mac 7 co	Ol mac 7 rim	Ol mac 8 co	Ol mac 8 rim
SiO_2	40.5	40.5	41.2	41.3	41.4	40.7	40.6	40.1
TiO_2	0.00	0.00	0.01	0.00	0.00	0.00	0.00	0.00
Al_2O_3	0.00	0.00	0.00	0.00	0.00	0.00	0.00	0.00
Cr_2O_3	0.02	0.06	0.01	0.03	0.01	0.01	0.04	0.03
FeO*	7.15	11.2	8.34	6.16	7.04	7.05	10.4	10.4
MnO	0.09	0.28	0.10	0.07	0.09	0.07	0.12	0.12
MgO	50.9	48.1	49.6	52.2	51.2	51.3	48.0	48.8
CaO	0.01	0.03	0.01	0.01	0.00	0.01	0.02	0.03
NiO	0.42	0.02	0.43	0.40	0.42	0.40	0.49	0.49
Total	99.0	100.2	99.7	100.2	100.2	99.5	99.7	99.9
Fo cont.	0.93	0.90	0.92	0.94	0.94	0.94	0.90	0.90

Dyke	Wynandsfontein Dyke				Barren Dyke (less-micaceous)			
Sample	JJG 6360	JJG 6361	JJG 6362	JJG 6363	NC 054	NC 054	NC 054	NC 054
Description	Ol mac 1 co	Ol mac 1 rim	Ol mac 5 co	Ol mac 5 rim	Ol mac 3 co	Ol mac 3 rim	Ol mac 8 co	Ol mac 8 rim
SiO_2	41.5	40.4	40.7	40.9	40.9	41.0	41.4	41.2
TiO_2	0.00	0.00	0.00	0.00	0.00	0.00	0.00	0.00
Al_2O_3	0.00	0.00	0.00	0.00	0.00	0.00	0.00	0.00
Cr_2O_3	0.06	0.05	0.03	0.02	0.07	0.08	0.05	0.04
FeO*	8.04	7.92	9.38	9.21	7.86	7.97	7.04	7.10
MnO	0.09	0.10	0.10	0.13	0.10	0.11	0.10	0.08
MgO	50.8	50.5	49.5	49.0	50.4	49.8	50.8	51.0
CaO	0.05	0.03	0.02	0.01	0.06	0.07	0.04	0.03
NiO	0.42	0.42	0.39	0.38	0.41	0.39	0.42	0.42
Total	101.0	99.4	100.1	99.7	99.8	99.4	99.8	99.8
Fo cont.	0.93	0.93	0.91	0.91	0.93	0.93	0.93	0.93

JJG 6360, Wynandsfontein Dyke; SJH 78, Byrnes Dyke) partial alteration of the phlogopite macrocrysts to chlorite has occurred, although this is generally not pervasive throughout individual macrocrysts.

Although olivine and phlogopite are by far the most abundant macrocrysts in the Star kimberlites, rare eclogitic garnets are also present in samples from the Clewer Dyke (JJG 2833), the East Wynandsfontein Dyke (SJH 37, JJG 6361B) and the East Star Dyke (SJH 38) (Plate 3.2h). These are red-brown in colour and approximately 1mm in size. The garnets are anhedral and fractured, with fractures infilled with calcite, or disaggregated into fragments.

3.4.3 Phenocryst Phases

Phlogopite is by far the most abundant phenocryst phase present in the Star kimberlites. In all the dykes except the Clewer Dyke, phlogopite forms the entire phenocryst suite and in the Clewer Dyke, where diopside and olivine phenocrysts are also present, phlogopite forms at least 90% of the phenocryst suite. There are no phlogopite phenocrysts in the non-micaceous Barren Dyke, although they form up to 5 volume % of the micaceous Barren Dyke (Table 3.4). In the East Star and Wynandsfontein Dykes phlogopite

phenocrysts are slightly more abundant, forming 5 to 10 volume % of these dykes, whereas the Byrnes Dyke contains between 5 and 20 volume % phlogopite phenocrysts (Table 3.4). The Clewer Dyke, on average, has the most abundant phlogopite phenocrysts, ranging from 15 to 20 volume % (Table 3.4). The phlogopite phenocrysts range up to approximately 1.5 mm in size, and commonly form subhedral elongate laths, some of which are distinctly zoned. Thin rims of tetraferriphlogopite are present around the phlogopite phenocrysts in some samples (e.g. JJG 4570 from the East Star Dyke). In the more altered samples, such as JJG 6361A, JJG 6361C (Wynandsfontein Dyke) and SJH 78 (Byrnes Dyke), partial alteration of the phlogopite phenocrysts to chlorite has occurred, although this is not pervasive throughout entire thin sections.

Olivine phenocrysts were observed in sections from the Clewer Dyke (0 – 2 volume %; Table 3.4), Wynandsfontein Dyke (0 – 3 volume %) and the Barren Dyke (<3 volume %; Table 3.4). The olivine

Table 3.6 Representative major element analyses of phlogopite macrocrysts in the Star kimberlite dykes acquired using an electron microprobe, University of Cape Town. Phlog = phlogopite; mac = macrocryst; FeO* = total iron as FeO; Mg# = atomic Mg/ (Mg + Fe^{2+}) with Fe_2O_3/ FeO = 0.1. Atomic proportions for these analyses have been calculated and are reported in Appendix 2.

Dyke	Clewer Dyke				East Star Dyke		
Sample	JJG 2833	JJG 2833	SJH 39	SJH 39	JJG 4570	JJG 4570	SJH 30
Description	Phlog mac 1	Phlog mac 2	Phlog mac 3	Phlog mac 4	Phlog mac 5	Phlog mac 6	Phlog mac 7
SiO_2	42.6	39.2	40.6	40.6	41.9	37.7	40.6
TiO_2	1.50	2.08	1.87	2.07	1.66	1.69	1.77
Al_2O_3	12.7	12.6	13.9	13.5	13.5	12.7	14.8
FeO*	4.63	5.16	4.07	5.52	4.65	7.10	4.81
MnO	0.04	0.03	0.05	0.06	0.01	0.05	0.03
MgO	22.8	23.8	21.4	21.2	21.6	21.4	24.8
CaO	0.09	0.02	0.07	0.03	0.03	0.01	0.02
Na_2O	0.27	0.17	0.17	0.09	0.23	0.14	0.23
K_2O	9.88	9.53	10.1	10.5	10.3	10.0	9.64
Total	94.5	92.6	92.1	93.6	93.9	90.8	96.7
Mg#	0.91	0.90	0.91	0.88	0.90	0.86	0.91

Dyke	East Star	Byrnes Dyke					
Sample	SJH 30	SJH 79	SJH 79	SJH 79	SJH 79	SJH 79	SJH 79
Description	Phlog mac 8	Phlog mac 9	Phlog mac 10	Phlog mac 11 rim	Phlog mac 12	Phlog mac 13	Phlog mac 14
SiO_2	42.4	41.4	41.2	46.7	39.0	43.1	40.0
TiO_2	1.72	1.57	1.57	0.33	1.94	0.40	1.67
Al_2O_3	13.6	13.3	12.5	0.83	13.1	13.0	11.9
FeO*	5.46	5.08	5.58	15.4	4.89	2.81	5.25
MnO	0.03	0.03	0.03	0.15	0.05	0.01	0.05
MgO	24.3	25.0	24.9	23.6	24.8	26.8	25.1
CaO	0.13	0.03	0.03	0.12	0.02	0.01	0.06
Na_2O	0.14	0.19	0.26	0.13	0.15	0.16	0.29
K_2O	9.80	10.4	10.4	8.40	10.2	10.7	10.7
Total	97.6	97.0	96.4	95.7	94.2	96.9	95.0
Mg#	0.90	0.91	0.90	0.75	0.91	0.95	0.90

phenocrysts are euhedral to subhedral, and usually approximately 1mm in size. They are commonly completely altered to serpentine. Olivine phenocrysts were not observed in the Byrnes or East Star Dyke samples. Diopside occurs as a phenocryst phase only in the Clewer Dyke, as subhedral lath-shaped crystals up to 1.5mm in length, which are generally smaller and thinner than the phlogopite phenocrysts. The diopside phenocrysts are generally fresh, although some are slightly altered around the edges.

3.4.4 Groundmass Mineralogy

With the exception of the less-micaceous Barren Dyke sample, the groundmass of all the Star kimberlite dykes is similar, consisting of abundant (50 - 80% of the groundmass) phlogopite in a finer grained or interstitial matrix. Groundmass phlogopite constitutes between 30 and 55 volume % (Table 3.4) of all these dykes and usually occurs as euhedral or subhedral equigranular stubby laths, which are often rimmed by tetraferriphlogopite (Plate 3.2j). The less-micaceous Barren dyke differs in having less abundant phlogopite in the groundmass, with phlogopite constituting only 25 volume % of this dyke (Table 3.4). The groundmass phlogopite is altered to chlorite to varying degrees, particularly in samples JJG 6369, JJG 6361A, JJG 6361C (Wynandsfontein Dyke), SJH 78 and SJH 80 (Bymes Dyke) and the less-micaceous part of the Barren Dyke, although in the majority of samples the groundmass phlogopite is unaffected. Microphenocrysts of diopside constitute up to 2 volume % of the Clewer Dyke, but are absent from the other Star kimberlite dykes (Table 3.4).

Much of the rest of the groundmass of all the Star kimberlite dykes, with the exception of the non-micaceous Barren Dyke sample (NC 054), consists of calcite, which occurs as euhedral crystal up to 0.2mm in size, but most commonly as an interstitial phase. Groundmass carbonate appears to be related to some extent to the degree of alteration of the samples, as in the most altered samples calcite constitutes up to 50% of the groundmass, whereas in the less altered samples it constitutes only around 20% (Table 3.4). However, although the non-micaceous part of the Barren Dyke has an altered groundmass it contains only a minor amount of interstitial carbonate, the matrix of this dyke consisting primarily of interstitial serpentine and chlorite. Interstitial serpentine is present in subordinate amounts in the other Star kimberlite Dykes, constituting up to approximately 10 volume % of the East Star, Byrnes and micaceous Barren Dykes, up to 5 volume % of the Wynandsfontein Dyke and only 1 volume % of the Clewer Dyke (Table 3.4). Minor amounts of perovskite (<0.2mm in size) and Fe-Ti oxides (<0.1mm in size) are scattered throughout all dykes. In addition to being associated with relic olivine macrocrysts, Fe-Ti oxides are more abundant in the groundmass of the more altered samples such as JJG 6361A and JJG 6361C from the Wynandsfontein Dyke.

3.4.5 Classification of Star kimberlites

Based on the classification system of Skinner and Clement (1979), and the modal mineralogies reported in table 3.4, the Star kimberlite dykes are classified as reported in Table 3.7.

Table 3.7 Classification of the Star kimberlite dykes (after Skinner and Clement, 1979).

Clewer Dyke	Diopside bearing phlogopite kimberlite
Wynandsfontein Dyke East Star Byrnes Dyke	Calcite phlogopite kimberlite to phlogopite kimberlite
Barren Dyke	Phlogopite kimberlite

However, care should be taken with the application of this classification system, as the abundance of calcite may be in part a secondary feature due to alteration, rather than a reflection of the initial kimberlite composition.

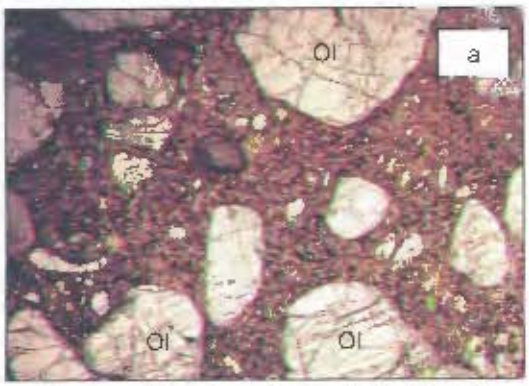

a) Macrocrystic texture in the East Star Dyke (sample JJG 4570). Despite being strained, the olivine in this sample is fresh. FOV approx. 20mm.

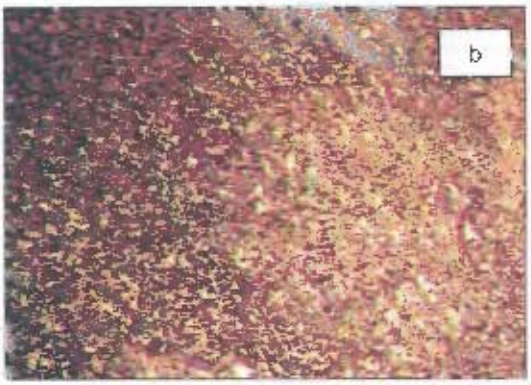

b) Aphanitic texture in the Byrnes Dyke (sample SJH 77). FOV approx. 20mm.

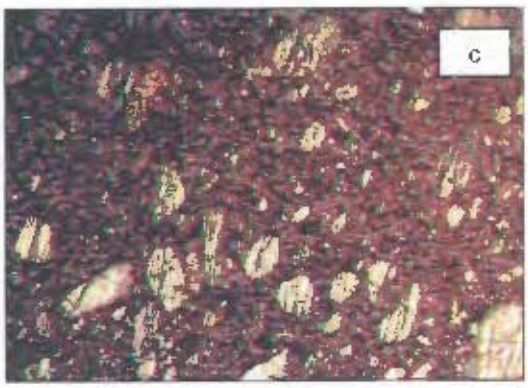

c) Macrocrystic texture in the less-micaceous Barren Dyke (NC 054). Small (<1mm) fragments of olivine macrocrysts are abundant in the groundmass. FOV approx. 20mm.

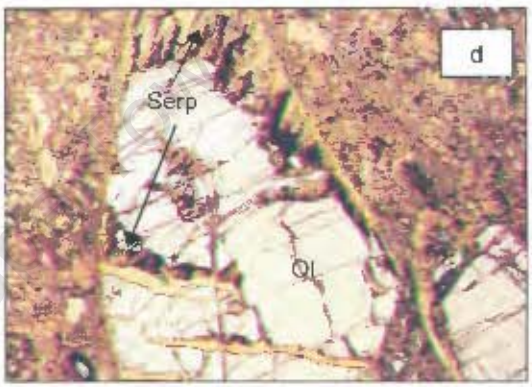

d) Olivine macrocryst which is fresh in the centre but has been altered to serpentine around the edges and along fractures (sample JJG 6360: Wynandsfontein Dyke). FOV approx. 2.5mm.

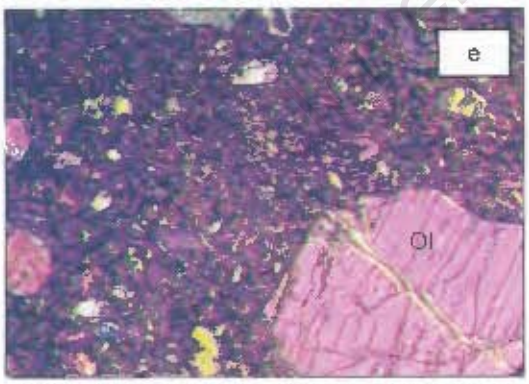

e) Olivine macrocrysts taken under crossed polars to illustrate their fresh nature (sample SJH 38; East Star Dyke). FOV approx 6mm.

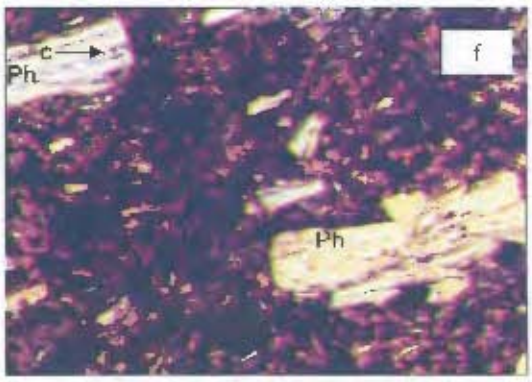

f) Strained, kink-banded phlogopite macrocrysts in the Byrnes Dyke (sample SJH 78). The macrocryst in the top left corner has been fractured along a cleavage plane and infilled with calcite. FOV approx. 4mm.

Plate 3.2 Photomicrographs of selected features of the Star kimberlite dykes, taken under plane polarised light except (e). FOV = field of view; Ol = olivine; Ph = phlogopite; serp = serpentine; c = calcite.

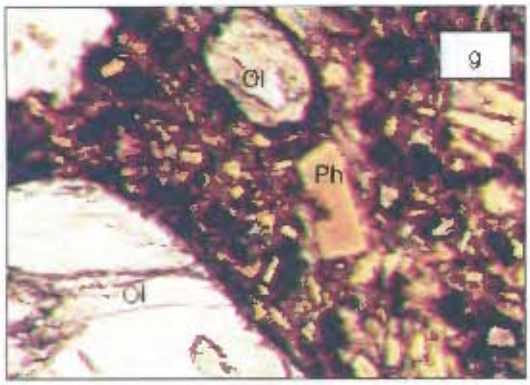

g) Strongly zoned phlogopite macrocryst and fresh olivine macrocrysts (sample NC 050; Wynandsfontein Dyke) FOV approx. 3mm.

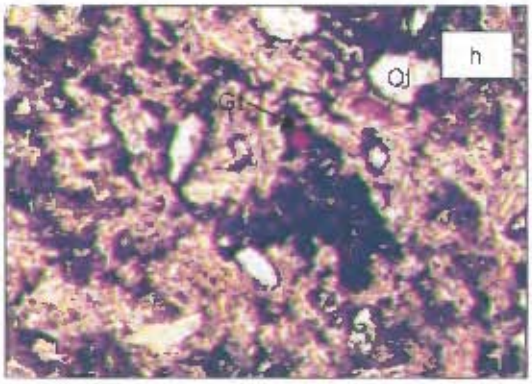

h) Red-brown anhedral eclogitic garnet, together with relic olivine macrocrysts now replaced by calcite in a carbonate-rich groundmass (sample SJH 37; Wynandsfontein Dyke). FOV approx. 4mm.

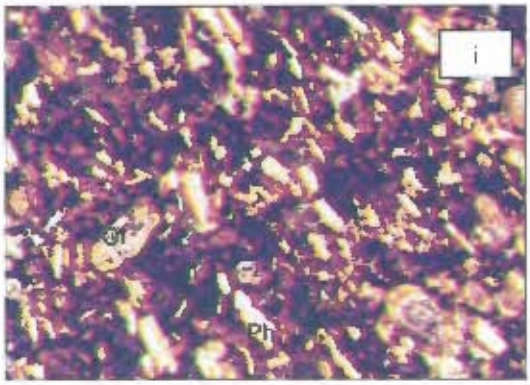

i) The groundmass of the Byrnes Dyke (sample SJH 77) showing the alignment of the phlogopite laths and the presence of small fragments of serpentinised olivine macrocrysts. FOV approx. 4mm.

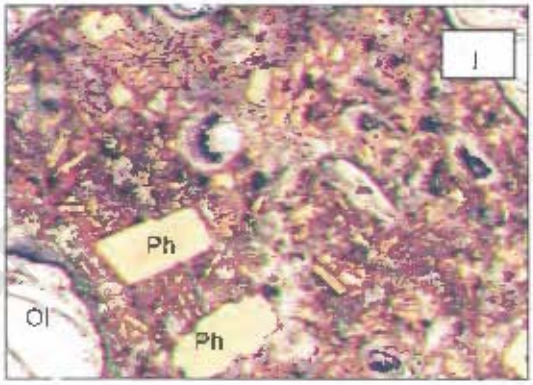

j) Phlogopite laths in the groundmass of the East Star Dyke (sample JJG 4570) rimmed by tetraferri phlogopite, in a carbonate matrix. The labelled phlogopites are macrocrysts. FOV approx. 4mm.

Plate 3.2 Continued.

Chapter 4

Major element geochemistry

4.1 Introduction

According to their major element geochemistry, kimberlites are classified as volatile rich, potassic, ultrabasic rocks (Clement *et al.*, 1984), but they have widely diverse major element compositions both between and within individual intrusions. Although the major element compositions of South African Group I and Group II kimberlites overlap considerably, their mineralogical differences reflect differences in their major element geochemistry. Group II kimberlites have more abundant groundmass phlogopite and diopside, reflecting their enriched SiO_2, Al_2O_3, MnO, and K_2O concentrations relative to Group I kimberlites, whereas Group I kimberlites have more abundant groundmass calcite, spinel, monticellite, ilmenite and apatite reflecting their enriched TiO_2, MgO, CaO, Na_2O, P_2O_5, and CO_2 concentrations relative to Group II kimberlites. FeO* (total) and H_2O^+ are present in similar concentrations in Group I and Group II kimberlites (Shee, 1985; Smith *et al.*, 1985b).

The major element geochemistry of kimberlites is complicated by their susceptibility to alteration (e.g. Berg, 1994), as well as entrainment of peridotite and assimilation of crust *en route* to the surface (e.g. le Roex *et al.*, 2003). In addition, much of the volatile component together with other mobile elements may be lost from the kimberlites during emplacement (e.g. Dawson, 1980). It has therefore generally been considered that bulk rock geochemistry does not reflect the true characteristics of the original kimberlite magma (e.g. Mitchell, 1995) and thus although the major element concentrations of many kimberlites have been documented, they have until recently been little used in evaluating petrogenetic processes. However, it was suggested by Dawson (1980) that analysis of fresh hypabyssal material minimises some of the problems described above, as fewer xenoliths are usually present and the xenoliths are usually smaller. The freshest available samples from the kimberlite dykes at Swartruggens and Star have been analysed to minimise the effects of weathering, and the jaw-crushed samples were hand-picked to avoid crustal xenoliths as far as possible. However, very small crustal fragments may have been included. In addition, since crustal material has a low melting temperature, it may have become fully assimilated into the kimberlite magma, thus affecting the geochemistry without being visibly detectable. Crustal material is typically enriched in SiO_2, Al_2O_3, Na_2O and less enriched in MgO and K_2O relative to kimberlite magmas, and on this basis Clement (1982) devised the following contamination index (C. I.):

$$\text{C. I.} = \frac{SiO_2 + Al_2O_3 + Na_2O}{MgO + 2K_2O}$$

and noted that extensively weathered, as well as crustally contaminated, samples will have high C. I., whereas apparently uncontaminated Group II kimberlites may have C. I.s of up to 1.5 (Clement, 1982). The C. I. of the Swartruggens and Star kimberlites has been calculated and is reported in Tables 4.1 and 4.2, and the effects of crustal contamination and weathering on the major element geochemistry of these kimberlites will be discussed in Chapter 7.

Kaapvaal craton peridotites are typically more enriched in MgO and SiO_2, have similar Fe_2O_3 and Al_2O_3 contents, and are less enriched in TiO_2, K_2O and CaO than kimberlites (e.g. Gregoire *et al.*, 2003). Trends in major element geochemistry within the Swartruggens and Star kimberlites can thus be used to evaluate the extent to which peridotite entrainment has affected the bulk rock geochemistry of the samples studied. With this intention, both macrocrystic and aphanitic samples from both localities have been analysed for their major element compositions.

A suite of samples from each of the exposed kimberlite dykes at Swartruggens and Star, and the Swartruggens Muil lamprophyre, have been analysed for their major element compositions by X-ray fluorescence spectrometry with three principal aims, summarised below:
1 – To characterise the whole rock major element abundances of the two kimberlite dyke swarms.
2 – To quantitatively assess the effects of late-stage alteration, crystal fractionation and accumulation of mantle and crust by the kimberlite magmas *en route* to the surface, thus constraining the primary magma compositions of these kimberlites.
3 – Using the inferred primary magma major element abundances, to place constraints on the source region characteristics of the two kimberlites.
Details of the analytical techniques are reported in Appendix 3. This chapter documents and describes the variations seen in a range of major elements of the Swartruggens and Star kimberlites, which are used in Chapter 7 to interpret petrogenetic processes.

Previous work involving the use of trends in major element geochemistry to isolate primary kimberlite magma compositions includes studies on the Jericho Pipe in Canada (Price *et al.*, 2000), off craton Group 1 kimberlites (Harris *et al.*, 2004), and Kimberley Group 1 kimberlites (le Roex *et al.*, 2003).

4.2 Major element geochemistry of the Swartruggens kimberlite, and the Muil lamprophyric, dykes

Nineteen samples from the Swartruggens kimberlite dykes (3 from the Third Lease, 7 from the Main Dyke, 4 from the Changehouse Dyke and 4 from the South Fissure) and 6 samples from the Muil lamprophyric dyke have been analysed for a range of major element abundances. Individual analyses are reported in Table 4.1 and selected variation diagrams are shown in Figure 4.1. Kimberlite magmas are known to contain a primary volatile component (e.g. Dawson, 1980; Berg and Allsopp, 1972). In the absence of any further quantifying information, H_2O^+ and CO_2 concentrations in the Swartruggens samples are assumed largely to

Table 4.1 Major element geochemistry (wt %) of the Swartruggens kimberlite dykes and the Mull lamprophyre. M = more macrocrystic, LM = less macrocrystic; * = average of 2 analyses, individual analyses reported in Appendix 2; LOI = loss on ignition; H_2O^+ calculated as LOI – H_2O^- (measured); Mg# = atomic Mg/(Mg + Fe^{2+}) with Fe_2O_3/ FeO = 0.2 (typical for alkaline rocks); C.I. = contamination index = $(SiO_2 + Al_2O_3 + Na_2O)/(MgO + 2K_2O)$ (Clement, 1982).

Dyke	3rd Lease			Main Dyke							Changehouse	
Sample	NC 001	NC 002	NC 003	NC 004	NC 006	NC 010	NC 011	SR 6	JJG 3143	Hons 95-4	NC 005	NC 007
Macro	M	LM	LM	M	LM	M	LM	M	M	LM	M	M
SiO_2	33.4	25.1	38.6	37.5	37.3	37.1	36.7	35.9	33.9	36.4	38.3	37.5
TiO_2	1.34	1.49	1.46	1.37	1.60	1.28	1.33	1.42	1.43	1.53	1.27	1.30
Al_2O_3	4.09	4.15	4.33	3.87	4.66	4.19	4.14	4.60	4.37	4.59	4.04	3.92
Fe_2O_3	6.71	7.26	7.49	8.69	8.67	7.26	7.84	8.26	8.14	8.46	8.22	7.82
MnO	0.17	0.20	0.15	0.17	0.15	0.15	0.14	0.16	0.15	0.15	0.13	0.16
MgO	12.3	12.5	12.0	21.3	20.6	21.6	22.0	22.1	22.4	20.3	24.7	19.3
CaO	21.0	24.5	18.8	8.67	8.35	9.95	9.56	9.32	10.0	10.3	7.42	11.7
Na_2O	0.06	0.06	0.08	0.15	0.20	0.12	0.04	0.12	0.04	0.19	0.16	0.16
K_2O	2.78	3.07	2.44	4.79	6.49	5.77	4.65	5.55	4.35	4.93	4.87	4.52
P_2O_5	1.03	1.53	1.28	1.14	1.82	0.39	0.44	1.39	1.55	1.56	0.81	0.75
SO_3	0.45	0.39	0.69	0.42	0.33	0.57	1.01	0.29	0.44	0.21	0.38	0.61
NiO	0.11	0.09	0.11	0.15	0.09	0.12	0.11	0.12	0.12	0.12	0.18	0.18
Cr_2O_3	0.15	0.15	0.16	0.17	0.22	0.16	0.15	0.16	0.16	0.18	0.24	0.21
H_2O^-	0.71	0.87	0.89	2.35	2.30	1.33	2.19	1.39	2.07	1.95	2.69	2.70
LOI	15.4	18.2	10.9	8.40	6.41	9.48	9.39	9.03	10.4	8.42	7.30	8.67
Total	99.8	99.6	99.4	99.2	99.2	99.5	99.7	99.7	99.5	99.3	100.8	99.6
CO_2	13.6	16.1	11.5	5.04	3.99	6.39	6.10	3.52	4.69	4.87	3.20	6.30
H_2O^+	1.81	2.06	0.00	3.36	2.42	3.09	3.29	5.51	5.71	3.55	4.10	2.37
Mg#	0.81	0.80	0.79	0.85	0.85	0.87	0.87	0.86	0.87	0.85	0.88	0.85
C. I.	2.1	1.6	2.6	0.3	1.3	1.3	1.3	1.2	1.2	1.4	1.2	1.5

Dyke	Changehouse		South Fissure				Mull Dyke					
Sample	NC 009	SR 7	JJG 3149	JJG 3145	JJG 3150	JJG 3148	NC 008*	NC-012	NC-014	NC-015	JJG 3141	SR 9
Macro	M	M	LM	M	LM	M	LM	M	M	M	LM	M
SiO_2	41.6	40.2	34.6	36.1	37.6	32.5	40.9	42.0	45.4	42.4	38.8	41.5
TiO_2	1.29	1.29	1.79	1.54	2.66	2.13	2.10	1.49	1.64	1.70	2.27	1.47
Al_2O_3	3.62	4.25	3.57	3.93	2.90	4.10	7.06	5.32	6.10	5.85	7.07	5.46
Fe_2O_3	8.45	8.48	9.59	8.24	11.2	9.59	10.2	9.72	9.46	9.01	9.40	9.66
MnO	0.16	0.13	0.25	0.23	0.26	0.30	0.14	0.16	0.16	0.15	0.15	0.14
MgO	20.4	20.1	19.6	15.5	17.2	17.7	16.3	21.0	16.4	19.5	10.3	20.0
CaO	8.03	8.37	10.7	14.2	11.3	12.3	8.42	7.61	8.64	10.0	16.2	7.71
Na_2O	0.38	0.24	0.20	0.06	0.32	0.17	1.35	0.73	1.11	0.89	1.44	0.53
K_2O	3.35	3.46	5.45	5.24	4.52	5.63	2.04	2.00	3.77	2.34	2.61	1.53
P_2O_5	0.95	0.99	2.27	1.71	2.32	2.53	0.82	0.55	0.63	0.62	0.83	0.58
SO_3	0.33	0.47	0.51	0.49	0.70	0.39	0.29	0.25	0.08	0.09	0.14	0.46
NiO	0.19	0.19	0.10	0.12	0.07	0.08	0.04	0.11	0.08	0.09	0.01	0.13
Cr_2O_3	0.20	0.23	0.15	0.17	0.09	0.18	0.14	0.29	0.24	0.27	0.09	0.30
H_2O^-	3.72	3.35	2.02	0.90	2.66	2.40	4.80	3.07	2.56	2.80	2.72	4.81
LOI	6.97	7.32	8.91	10.9	5.19	9.60	4.90	5.55	3.43	4.33	7.88	5.67
Total	99.6	99.1	99.7	99.4	99.1	99.6	99.6	99.8	99.7	99.9	99.9	99.9
CO_2	3.15	3.17	3.58	7.27	2.35	5.04	0.59	0.59	0.53	0.41	4.34	0.59
H_2O^+	3.82	4.15	5.33	3.64	2.84	4.56	4.31	4.96	2.90	3.92	3.54	5.08
Mg#	0.85	0.85	0.83	0.82	0.78	0.81	0.79	0.83	0.80	0.83	0.72	0.83
C. I.	1.7	1.7	1.3	1.5	1.6	1.3	2.4	1.9	2.2	2.0	3.1	2.1

reflect those of the original magma. Data are normalised to an H_2O^- free basis before plotting.

Across the suite of dykes, the Swartruggens kimberlites show wide variation in major element abundances (Table 4.1). There are with no strong inter-element correlations and the more macrocrystic samples are not readily distinguished from the less macrocrystic samples either within individual dykes or across the suite of dykes based on major element abundances (Table 4.1; Figure 4.1). All the kimberlite dykes are ultrabasic, with SiO_2 concentrations ranging from 25.1 to 41.6 wt % and, despite a wide range in MgO concentrations (12.0 to 25.4 wt %; Table 4.1), all the dykes have high Mg# (Mg# = 0.79 to 0.88; Table 4.1). The major elements, Fe and K show variable concentrations, both within dykes and across the suite of dykes, (Fe_2O_3 = 7.26 – 11.2 wt %; K_2O = 2.44 – 5.77 wt %) and considerable scatter when plotted against MgO (Figures 4.1 c and d). Although still variable in abundance, SiO_2, Al_2O_3 and CaO are more robust and show smaller within-dyke ranges and more coherent behaviour across the suite of dykes (Al_2O_3 = 2.90 – 4.66 wt %; CaO = 7.42 – 24.5 wt %). CO_2 concentrations in the Swartruggens kimberlites show a considerable range (CO_2 = 2.35 to 16.1 wt %) and define a broad positive correlation with CaO concentrations. All the Swartruggens kimberlite dykes have low Na_2O and relatively high P_2O_5 concentrations (Na_2O < 0.38 wt %; P_2O_5 = 0.39 – 2.53 wt %). Ni and Cr abundances in the Swartruggens kimberlites will be discussed in Chapter 5.

Despite considerable overlap, the individual kimberlite dykes define smaller ranges in major element composition. The Main dyke shows little variation in MgO and SiO_2 concentrations (MgO = 20.7 – 22.9 wt %; SiO_2 = 34.7 – 38.4 wt %; Table 4.1) and, although the more macrocrystic samples tend to have higher MgO contents than the less macrocrystic samples, there is no coherent correlation between these two oxides (Figure 4.1a). CaO concentrations of the Main Dyke samples range between 8.35 and 10.3 wt %, and show a broad negative correlation with SiO_2 content (Figure 4.1b). The majority of Main Dyke samples have Fe_2O_3 between 7.84 and 8.69 wt % and define a broad negative correlation with MgO content (Figure 4.1c). Sample NC 010 plots below the broad trend of the other Main Dyke samples, with lower Fe_2O_3 content (Fe_2O_3 = 7.26 wt %). K_2O shows considerable scatter with MgO for the Main Dyke samples (Figure 4.1d), with a range in K_2O from 4.35 to 6.49 wt %. Although there is little variation in TiO_2 or Al_2O_3 concentrations within the Main Dyke (TiO_2 = 1.28 – 1.53 wt %; Al_2O_3 = 3.87 – 4.66 wt %) there is a broad negative correlation between these two oxides (Figure 4.1e), with the more macrocrystic samples tending to have lower Al2O3 and TiO_2 contents than the less macrocrystic samples. CO_2 ranges from 3.52 to 6.39, but does not vary consistently with CaO content in the Main Dyke samples (Figure 4.1f).

The Third Lease samples have the lowest MgO (12.0 – 12.5 wt %), Fe_2O_3 (6.71 – 7.48 wt %) and K_2O (2.44 – 3.07 wt %) contents of the Swartruggens kimberlite dykes. Fe_2O_3 shows no coherent within-dyke correlation with MgO (Figure 4.1c) although there is a positive correlation between MgO and K_2O (Figure 4.1d). The Third Lease samples also have the highest CaO and CO_2 contents of the Swartruggens kimberlite dykes (CaO = 18.8 – 24.5 wt %; CO_2 = 11.5 – 16.1 wt%). SiO_2 concentrations vary widely between the Third Lease samples (SiO_2 = 25.1 to 38.6 wt %) and there is a negative correlation between SiO_2 and CaO content for these samples (Figure 4.1b). There is little variation in TiO_2 or Al_2O_3 concentrations between these samples (TiO_2 = 1.34 – 1.49 wt %; Al_2O_3 = 4.09 – 4.33 wt %), which fall within

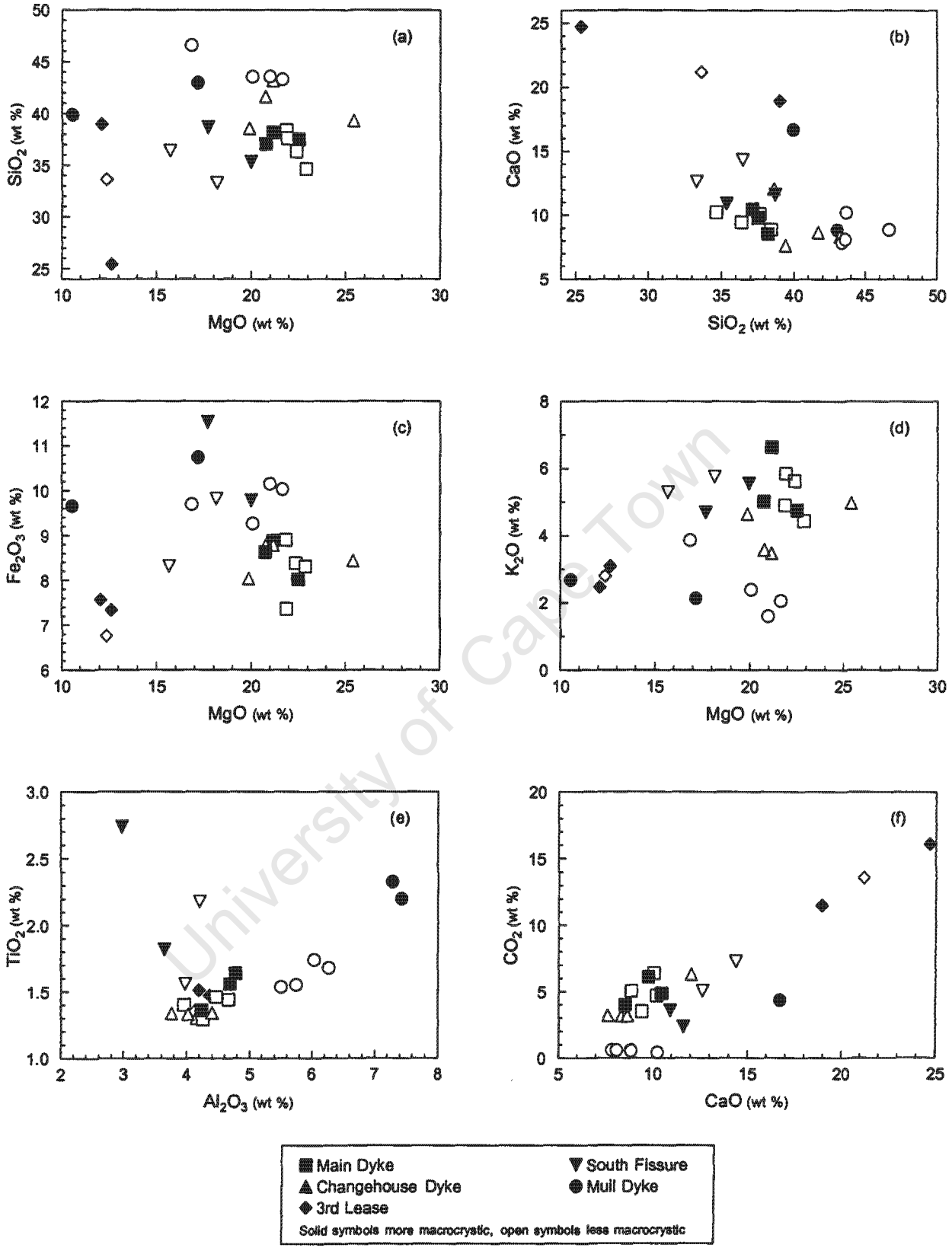

Figure 4.1 Variations of selected major elements in the Swartruggens kimberlite dykes and the Muil lamprophyre.

the range defined by the Main Dyke.

Despite having similar MgO content to the other Swartruggens kimberlite Dykes, the Changehouse Dyke has higher SiO_2, ranging from 37.5 to 41.6 wt %. Three of the Changehouse Dyke samples (NC 007, NC 009 and SR 7) have similar MgO concentrations (MgO = 19.3 and 20.4 wt %) and define a positive correlation between MgO and SiO_2 (Figure 4.1a). Sample NC 005, with higher MgO (24.7 wt %), does not lie on this trend. Sample NC 007 differs from the other Changehouse Dyke samples in having higher CaO and CO_2 (CaO = 11.7 wt %; CO_2 = 6.30 wt %). The other three Changehouse Dyke samples show a limited range in, and have relatively low contents of, both CaO and CO_2 relative to the other kimberlite dykes (CaO = 7.42 - 8.37 wt %; CO_2 = 3.15 to 3.20 wt %). These three samples also have similar Fe_2O_3 contents (Fe_2O_3 = 8.22 to 8.48 wt %) whereas NC 007 has lower Fe_2O_3 (Fe_2O_3 = 7.82 wt %). However, all the Changehouse Dyke samples have Fe_2O_3 contents within the range of the Main Dyke. K_2O concentrations are generally lower in the Changehouse Dyke than the Main Dyke, although they are variable and range from 3.35 to 4.87 wt %, with no correlation between K_2O and MgO (Figure 4.1d). There is little range in TiO_2 or Al_2O_3 content (TiO_2 = 1.27 to 1.30 wt %; Al_2O_3 = 3.62 – 4.25 wt %) within the Changehouse Dyke.

The South Fissure samples have similar SiO_2, K_2O and CO_2 contents to (South Fissure SiO_2 = 32.5 - 37.6 wt %; K_2O = 4.52 – 5.63; CO_2 = 2.35 – 7.27 wt %; Table 4.1), but lower MgO and higher CaO and Fe_2O_3 concentrations than, the Main Dyke (South Fissure MgO = 15.5 - 19.6 wt %; CaO = 10.7 - 14.2 wt %; Fe_2O_3 = 8.24 – 11.2 wt %; Table 4.1). Al_2O_3 and TiO_2 form a broad negative correlation within the South Fissure, with this dyke trending to slightly lower Al_2O_3 and considerably higher TiO_2 concentrations than the other Swartruggens kimberlite dykes (South Fissure Al_2O_3 = 2.90 – 4.10 wt %; TiO_2 = 1.52 – 2.66 wt %; Table 4.1). Although there are no strong major element correlations within the South Fissure, samples JJG 3148 and JJG 3149 form a trend of decreasing MgO and SiO_2 contents away from the main field of the Main Dyke samples. These two South Fissure samples also lie approximately on low SiO_2 and MgO extensions of the trends between CaO and SiO_2, and Fe_2O_3 and MgO defined by the Main Dyke. The other two South Fissure samples, JJG 3145 and JJG 3150 have relatively elevated SiO_2 contents, and Fe_2O_3 is higher in JJG 3150, and lower in JJG 3145, relative to these trends.

The lamprophyric Muil Dyke has lower MgO content than the Main Dyke and generally lower Mg# than the Swartruggens kimberlites (MgO = 10.3 – 21.0; Mg# = 0.72 – 0.83; Table 4.1), although the range in MgO within the Muil Dyke is similar to that present across the suite of kimberlite dykes. However, the Muil Dyke has considerably higher SiO_2 and Al_2O_3 contents (SiO_2 = 38.8 – 45.4%; Al_2O_3 = 5.32 – 7.07 wt %; Table 4.1) than the kimberlite dykes. With the exception of sample NC 014, with much higher K_2O than the other Muil Dyke samples (3.77 wt %), K_2O in the Muil Dyke is lower than in the kimberlite dykes (Muil Dyke K_2O = 1.53 - 2.61 wt %; Table 4.1) and shows more coherent behaviour, defining a shallow negative trend with MgO content. The Muil Dyke also differs from the kimberlite dykes in that aphanitic and macrocrystic samples are more clearly distinguished by their major element concentrations (Figure 4.1). There is a strong positive correlation between TiO_2 and Al_2O_3 within the Muil Dyke, with the macrocrystic samples having lower Al_2O_3

and TiO_2 contents (Al_2O_3 = 5.32 – 6.10 wt %; TiO_2 = 1.47 – 1.70 wt %; Table 4.1) than the aphanitic samples (Al_2O_3 = 7.06 – 7.07 wt %; TiO_2 = 2.10 – 2.27 wt %; Table 4.1). The macrocrystic Muil Dyke samples also have higher MgO concentrations (MgO = 16.4 – 21.0 wt %) than the aphanitic samples (MgO = 10.3 – 16.3 wt %; Table 4.1), and this distinction is even more marked if sample NC 014, with much lower MgO than the other macrocrystic samples (in addition to anomalously high K_2O) is ignored. The majority of the Muil Dyke samples have relatively low and restricted CaO contents (CaO = 7.61 – 10.0 wt %; Table 4.1) compared to the kimberlite samples, and differ from the kimberlite samples in having very low CO_2 concentrations (CO_2 = 0.41 – 0.59 wt %; Table 4.1). However, sample JJG 3141, with extremely low MgO (MgO = 10.0 wt %), has elevated CaO and CO_2 concentrations relative to the other Muil Dyke samples (CaO = 16.2 wt %; CO_2 = 4.34 wt %; Table 4.1).

4.3 Major element geochemistry of the Star kimberlite dykes

Twenty-two samples from the Star kimberlite dykes (2 from the Clewer Dyke, 7 from the Wynandsfontein Dyke, 4 from the East Star Dyke, 4 from the Byrnes Dyke and 4 from the Barren Dyke) have been analysed for a range of major element abundances. Individual analyses are reported in Table 4.2, and selected variation diagrams are shown in Figure 4.2. Kimberlite magmas are known to contain a primary volatile component (e.g. Dawson, 1980; Berg and Allsopp, 1972). In the absence of any further quantifying information, H_2O^+ and CO_2 concentrations in the Star kimberlite samples are assumed largely to reflect those of the original magma. Data are normalised to an H_2O^- free basis before plotting

The Star kimberlite dykes show wide variation in major element abundances across the suite of dykes, with SiO_2 ranging from 22.7 to 43.7 wt % and defining a broad positive correlation with MgO content (MgO = 5.50 to 36.7 wt %; Table 4.2; Figure 4.2a). Mg# shows less variation and is high in all the kimberlite dykes (Mg# = 0.72 – 0.90; Table 4.2). With the exception of the Barren dyke, the Star kimberlite dykes show coherent trends between major elements, with individual dykes showing similar correlations and overlapping major element concentrations. There is a strong negative correlation between MgO and CaO (CaO = 2.15 – 30.1 wt %; Table 4.2; Figure 4.2b), although there is a distinct break in slope at approximately 20 wt % MgO; the higher MgO samples define a shallow negative correlation with CaO whereas the lower MgO samples show a much sharper increase in CaO with decreasing MgO. Despite their variable concentrations in the Star kimberlite dykes, the major elements Fe and K (Fe_2O_3 = 4.10 – 9.23 wt %; K_2O =0.64 – 4.22 wt %; Table 4.2) show coherent behaviour with when plotted against MgO and SiO_2 (Figure 4.2c and d). The higher MgO and SiO_2 samples define stronger trends between MgO or SiO_2 and Fe_2O_3 and K_2O, whereas the lower MgO samples show more scatter. Al_2O_3 and TiO_2 are less variable in abundance (Al_2O_3 = 2.15 – 3.32 wt %; TiO_2 = 0.76 – 1.55 wt %; Table 4.2) and there is a broad positive correlation between these two oxides (Figure 4.2e). CO_2 concentrations in the Star kimberlites show a considerable range (CO_2 = 0.28 – 16.2 wt %; Table 4.2) and show a broad positive correlation with CaO concentrations (Figure 4.2f). With a few notable exceptions, discussed below, the more macrocrystic Star kimberlite samples have higher MgO, SiO_2 and Fe_2O_3 concentrations, and lower abundances of CaO, K_2O and CO_2, than the less macrocrystic

Table 4.2 Major element geochemistry of the Star kimberlite dykes. Mic = micaceous Barren Dyke, l. mic = less micaceous Barren Dyke; M = more macrocrystic, LM = less macrocrystic; LOI = loss on ignition; H_2O^+ calculated as LOI – H_2O^- (measured); Mg# = atomic Mg/(Mg + Fe^{2+}) with Fe_2O_3 / FeO = 0.2 (typical for alkaline rocks); C.I. = contamination index = (SiO_2 + Al_2O_3 + Na_2O)/(MgO + $2K_2O$) (Clement, 1982); bd = below detection.

Dyke	Clewer Dyke		Wynandsfontein Dyke							East Star Dyke	
Sample	JJG 2833	JJG 2837	SJH 37	JJG 6361A	JJG 6361C	JJG 6369	JJG 6362	JJG 6360	NC 050	JJG 4570	SJH 101
Macro	M	M	LM	M	M	LM	M	M	LM	M	LM
SiO_2	33.9	34.1	22.7	26.1	31.0	28.4	35.2	32.9	31.2	33.9	34.6
TiO_2	0.85	1.10	1.17	1.14	1.19	1.24	1.27	1.18	1.13	1.01	1.18
Al_2O_3	2.44	2.83	2.93	3.03	3.00	2.94	3.07	2.90	2.60	2.34	2.68
Fe_2O_3	8.15	8.62	4.10	4.94	5.91	7.60	8.96	8.40	7.94	8.82	8.57
MnO	0.14	0.19	0.56	0.56	0.34	0.33	0.28	0.17	0.15	0.16	0.18
MgO	33.2	28.8	9.20	5.50	15.5	15.3	21.2	27.5	25.0	33.0	23.9
CaO	6.63	7.84	29.4	30.1	19.4	19.4	10.2	8.90	9.89	6.45	9.40
Na_2O	bd	0.04	0.05	bd	0.11	0.15	0.21	0.07	0.13	0.05	0.21
K_2O	2.07	3.13	2.34	0.64	3.23	2.66	3.23	3.16	3.41	2.55	3.22
P_2O_5	0.31	0.69	2.73	1.16	1.44	1.68	1.06	0.86	0.98	1.12	1.26
SO_3	0.41	0.34	0.92	2.10	0.37	0.38	0.24	0.11	0.60	0.14	0.44
NiO	0.19	0.16	0.10	0.09	0.12	0.12	0.15	0.16	0.13	0.19	0.15
Cr_2O_3	0.29	0.30	0.22	0.26	0.24	0.24	0.30	0.32	0.27	0.24	0.28
H_2O^-	0.44	0.89	1.21	0.32	1.90	2.84	2.57	0.80	0.74	0.41	1.63
LOI	10.2	10.2	21.5	23.5	16.2	16.4	11.8	12.1	15.2	9.02	11.5
Total	99.2	99.2	99.2	99.4	99.9	99.7	99.7	99.6	99.4	99.5	99.2
CO_2	4.17	4.36	10.4	12.1	8.72	9.46	5.66	6.49	7.51	0.28	5.10
H_2O^+	6.01	5.83	11.12	11.43	7.46	6.98	6.11	5.65	7.72	8.74	6.40
Mg#	0.90	0.89	0.84	0.72	0.86	0.83	0.85	0.88	0.88	0.90	0.87
C. I.	1.0	1.1	1.9	4.3	1.6	1.5	1.4	1.1	1.1	1.0	1.2

Dyke	East Star Dyke			Byrnes Dyke				Barren Dyke			
Sample	SJH 30	SJH 38	SJH 104	SJH 80	SJH 79	SJH 78	SJH 77	mic NC 051	mic NC 052	mic NC 053	l. mic NC 054
Macro	LM	M	M	LM	LM	M	LM	M	M	M	M
SiO_2	32.5	30.9	35.3	26.8	29.8	33.8	27.1	43.6	43.1	43.7	38.7
TiO_2	1.24	1.15	1.09	1.55	1.33	1.05	1.35	1.11	1.06	1.19	0.76
Al_2O_3	2.77	2.79	2.73	3.24	2.86	2.61	3.03	3.19	2.88	3.32	2.15
Fe_2O_3	7.91	8.05	8.56	7.27	7.81	8.32	6.72	9.07	9.15	9.23	9.12
MnO	0.19	0.18	0.18	0.64	0.51	0.47	0.58	0.37	0.39	0.36	0.17
MgO	17.9	26.0	26.9	16.6	18.4	19.7	16.2	23.4	23.2	23.7	36.7
CaO	15.3	9.52	8.43	18.5	14.8	11.7	17.8	3.25	3.55	2.86	2.15
Na_2O	0.02	0.03	0.13	0.02	0.07	0.17	0.02	0.08	0.09	0.09	0.10
K_2O	3.83	3.35	2.73	4.12	4.22	2.87	3.33	3.00	2.96	3.08	1.81
P_2O_5	0.98	0.76	0.64	1.44	1.31	0.92	1.25	0.62	0.63	0.63	0.50
SO_3	0.37	0.21	0.39	0.88	0.51	0.33	0.45	0.22	0.19	0.21	0.13
NiO	0.12	0.13	0.17	0.08	0.10	0.17	0.07	0.21	0.22	0.21	0.22
Cr_2O_3	0.29	0.28	0.33	0.26	0.27	0.29	0.28	0.40	0.40	0.37	0.38
H_2O^-	1.25	0.78	1.58	0.24	0.59	1.85	0.40	4.54	4.61	4.83	1.55
LOI	14.7	15.0	10.4	18.0	16.5	15.1	20.6	6.67	7.09	6.06	4.89
Total	99.3	99.1	99.6	99.6	99.1	99.4	99.2	99.7	99.4	99.7	99.3
CO_2	9.09	7.79	4.64	13.6	11.8	9.37	16.2	1.30	1.39	0.97	0.42
H_2O^+	5.58	7.18	5.79	4.35	4.70	5.77	4.39	5.37	5.70	5.09	4.47
Mg#	0.84	0.88	0.88	0.84	0.85	0.85	0.72	0.86	0.86	0.86	0.90
C. I.	1.4	1.0	1.2	1.2	1.2	1.4	1.3	1.6	1.6	1.6	1.0

samples (Table 4.2; Figure 4.2).

The Wynandsfontein Dyke samples define a broad positive correlation between MgO and SiO_2, with a range in SiO_2 from 22.7 to 35.2 wt % for a wide range in MgO content (MgO = 5.50 – 27.5 wt %; Table 4.2). CaO in the Wynandsfontein Dyke is also extremely variable, and ranges from 8.90 to 30.1 wt %, and there is a negative correlation between CaO and MgO (Figure 4.2b). The lower MgO samples (<20 wt % MgO) form a much steeper negative correlation than the higher MgO samples. A similar break in slope is present on a plot of K_2O versus MgO for the Wynandsfontein Dyke samples (Figure 4.2d), with samples containing less than 20 wt % MgO having a range in K_2O from 0.64 to 3.23 wt % and defining a positive correlation between K_2O and MgO. Samples containing more than 20 wt % MgO, however, have similar K_2O concentrations (K_2O = 3.16 – 3.41 wt %) for a range in MgO. The majority of the Wynandsfontein Dyke samples contain between 7.64 and 8.96 wt % Fe_2O_3, and define a strong positive correlation with SiO_2 similar to that of all the Star kimberlite dykes (Figure 4.2c). However samples SJH 37, JJG 6361A and JJG 6361C, with low MgO contents, have lower Fe_2O_3 (Fe_2O_3 = 4.10 – 5.91 wt %) and plot below the main trend, defining a separate positive correlation with SiO_2. There is a broad positive correlation between TiO_2 and Al_2O_3 within the Wynandsfontein Dyke, with TiO_2 ranging from 1.13 to 1.27 wt % and Al_2O_3 ranging from 2.60 to 3.07 wt % (Table 4.2).

Within the East Star Dyke there is a broad range in MgO content, from 17.9 to 33.0 wt %, with the three more macrocrystic samples (JJG 4570, SJH 38 and SJH 104) having higher MgO contents than the less macrocrystic samples (Table 4.2). However, other major element concentrations are less variable within the East Star Dyke than the Wynandsfontein Dyke (e.g. SiO_2 = 30.9 – 35.3 wt %; Table 4.2). Although there is no correlation between MgO and SiO_2 within the East Star Dyke, the range in composition of this dyke lies approximately at the higher MgO end of the positive correlation shown by the Wynandsfontein Dyke (Figure 4.1a). Four of the East Star Dyke samples show little variation in CaO content (CaO = 6.45 – 9.52; Table 4.2) and these samples define a shallow negative correlation between MgO and CaO (Figure 4.2b). Sample SJH 30 has the higher CaO content of 15.3 wt %, and lies on the steeper negative trend between CaO and MgO defined by the Star kimberlite samples with lower MgO contents. Fe_2O_3 concentrations show little variation within the East Star Dyke (7.91 – 8.82 wt %; Table 4.2) and there is a broad positive correlation between Fe_2O_3 and SiO_2 within this dyke (Figure 4.2c). The more macrocrystic East Star Dyke samples trend to lower K_2O contents (K_2O = 2.55 – 3.35 wt %; Table 4.2) than the less macrocrystic samples (K_2O = 3.22 – 3.83 wt %; Table 4.2) and there is a broad negative correlation between K_2O and MgO within the dyke (Figure 4.2d). Although there is little variation in the abundance of TiO_2 or Al_2O_3 within the East Star Dyke (TiO_2 = 1.01 – 1.24 wt %; Al_2O_3 = 2.34 – 2.79 wt %; Table 4.2), there is a broad positive correlation between these two oxides with the more macrocrystic samples trending to lower Al_2O_3 and TiO_2 contents than the Wynandsfontein Dyke (Figure 4.2e).

The Byrnes Dyke has lower MgO and SiO_2 contents than the East Star Dyke (Byrnes Dyke MgO = 16.2 - 19.7 wt %; SiO_2 = 26.6 – 33.8 wt %; Table 4.2), although still within the range of the Wynandsfontein Dyke. The most macrocrystic Byrnes Dyke sample (SJH 78) has the highest SiO_2 and MgO contents. CaO

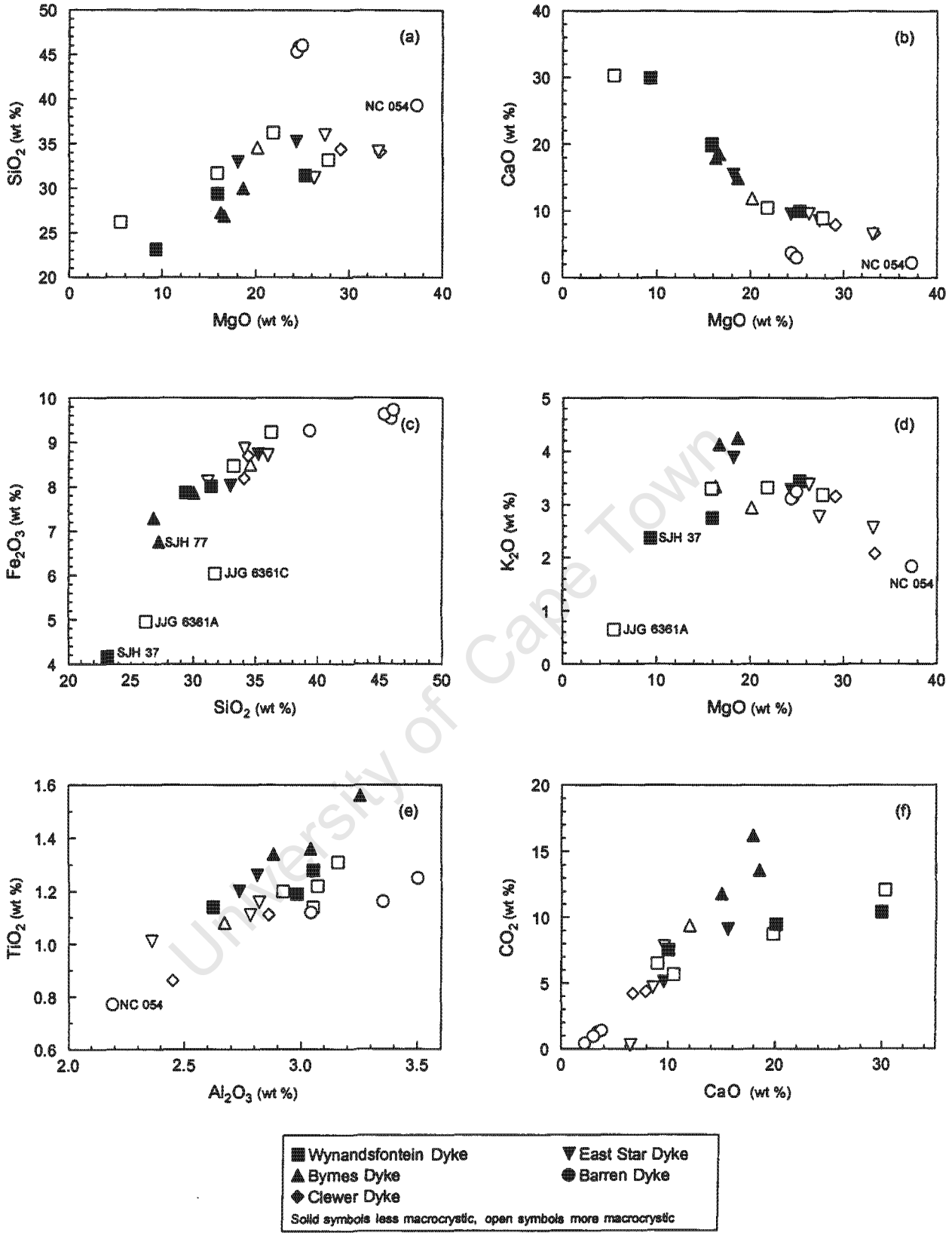

Figure 4.2 Variations of selected major elements in the Star kimberlite dykes.

contents of the Byrnes Dyke range from 11.7 to 18.5 wt %, and form a strong negative correlation with MgO content, with the more macrocrystic sample having the lowest CaO (Figure 4.2b). There is a broad positive correlation between Fe_2O_3 and SiO_2 within the Byrnes Dyke (Fe_2O_3 = 6.72 - 8.32 wt %; Table 4.2), although sample SJH 77 lies below the main trend of the Star kimberlite dykes, with lower Fe_2O_3 (Figure 4.2c). The macrocrystic sample (SJH 78) has the highest Fe_2O_3 content of the Byrnes Dyke samples. There is a range in K_2O concentrations from 2.87 to 4.22 wt % within the Byrnes Dyke for little variation in MgO content (Table 4.2; Figure 4.2d). However, the aphanitic samples SJH 80 and SJH 79 contain more K_2O than any of the other Star kimberlite samples and have similar K_2O contents of 4.12 and 4.22 wt % respectively, whereas the more macrocrystic sample (SJH 78) has lower K_2O with a slightly higher MgO content. SJH 77, with lower Fe_2O_3 than the main Star kimberlite trend, also has lower K_2O and slightly lower MgO content than the other aphanitic Byrnes Dyke samples. All three aphanitic Byrnes Dyke samples have higher TiO_2 contents than any of the other Star kimberlite dykes, ranging from 1.33 to 1.55 wt %, and there is a within-dyke positive correlation between TiO_2 and Al_2O_3 (Al_2O_3 = 2.86 – 3.24 wt %; Table 4.2) broadly consistent with the trend shown by the Star kimberlites as a whole (Figure 4.2e). The more macrocrystic Byrnes Dyke sample (SJH 78) has lower TiO_2 and Al_2O_3 (TiO_2 = 1.05 wt %; Al_2O_3 = 2.61 wt %; Table 4.2) than the aphanitic Bymes Dyke samples.

The Clewer Dyke has MgO and SiO_2 concentrations towards the more enriched compositions, but within the range, of the other Star kimberlite dykes (MgO = 28.8 to 32.2 wt %; SiO_2 = 34.1 wt %; Table 4.2). This dyke is also the least enriched in CaO (CaO = 6.63 – 7.84; Table 4.2) and its composition lies on the shallow negative trend between CaO and MgO defined by the high MgO Star kimberlite samples (Figure 4.2b). There is little variation in Fe_2O_3 contents within the Clewer Dyke (Fe_2O_3 = 8.15 – 8.62; Table 4.2) and the Clewer Dyke samples plot within the range of the broad positive correlation between Fe_2O_3 and SiO_2 defined by the majority Star kimberlite samples (Figure 4.2c). Although K_2O is slightly more variable within this dyke, ranging from 2.07 to 3.13 wt % (Table 4.2), the Clewer Dyke samples plot on the trend of decreasing K_2O with increasing MgO defined by the other high MgO Star kimberlite samples. Sample JJG 2833 from the Clewer Dyke has lower TiO_2 and Al_2O_3 than any of the other samples from the Star diamondiferous dykes (JJG 2833 TiO_2 = 0.85 wt %; Al_2O_3 = 2.44 wt %; Table 4.2), whereas sample JJG 2837 has TiO_2 and Al_2O_3 contents within the range of the other diamondiferous dykes.

Despite having similar MgO contents, the Barren Dyke has considerably higher SiO_2, higher Fe_2O_3 and lower CaO contents than the other Star kimberlite dykes. The three micaceous samples have very similar compositions (e.g. MgO = 23.2 – 23.7 wt %; SiO_2 = 43.1 – 43.7 wt %; CaO = 2.86 – 3.55 wt %; K_2O = 2.96 – 3.08 wt %; Table 4.2) and these samples do not consistently plot on the trends defined by the other Star kimberlite dykes (Figure 4.2). The micaceous samples have TiO_2 contents ranging from 1.06 – 1.19 wt %, within the range of the other Star kimberlite dykes, and define a broad positive correlation between TiO_2 and Al_2O_3 but trend to higher Al_2O_3 contents than the other Star Dykes (micaceous Barren Dyke Al_2O_3 = 2.88 – 3.32 wt %; Table 4.2). The less micaceous Barren Dyke sample (NC 054) has higher MgO and lower SiO_2 contents than the micaceous samples (MgO = 36.7 wt %; SiO_2 = 38.7 wt %; Table 4.2). This sample lies approximately at the MgO-rich end of the trends defined by the other Star Dykes for SiO_2, CaO and K_2O vs.

MgO, and the high SiO_2 end of the trend between Fe_2O_3 and SiO_2 (Figure 4.2a, b, c and d). NC 054 also has considerably lower Al_2O_3 and TiO_2 than the micaceous Barren Dyke samples (NC 054 Al_2O_3 = 2.15; TiO_2 = 0.76 wt %) and its composition is a less enriched extension of the trend defined by the other Star kimberlite dykes (Figure 4.2e). All the Barren Dyke samples have lower CO_2 concentrations than the Star kimberlite dykes (CO_2 = 0.42 – 1.39 wt %; Table 4.2).

4.3 Comparison in major element geochemistry between the Swartruggens, Star and other South African kimberlites

Both the Swartruggens and Star kimberlites show a wide range in major element composition and have similar abundances of most elements (e.g. MgO, CO_2, Na_2O and Fe_2O_3; Tables 4.1 and 4.2). However, for a similar range in MgO, the Swartruggens kimberlites are more enriched in SiO_2, K_2O and Al_2O_3 than the Star kimberlites (Figure 4.3a-d). The Swartruggens South Fissure samples also extend to higher TiO_2 contents than any of the Star samples (Figure 4.3d).

The Swartruggens and Star kimberlites have SiO_2 concentrations broadly similar to those of other Group II kimberlites, although the Swartruggens kimberlites extend to slightly higher, and the Star kimberlites extend to lower, SiO_2 contents than the field for other South African Group II kimberlites illustrated in Figure 4.3a. The Star micaceous Barren Dyke samples have higher SiO_2 concentrations than the Swartruggens kimberlites or the field of Group II kimberlites, and both the Swartruggens and Star kimberlites extend to lower MgO contents than the fields for Group II or Group I kimberlites (Figure 4.3a). Both South African Group I and Group II kimberlites define shallow negative trends between CaO and SiO_2, with Group I kimberlites extending to higher CaO contents (up to ~20 wt %) and lower SiO_2 contents (Figure 4.3b). With the exception of the Third Lease samples, with higher CaO contents, the Swartruggens kimberlites show no correlation between CaO and SiO_2, and lie within the range of approximately 2 to 14 wt % CaO defined by other South African kimberlites. However, they are relatively enriched in CaO for a given SiO_2 content than the field for Group II kimberlites (Figure 4.3b). The negative correlation between CaO and SiO_2 defined by the Star kimberlites, extends to much higher CaO contents than the field for other South African Group II and even the Kimberley Group I kimberlites, with only the high MgO (up to 20 wt %) samples having CaO contents within the range of other South African Group II kimberlites (Figure 4.3b).

The Star kimberlites have K_2O concentrations within the field of Group II kimberlites, with those samples containing greater than 20 wt % MgO defining a similar negative trend between K_2O and MgO (Figure 4.3c). The Swartruggens kimberlites, with the exception of the low K_2O Third Lease samples, generally have more enriched K_2O concentrations than the Star kimberlites or other South African Group II kimberlites. Although there is no convincing trend between K_2O and MgO within the Swartruggens samples, as a group they plot approximately on a higher K_2O, lower MgO, extension of the field of other Group II kimberlites. In contrast, Group I kimberlites have much lower K_2O contents (up to ~2 wt %) than Swartruggens, Star, or other Group II kimberlites. South African Group I and Group II kimberlites define positive correlations between Al_2O_3 and

TiO_2, with Group I kimberlites defining a much steeper trend to higher TiO_2 contents (up to ~3.8 wt %) and Group II kimberlites defining a shallower trend to approximately 1.4 wt % TiO_2, for a similar range in Al_2O_3 (Figure 4.3d). The Star kimberlites lie within the range of other Group II kimberlites for Al_2O_3 content, but define a crosscutting, slightly steeper trend towards slightly higher TiO_2 contents. The Swartruggens kimberlites have higher Al_2O_3 than the Star kimberlites and, with the exception of the South Fissure, overlap the high TiO_2, high Al_2O_3, end of the field of Group II kimberlites, extending the field to slightly higher Al_2O_3 and TiO_2 contents. The Swartruggens South Fissure sample JJG 3150 has a much higher TiO_2 content (TiO_2 = 2.66 wt %) than other Group II kimberlites.

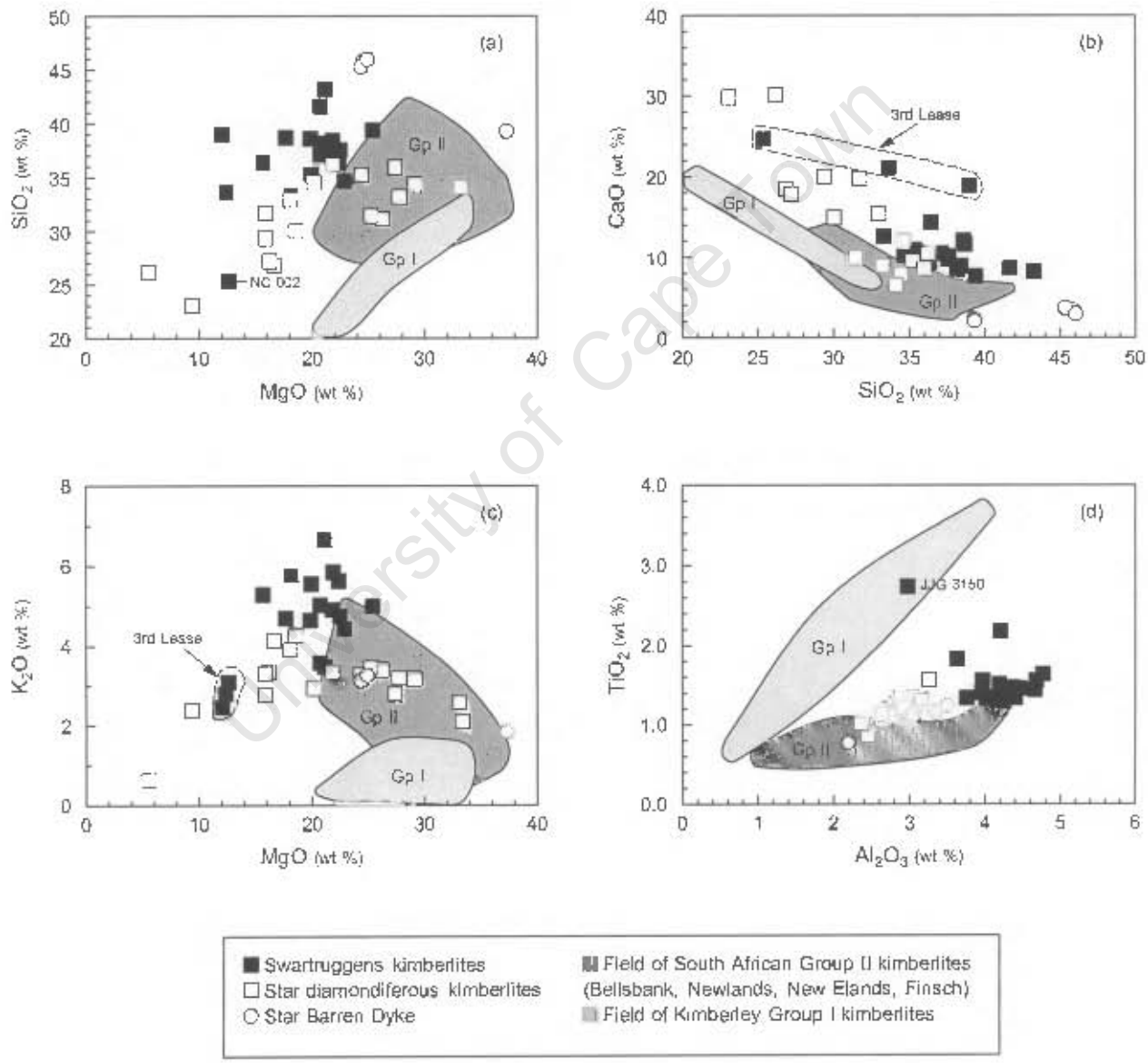

Figure 4.3 Comparison of the variations of selected major elements in the Swartruggens and Star kimberlite dykes with other South African Group II and Group I kimberlites. The Swartruggens Muil lamprophyre is not shown. Field for Group I kimberlites from le Roex *et al.* (2003); field for Group II kimberlites from le Roex (unpublished data) and Tainton (1992).

Chapter 5

Trace element geochemistry

5.1 Introduction

Kimberlites are unusual rocks in that they contain very high abundances of both compatible and incompatible elements (e.g. Mitchell, 1995). They are strongly enriched in the incompatible elements relative to primitive mantle, and typically have steep primitive mantle normalised incompatible element patterns with strongest enrichment in the more incompatible elements. The trace element geochemistry of kimberlites is complicated by such processes as alteration, which may disturb the concentrations of the more mobile elements (e.g. the large ion lithophile elements; e.g. le Roex *et al.*, 2003) and assimilation of crust, which may cause enrichment in the magmas of elements present in higher abundance in crustal material, as well as dilution of those elements present in higher abundance in the primary kimberlite magma (e.g. Clement, 1982). In addition, the concentrations of the compatible elements may be decreased by fractional crystallisation or increased by peridotite entrainment, with consequent enrichment or dilution of the incompatible trace elements by the same processes. Partly as a result of these complications, although the bulk rock trace element geochemistry of kimberlites has been well documented on a regional scale (e.g. Clement, 1982; Shee, 1985; Tainton, 1992), few attempts have been made to characterise the trace element concentrations of primary kimberlite magmas, or to use these compositions to quantitatively model source region characteristics of kimberlites. Notable exceptions are the studies of Tainton and McKenzie (1994), on southern African Group II kimberlites, and le Roex *et al.* (2003) and Harris *et al.* (2004) on South African Group I kimberlites. These studies have demonstrated that data from a suite of samples from the same intrusion can be used to isolate these effects and so constrain the primary kimberlite magma composition, allowing the source region trace element composition to be modelled, as will be shown in Chapter 7.

A suite of samples from each of the exposed kimberlite dykes at Swartruggens and Star, and the Swartruggens Muil lamprophyre, have been analysed for a range of trace elements with four principal aims, summarised below:

1 – To characterise the whole rock trace element abundances of the two kimberlite dyke swarms.

2 – To isolate the effects of late-stage alteration, crystal fractionation and assimilation of mantle and crust by the kimberlites *en route* to the surface, thus constraining the primitive magma compositions of these kimberlites.

3 – Using simple partial melting calculations on the primary kimberlite magma compositions, to constrain the mineralogy and geochemical signature of the respective source regions of the kimberlites.

4 – To gain an understanding of the evolution of the source regions and the petrogenetic processes giving rise to the kimberlite magmas.

This chapter concentrates on documenting and describing the trace element variation in the Swartruggens and Star kimberlite dykes. Points 2 – 4 (above) are considered in more detail in Chapter 7.

The abundances of a range of trace elements in the Swartruggens and Star kimberlites and the Muil lamprophyre were determined by inductively coupled plasma mass spectrometry (ICP-MS) and X-ray fluorescence spectrometry (XRF). Details of the analytical techniques are reported in Appendix 3. For comparison, the concentrations of a number of trace elements were determined by both techniques. As reported in Appendix 3, a small number of the Star samples have lower measured Nb concentrations when analysed by ICP-MS relative to XRF. This is believed to be due to incomplete dissolution of Nb bearing phases prior to ICP-MS analyses and XRF Nb data have therefore been reported in this chapter. Given the similar geochemical behaviour of Nb and Ta, the Ta concentrations reported in Tables 5.1 and 5.2, determined by ICP-MS, may also be slightly low.

5.2 Trace element geochemistry of the Swartruggens kimberlite dykes and the Muil lamprophyric dyke

Nineteen samples from the Swartruggens kimberlite dykes (3 from the Third Lease, 7 from the Main Dyke, 4 from the Changehouse Dyke and 4 from the South Fissure), and 6 samples from the Muil lamprophyric dyke, have been analysed for their trace element content. Individual analyses are reported in Table 5.1, and selected trace element variations are shown in Figures 5.1 to 5.5.

5.2.1 Compatible trace elements

Compatible trace element variations in the Swartruggens kimberlite dykes are illustrated with respect to La in Figure 5.1. Ni and Cr show similar behaviour, both showing broad ranges in abundance (Ni = 617 - 1814 ppm; Cr = 1270 - 1845 ppm; Table 5.1) and defining positive correlations with MgO, and negative correlations with La, content (Figure 5.1a and b). Within the Main Dyke, Ni ranges between 862 and 1304 ppm and defines a within-dyke negative correlation with La content, with the more macrocrystic samples trending to higher Ni contents than the less macrocrystic samples (Figure 5.1a). A particularly strong negative correlation is defined by samples NC 004, NC 006, SR 6, JJG 3143 and Hons 95-4, whereas NC 010 and NC 011 lie below this trend with lower Ni concentrations for a given MgO content. Cr shows a similar range in concentrations (Cr = 1306 - 1425 ppm; Table 5.1) and shows no within-dyke correlation with La content (Figure 5.1b). The Third Lease samples have Ni contents within the range of the Main Dyke although they extend to slightly higher Cr content (up to 1644 ppm), whereas the Changehouse Dyke has higher Ni and Cr contents (Ni = 1592 to 1814 ppm; Cr = 1574 to 1845 ppm; Table 5.1) than the Main Dyke. Within the Changehouse Dyke there are no correlations between Ni or Cr and La (Figure 5.1a and b), although the Changehouse Dyke plots approximately on the trend of the Main Dyke samples for Ni versus La. The range of Ni and Cr contents of the South Fissure overlap those of the Main Dyke, but extend to

Table 5.1 Bulk rock trace element analyses, in ppm, of the Swartruggens kimberlite dykes and the Muil lamprophyre dyke. Macro = no. of macrocrysts present in thin section; M = more macrocrystic, LM = less macrocrystic; * = elements analysed by XRF, all other elements analysed by ICP-MS; ** = average of 2 separate analyses, individual analyses are reported in Appendix 2.

Dyke	3rd Lease			Main Dyke							Changehouse	
Sample	NC 001	NC 002	NC 003	NC 004	NC 006	NC 010	NC 011	SR 6	JJG 3143	Hons 95-4	NC-005	NC-007
Macro	M	LM	LM	M	LM	M	LM	M	M	LM	M	M
Sc	19.6	19.3	19.0	19.0	20.5	18.1	19.3	19.9	20.7	21.1	16.0	16.8
V	90.9	162	269	119	190	170	115	152	151	144	125	124
Cr*	1540	1644	1442	1367	1419	1425	1306	1328	1332	1415	1845	1732
Co	58.9	56.1	57.0	73.2	60.4	65.5	62.5	66.9	66.6	66.3	75.2	80.5
Ni*	1038	938	1004	1304	862	1012	946	1058	1142	1093	1592	1600
Cu	30.8	43.4	38.4	25	40.6	20.5	30.4	33.5	36.0	34.3	30.5	32.5
Zn*	93.6	116	113	84.0	95.8	84.7	79.9	93.1	87.3	85.6	77.8	81.3
Rb	120	134	102	200	273	221	198	244	195	213	187	185
Sr	1270	1605	890	1198	1422	743	1009	750	473	1906	973	850
Cs	5.20	4.76	5.89	7.57	6.62	5.05	4.67	7.37	3.88	8.03	7.22	8.56
Ba	1747	1494	954	4129	3452	8226	5263	2699	4107	2996	3200	3922
Y	24.1	26.4	22.0	24.1	27.7	12.7	18.4	24.6	23.0	32.4	14.0	16.4
Zr	388	415	413	378	395	173	374	340	329	355	264	395
Nb*	120	144	147	140	171	105	83.4	133	144	143	86.5	80.1
Hf	8.22	9.02	8.74	8.14	8.63	4.54	8.09	8.69	7.51	8.16	5.76	9.80
Ta	5.17	5.55	5.37	6.25	5.93	5.41	4.97	6.00	6.41	6.39	3.43	4.14
Pb	50.6	54.8	61.1	28.6	40.3	48.5	33.3	43.6	37.1	35.4	27.6	29.6
Th	26.6	26.7	25.5	26.6	30.6	18.9	22.0	25.5	26.7	28.4	15.1	18.2
U	7.25	8.33	8.33	6.62	7.89	1.83	4.82	7.01	6.94	7.06	4.15	5.05
La	210	217	208	185	257	193	195	221	207	229	124	146
Ce	401	411	402	356	493	383	375	427	409	446	242	284
Pr	42.2	43.3	42.5	37.7	52.1	40.2	39.5	45.3	43.3	47.6	25.9	30.2
Nd	150	155	153	134	187	141	142	160	155	171	95.2	109
Sm	19.1	20.0	18.7	17.7	23.6	16.7	17.9	19.7	19.2	21.7	12.4	14.1
Eu	4.60	4.89	4.41	4.51	5.77	4.01	4.43	4.88	4.91	5.41	3.20	3.53
Gd	11.9	13.3	11.7	11.5	14.7	8.5	10.7	12.4	11.8	14.3	7.67	8.78
Tb	1.42	1.55	1.38	1.40	1.74	0.94	1.22	1.44	1.39	1.67	0.89	1.04
Dy	5.75	6.34	5.42	5.94	6.85	3.30	4.79	5.67	5.74	6.97	3.61	4.09
Ho	0.93	1.03	0.87	0.96	1.10	0.51	0.77	0.90	0.91	1.13	0.57	0.64
Er	2.33	2.49	2.06	2.39	2.58	1.19	1.76	2.03	2.11	2.53	1.33	1.50
Tm	0.27	0.30	0.25	0.29	0.32	0.15	0.22	0.25	0.26	0.29	0.16	0.19
Yb	1.54	1.66	1.39	1.70	1.76	0.84	1.26	1.42	1.50	1.62	0.91	1.05
Lu	0.19	0.22	0.19	0.23	0.24	0.11	0.17	0.19	0.20	0.22	0.12	0.14
Ce/Pb	7.92	7.51	6.58	12.5	12.2	7.90	11.3	9.81	11.0	12.6	8.77	9.60
U/Th	0.27	0.31	0.33	0.25	0.26	0.10	0.22	0.27	0.26	0.25	0.28	0.28
Zr/Nb	3.25	2.88	2.82	2.69	2.32	1.65	4.48	2.56	2.29	2.48	3.05	4.93
Zr/Y	16.1	15.7	18.8	15.7	14.3	13.6	20.3	13.8	14.3	10.9	18.9	24.1
Zr/Hf	47.2	46.0	47.3	46.4	45.8	38.1	46.2	39.1	43.8	43.5	45.9	40.3
Ba/Nb	14.6	10.4	6.51	29.4	20.2	78.6	63.1	20.3	28.5	20.9	37.0	49.0
La/Nb	1.76	1.50	1.42	1.32	1.51	1.85	2.34	1.66	1.44	1.60	1.43	1.83
La/Th	7.90	8.12	8.15	6.96	8.40	10.2	8.90	8.65	7.75	8.07	8.24	8.05

Table 5.1 Continued.

Dyke	Changehouse		South Fissure				Muil Dyke					
Sample	NC-009	SR 7	JJG 3149	JJG 3145	JJG 3150	JJG 3148	NC 008**	NC 012	NC 014	NC 015	JJG 3141	SR 9
Macro	M	M	LM	M	LM	M	LM	M	M	M	LM	M
Sc	15.4	16.8	12.3	10.3	17.9	19.4	23.0	18.7	23.1	26.8	30.8	17.8
V	122	131	270	228	328	293	274	180	247	179	219	187
Cr*	1574	1738	1270	1462	802	1459	991	1946	1650	2088	620	2068
Co	87.8	84.7	64.8	70.3	61.9	62.9	52.5	77.5	68.6	71.0	35.9	81.3
Ni*	1814	1714	924	1048	617	756	441	1071	817	1087	71.7	1191
Cu	33.0	32.1	78.8	35.7	195	82.4	87.2	60.2	60.2	63.4	76.3	58.2
Zn*	82.4	82.0	136	123	143	134	92.6	76.9	71.6	85.9	65.5	80.3
Rb	146	154	226	216	183	257	98	125	150	134	103	68
Sr	1302	1667	2841	2127	3154	2144	938	772	765	674	604	750
Cs	7.87	19.3	3.62	3.84	4.01	3.78	7.79	11.2	6.67	4.69	4.81	16.9
Ba	3141	3329	7003	6975	10649	5356	1725	1210	1518	1185	2359	1553
Y	16.2	17.1	36.1	29.3	59.1	47.6	10.3	7.7	7.5	8.5	11.7	8.0
Zr	264	368	427	310	1145	668	223	152	183	142	227	160
Nb*	101	91.1	191	144	351	227	81.9	53.9	57.6	50.0	81.4	54.0
Hf	6.08	9.29	9.21	5.94	22.3	13.9	5.41	3.70	4.38	3.68	5.69	4.00
Ta	3.76	4.27	5.79	5.83	9.57	7.08	3.87	2.75	3.10	2.70	4.97	3.25
Pb	26.7	26.6	78.7	56.2	110	101	15.9	10.3	9.9	9.1	13.4	10.0
Th	17.9	17.4	28.3	25.9	44.1	34.9	10.6	7.6	8.0	7.2	10.4	7.5
U	4.70	4.57	13.02	9.57	14.7	15.5	2.66	2.34	2.92	1.56	3.13	2.35
La	138	142	287	244	293	300	88.9	59.4	58.1	62.6	85.1	57.2
Ce	267	277	531	455	559	599	179	119	118	128	176	118
Pr	28.4	29.3	54.9	48.5	59.7	65.6	19.4	13.1	12.9	14.4	19.7	12.9
Nd	102	106	195	172	214	240	72	49	47	54	74	48
Sm	13.2	13.5	25.8	22.1	31.7	31.4	9.24	6.33	6.02	7.12	9.83	6.40
Eu	3.32	3.55	6.34	5.67	8.66	8.20	2.28	1.60	1.56	1.80	2.52	1.62
Gd	8.36	8.59	15.6	13.8	22.1	20.9	5.73	4.01	3.85	4.39	6.04	3.91
Tb	0.97	0.99	1.88	1.61	2.87	2.43	0.64	0.44	0.43	0.49	0.70	0.45
Dy	3.99	4.11	7.83	6.78	13.5	10.3	2.60	1.83	1.87	2.00	2.93	1.84
Ho	0.64	0.66	1.31	1.10	2.31	1.65	0.43	0.31	0.30	0.33	0.48	0.31
Er	1.49	1.50	3.17	2.58	5.82	3.89	1.03	0.76	0.69	0.82	1.16	0.77
Tm	0.18	0.19	0.40	0.31	0.76	0.48	0.14	0.10	0.10	0.10	0.15	0.09
Yb	1.04	1.07	2.28	1.70	4.48	2.69	0.83	0.59	0.59	0.59	0.89	0.58
Lu	0.14	0.14	0.30	0.21	0.60	0.36	0.11	0.08	0.08	0.09	0.12	0.08
Ce/Pb	10.0	10.4	6.75	8.09	5.07	5.93	11.2	11.6	11.9	14.1	13.2	11.7
U/Th	0.26	0.26	0.46	0.37	0.33	0.45	0.25	0.31	0.37	0.22	0.30	0.31
Zr/Nb	2.61	4.04	2.24	2.16	3.26	2.94	2.73	2.83	3.18	2.84	2.78	2.97
Zr/Y	16.3	21.5	11.8	10.6	19.4	14.0	21.6	19.8	24.2	16.8	19.4	20.1
Zr/Hf	43.4	39.6	46.3	52.2	51.3	48.1	41.3	41.2	41.8	38.6	39.9	40.0
Ba/Nb	31.0	36.5	36.7	48.5	30.3	23.6	21.0	22.4	26.4	23.7	29.0	28.8
La/Nb	1.37	1.56	1.50	1.69	0.83	1.32	1.09	1.10	1.01	1.25	1.05	1.06
La/Th	7.73	8.14	10.14	9.41	6.65	8.61	8.35	7.86	7.29	8.63	8.18	7.61

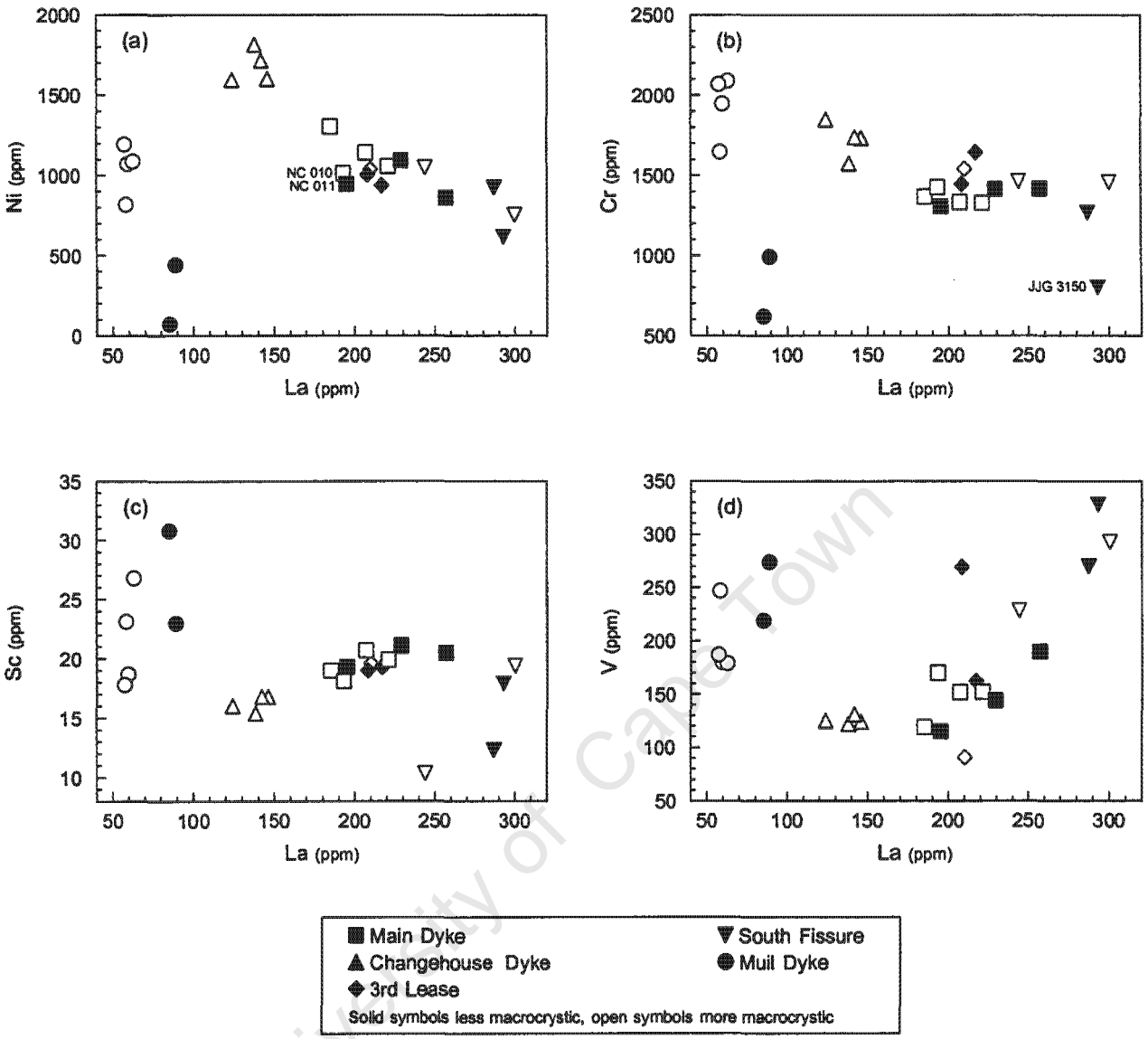

Figure 5.1 Variation of selected compatible trace elements within the Swartruggens kimberlite dykes and the Muil lamprophyre.

lower concentrations (Ni = 617 - 1048 ppm; Cr = 802 – 1462 ppm; Table 5.1). The South Fissure samples define an extension of the broad negative correlation between Ni and La of the Main Dyke (Figure 5.1a), but show no correlation between Cr and La (Figure 5.1b). Sample JJG 3150 from the South Fissure has anomalously low Cr and lies below the broad trend between Cr and La of the Swartruggens dykes collectively.

The Swartruggens kimberlite dykes have a limited range of Sc concentrations, from 10.3 ppm to 21.1 ppm, and a far wider range of V contents from 90.9 to 328 ppm, although individual dykes show less variation (Table 5.1). The range in Sc concentrations shown by the Main Dyke (Sc = 18.1 – 21.1 ppm; Table 5.1) encompasses that of the Third Lease samples (Sc = 19.0 – 19.6 ppm; Table 5.1), whereas the

Changehouse Dyke is less enriched (Sc = 15.4 – 16.8 ppm). These three dykes collectively define a broad positive correlation between Sc and La but the South Fissure samples (with Sc = 10.3 to 19.4 ppm Sc) define a separate, steeper, within-dyke positive correlation with lower Sc concentrations for a given La content than the Main Dyke (Figure 5.1c). The Third Lease samples show a wide range in V concentrations from 90.9 to 269 ppm, which encompasses the smaller ranges of the Main and Changehouse Dykes (V = 115 – 190 ppm and 122 – 131 ppm, respectively; Table 5.1), whereas the South Fissure extends to more enriched concentrations (V = 228 – 328 ppm; Table 5.1). The Swartruggens kimberlite dykes collectively define a broad positive correlation between V and La, with the South Fissure showing a particularly strong within-dyke correlation (Figure 5.1d).

The Muil Dyke has widely varied abundances of the compatible elements, which define trends with La that are unrelated to those of the kimberlite dykes (Figure 5.1), with Ni ranging from 71.7 to 1191 ppm and Cr ranging from 620 to 2088 ppm (Table 5.1). Both Ni and Cr define steep negative correlations with La within the Muil Dyke, with the more macrocrystic samples having considerably higher abundances of Ni and Cr (Ni = 817 – 1191 ppm, Cr = 1650 – 2088 ppm) than the aphanitic samples (Ni = 71.7 – 441 ppm, Cr = 620 – 991 ppm). The macrocrystic Muil Dyke samples show a wide range in Sc and V concentrations (macrocrystic Sc = 17.8 – 30.8 ppm; V = 179 – 274 ppm; Table 5.1) and the aphanitic samples trend to higher Sc and V contents than the macrocrystic samples (aphanitic Sc = 23.0 – 30.8 ppm, V = 219 – 274 ppm; Table 5.1). Sc and V define steep positive correlations with La for the Muil dyke (Figure 5.1 c and d), and also define broad positive correlations with MgO content (Tables 4.1 and 5.1). Although the range in V content shown by the Muil Dyke is within the range of the kimberlite dykes, the majority of Muil Dyke samples are enriched in Sc relative to the kimberlite dykes.

5.2.2 Incompatible trace elements

5.2.2.1 Rare earth elements (REE)

The REE show considerable variation amongst the Swartruggens kimberlite dykes (e.g. La = 124 to 300 ppm; Table 5.1), although individual dykes show little variation. The South Fissure is the most enriched of the dykes, with La = 244 to 300 ppm, Ce = 455 to 599 ppm, Yb = 1.70 to 4.48 ppm. The Third Lease and Main Dyke samples share a common range (185 to 229 ppm La), whereas the Changehouse Dyke is slightly less enriched (La = 124 to 146 ppm). Chondrite normalised REE patterns for the Swartruggens kimberlite dykes are shown in Figure 5.2a-d. All the kimberlite dykes are strongly enriched in the light REE relative to the heavy REE (La/Yb_n = 78 – 165), with individual dykes showing smooth, sub-parallel patterns. Within the individual kimberlite dykes, there is no consistent variation between more macrocrystic and less macrocrystic samples. The South Fissure is enriched up to 1299 times chondrite in La and has the lowest average La/Yb_n of the Swartruggens kimberlite dykes (La/Yb_n = 91.0 ± 11.3). Sample JJG 3150 (South Fissure) has been excluded from this ratio due to its raised heavy REE, and consequently lower La/Yb_n (La/Yb_n = 47.0), which is interpreted to be a feature of crustal contamination (le Roex *et al.*, 2003; Figure 5.2d; see discussion in Chapter 7). The Main Dyke samples (with La up to 1085 times chondrite) have the highest La/Yb_n of the kimberlite dykes, with the majority of the Main Dyke samples having La/Yb_n = 106 ± 5.7 (Figure 5.2b). Sample NC 004 has been excluded due to its elevated heavy REE abundances (see

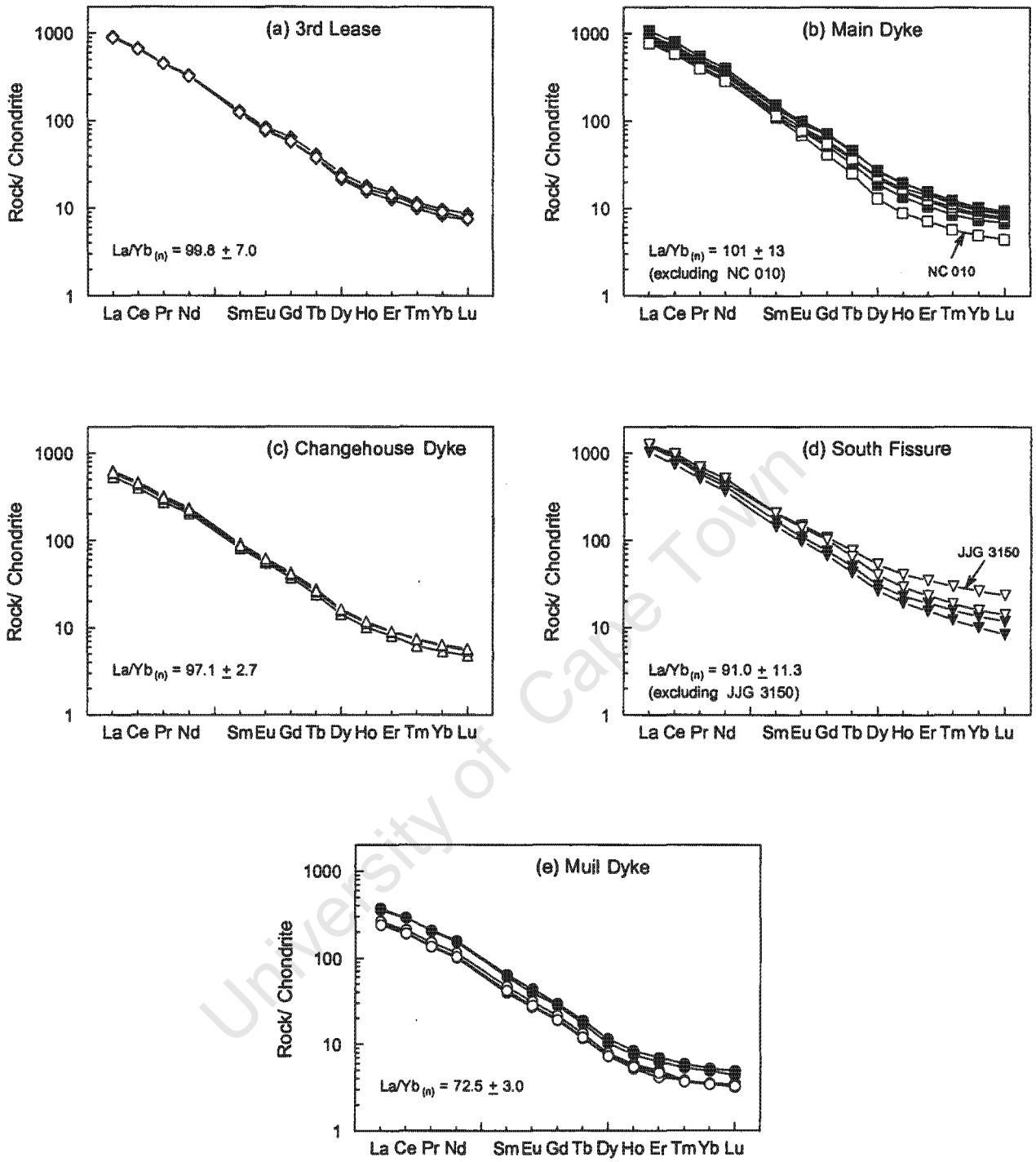

Figure 5.2 Chondrite normalised rare earth element patterns for the Swartruggens kimberlite dykes and the Muil lamprophyre. Open symbols more macrocrystic samples, solid symbols less macrocrystic samples. Chondrite values from Sun and McDonough (1989).

above) and consequently lower La/Yb_n (La/Yb_n = 78; Figure 5.2b). NC 010 (Main Dyke) is anomalous, being significantly depleted in the heavy REE relative to the other Main Dyke samples (La/Yb_n = 165; Figure 4.2a), and has also been excluded from the average ratio. The Third Lease samples (with enrichment in La up to

922 times chondrite), and the less enriched Changehouse Dyke (La up to 617 times chondrite), have La/Yb_n of 99.8 ± 7.0 and 97.1 ± 2.7 respectively, intermediate between those of the Main Dyke and South Fissure (Figure 5.2a and c).

The Muil Dyke is less enriched in the REE than the Swartruggens kimberlite dykes, with La concentrations ranging from 57.2 to 88.9 ppm (Table 5.1). The Muil Dyke samples also show smooth, steep chondrite normalised REE patterns with greater enrichment in the light REE than the heavy REE, although with significantly lower La/Yb_n than the kimberlite dykes (La/Yb_n = 72.5 ± 3.0). Unlike the kimberlite dykes, the Muil Dyke macrocrystic samples are considerably less enriched than the aphanitic samples (macrocrystic La = 252 - 272 times chondrite; aphanitic La = 369 - 394 times chondrite) although their chondrite normalised patterns are sub-parallel (Figure 5.2e).

5.2.2.2 *High field strength (HFS) and large ion lithophile (LIL) elements*

The HFS elements are high in abundance in all the Swartruggens kimberlite dykes (e.g. Zr = 264 – 1145 ppm; Nb = 80.1 – 351 ppm; Table 5.1). The range in absolute abundance of this group of elements within the Main Dyke (e.g. Zr = 173 – 395 ppm; Nb = 83.4 – 171 ppm) approximately spans that of the Changehouse Dyke and Third Lease samples, although the Changehouse Dyke is significantly less enriched in Ta (Ta = 3.43 - 4.27 ppm; Table 5.1) than the Main Dyke (Ta = 4.97 - 6.25 ppm; Table 5.1), whereas the South Fissure samples extend to higher concentrations (Zr up to 1145 ppm; Nb up to 351 ppm; Table 5.1). The HFS elements generally show very good mutual correlations (Figure 5.3) with constant inter-element ratios across the suite of kimberlite dykes (Zr/Nb = 2.9 ± 0.8; Zr/Hf = 45.0 ± 3.9; La/Nb = 1.6 ± 0.25, excluding JJG 3150, South Fissure, with anomalously low La for a high Nb concentration). Strong within dyke correlations are also shown by the Main Dyke and South Fissure, whereas the Changehouse Dyke shows more scatter, with samples NC 007 and SR7 having slightly higher abundances of Zr and Ta for a given Nb content than the other two Changehouse Dyke samples (Table 5.1; Figure 5.3a and c).

Th defines a strong positive correlation with U for the Swartruggens kimberlite dykes collectively (U/Th = 0.29 + 0.08; Table 5.1; Figure 5.3e), despite the known mobility of U, but a stronger correlation with La content, with La/Th = 8.3 ± 0.9 (Table 5.1; Figure 5.3f). Sample NC 010 from the Main Dyke plots away from the correlations, with lower U and slightly higher La for a given Th content. The range in Th and U concentrations of the Main Dyke (Th = 18.9 – 30.6ppm; U = 1.83 – 7.89 ppm; Table 5.1) spans that of the Third Lease samples, whereas, despite having U concentrations within the range of the Main dyke (U = 4.15 – 5.05 ppm; Table 5.1), the Changehouse Dyke is less enriched in Th (15.1 – 18.2 ppm; Table 5.1). The South Fissure is the most enriched dyke in both Th and U (Th = 25.9 – 44.1 ppm; U = 9.57 – 15.5 ppm; Table 5.1), and defines a within-dyke positive correlation between these two elements that is less steep than that of the Swartruggens Dykes collectively (Figure 5.3e). Sample JJG 3150 from this dyke has lower U/Th and La/Th than the other South Fissure samples (Table 5.1).

The Muil Dyke is less enriched in the HFS elements than the Swartruggens kimberlite dykes (e.g. Zr = 142 to 244, Nb = 50.0 to 81.9 ppm; Table 5.1), but it has within dyke inter-element ratios similar to those of the

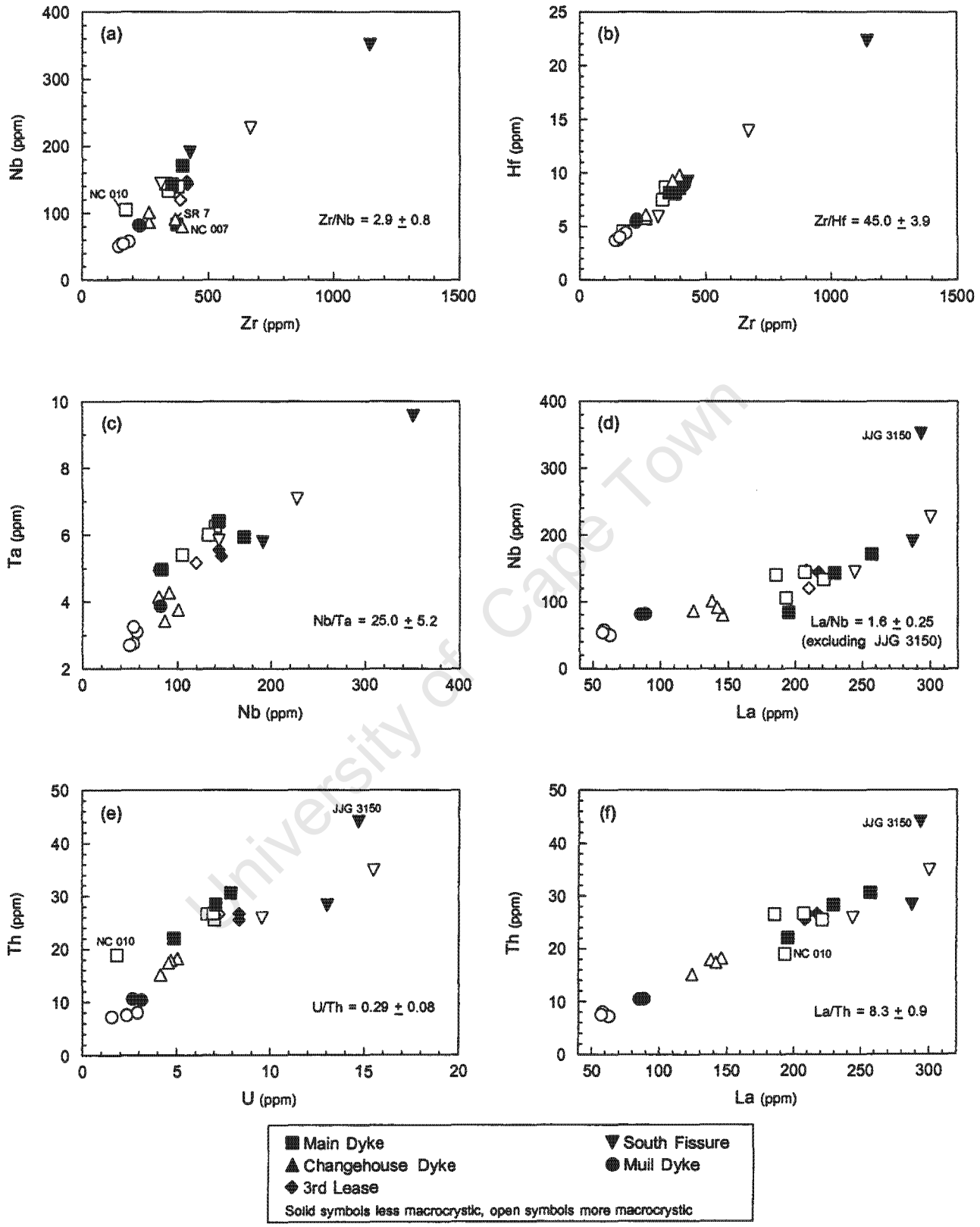

Figure 5.3 Variation of selected high field strength elements within the Swartruggens kimberlite dykes and the Muil lamprophyre.

kimberlite dykes and appears to plot on the same trends (e.g. Zr/Nb = 2.89 ± 0.16, Zr/Hf = 40.5 + 1.2, La/Th = 7.99 + 0.50; Figure 5.3). The HFS elements are lower in abundance in the macrocrystic Muil Dyke samples than the aphanitic samples (Table 5.1; Figure 5.3).

The LIL elements are present in high and variable abundances in the Swartruggens kimberlites (e.g. Ba = 954 – 10649 ppm; Rb = 102 – 273 ppm; Table 5.1). At best, the LIL elements show poor correlations with each other over the suite of kimberlite dykes and weak positive correlations are also present between the LIL elements and the more immobile HFS elements (Figure 5.1). However, there is a strong positive correlation between Rb and K, with K/Rb = 202 ± 9.7 for the kimberlite dykes (Figure 5.4a). The Main Dyke shows a broad range in Sr and Ba concentrations (Sr = 473 – 1422 ppm; Ba = 2699 - 8226 ppm; Table 5.1), with sample NC 010 being notably enriched in Ba relative to the other Main Dyke samples, which encompasses the range of the Changehouse Dyke samples. However, Rb concentrations are higher in the Main Dyke than the Changehouse Dyke (Main Dyke Rb = 195 – 273 ppm; Changehouse Dyke Rb = 146 – 187 ppm; Table 5.1). The South Fissure has Rb contents within the range of the Main and Changehouse Dykes, but extends to the highest Sr and Ba concentrations of the Swartruggens kimberlite dykes (Sr up to 3154 ppm; Ba up to 10649 ppm; Table 5.1). The Third Lease samples are the least enriched of the Swartruggens kimberlite dykes in Rb and Ba (Rb = 102 – 134 ppm; Ba = 954 – 1747 ppm; Table 5.1), although they have Sr concentrations within the range of the Main and Changehouse Dykes.

Although Pb shows only weak positive correlations or no correlation with the other LILE (Figure 5.4e), it shows a strong positive correlation with Ce (Figure 5.4f), with an average Ce/Pb of 9.1 ± 2.3 for the suite of kimberlite dykes. Ce/Pb within the Main Dyke is slightly higher than the other kimberlite dykes, with most samples having Ce/Pb ranging from 11.01 – 12.58 (Pb = 28.6 – 43.6 ppm) and samples NC 020 and NC 010 being displaced to higher Pb concentrations (with Ce/Pb = 9.81 and 7.90, respectively). The Changehouse Dyke samples are slightly less enriched (Pb = 26.6 – 29.6 ppm) and have slightly lower Ce/Pb than the Main Dyke (Ce/Pb = 8.77 – 10.4). The South Fissure and Third Lease samples have higher Pb concentrations, and lower Ce/Pb, than the Main and Changehouse Dykes (South Fissure Pb = 56.2 – 110 ppm, Ce/Pb = 5.07 – 8.09; Third Lease Pb = 50.6 – 61.1 ppm, Ce/Pb = 6.58 – 7.92; Table 5.1).

Like the HFS elements, the LIL elements are generally slightly less enriched in the Muil Dyke than the Swartruggens kimberlite dykes (e.g. Muil Dyke Ba = 1185 to 2359 ppm, Rb = 68 to 150 ppm; Table 5.1), although the Sr concentrations of the Muil Dyke are within the range of the Main Dyke. However, the Muil Dyke does not deviate significantly from the broad trends shown by the Swartruggens kimberlites (Figure 5.4). The Muil Dyke also has lower Pb concentrations than the kimberlite dykes (Pb = 26.6 – 19.6), with the more macrocrystic samples having slightly lower Pb contents than the aphanitic samples. This dyke plots approximately on the broad trend between Ce and Pb defined by the kimberlite dykes (Figure 5.4f), although it has slightly higher Ce/Pb ratios than the kimberlite samples (Ce/Pb = 11.2 – 14.1).

Primitive mantle normalised incompatible element diagrams for the Swartruggens kimberlite dykes are shown in Figure 5.5a-d. All the kimberlite dykes are enriched relative to primitive mantle, with greatest

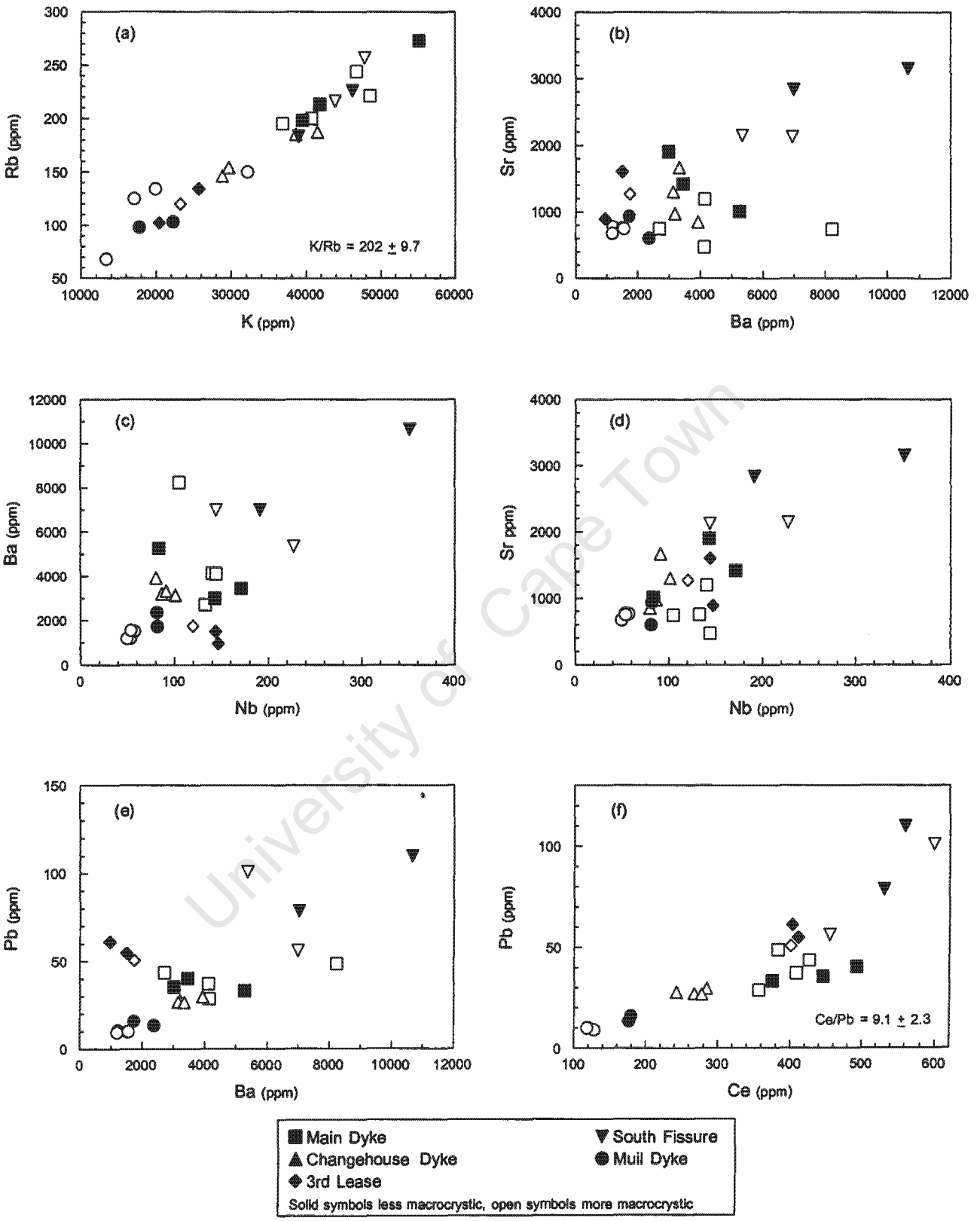

Figure 5.4 Variation of selected large ion lithophile elements within the Swartruggens kimberlite dykes and the Muil lamprophyre.

enrichment in the more incompatible elements. The South Fissure is the most enriched dyke, with enrichment in Rb up to 404 times primitive mantle (Figure 5.5d), and the Changehouse Dyke is generally the least enriched (Figure 5.5c). The Main Dyke and Third Lease samples have similar degrees of enrichment (Figure 4.5a and b). The more, and less, macrocrystic samples from individual kimberlite dykes cannot be distinguished with respect to their primitive mantle normalised patterns.

Superimposed upon relatively smooth enrichment patterns, strong K, Ti variable Sr, and subdued Nb-Ta negative anomalies occur in all the kimberlite dykes. The magnitude of these anomalies can be expressed as X/X* for element X, where X* is the interpolated primitive mantle normalised value assuming a smooth variation between the normalised values of the two adjacent elements (after le Roex *et al.*, 2003) and for K is here calculated with respect to Th and Nb, given the variability of U and Ta in these samples (Figure 5.3). The Main Dyke samples show K anomalies which range in size from K/K* = 0.58 to 0.90 (except NC 010, which is anomalous in having a slight positive K anomaly, with K/K* = 1.03; Figure 5.5b), whereas the South Fissure and Third Lease samples show slightly larger K anomalies (K/K* = 0.30 – 0.71 and 0.33 – 0.44 respectively). The Changehouse Dyke samples show smaller K anomalies, with three samples ranging from K/K* = 0.66 to 0.97 and the fourth (NC 005) having a slight positive anomaly relative to Nb and Th (K/K* = 1.34; Figure 5.5c). The Ti anomalies in the Main Dyke, South Fissure and Third Lease samples are of similar size, with Ti/Ti* ranging from 0.24 to 0.30, whereas the Changehouse Dyke has a slightly larger Ti anomaly (Ti/Ti* = 0.35 – 0.38). The Main Dyke shows widely variable Sr anomalies, with Sr/Sr* ranging from 0.17 to 0.49 and the Third Lease samples Sr anomalies are within this range of magnitude, whereas the Changehouse Dyke and South Fissure have slightly smaller Sr anomalies (Sr/Sr* = 0.43 – 0.87 and 0.50 – 0.81 respectively). Slight negative Zr-Hf anomalies are present in the Main Dyke, South Fissure (except JJG 3150; Figure 5.5d) and two samples from the Changehouse Dyke (NC 005 and NC 009). The other two Changehouse Dyke samples (NC 007 and SR 7), and JJG 3150 from the South Fissure, show slight positive anomalies for Zr and Hf. JJG 3150 is also slightly enriched in HREE relative to primitive mantle when compared to the other samples from the South Fissure, as previously described in section 5.2.2.1 (Figure 5.5c and d). Sample NC 010 is anomalous relative to the other Main Dyke samples in having particularly pronounced negative Zr-Hf and Sr anomalies, in addition to being the only Swartruggens sample with a strong negative U anomaly, and has lower abundances of the heavy REE elements as previously discussed. NC 010 and NC 011 (both from the Main Dyke) also have strong negative P anomalies, which are not present in the other Swartruggens kimberlites samples (Figure 5.5b).

All the Swartruggens kimberlite dykes have strong positive Pb anomalies, which range in magnitude within the Main Dyke from Pb/Pb* = 2.40 to 3.09, except NC 010 which has a Pb/Pb* of 3.85. The South Fissure and Third Lease samples have the largest Pb anomalies (Pb/Pb* = 3.73 – 5.95 and 3.84 – 4.60) with the strongest anomalies present in samples JJG 3150 and JJG 3148 from the South Fissure. The Changehouse Dyke has positive Pb anomalies between these two ranges in magnitude (Pb/Pb* = 2.92 – 3.44). With the exception of the Third Lease samples, Ba is enriched relative to Rb in all the Swartruggens kimberlite dykes, and a positive U anomaly is also present in the South Fissure samples.

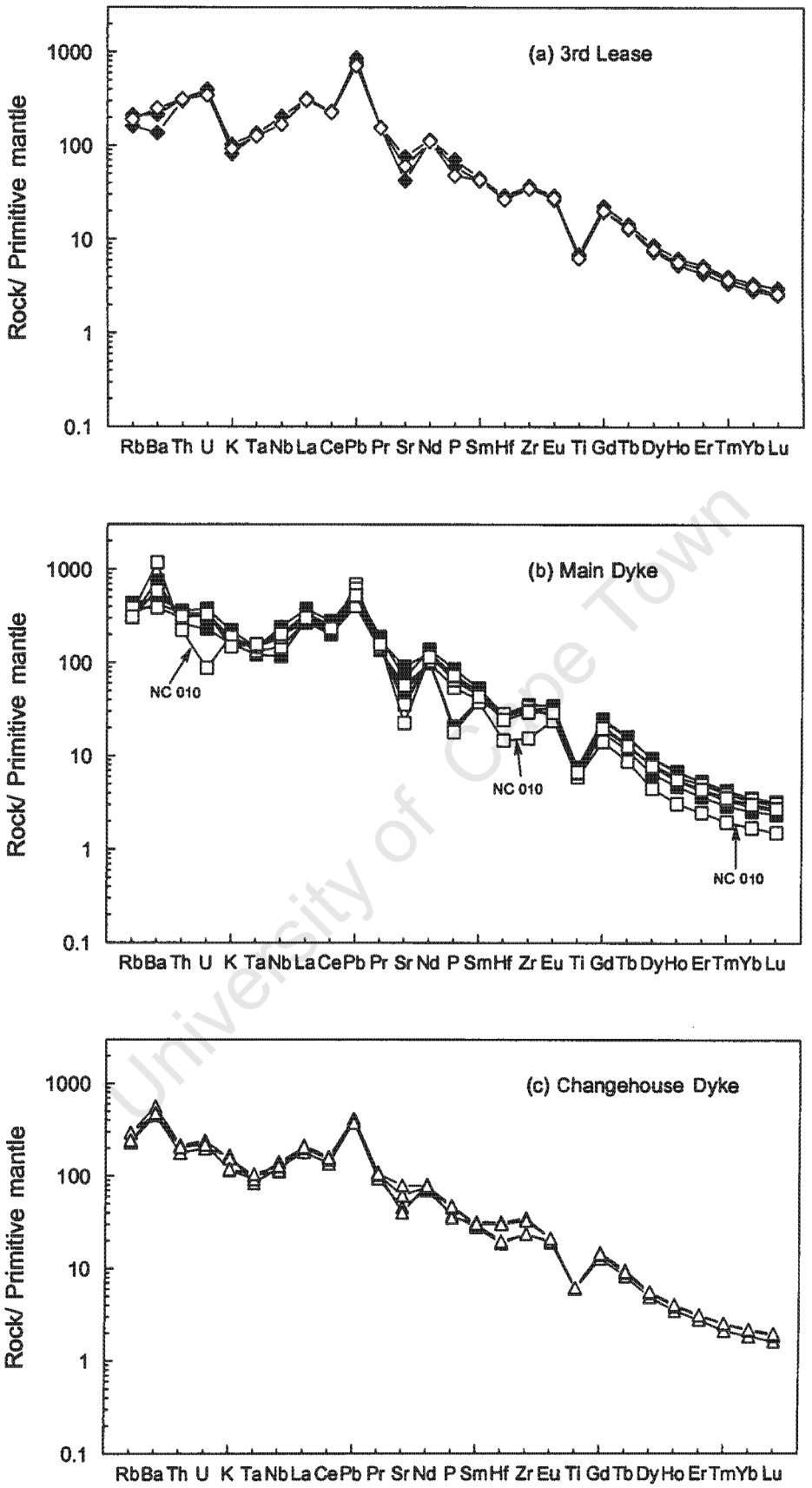

Figure 5.5 Primitive mantle normalised incompatible trace element variation in the Swartruggens kimberlite dykes and the Muil lamprophyre. Open symbols more macrocrystic samples, solid symbols less macrocrystic samples. Primitive mantle values from Sun and McDonough (1989).

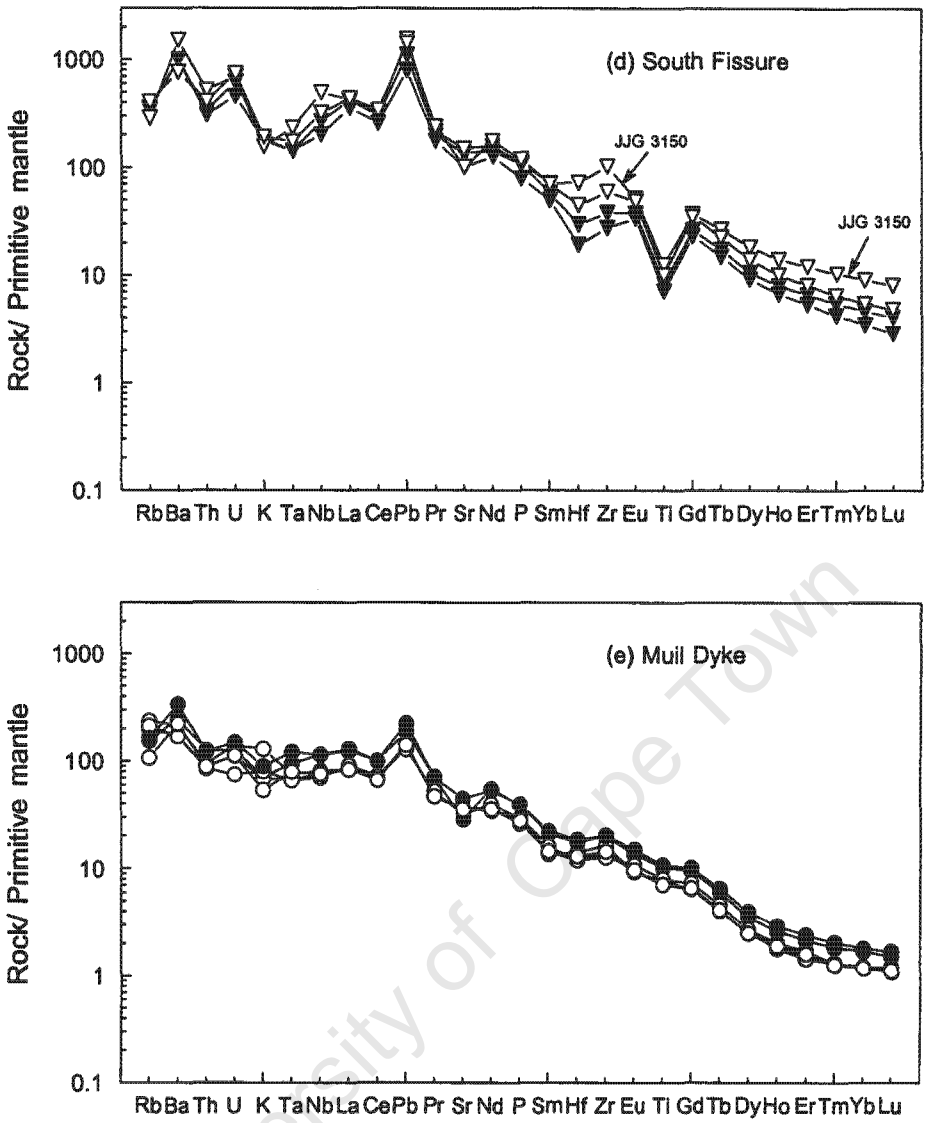

Figure 5.5 Continued.

The Muil Dyke is less enriched than the Swartruggens kimberlite dykes, but is still strongly enriched relative to primitive mantle, with greatest enrichment in the more incompatible elements (Rb = 105 to 235 times primitive mantle; Figure 5.5e). The samples can be split into two groups based on their mantle-normalised patterns, one of which is more enriched than the other. The more enriched samples correspond to the least macrocryst-rich samples, whereas the more macrocryst-rich samples are less enriched relative to primitive mantle. The Muil Dyke shows a remarkably sub parallel pattern to the Swartruggens kimberlite dykes, with similarly sized negative K ($K/K^* = 0.58 – 0.82$, except samples NC 014 and NC 015 where $K/K^* = 1.46$ and 1.01 respectively) and Sr anomalies ($Sr/Sr^* = 0.70 – 0.90$, except sample JJG 3141 which has a much larger Sr anomaly, with $Sr/Sr^* = 0.46$). Nb and Ta are also slightly less enriched relative to primitive mantle with respect to La and U in the Muil Dyke, although this is not so marked as in the Swartruggens kimberlite dykes. Ba in the Muil Dyke is enriched relative to Rb in the majority of samples, and all the Muil Dyke samples have moderate positive Pb anomalies, although these are slightly smaller than those of the

kimberlite samples (Pb/Pb* = 2.09 – 2.56). However, in contrast to the Swartruggens kimberlite dykes, the Muil Dyke shows no negative Ti anomaly (Figure 5.5e).

5.3 Trace element geochemistry of the Star kimberlite dykes

The trace element geochemistry of twenty-two samples from the Star kimberlite dykes (2 from the Clewer Dyke, 7 from the East Wynandsfontein Dyke, 5 from the East Star Dyke, 4 from the Byrnes Dyke, and 4 from the Barren Dyke), has been determined. Individual analyses are reported in Table 5.2 and selected variations are illustrated in Figures 5.6 to 5.10.

5.3.1 Compatible trace elements

Compatible trace element variations in the Star kimberlite dykes are illustrated with respect to La in Figure 5.6. Both Ni and Cr vary widely in abundance, with Ni ranging from 684 to 1988 ppm and Cr ranging from 1800 to 2733 ppm, and both these elements define broad negative correlations with La content, with the more macrocrystic samples trending to higher Ni and Cr abundances (Figure 5.6a and b; Table 5.2). Individual dykes also show wide ranges in Ni and Cr abundances, with the more macrocrystic samples tending to be more enriched. Moderate negative correlations between Ni and La and present within individual dykes (Figure 5.6a), whereas Cr shows more scatter with La and within-dyke correlations are poor. The Byrnes Dyke is the least enriched in Ni, with the less macrocrystic samples showing a range from 684 to 905 ppm and the more macrocrystic sample (SJH 78) having the much higher Ni concentration of 1704 ppm (Table 5.2; Figure 5.6a) and this dyke also has relatively low Cr concentrations (Cr = 2147 to 2442 ppm; Table 5.2; Figure 5.6b). The Wynandsfontein Dyke shows a broad range in Ni and Cr concentrations (Ni = 880 - 1401 ppm; Cr = 2104 - 2600 ppm; Table 5.2) and defines relatively strong within-dyke negative correlations for Ni and Cr vs. La (with the exception of sample NC 050 with anomalously low Cr content; Figure 5.6a and b), whereas the East Star Dyke also has a wide range in Ni concentrations (Ni = 1148 to 1678 ppm; Figure 5.6a) but extends to higher Ni contents than the Wynandsfontein Dyke. Four of the East Star Dyke samples have Cr concentrations ranging from 2258 to 2525 ppm (Table 5.2), within the range of the Wynandsfontein Dyke, although sample JJG 4570 has anomalously low Cr (1800 ppm; Table 5.2) and plots outside the range of the other Star kimberlite dykes (Figure 5.6b). Despite having Cr concentrations within the range of the other Star diamondiferous kimberlite dykes (Cr = 2212 to 2341 ppm; Table 5.2; Figure 5.6b), with sample JJG 2833 plotting below the main negative trend between Cr and La defined by Star kimberlite dykes collectively, the Clewer Dyke extends to higher Ni abundances than these dykes (Ni = 1710 to 1482 ppm; Table 5.2; Figure 5.6a). The Barren Dyke is the most enriched of the Star kimberlite dykes in Ni and Cr (Ni = 1867 - 1988 ppm; Cr = 2548 - 2733 ppm; Table 5.2) and this dyke plots approximately on the negative trends of Ni and Cr vs. La defined by the Star diamondiferous kimberlite dykes (Figure 5.6a and b). The micaceous samples define broad within-dyke negative correlations on these diagrams whereas the less-micaceous sample (NC 054), despite having similar concentrations of Ni and Cr to the micaceous samples, has lower La and deviates slightly from the within-dyke trend.

Table 5.2 Bulk rock trace element analyses, in ppm, of the Star kimberlite dykes. Mic = micaceous Barren Dyke, l. mic = less micaceous Barren dyke; Macro = quantity of macrocrysts in thin section, M = more macrocrystic, LM = less macrocrystic; * = elements analysed by XRF, all other elements analysed by ICP-MS.

Dyke	Clewer Dyke		Wynandsfontein Dyke							East Star Dyke	
Sample	JJG 2833	JJG 2837	SJH 37	JJG 6361A	JJG 6361C	JJG 6369	JJG 6362	JJG 6360	NC 050	JJG 4570	SJH 101
Macro	M	M	LM	M	M	LM	M	M	LM	M	LM
Sc	12.8	16.2	21.3	20.2	20.5	21.8	22.0	17.9	19.7	14.2	19.6
V	53.4	63.9	81.7	150	84.6	139	144	54.5	152	101	85.9
Cr*	2212	2341	2104	2531	2279	2373	2389	2600	2187	1800	2258
Co	85.2	80.2	60.6	56.1	67.5	69.9	79.0	75.5	70.7	81.1	76.7
Ni*	1710	1482	966	880	1037	1073	1401	1244	1221	1678	1282
Cu*	27.2	23.0	75.8	48.9	6.08	59.8	36.0	36	47.1	36.05	31.74
Zn*	53.1	63.4	65.7	75.2	80.5	83.8	78.5	69.5	68.0	64.4	69.1
Rb	82.4	118	100	27.3	135	115	137	135	139	109	137
Sr	967	1366	1524	1010	971	1673	2383	2140	2133	1266	1756
Cs	1.71	2.58	1.44	1.09	2.28	1.99	3.75	3.20	3.88	1.78	3.71
Ba	2280	2542	5064	1029	4230	3309	5060	2839	4357	2451	4428
Pb	10.9	17.0	51.2	40.0	25.8	50.4	31.8	30.7	27.7	23.1	29.9
Y	10.3	11.2	24.3	20.3	14.0	15.0	12.5	12.3	10.8	9.05	13.1
Zr	31.3	187	336	316	281	410	264	203	266	257	237
Nb*	68	104	189	143	130	188	152	144	126	136	148
Hf	1.19	4.62	9.86	7.34	6.45	8.21	6.14	4.75	6.08	5.55	6.41
Ta	6.16	7.04	5.66	8.04	7.81	7.23	8.08	8.54	7.74	5.51	7.07
Th	25.1	29.0	29.1	30.9	22.9	31.4	33.6	33.3	29.6	21.8	32.0
U	1.84	2.92	8.57	7.63	8.23	11.62	7.39	7.52	5.98	5.12	7.74
La	131	178	285	214	222	233	223	201	199	164	202
Ce	282	356	503	415	419	432	440	408	394	313	398
Pr	30.9	38.2	51.6	43.8	43.6	44.7	46.6	43.2	41.4	32.9	42.5
Nd	107	133	177	150	151	153	160	150	143	113	147
Sm	11.4	14.3	20.4	16.6	17.1	17.0	17.3	15.9	15.6	12.4	16.5
Eu	2.62	3.34	5.41	3.80	3.96	4.06	4.04	3.67	3.65	2.89	4.06
Gd	6.27	7.84	13.3	9.47	9.72	9.48	8.70	8.22	7.80	6.61	8.71
Tb	0.69	0.87	1.49	1.13	1.05	1.02	0.96	0.91	0.84	0.70	0.97
Dy	2.65	3.12	5.65	4.33	3.74	3.70	3.42	3.24	2.96	2.51	3.54
Ho	0.42	0.46	0.82	0.68	0.53	0.54	0.51	0.49	0.43	0.37	0.53
Er	0.89	1.00	1.69	1.44	1.03	1.11	1.01	1.05	0.88	0.80	1.16
Tm	0.12	0.12	0.18	0.16	0.12	0.13	0.12	0.14	0.11	0.09	0.14
Yb	0.63	0.71	0.94	0.83	0.64	0.69	0.66	0.71	0.59	0.51	0.78
Lu	0.09	0.09	0.12	0.10	0.08	0.08	0.09	0.10	0.08	0.06	0.10
Ce/Pb	25.8	21.0	9.8	10.4	16.3	8.6	13.8	13.3	14.2	13.5	13.3
U/Th	0.07	0.10	0.29	0.25	0.36	0.37	0.22	0.23	0.20	0.23	0.24
Zr/Nb	0.46	1.80	1.78	2.21	2.16	2.18	1.73	1.41	2.12	1.89	1.60
Zr/Y	3.0	16.8	13.8	15.6	20.1	27.4	21.0	16.4	24.7	28.4	18.0
Zr/Hf	26.3	40.6	34.1	43.1	43.6	49.9	42.9	42.7	43.9	46.3	36.9
Ba/Nb	33.6	24.4	26.7	7.2	32.5	17.6	33.2	19.7	34.6	18.1	29.9
La/Nb	1.92	1.71	1.51	1.49	1.70	1.24	1.47	1.39	1.58	1.21	1.36
La/Th	5.20	6.15	9.80	6.93	9.71	7.43	6.65	6.02	6.72	7.53	6.31

Table 5.2 Continued.

Dyke	East Star Dyke			Byrnes Dyke				Barren Dyke			
								mic	mic	mic	i. mic
Sample	SJH 30	SJH 38	SJH 104	SJH 80	SJH 79	SJH 78	SJH 77	NC 051	NC 052	NC 053	NC 054
Macro	LM	M	M	LM	LM	M	LM	M	M	M	M
Sc	18.7	18.2	16.4	30.9	23.3	19.9	26.7	16.1	16.3	16.7	11.5
V	117	102	120	159	254	149	191	112	128	106	63.7
Cr*	2477	2327	2525	2198	2147	2221	2442	2733	2697	2548	2665
Co	69.7	71.4	85.1	53.5	61.3	85.9	52.6	107	107	103	99.8
Ni*	1148	1246	1555	684	905	1704	693	1967	1988	1906	1867
Cu*	75.8	26.0	33.5	30.2	45.4	36.1	39.7	84.7	58.2	86.4	50.1
Zn*	69.1	66.0	65.9	72.7	74.0	71.4	67.9	76.0	75.1	76.4	65.5
Rb	160	127	117	174	178	123	142	150	146	158	96
Sr	1532	2059	1775	2542	2771	1924	2523	872	871	891	724
Cs	3.60	2.57	3.02	2.53	3.15	2.77	1.85	3.03	2.96	2.93	2.07
Ba	4192	3207	4533	4589	6054	4703	5909	1920	1873	2049	1935
Pb	29.3	21.6	26.9	27.5	34.8	28.0	45.4	17.9	19.0	19.4	14.3
Y	10.4	13.1	10.4	23.7	12.4	13.3	16.3	9.28	10.1	9.33	7.83
Zr	273	186	141	362	156	188	172	156	169	148	113
Nb*	141	129	108	163	158	121	155	97.9	98.2	104	73.5
Hf	6.46	4.17	3.63	8.50	4.02	5.19	6.28	3.63	3.84	3.51	2.62
Ta	8.45	8.43	7.99	8.62	7.91	7.32	8.78	6.53	6.02	6.91	4.91
Th	30.0	33.8	31.8	39.7	25.3	26.6	28.7	24.7	23.2	25.7	18.8
U	5.48	6.33	5.27	5.82	5.39	7.19	7.86	4.56	4.79	4.57	3.27
La	210	192	178	275	227	193	242	153	145	168	119
Ce	419	394	371	517	422	373	463	322	304	345	242
Pr	45.0	42.6	40.2	55.9	44.1	39.9	48.6	34.2	32.0	36.1	25.5
Nd	156	146	139	197	150	137	167	117	111	123	88
Sm	16.6	16.1	14.9	22.6	16.1	15.5	18.5	12.4	12.0	12.8	9.25
Eu	3.49	3.71	3.48	5.10	3.31	3.73	4.41	2.59	2.63	2.71	2.14
Gd	8.66	8.53	7.26	11.69	7.80	8.23	9.65	6.35	6.47	6.46	4.89
Tb	0.91	0.96	0.82	1.35	0.87	0.91	1.07	0.69	0.73	0.69	0.55
Dy	3.04	3.55	2.86	5.55	3.09	3.35	4.15	2.46	2.64	2.61	2.01
Ho	0.44	0.54	0.43	0.95	0.50	0.52	0.65	0.38	0.41	0.39	0.31
Er	0.89	1.24	0.92	2.39	1.17	1.18	1.49	0.83	0.85	0.82	0.67
Tm	0.10	0.15	0.11	0.33	0.16	0.15	0.19	0.10	0.11	0.10	0.08
Yb	0.54	0.79	0.62	1.99	0.92	0.85	1.16	0.57	0.61	0.54	0.45
Lu	0.06	0.11	0.08	0.27	0.13	0.11	0.16	0.07	0.08	0.08	0.06
Ce/Pb	14.3	18.2	13.8	18.8	12.1	13.3	10.2	17.9	16.0	17.8	16.9
U/Th	0.18	0.19	0.17	0.15	0.21	0.27	0.27	0.18	0.21	0.18	0.17
Zr/Nb	1.93	1.44	1.30	2.22	0.99	1.55	1.11	1.59	1.72	1.42	1.54
Zr/Y	26.2	14.2	13.5	15.3	12.6	14.1	10.5	16.8	16.7	15.9	14.5
Zr/Hf	42.2	44.7	38.7	42.6	38.8	36.2	27.3	42.9	43.9	42.2	43.3
Ba/Nb	29.7	24.9	41.9	28.1	38.4	38.8	38.0	19.6	19.1	19.6	26.3
La/Nb	1.49	1.49	1.65	1.68	1.44	1.59	1.56	1.56	1.48	1.61	1.62
La/Th	7.01	5.69	5.59	6.92	8.96	7.25	8.43	6.20	6.27	6.54	6.32

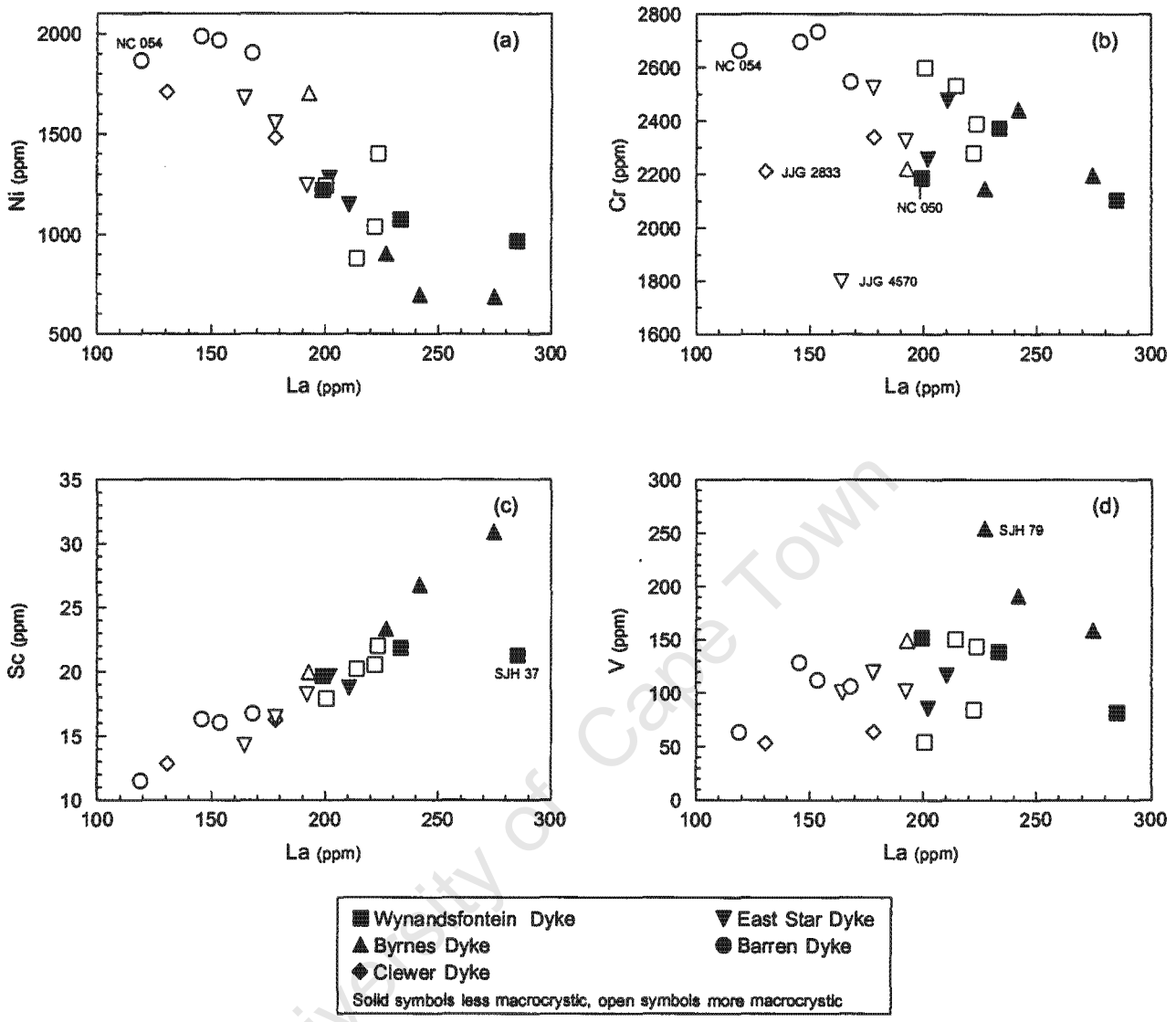

Figure 5.6 Variation of selected compatible trace elements within the Star kimberlite dykes.

The Star kimberlite dykes display a wide range in V concentration, from 53.4 to 254 ppm, with a much smaller range in Sc concentration from 11.5 to 30.9 ppm. Both these elements define positive correlations with La (Figure 5.6c and d) although the correlation is much stronger for Sc than for V. Within individual dykes the ranges in concentrations of these elements are much smaller, and strong within-dyke positive correlations are defined between Sc and La (Figure 5.6c), although only weak within-dyke correlations are defined between V and La (Figure 5.6d). The more macrocryst-rich samples tend to be less enriched than the less macrocryst-rich samples in Sc and V (Table 5.2; Figure 5.6c and d). The Wynandsfontein Dyke has a relatively small range in Sc concentrations (Sc = 17.9 to 22.0 ppm; Table 5.2) and, with the exception of macrocrystic sample JJG 6362, the less macrocrystic samples tend to have slightly higher Sc concentrations than the macrocrystic samples. Sample SJH 37, from this dyke, deviates considerably from the trend between Sc and La of the Star kimberlite dykes collectively, having a much higher La

concentration despite its Sc concentration being within the range of the other samples from the dyke (Figure 5.6c). V concentrations are more variable within the Wynandsfontein Dyke (V = 54.5 to 152 ppm; Table 5.2) showing considerable scatter with respect to La content (Figure 5.6d), and there is no apparent correlation between macrocryst content and V concentration within this dyke. The East Star Dyke trends to lower Sc concentrations, but has V concentrations within the range of the Wynandsfontein Dyke (East Star Dyke Sc =14.2 to 19.6 ppm; V = 85.9 to 120ppm Sc; Table 5.2), whereas the Byrnes Dyke is more enriched in both Sc and V (Sc = 19.9 to 30.9 ppm; V = 149 to 254 ppm; Table 5.2). The lowest Sc and V concentrations of the Star diamondiferous kimberlite dykes are present in the Clewer Dyke (Sc =12.8 to 16.2 ppm; V = 53.4 to 63.9 ppm; Table 5.2) although the less micaceous Barren dyke sample is less enriched in Sc (Sc = 11.5 ppm; Table 5.2). The micaceous Barren Dyke samples show little variation in Sc content, and lie within the range of Sc concentrations of the East Star Dyke (micaceous Barren Dyke Sc = 16.1 – 16.7 ppm; Table 6.2). However, these samples define a broad within-dyke positive correlation between Sc and La that is oblique to that defined by the Star diamondiferous Dykes collectively (Figure 5.6c). V concentrations in the Barren Dyke are within the range of the Star diamondiferous kimberlite dykes, with the micaceous samples showing little variation in V content and the less-micaceous sample (NC 054) having a considerably lower V concentration (micaceous Barren Dyke V =106 - 128 ppm; less micaceous Barren Dyke V = 63.7 ppm; Table 5.2).

5.3.2 Incompatible trace elements

5.3.2.1 Rare earth elements (REE)

The REE show a wide range in abundance across the suite of Star kimberlite dykes (e.g. La = 131 – 285 ppm; Table 5.2). Individual dykes also show considerable, and overlapping, variation; the Clewer and Barren Dykes are the least enriched (La = 131 - 178 ppm and 119 - 168 ppm respectively; Table 5.2) and the Wynandsfontein and Byrnes Dykes are the most enriched (La = 199 - 285 ppm and 193 - 275 respectively; Table 5.2). The East Star Dyke, with La ranging from 164 to 210 ppm, falls between these two extremes. Chondrite normalised REE patterns for the Star kimberlite dykes are shown in Figure 5.7. All the dykes are strongly enriched in the light REE relative to the heavy REE (La/Yb_n = 99 – 282) and individual dykes show smooth sub-parallel patterns. In general, there is no systematic variation between the more macrocrystic and less macrocrystic samples of individual dykes, although the most macrocrystic Byrnes Dyke sample (SJH 78) is less enriched in the REE than the less macrocrystic samples from this dyke (Table 5.2; Figure 5.7d). The Clewer and Byrnes Dykes (with enrichment in La of 551 – 751 and 814 – 1159 times chondrite respectively) have similar average La/Yb_n (Clewer Dyke La/Yb_n = 165 ± 22; Byrnes Dyke La/Yb_n = 163 ± 13; Figure 5.7a and d), whereas the East Star and Wynandsfontein Dykes (La = 693 – 888 and 841 – 1202 respectively) have higher average La/Yb_n than the Byrnes or Clewer Dykes (East Star Dyke La/Yb_n = 199 ± 25; Wynandsfontein Dyke La/Yb_n = 226 ± 25; Figure 5.7b and c). Samples SJH 30 (East Star Dyke) and SJH 80 (Byrnes Dyke) have similar abundances of the light REE to the other samples from these dykes, but have elevated heavy REE abundances and consequently lower La/Yb_n. This has been attributed to crustal contamination, and consequently these samples have been excluded from the average ratios for these dykes (le Roex *et al.*, 2003; Figure 5.7c and d; see discussion in Chapter 7). The three micaceous Barren Dyke samples have very similar abundances of the REE (La = 614 – 708 times chondrite) and

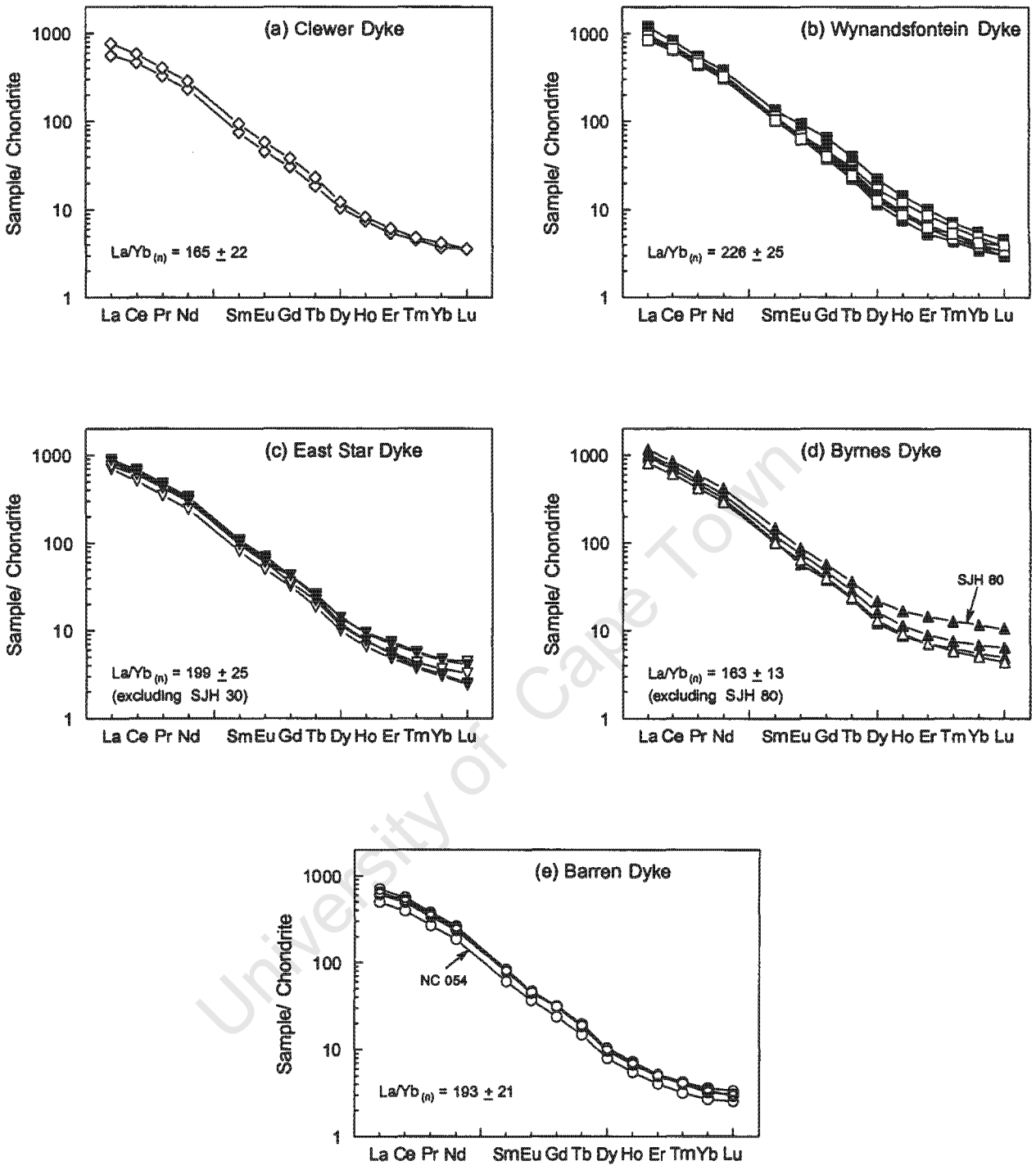

Figure 5.7 Chondrite normalised rare earth element patterns for the Star kimberlite dykes. Open symbols more macrocrystic samples, solid symbols less macrocrystic samples. Chondrite values from Sun and McDonough (1989).

almost identical chondrite normalised REE patterns, with average La/Yb_n within the range of the Star diamondiferous kimberlite dykes (La/Yb_n = 195 ± 25). Although the less-micaceous Barren Dyke sample (NC 054) is less enriched in the REE (La = 502 times chondrite), it has a chondrite normalised REE pattern sub-parallel to that of the micaceous samples, and a similar La/Yb_n of 188 (Figure 5.7e).

5.3.2.2 High field strength (HFS) and large ion lithophile (LIL) elements

The HFS elements are present in high but variable abundances in the Star kimberlite dykes (e.g. Zr = 31.3 – 410 ppm; Nb = 68 – 189 ppm), generally defining good positive mutual correlations (Figure 5.8) and broad negative correlations with MgO (Tables 4.2 and 5.2). With the exception of Th, which is more variable, the more macrocryst-rich samples from individual dykes are generally less enriched in the HFS elements than the less macrocryst-rich samples (Table 5.2; Figure 5.8). The Wynandsfontein and Byrnes Dykes tend to be the most enriched of the Star kimberlite Dykes (e.g. Wynandsfontein Dyke Zr = 203 – 410 ppm, Nb = 126 – 189 ppm; Byrnes Dyke Zr = 156 – 362 ppm, Nb = 121 – 163 ppm; Table 5.2), whereas the Clewer and Barren Dykes tend to be the least enriched (Clewer Dyke Zr = 31.3 - 187 ppm, Nb = 68 - 104 ppm; Barren Dyke Zr = 113 - 169 ppm, Nb = 73.5 - 104 ppm; Table 5.2), with the less-micaceous Barren dyke sample (NC 054) having lower abundances than the micaceous Barren Dyke samples (Table 5.2). The East Star Dyke (Zr = 141 to 273 ppm, Nb = 108 to 148 ppm) has a composition intermediate between these two extremes. Zr, and Nb and Hf show strong positive correlations for the Star kimberlite dykes collectively, with Zr/Nb = 1.6 ± 0.4 and Zr/Hf = 40.6 ± 5.6 (Figure 5.8a and b). Ta shows only a weak, and U a moderate, positive correlation with Nb over the suite of dykes, with Nb/Ta = 18.1 ± 4.8 and Nb/U = 22.7 ± 5.6, and within dyke correlations are poorly defined (Figure 5.8c and d). Four samples (JJG 4570 and SJH 101 from the East Star Dyke, and JJG 6369 and SJH 37 from the Wynandsfontein Dyke) deviate most significantly from the broad trend between Nb and Ta, with lower Ta concentrations for their Nb content (Figure 5.8c). However there is some analytical uncertainty with respect to the Ta concentrations of these samples (see Appendix 3), as their measured Nb concentrations were significantly lower when analysed by ICP-MS relative to XRF. This is believed to be due to incomplete dissolution of Nb-bearing phases prior to ICP-analysis, and given the geochemical similarity of Nb and Ta, the Ta concentrations reported here (analysed by ICP-MS) may also be slightly low.

Th defines a weak positive correlation with U for the Star kimberlite dykes collectively (U/Th = 0.22 ± 0.07; Figure 5.8e) and a stronger positive correlation with La content, with La/Th = 7.0 ± 1.2 (Figure 5.8f), with a particularly good within-dyke correlation between La and Th (La/Th = 6.3 ± 0.1) for the Barren Dyke. The Barren Dyke has slightly lower abundances of both Th (micaceous Th = 23.2 – 25.7ppm; less micaceous Th = 18.8 ppm) and U (micaceous U = 4.56 – 4.79 ppm; less micaceous U = 3.27 ppm; Table 5.2) compared to the other dykes at Star, although the Clewer Dyke (Th = 25.1 – 29.0 ppm; U = 1.84 – 2.92 ppm) also contains relatively low U but has slightly higher Th than the Barren Dyke. The East Star and Wynandsfontein dykes show a similar range of Th contents (21.8 - 33.8 ppm and 22.9 – 33.6 ppm respectively; Table 5.2), although the Wynandsfontein Dyke tends to have higher U (5.98 - 11.62 ppm U; Table 5.2) than the East Star Dyke (5.12 - 7.74 ppm U; Table 5.2). The Byrnes Dyke concentrations fall within the range described for the Wynandsfontein and East Star Dykes, with the exception of sample SJH 80, which has anomalously high Th (39.7 ppm; Table 5.2). The LIL elements are present in high and variable concentrations in the Star kimberlite dykes (e.g. Rb = 27.3 – 178 ppm; Sr = 724 – 2771 ppm; Ba = 1029 – 6054 ppm; Table 5.2) and generally define moderate positive mutual correlations (Figure 5.9). Individual dykes also show wide ranges in abundances of these elements, with a particularly wide range shown by the Wynandsfontein Dyke (Rb = 27.3 – 139 ppm; Sr = 971 – 2140 ppm; Ba = 1029 – 5064 ppm;

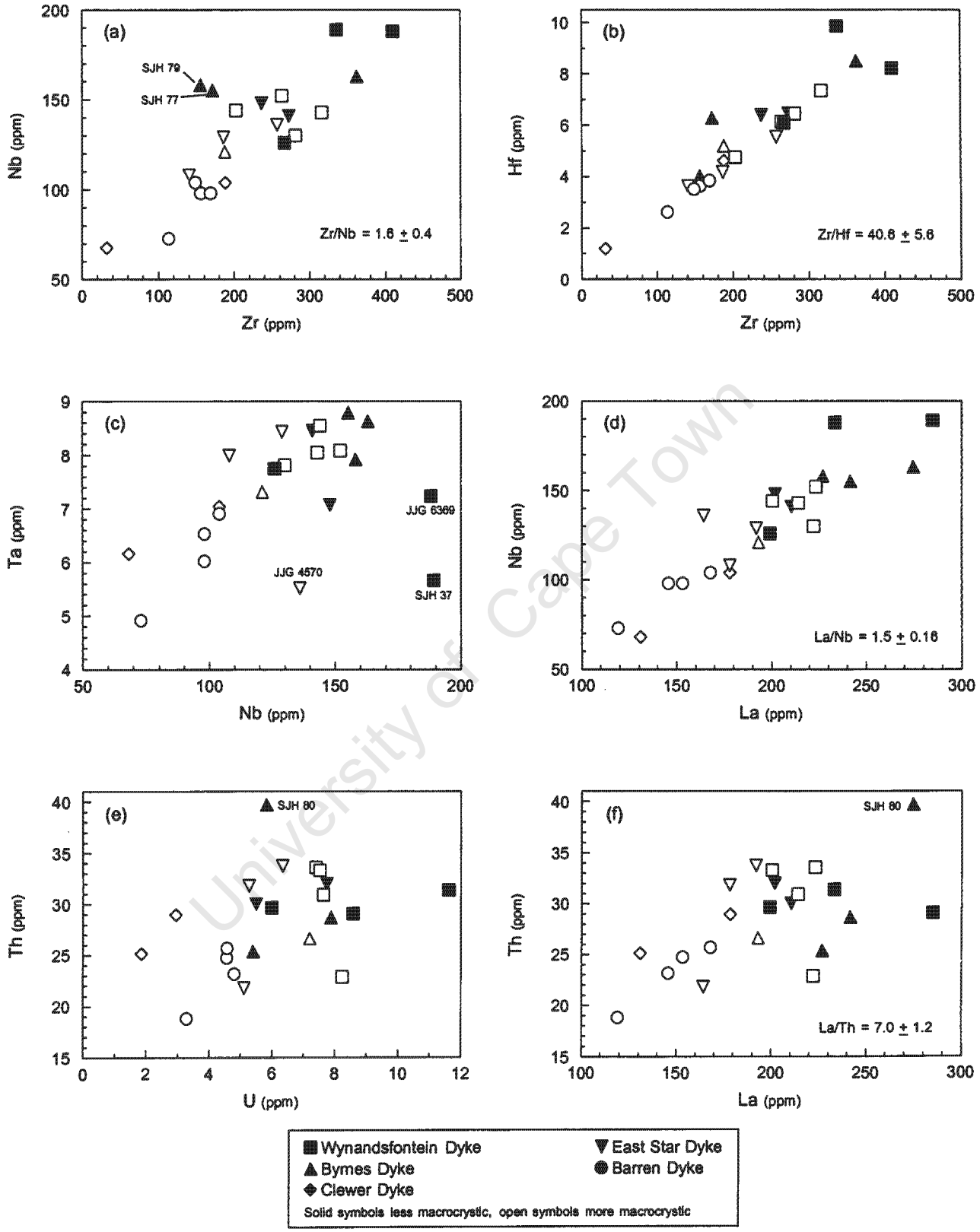

Figure 5.8 Variation of selected high field strength elements within the Star kimberlite dykes.

Table 5.2) which broadly encompasses the smaller range shown by the East Star Dyke (Rb = 109 – 160 ppm; Sr = 1266 – 2059 ppm; Ba = 2451 – 4533 ppm; Table 5.2). The least macrocrystic East Star Dyke sample (SJH 30) has higher Rb content than the more macrocrystic samples from this dyke, but Sr and Ba within the range of the macrocrystic samples and the more macrocrystic samples from the Wynandsfontein Dyke cannot be distinguished from the less macrocrystic samples by their LIL element content. The LIL element concentrations of the Clewer Dyke are similar to those of the less enriched Wynandsfontein Dyke samples (Rb = 82.4 – 118 ppm; Sr = 967 – 1366 ppm; Ba = 2280 – 2542 ppm; Table 5.2), whereas the Byrnes Dyke extends to more enriched compositions than the other Star kimberlite dykes (Rb = 123 – 178 ppm; Sr = 1924 – 2771 ppm; Ba = 4589 – 6054 ppm; Table 5.2) with the most macrocrystic Byrnes Dyke sample (SJH 78) having lower Rb and Sr contents, and relatively low Ba content, compared to the less macrocrystic samples from this dyke. Although the Barren Dyke has average Rb concentrations within the range of the diamondiferous Star kimberlite dykes (micaceous Rb = 146 – 158 ppm; less micaceous Rb = 96 ppm; Table 5.2), it has relatively low Ba (1873 – 2049 ppm; Table 5.2) and is less enriched in Sr (micaceous = 871 – 891 ppm; less micaceous = 724 ppm; Table 5.2) than the Star diamondiferous kimberlite dykes, with the less micaceous Barren Dyke sample (NC 054) being less enriched in Rb and Sr than the micaceous samples. Broad positive correlations are defined between the LIL elements and the immobile HFS elements and the variations of Ba and Sr with Nb is shown in Figure 5.9c and d. The two samples from the Wynandsfontein Dyke (SJH 37 and JJG 6369) noted in the previous section to have anomalously low Ta concentrations for their high Nb contents, also deviate from these two trends to lower Ba and Sr concentrations. Sample JJG 6361A, from the Wynandsfontein dyke, also deviates from the main correlation between Ba and Nb of the Star kimberlite dykes, with a lower Ba content for a given Nb concentration (Figure 5.9c).

The Star kimberlite dykes have a range in Pb concentrations from 10.9 to 51.2 ppm (Table 5.2). The Wynandsfontein dyke shows a wide range in Pb content (Pb = 25.8 - 50.4 ppm; Table 5.2) which encompasses the range of the Byrnes Dyke (Pb = 27.5 to 45.4ppm; Table 5.2), whereas the East Star Dyke trends to lower Pb concentrations (Pb = 21.6 – 29.9 ppm; Table 5.2). The Clewer (Pb = 10.9 – 17.0 ppm; Table 5.2) and Barren (micaceous Pb = 17.9 – 19.4 ppm; less micaceous Pb = 14.3 ppm; Table 5.2) Dykes are the least enriched and show the least variable Pb content of the Star kimberlite dykes. Pb shows a broad positive correlation with Ba (Figure 5.9e), and a strong positive correlation with Ce (Figure 4.9f), with an average Ce/Pb of 15.0 ± 4.0. The correlations are best defined by the East Star, Barren and Clewer Dykes, whereas the Byrnes and Wynandsfontein Dykes contain a subset of samples, SJH 37, JJG 6361A and JJG 6369 (Wynandsfontein dyke) and SJH (Byrnes Dyke), which are displaced from the main trend towards higher Pb concentrations for a given Ce content.

Primitive mantle normalised incompatible trace element diagrams from the Star kimberlite dykes are shown in Figure 5.10a-e. All the Star kimberlite dykes are enriched relative to primitive mantle, with greater enrichment in the more incompatible elements than the less incompatible elements. The Star diamondiferous dykes all have subdued Rb relative to Ba, with the East Star (Rb = 172 – 253 times primitive mantle) and Wynandsfontein Dyke (Rb = 157 – 219 times primitive mantle, excluding JJG 6361A) showing

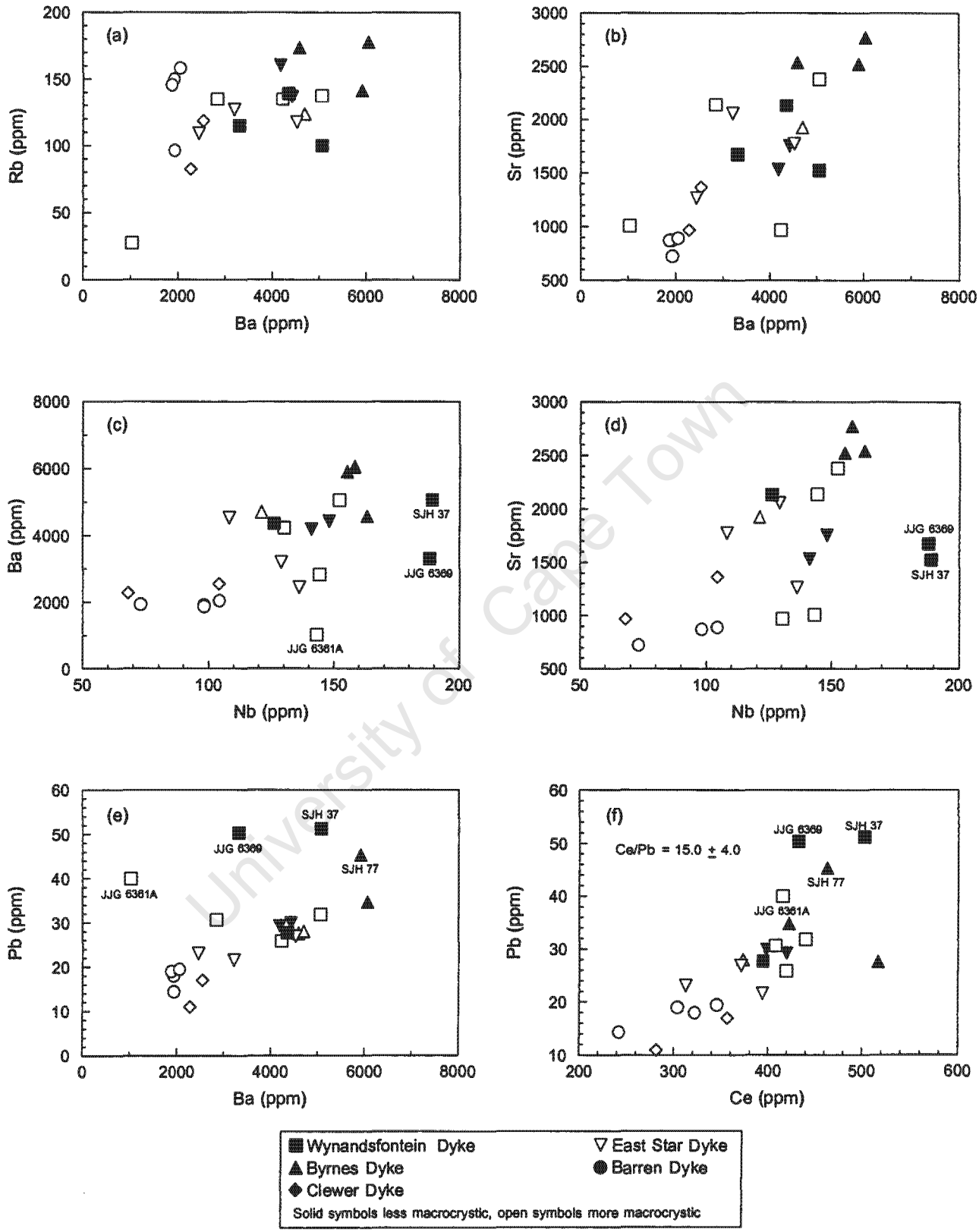

Figure 5.9 Variation of selected large ion lithophile elements within the Star kimberlite dykes.

similar, wide ranges of enrichment in Rb relative to primitive mantle. Sample JJG 6361A is less enriched than the other Wynandsfontein Dyke samples in both Rb (Rb = 43 times primitive mantle) and Ba, despite having similar degrees of enrichment in Th and U (Figure 5.10b). The Clewer Dyke extends to less enriched (Rb = 130 – 187 times primitive mantle), and the Byrnes dyke extends to slightly more enriched (Rb = 185 – 273 time primitive mantle), Rb relative to primitive mantle than the East Star or Wynandsfontein Dykes. The micaceous Barren Dyke samples differ from the Star diamondiferous dykes in having similar Rb and Th relative to primitive mantle, and are enriched in Rb from 229 to 249 times primitive mantle. The less micaceous Barren dyke sample (NC 054) has a sub-parallel pattern to the micaceous samples, but is less enriched in all the incompatible elements except for Ba. This sample shows slight depletion in Rb relative to Ba and is enriched in Rb 152 times primitive mantle.

The Star kimberlite dykes show sub-parallel, relatively smooth enrichment patterns, superimposed on which are strong negative Ti, variable negative Sr and K and subdued negative Nb and Ta anomalies. The Wynandsfontein dyke has the strongest and most variable Ti anomaly (Ti/Ti* = 0.20 – 0.32), whereas in the Byrnes dyke the anomaly is slightly smaller (Ti/Ti* = 0.28 – 0.39) and the Clewer (Ti/Ti* = 0.31 – 0.32) and East Star (Ti/Ti* = 0.30 – 0.34) Dykes have intermediate and less variable Ti anomalies. The Wynandsfontein Dyke also has the most variable K anomalies (K/K* = 0.21 – 0.37 except JJG 6361A) and the Byrnes (K/K* = 0.31 – 0.33 except SJH 79), Clewer (K/K* = 0.28 – 0.34) and East Star (K/K* = 0.29 – 0.39) Dykes have K anomalies approximately within this range. Sample JJG 6361A (Wynandsfontein Dyke) has an exceptionally large K anomaly (K/K* = 0.06) in addition to the suppressed Rb and Ba mentioned above, and sample SJH 79 (Byrnes Dyke) has a much smaller K anomaly (K/K* = 0.45) than the other samples from this dyke. The Sr anomaly in the Wynandsfontein Dyke varies widely in size (Sr/Sr* = 0.35 – 0.80) and the East Star and Clewer Dykes have anomalies within the range, whereas the Byrnes Dyke has a less strong Sr anomaly (Sr/Sr* = 0.70 – 0.99). The Barren Dyke samples have Sr anomalies of a similar size to the other Star kimberlite dykes (Sr/Sr* = 0.39 – 0.44), although the micaceous samples have slightly smaller Ti (Ti/Ti* = 0.39-0.44) and K (K/K* = 0.39 - 0.42) anomalies. These anomalies are slightly larger in the less-micaceous sample (NC 054) and within the range of the other Star kimberlite dykes (Ti/Ti* = 0.35; K/K* = 0.30). Sample JJG 2833 from the Clewer dyke has an extremely pronounced negative Zr-Hf anomaly, as well as a negative P anomaly, whereas the other Star samples show only slight negative Zr-Hf anomalies and generally no P anomaly. Sample SJH 80, from the Byrnes Dyke, has no Zr-Hf anomaly, and this sample is also enriched in the HREE relative to the other Byrnes Dyke samples, as mentioned in section 5.3.2.1 (Figure 5.10d).

Moderately sized positive Pb anomalies are present in all the dykes. The Pb anomaly is particularly variable in size in the Wynandsfontein Dyke (Pb/Pb* = 1.88 – 3.57), with samples JJG 6369 and SJH 37 having the largest anomalies. The Clewer (Pb/Pb* = 1.16 – 1.43) and Barren (Pb/Pb* = 1.69 – 1.89) Dykes have the smallest Pb anomalies, and the Byrnes (Pb/Pb* = 1.60 – 2.98) and East Star (Pb/Pb * = 1.64 – 2.27) Dykes have Pb anomalies between the two extremes. In the Clewer Dyke, Th is enriched to a similar degree to Ba relative to primitive mantle, and U is less enriched relative to these two elements, whereas in the other dykes Th and U are similarly enriched and Ba is elevated relative to these two elements (Figure 5.10).

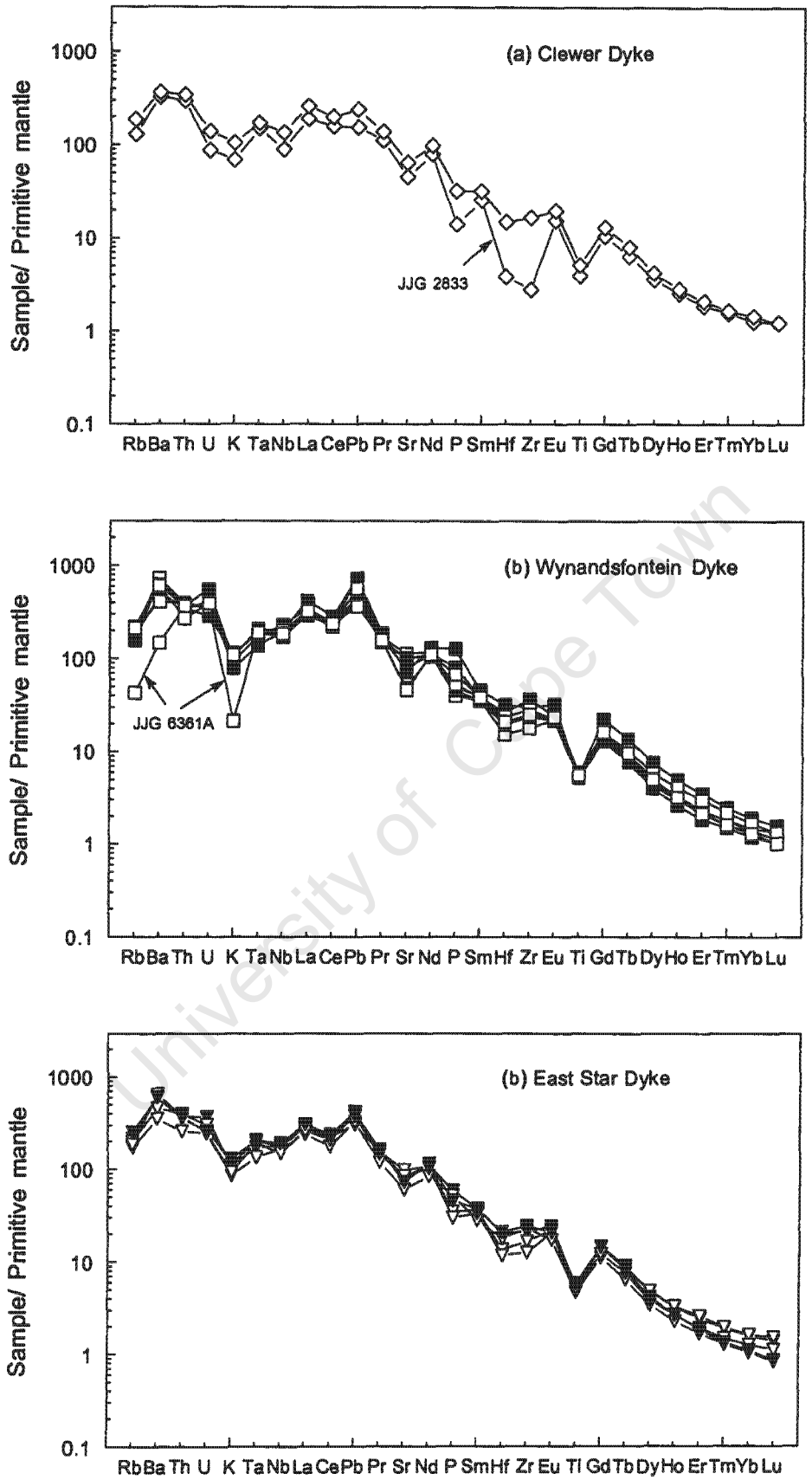

Figure 5.10 Primitive mantle normalised incompatible trace element variation in the Star kimberlite dykes. Open symbols = more macrocrystic samples, solid symbols = less macrocrystic samples. Primitive mantle values from Sun and McDonough (1989).

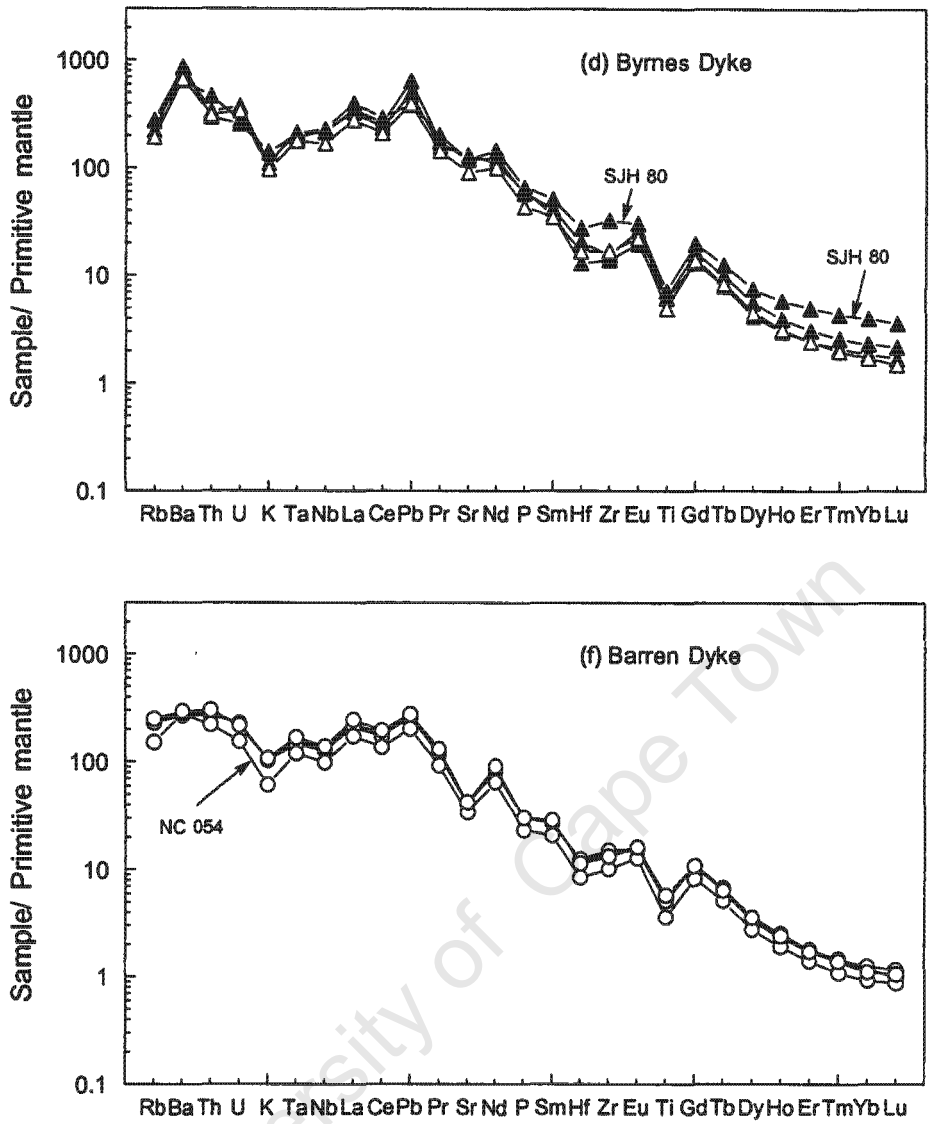

Figure 5.10 Continued.

5.4 Comparison in trace element geochemistry between Swartruggens, Star and other South African kimberlites

5.4.1 Compatible trace elements

Both the Swartruggens and Star kimberlites have high and variable concentrations of the compatible elements, and for most elements show a similar range in abundances (Table 5.1 and 5.2). The variation of Ni and Cr with La is shown in Figure 5.11 and, for comparison, fields are plotted for other South African Group II kimberlites (Finsch, Bellsbank, New Elands and Newlands, data from le Roex, unpublished) and Group I kimberlites from Kimberley (data from le Roex *et al.*, 2003). For a similar range in La, the Star kimberlites are more enriched in Cr (Cr = 1800 to 2733 ppm) than the Swartruggens kimberlites (Cr = 802 –

1946 ppm; Figure 5.11a). Both the Swartruggens and Star kimberlites show strong and overlapping negative correlations between Ni and La (Figure 4.11b), with Ni ranging from approximately 600 to 2000 ppm. The Swartruggens and Star kimberlites define fields, which overlap with those of some other Group II South African kimberlites, but extend to slightly lower and higher Cr contents, respectively (Figure 5.11a). With respect to Ni, the broad ranges in concentration shown by both the Swartruggens and Star kimberlites encompass those shown by other Group II kimberlites (Figure 5.11b). Relative to Group I kimberlites, the Star kimberlites are enriched in Ni at lower La concentrations, whereas the Swartruggens kimberlites have Ni concentrations within the range of Group I kimberlites. Both the Swartruggens and Star kimberlites are enriched in Cr at lower La concentrations relative to Group I kimberlites. The composition of the Swartruggens Muil lamprophyre lies outside the fields for South African Group I and Group II kimberlites, with lower Ni and Cr concentrations for a given La content.

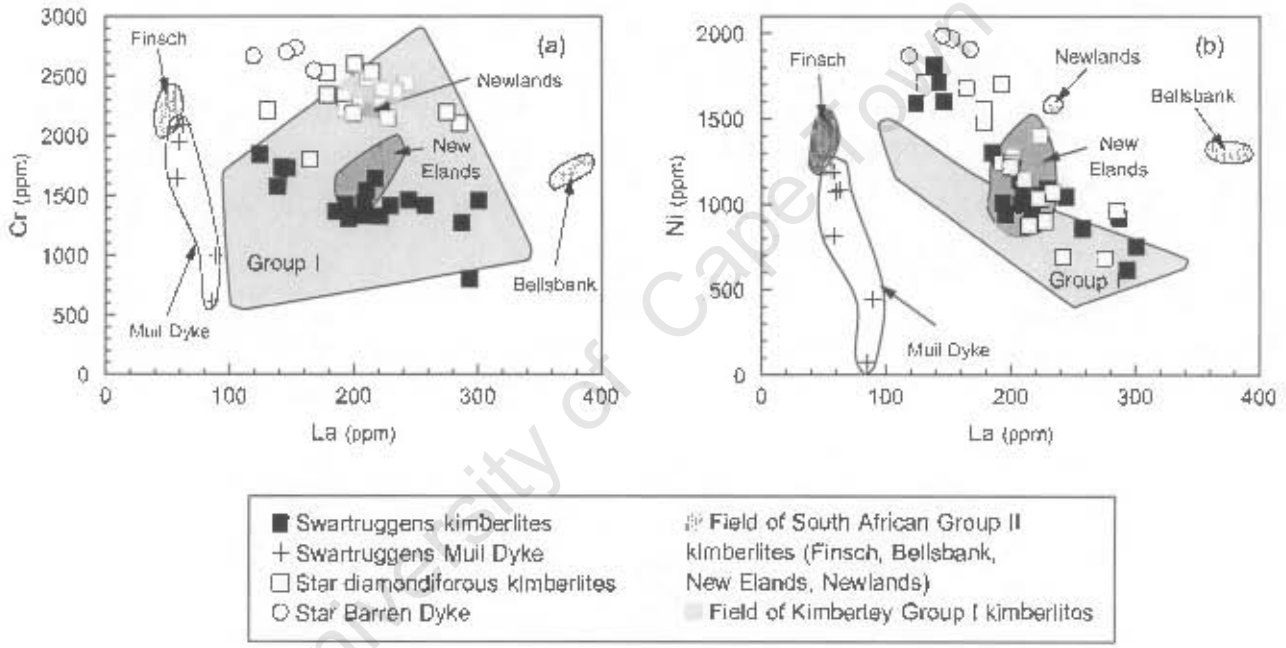

Figure 5.11 Variation of selected compatible trace elements in the Swartruggens and Star kimberlites, and the Muil lamprophyre. Field for Group II kimberlites from le Roex (unpublished data), field for Kimberley Group I kimberlites from le Roex *et al.* (2003).

5.4.2 Incompatible elements

5.4.2.1 Rare earth elements (REE)

The Swartruggens and Star kimberlites both have steep chondrite normalised REE patterns (Figure 5.12), although for a similar degree of enrichment in La, the Swartruggens kimberlites are more enriched in the HREE than the Star kimberlites. Consequently the average La/Yb_n of the Swartruggens kimberlite (La/Yb_n = 94 ± 21) is much lower than that of the Star kimberlites (La/Yb_n = 202 ± 36). Fields for South African Group II kimberlites and Kimberley Group I kimberlites are also shown on Figure 5.12 for comparison. Whereas the Star kimberlites fall within the range shown by other Group II kimberlites, the Swartruggens kimberlites are more enriched in the heavy REE than either the Group II or Group I kimberlites. The average La/Yb_n

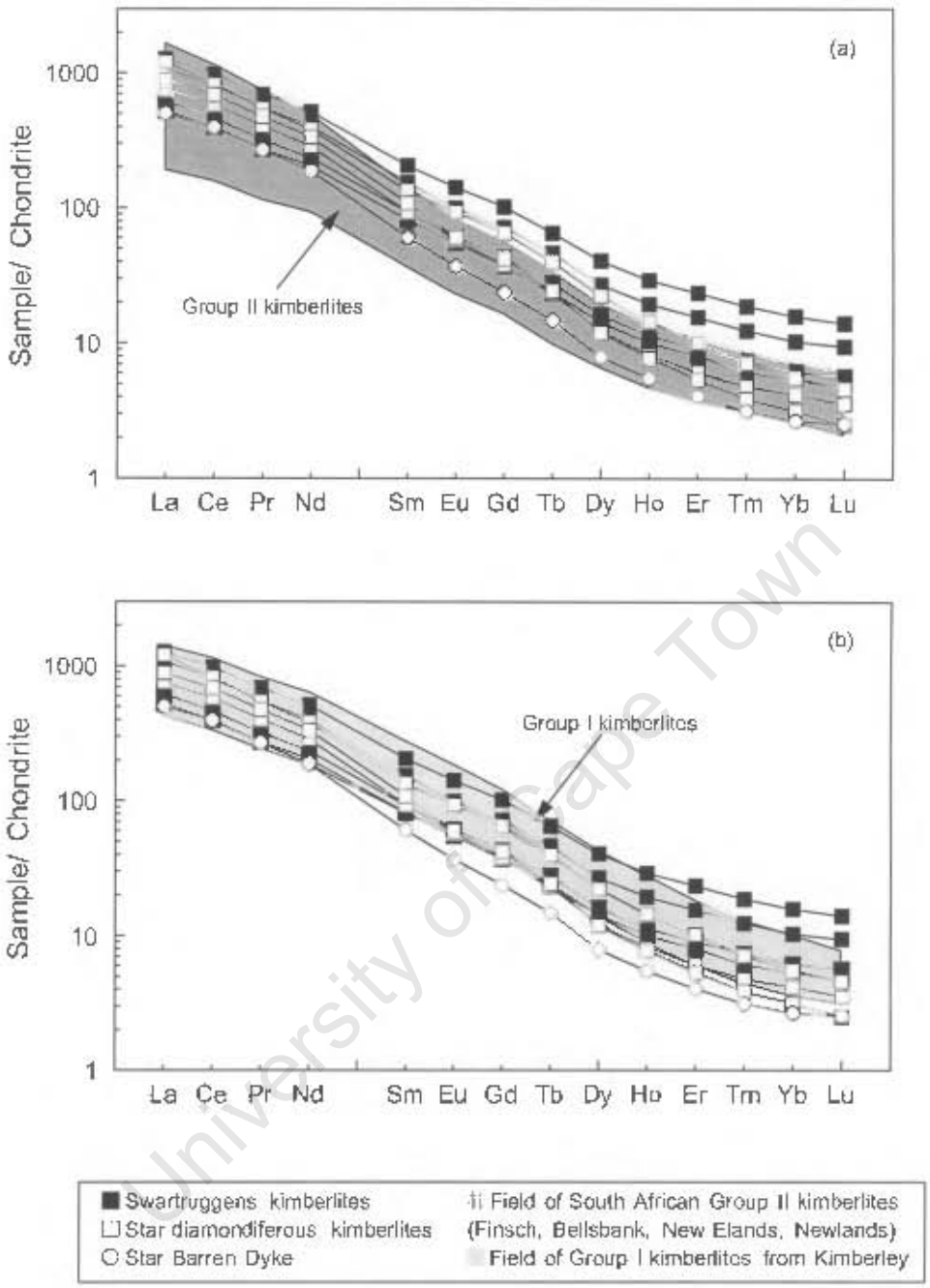

Figure 5.12 Chondrite normalised rare earth element patterns for selected representative samples from the Swartruggens and Star kimberlites. Data sources for Group I and Group II kimberlites as for Figure 5.11, chondrite values from Sun and McDonough (1989).

ratios of both the Swartruggens and Star kimberlites fall within the broad range of 67 to 403 of the other Group II kimberlites (le Roex, unpublished), although the lower average La/Yb_n of the Swartruggens kimberlites is more similar than that of the Star kimberlites to the Kimberley Group I kimberlites (which have an average La/Yb_n of 122 ± 21; le Roex *et al.*, 2003). For clarity, the Swartruggens Muil Dyke is not shown on Figure 5.12. The sub-parallel chondrite normalised REE pattern of this dyke lies within, but towards the less enriched edge of, the field of South African Group II kimberlites.

5.4.2.2 High field strength and large ion lithophile elements

Variations of selected HFS and LIL elements in the Swartruggens and Star kimberlites are shown in Figure 5.13, with fields for South African Group II kimberlites and Group I kimberlites from Kimberley shown for comparison. Despite the strikingly similar co-variation of Zr and Hf in the Swartruggens and Star kimberlites (Figure 5.13a), the Star kimberlites are more enriched in Nb at a given Zr than the Swartruggens kimberlites (Figure 5.13b). The Star kimberlites are also more enriched in Ta for a given Nb than the Swartruggens kimberlites (Figure 5.13c), and have higher Th contents at low U concentrations (Figure 5.13d). Zr/Hf and La/Nb of the Swartruggens and Star kimberlites are similar (Swartruggens Zr/Hf = 45.0 ± 3.9, La/Nb = 1.6 ± 0.25; Star Zr/Hf = 40.6 ± 5.6, La/Nb = 1.5 ± 0.16), although the Swartruggens kimberlites have slightly higher average Zr/Nb and Nb/Ta than the Star kimberlites (Swartruggens Zr/Nb = 2.9 ± 0.8, Nb/Ta = 25.0 ± 5.2; Star Zr/Nb = 1.6 ± 0.4, Nb/Ta = 18.1 ± 4.8). The Swartruggens and Star kimberlites both fall largely within the range of the other South African Group II kimberlites and the Kimberley Group I kimberlites for most of the HFSE elements, although the Swartruggens South Fissure trends to more enriched concentrations of Zr, Hf and Nb. The Zr/Hf ratios of the Swartruggens and Star kimberlites are similar to those of other Group II and Group I kimberlites (Figure 5.13a), whereas the correlation between Zr and Nb in the Swartruggens and Star kimberlites, although similar to that of Group I kimberlites, is much better defined by these kimberlites than by the field for other Group II kimberlites (Figure 5.13b). Although the Swartruggens kimberlites have Nb and Ta concentrations within the field of other Group II kimberlites at lower concentrations, at higher Nb concentrations they have lower Ta concentrations than other Group II or Group I kimberlites. At low Nb concentrations, the Star kimberlites are slightly enriched in Ta compared to the field of Group II kimberlites or Group I kimberlites (Figure 5.13c). Both the Swartruggens and Star kimberlites have higher U/Th ratios than the fields for either Group I or Group II kimberlites, and at high U contents both the Swartruggens and Star kimberlites are less enriched in Th than the other Group II or Group I kimberlites (Figure 5.13d).

The Swartruggens kimberlites trend towards higher concentrations of the LILE than the Star kimberlites (e.g. Rb and Ba in Figure 5.13e). Both kimberlites show broad positive correlations between Rb and Ba (with considerable scatter), with the Star kimberlites being slightly enriched in Ba relative to the Swartruggens kimberlites for a given Rb concentration, and strong positive correlations between Ce and Pb, with the Swartruggens kimberlites being slightly enriched in Pb relative to the Star kimberlites for a given Ce concentration (Swartruggens Ce/Pb = 9.1 ± 2.3; Star Ce/Pb = 15.0 ± 4.0; Figure 5.13f). The positive correlations between Rb and Ba of the Swartruggens and Star kimberlites crosscut the field of Group II kimberlites and the Swartruggens kimberlites extend to higher Rb and Ba concentrations than this field. The majority of samples from both Swartruggens and Star have Pb concentrations within the field of other Group II kimberlites and samples with lower Ce content have Ce/Pb similar to this field. However the more enriched samples have higher Ce/Pb than the Group II kimberlite field, with elevated Pb concentrations for a given Ce content.

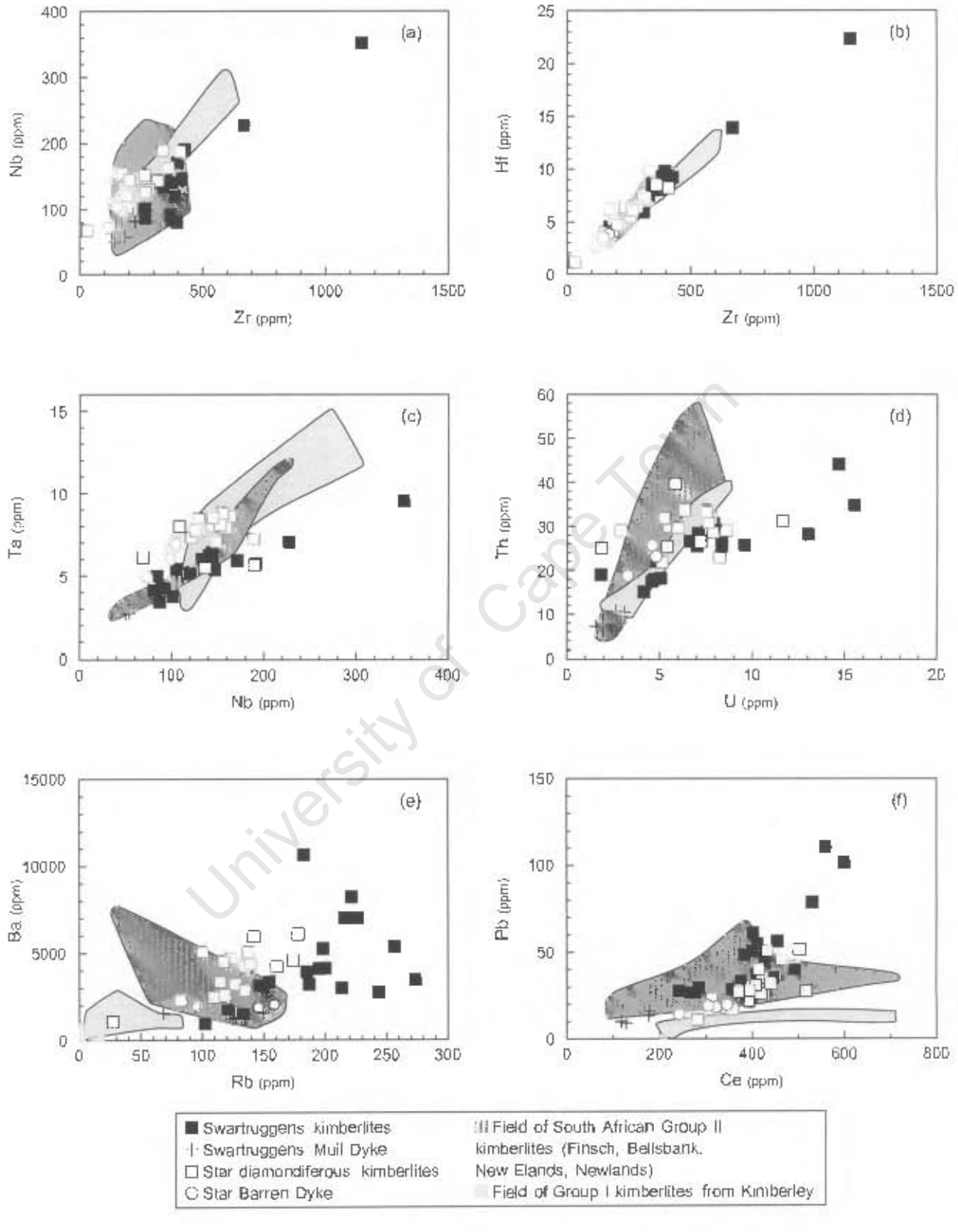

Figure 5.13 Variation in selected high field strength and large ion lithophile elements in the Swartruggens and Star kimberlites. Data sources for Group I and Group II kimberlites as for Figure 5.11.

Primitive mantle normalised incompatible trace element variation in representative samples from the Swartruggens and Star kimberlites are shown in Figure 5.14 with fields for South African Group II (Figure 5.13a) and Kimberley Group I (Figure 5.13b) kimberlites shown for comparison. Both the Swartruggens and Star kimberlites show similar, sub parallel patterns, with similar degrees of enrichment in the more incompatible As noted previously, the Swartruggens kimberlites are slightly enriched relative to the Star kimberlites and the other South African Group II kimberlites in the heavy REE. The strong negative Sr and

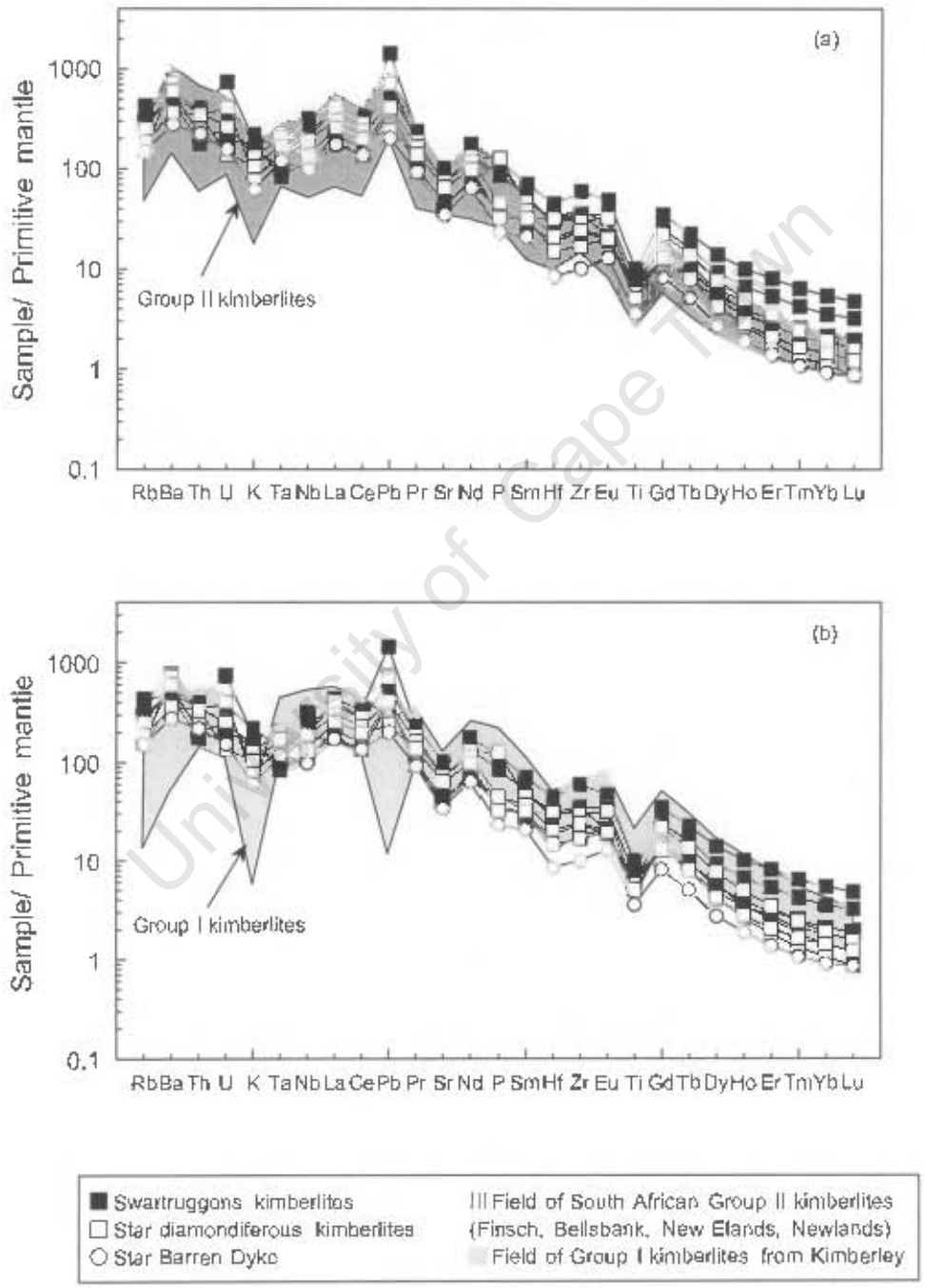

Figure 5.14 Primitive mantle normalised incompatible trace element variation in selected representative samples from the Swartruggens and Star kimberlites. Data sources for Group I and Group II kimberlites as for Figure 5.11, primitive mantle values from Sun and McDonough (1989).

both of the Group II and Group I kimberlites, whereas the subdued negative Nb – Ta anomalies present in the Swartruggens, Star and other Group II kimberlites are not present in Group I kimberlites (Figure 5.14). Ti, and slight negative Zr-Hf, anomalies present in both the Swartruggens and Star kimberlites are a feature The abundances of the more incompatible elements in the Swartruggens and Star kimberlites (Swartruggens Rb = 105 to 420 times primitive mantle; Star Rb = 43 to 249 times primitive mantle) largely within the range of other Group II kimberlites (Figure 5.14a).

Swartruggens, Star and other Group II kimberlites show similar, moderately sized, K anomalies and have suppressed Rb relative to Ba, whereas Group I kimberlites show much stronger K anomalies coupled with strong negative Rb anomalies. The strong positive Pb anomalies, which are a feature of both the Swartruggens and Star kimberlites, are also present in other South African Group II kimberlites but are absent from the Kimberley Group I kimberlites

Although the Swartruggens Muil Dyke (not shown in Figure 5.14, for clarity) lies within the range of enrichment shown by Group II kimberlites, the lack of Ti anomaly (Figure 5.5e) differentiates the primitive mantle normalised pattern of this dyke from those of either the South African Group I or Group II kimberlites.

Chapter 6

Isotope geochemistry

6.1 Introduction

In the 1970s, the Sr and Nd isotope characteristics of many southern African kimberlites were measured with the primary aim of obtaining age determinations (e.g. Berg and Allsopp, 1972, Allsopp and Barrett, 1975, Barrett and Berg, 1975, Allsopp and Kramers, 1977, Kramers, 1977). Following the pioneering work of Smith (1983a), radiogenic isotopes have since been used in attempts to understand kimberlite petrogenesis and constrain source region characteristics. Smith (1983a) observed that the two distinct petrographic groups of southern African kimberlites ("basaltic" and "micaceous"; Wagner, 1914), can also be distinguished based on their Sr and Nd isotope compositions, and further that the two groups have isotopically distinct mantle source regions. Group I kimberlites ($^{87}Sr/^{86}Sr_i$ = 0.7033 - 0.7049; $^{143}Nd/^{144}Nd_i$ = 0.51271 - 0.51277) have a source in undifferentiated to slightly depleted mantle, commonly interpreted to be convecting upper mantle, whereas Group II kimberlites ($^{87}Sr/^{86}Sr_i$ = 0.7074 - 0.7109, $^{143}Nd/^{144}Nd_i$ = 0.51208 - 0.51228) originate from mantle which has developed enriched isotopic compositions over time, commonly interpreted to be the lithosphere (Smith, 1983a). Sr and Nd isotope data for suites of samples from the same intrusion have also been used to constrain the effects of secondary processes such as assimilation of mantle lithosphere, contamination by crust and alteration on the isotopic characteristics of some kimberlites (e.g. Smith, 1983b; Fraser *et al.*, 1985; Tainton, 1992).

More recently, the Hf isotope character of some southern African kimberlites has been determined. Nowell *et al.* (1999, 2004) noted that whereas Group II kimberlites have Hf isotope signatures that cluster around the mantle array in Hf-Nd isotopic space, the Hf isotope compositions of Group I kimberlites deviate significantly below the mantle array. These authors argued for a contribution from subducted oceanic crust at depths greater than the lithospheric mantle in the source region of Group I kimberlites.

$^{87}Sr/^{86}Sr$ in the crust can be as high as 0.75 (Smith, 1983b and references therein; Barton *et al.*, 1999). This is significantly higher than that of kimberlite magmas, and as Sr is abundant in crustal rocks $^{87}Sr/^{86}Sr$ in kimberlites may be affected by crustal assimilation. In addition, it was noted by Kirkley (1987) that kimberlites such as Swartruggens, which intrude through the Chuniespoort dolomite have significantly higher $^{87}Sr/^{86}Sr$ than those such as Star, which do not. Both $^{143}Nd/^{144}Nd$ and $^{176}Hf/^{177}Hf$ are typically slightly lower in the crust than in kimberlite magmas (e.g. Archean crust $^{176}Hf/^{177}Hf$ = 0.280 – 0.2815, $^{143}Nd/^{144}Nd$ = 0.5101 – 0.5112; Vervoort and Patchett, 1996) and so assimilation of crust may lower these ratios in the kimberlite magmas.

The permeable and porous nature of kimberlites (e.g. Berg, 1994), combined with the mobility of both Rb and, to a lesser extent, Sr, renders their $^{87}Sr/^{86}Sr$ susceptible to post-emplacement alteration by meteoric fluids. Smith (1983b) concluded that assimilation of a few percent crust would only affect the Sr isotope composition of a kimberlite magma by a small amount (of the order of 0.05 percent), whereas alteration may substantially raise the $^{87}Sr/^{86}Sr$ ratios of kimberlites (Kramers *et al.*, 1981; Smith, 1983b). In contrast to Rb and Sr, Sm, Nd, Lu and Hf are all immobile elements in the weathering environment, and thus their isotopic compositions should not be affected by groundwater infiltration.

Due to the isotopic diversity of cratonic lithospheric mantle (e.g. Carlson, 1995; Pearson and Nowell, 2002; Pearson *et al.*, 2003b), the assimilation of mantle material by the kimberlite magmas *en route* to the surface may be less easily detected. However, cratonic lithosphere typically has $^{87}Sr/^{86}Sr$ of the order 0.70 to 0.71, εNd of –40 to 0 (Pearson and Nowell, 2002; Pearson *et al.*, 2003b). Hf isotope compositions of continental lithospheric mantle are even less constrained, and a range in εHf from –15 to +3800 has been recorded (Ionov and Weiss, 2002; Schmidberger *et al.*, 2002; Simon *et al.*, 2002).

Whole rock analyses of the Sr isotope composition of four samples from the Swartruggens Main Dyke have yielded a wide variation in initial ratios ($^{87}Sr/^{86}Sr_i$ = 0.708 - 0.7109; Smith, 1983b). Smith (1983b), considered that this range may be due to alteration or contamination, but as the samples showed no petrographic evidence of either of these two factors, he also considered that the kimberlite may not be isotopically homogenous.

The Swartruggens kimberlite has previously been classified as a Group II kimberlite (Smith *et al.*, 1985a). Although classified as micaceous (e.g. Gurney and Hatton, 1989), the Star kimberlite has not previously been classified according to its Sr and Nd isotope composition. A suite of samples from each of these two kimberlites have been analysed for their Sr, Nd and Hf isotope compositions, with 3 principal aims in mind:

1) To document the Sr, Nd and Hf isotope characteristics of the Swartruggens and Star kimberlites, and to assess the variation present at each locality, both within and between individual dykes.
2) To isolate, as far as possible, the effects of contamination by crustal material and weathering, and so determine the isotopic characteristics of the primary kimberlite magmas and any primary isotopic variations between individual dykes, and between the two localities.
3) By constraining the isotopic character of the respective kimberlite source regions, to constrain the petrogenetic processes giving rise to these two kimberlites and the likely physical location of the source regions (i.e. lithospheric vs. asthenospheric mantle).

The Sr, Nd and Hf isotope characteristics of the Swartruggens and Star kimberlites are documented and described in this chapter. Points 2 and 3 above are considered further in Chapter 7.

The analyses were obtained using a ThermoFinnigan Neptune Plasma Ionisation Multi-collector Mass Spectrometer at the Arthur Holmes Isotope Geosciences Laboratory, Department of Earth Sciences, University of Durham. Details of analytical techniques are reported in Appendix 3.

6.1.1 Data presentation

Nd, Sr and Hf analyses, together with 2σ uncertainties, for the Swartruggens and Star kimberlites are reported in Tables 6.1 and 6.2, respectively. Initial isotopic ratios have been calculated using an age of 156 Ma for the Swartruggens kimberlites (Smith *et al.*, 1985a) and of 124 Ma for the Star kimberlites (MacIntyre and Dawson, 1976). It is uncertain whether the Swartruggens lamprophyric Muil Dyke is the same age as, or younger than, the Swartruggens kimberlite dykes (Smith *et al.*, 1985a), although for comparative purposes an age of 156 Ma has been used to calculate the initial ratios given in Table 6.1.

ε_{Nd} is a measure of the deviation of $^{143}Nd/^{144}Nd$ from a hypothetical chondritic mantle at time (T) and is estimated as follows:

$$\varepsilon_{Nd} = \left\{ \frac{^{143}Nd/^{144}Nd \text{ sample initial ratio } (T)}{^{143}Nd/^{144}Nd \text{ CHUR } (T)} - 1 \right\} \times 10^4$$

where CHUR is a chondritic uniform reservoir (DePaolo and Wasserberg, 1976, O'Nions *et al.* 1979). ε_{Hf} is estimated in the same way, but with $^{176}Hf/^{177}Hf$ substituted for $^{143}Nd/^{144}Nd$. Following Johnson and Beard (1993), the notation $\Delta\varepsilon_{Hf}$ is used to refer to the degree of displacement of ε_{Hf} from the well-defined mantle array in ε_{Hf}-ε_{Nd} space ($\varepsilon_{Hf} = 1.33\varepsilon_{Nd} + 3.19$; Vervoort *et al.*, 1999) illustrated in Figure 6.5c.

6.2 Isotope geochemistry of the Swartruggens kimberlite dykes and the Muil lamprophyre

Six samples from the Swartruggens kimberlite dykes (2 from the Main Dyke, 2 from the Changehouse Dyke and 2 from the South Fissure) have been analysed for their Sr, Nd and Hf isotope compositions. Four samples from the Muil lamprophyre have also been analysed for their Sr and Nd isotopic compositions. The data are reported in Table 6.1, and selected variations are shown in Figures 6.1 and 6.2.

6.2.1 Neodymium and Strontium isotopes

The Swartruggens kimberlite dykes collectively have restricted initial $^{143}Nd/^{144}Nd$, ranging from 0.511825 ± 18 to 0.511855 ± 19. There is no significant variation in Nd isotope composition within individual dykes, with the Changehouse Dyke showing a range in $^{143}Nd/^{144}Nd_i$ from 0.511825 ± 18 to 0.511834 ± 16 which encompasses the range of the South Fissure samples (Table 6.1). Although the errors on the Main Dyke Nd analyses overlap those of these two dykes, the Main Dyke has slightly higher initial $^{143}Nd/^{144}Nd$ (0.511851 ± 19 to 0.511855 ± 19; Table 6.1). This is well illustrated on a Sm-Nd isochron diagram (Figure 6.1a), where the South Fissure and Changehouse Dyke samples show a broad positive correlation between $^{143}Nd/^{144}Nd$ and $^{147}Sm/^{144}Nd$ which approximates to a theoretical 156 Ma isochron. The Main Dyke samples define a separate trend, also approximating to a theoretical 156 Ma isochron, but with a slightly higher initial ratio. However, the Main and Changehouse Dykes define a negative correlation between initial $^{143}Nd/^{144}Nd$ and 1/Nd (Figure 6.1b), with the more macrocrystic Changehouse Dyke having lower Nd concentrations coupled

Table 6.1 Whole rock isotope analyses of the Swartruggens kimberlite dykes and the Muil lamprophyric dyke. M = more macrocrystic, LM = less macrocrystic. Initial ratios and ε values calculated assuming an age of 156 Ma (Smith, 1985a). Subscripts: m = measured, I = initial, o = present. Best (smallest uncertainty) analyses are reported. Repeat analyses are reported in Appendix 3; 2σ uncertainties include error on standards, standard reproducibility reported in Appendix 3.

Dyke	Main Dyke		Changehouse Dyke		South Fissure		Muil Dyke			
Sample	NC 008	NC 010	NC 005	NC 007	JJG 3149	JJG 3145	NC 008	NC 012	NC 014	NC 015
Macro	LM	M	M	M	LM	M	LM	M	M	M
Rb ppm	267	214	183	180	221	210	97.2	122	146	130
Sr ppm	1398	702	939	825	2777	2060	915	739	741	648
$^{87}Rb/^{86}Sr$	0.539013	0.862268	0.550923	0.617499	0.224421	0.287263	0.300126	0.466739	0.557626	0.565202
$^{87}Sr/^{86}Sr_m$	0.709505	0.711418	0.710331	0.711816	0.708209	0.708701	0.710463	0.709816	0.709467	0.709682
2σ uncertainty	0.000012	0.000013	0.000014	0.000015	0.000014	0.000014	0.000014	0.000016	0.000016	0.000016
$^{87}Sr/^{86}Sr_i$	0.708310	0.709506	0.709110	0.710447	0.707711	0.708063	0.709797	0.708781	0.708230	0.708429
Sm ppm	23.6	16.7	12.4	14.1	25.8	22.1	9.24	6.33	6.02	
Nd ppm	187	141	95.2	109	195	172	72.0	48.6	46.8	
$^{147}Sm/^{144}Nd$	0.076331	0.071946	0.079313	0.078560	0.080363	0.078189	0.077870	0.078945	0.078095	-
$^{143}Nd/^{144}Nd_m$	0.511933	0.511925	0.511906	0.511915	0.511914	0.511905	0.512062	0.512052	0.512070	-
2σ uncertainty	0.000019	0.000019	0.000018	0.000016	0.000019	0.000018	0.000010	0.000015	0.000011	-
$^{143}Nd/^{144}Nd_i$	0.511855	0.511851	0.511825	0.511834	0.511832	0.511825	0.511982	0.511971	0.511990	-
ε_{Nd_o}	-13.76	-13.91	-14.29	-14.11	-14.13	-14.30	-11.24	-11.44	-11.09	-
ε_{Nd_i}	-11.37	-11.43	-11.95	-11.76	-11.82	-11.95	-8.88	-9.10	-8.73	-
ε2σ uncertainty	0.36	0.37	0.34	0.32	0.37	0.35	0.20	0.29	0.21	-
Lu ppm	0.24	0.11	0.12	0.14	0.30	0.21				
Hf ppm	8.63	4.54	5.76	9.80	9.21	5.94				
$^{176}Lu/^{177}Hf$	0.003967	0.003521	0.002973	0.002087	0.004659	0.005089	-	-	-	-
$^{176}Hf/^{177}Hf_m$	0.282241	0.282170	0.282180	0.281976	0.282257	0.282253	-	-	-	-
2σ uncertainty	0.000004	0.000005	0.000005	0.000004	0.000004	0.000005	-	-	-	-
$^{176}Hf/^{177}Hf_i$	0.282230	0.282160	0.282172	0.281970	0.282244	0.282239	-	-	-	-
ε_{Hf_o}	-18.76	-21.27	-20.92	-28.14	-18.20	-18.34	-	-	-	-
ε_{Hf_i}	-15.74	-18.20	-17.79	-24.92	-15.24	-15.43	-	-	-	-
ε2σ uncertainty	0.15	0.18	0.18	0.15	0.15	0.17	-	-	-	-
$\Delta\varepsilon_{Hf}$	-3.81	-6.18	-5.09	-12.47	-2.72	-2.73	-	-	-	-

Decay constants used: Rb-Sr = 1.42 x 10^{-11}; Sm-Nd = 6.54 x 10^{-12}; Lu-Hf = 1.876 x 10^{-11};
CHUR: $^{143}Nd/^{144}Nd$ = 0.512638; $^{147}Sm/^{144}Nd$ = 0.1967; $^{176}Hf/^{177}Hf$ = 0.282772; $^{176}Lu/^{177}Hf$ = 0.0332

with slightly lower initial isotopic ratios and thus the variation in initial Nd ratio between these two dykes may be due to contamination by lithospheric mantle. This aspect will be discussed further in Chapter 7.

Initial $^{87}Sr/^{86}Sr$ in the Swartruggens kimberlites ranges from 0.707711 ± 14 to 0.710447± 15 and individual dykes show broad ranges, with the more macrocrystic samples from the Main Dyke and South Fissure having higher $^{87}Sr/^{86}Sr_i$ than the less macrocrystic samples from these dykes. The Main Dyke shows a range in $^{87}Sr/^{86}Sr_i$ from 0.708310 ± 12 to 0.709506 ± 13 (Table 6.1) and sample NC 005 from the Changehouse Dyke (with $^{87}Sr/^{86}Sr_i$ = 0.709110 ± 14; Table 6.1) lies within this range, whereas sample NC 007 (Changehouse Dyke) has the higher ratio of 0.710447 ± 15 (Table 6.1). The South Fissure has the lowest initial $^{87}Sr/^{86}Sr$ of the Swartruggens kimberlite dykes (0.707711 ± 14 to 0.708063 ± 14; Table 6.1).

Collectively, the Swartruggens kimberlite dykes define a strong positive correlation on a Rb-Sr isochron diagram (Figure 6.1c). However, all the samples analysed have consistently higher measured $^{87}Sr/^{86}Sr$ than would be expected for their $^{87}Rb/^{87}Sr$, if they were to fit an isochron of 156 Ma with an initial $^{87}Sr/^{86}Sr$ of 0.705, as calculated by Smith *et al.* (1985a) following analyses of phlogopite separates from Swartruggens

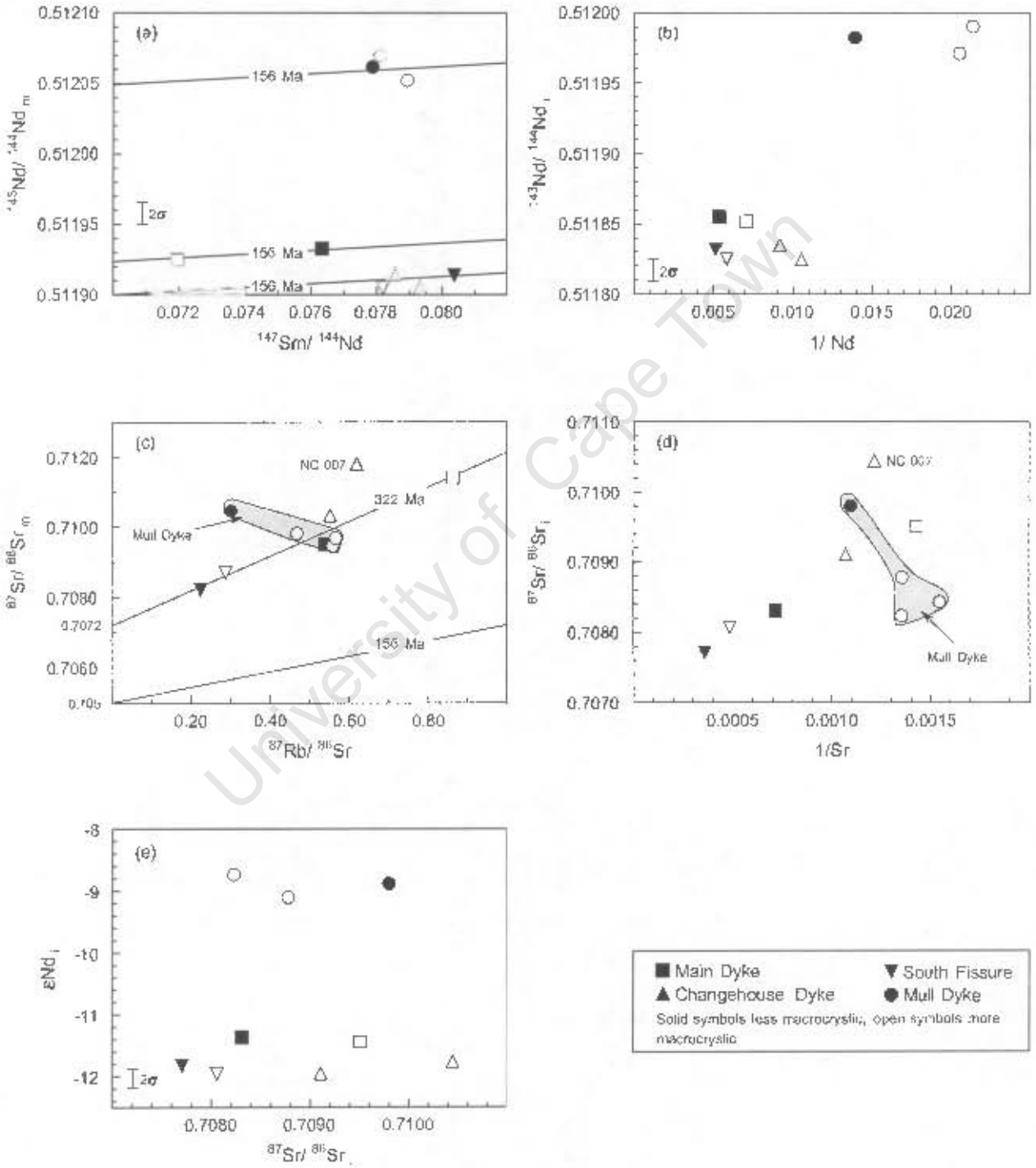

Figure 6.1 Variations in Sr and Nd isotope compositions in the Swartruggens kimberlite dykes and the Muil lamprophyre. Typical Nd 2σ uncertainties are shown by error bars, Sr 2σ uncertainties are smaller than symbol size. Regression lines are theoretical isochrons at indicated ages.

(Figure 6.1c). An errorchron can be drawn through the Swartruggens kimberlite whole-rock samples (excepting NC 007, Changehouse Dyke, with anomalously high $^{87}Sr/^{86}Sr$), but this yields an age of approximately 322 Ma, more than twice that calculated by Smith *et al.* (1985a) or Allsopp and Barrett (1975). In addition, there is a strong positive correlation between $^{87}Sr/^{86}Sr_i$ and 1/Sr (Figure 6.1d) for these samples. These consistent trends, together with the large within-dyke variations, are difficult to reconcile with primary isotopic heterogeneity, as suggested by Smith (1983b), especially given that there is little variation in Nd isotope composition for a wide range in $^{87}Sr/^{86}Sr$ for these samples (Figure 6.1e). The variation observed is therefore considered to represent a mixing trend, either due to assimilation of crust or interaction with groundwater. This aspect will be discussed in more detail in Chapter 7

The Muil Dyke samples show no systematic variation in $^{143}Nd/^{144}Nd_m$ with $^{147}Sm/^{144}Nd$, and so clearly do not define any isochron (Figure 6.1a). However, age-correcting the Muil Dyke to 156 Ma yields substantially higher initial $^{143}Nd/^{144}Nd$ ($^{143}Nd/^{144}Nd_i$ = 0.511971 ± 15 to 0.511990 ± 11; Table 6.1; Figure 6.1a) for this dyke than for the Swartruggens kimberlite dykes. The Muil Dyke cross cuts the kimberlite dykes and therefore cannot be older, and thus the difference in initial $^{143}Nd/^{144}Nd$ reported in Table 6.1 and illustrated in Figure 6.1a and b is a minimum. It will be argued in the next chapter that the difference in Nd isotope composition between the Muil Dyke and the Swartruggens kimberlite dykes cannot be produced by addition of reasonable quantities of mantle or crustal material, and the Muil Dyke is therefore believed to originate from a source that is isotopically distinct from the source of the Swartruggens kimberlites. The aphanitic Muil Dyke sample (NC 008) has a Nd isotope composition within the range of the macrocrystic samples, despite having a considerably higher absolute Nd concentration (Figure 6.1b).

Despite having substantially higher $^{143}Nd/^{144}Nd$ than the Swartruggens kimberlite dykes, the Muil Dyke has $^{87}Sr/^{86}Sr_i$ of 0.708230 ± 16 to 0.709797 ± 14, within the range of the kimberlite dykes. However, there is no consistent variation between measured $^{87}Sr/^{86}Sr$ and $^{87}Rb/^{86}Sr$ or 1/Sr for the Muil Dyke, and it appears to be unrelated to the trends observed within the Swartruggens kimberlite dykes (Figure 6.1 c and d). The Muil dyke shows a wide range in $^{87}Sr/^{86}Sr_i$ for a small variation in ε_{Nd} (Figure 6.1d) and, as with the Swartruggens kimberlites, the Sr isotope composition of the Muil Dyke may have been contaminated to variable degrees by crust or groundwater. This aspect will be discussed further in Chapter 7.

6.2.2 Hafnium isotopes

The majority of the Swartruggens kimberlite samples show little range in initial $^{176}Hf/^{177}Hf$, from 0.282160 + 5 to 0.282244 + 4 (Table 6.1). Sample NC 007 (from the Changehouse Dyke), already noted to have anomalously high $^{87}Sr/^{86}Sr$ compared to the other Swartruggens kimberlite samples, has a much lower $^{176}Hf/^{177}Hf_i$ of 0.281970 ± 4 and, as discussed further in Chapter 7, is likely to have been significantly contaminated by crust or groundwater. The South Fissure has the highest $^{176}Hf/^{177}Hf_i$ of the Swartruggens kimberlite dykes, and the variation within this dyke is within analytical error ($^{176}Hf/^{177}Hf_i$ = 0.282239 + 5 to 0.282244 + 4; Table 6.1). The Main Dyke shows a much wider range in $^{176}Hf/^{177}Hf_i$ ($^{176}Hf/^{177}Hf_i$ = 0.282160 ± 4 to 0.282230 ± 5; Table 6.1), which is significantly greater than analytical error, and Changehouse Dyke sample NC 005 lies within this range. The less macrocrystic Main Dyke sample (NC 006) has a similar Hf

isotopic composition to the South Fissure samples, and these three samples collectively scatter around a 156 Ma reference line on a Lu-Hf isochron diagram (Figure 6.2a). The more macrocrystic Main Dyke sample, together with sample NC 005 (Changehouse Dyke), lies significantly below this line. There is a negative correlation between $^{176}Hf/^{177}Hf_i$ and 1/Hf for the Swartruggens kimberlite dykes (excepting sample NC 007, Changehouse Dyke), suggestive of mixing with a component such as continental crust, with lower Hf contents and $^{177}Hf/^{176}Hf$. The broad negative correlation between initial $^{87}Sr/^{86}Sr_i$ and ε_{Hfi} (Figure 6.2c), suggests that the same process has altered both the Sr and Hf isotope compositions of these samples, as will be considered further in Chapter 7, whereas ε_{Ndi} does not show any systematic variation with ε_{Hfi} (Figure 6.2d).

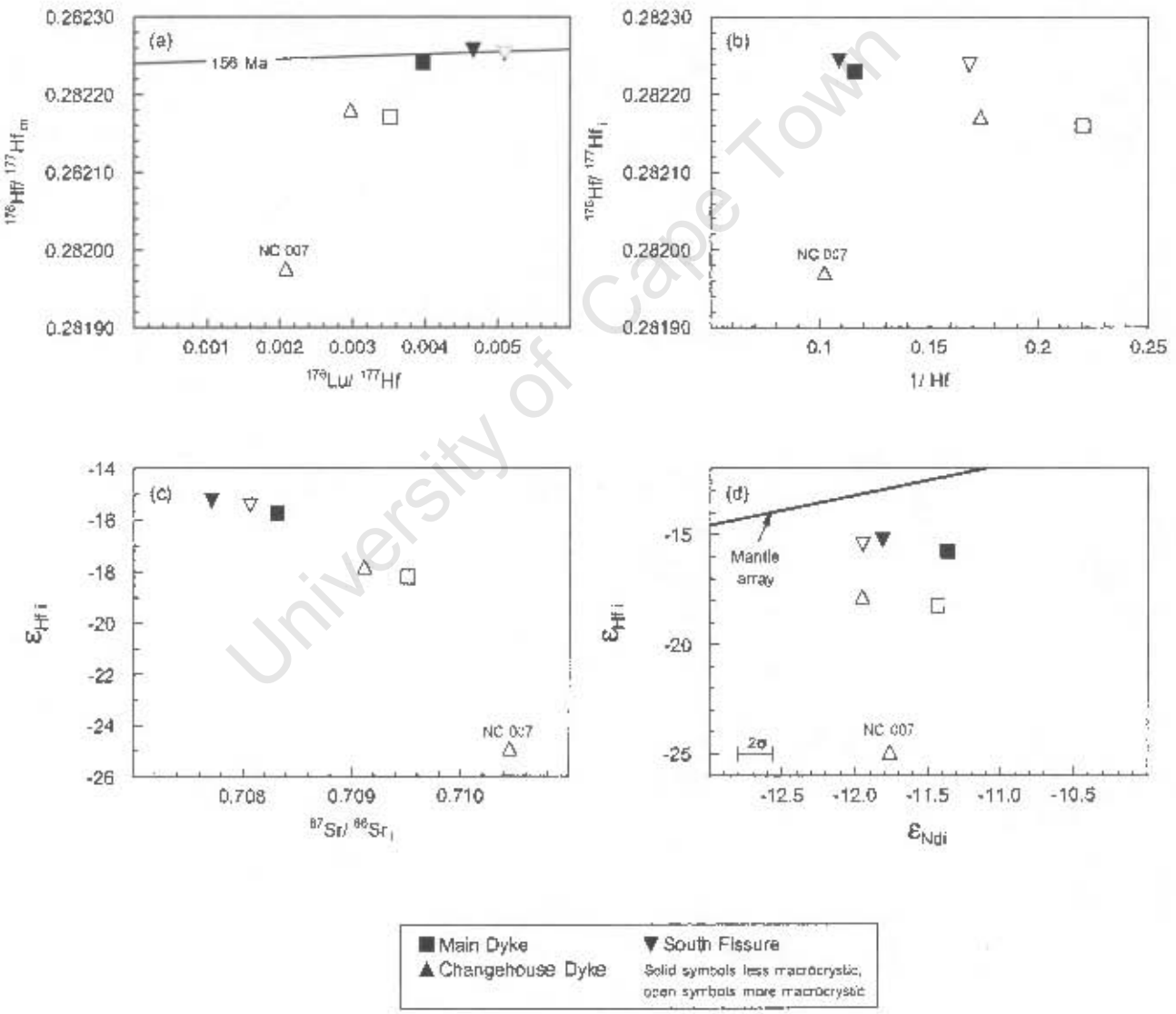

Figure 6.2 Variations in Hf isotope compositions in the Swartruggens kimberlite dykes. 2σ analytical uncertainties for Hf are approximately symbol size, 2σ uncertainties for Sr are smaller than symbol size, typical 2σ uncertainties for Nd shown by error bar. Regression line is a theoretical isochron calculated at 156 Ma. Mantle array shown in (d) from Vervoort *et al.* (1999).

6.3 Isotope geochemistry of the Star kimberlite dykes

Ten kimberlite samples from Star (1 from the Clewer Dyke, 2 from the Wynandsfontein Dyke, 2 from the East Star Dyke, 2 from the Byrnes Dyke and 2 from the Barren Dyke) were analysed for their Sr, Nd, and Hf isotope compositions. The data are reported in Table 6.2, and selected variations are shown in Figures 6.3 and 6.4.

6.2.1 Neodymium and Strontium isotopes

Initial $^{143}Nd/^{144}Nd$ for the Star diamondiferous kimberlites range from 0.511997 ± 18 to 0.512040 ± 10 (Table 6.2). However, the Byrnes Dyke (both macrocrystic and less macrocrystic) and Wynandsfontein Dyke (less

Table 6.2 Whole rock isotope analyses of the Star kimberlite. Initial ratios and ε values calculated assuming an age of 124 Ma (Macintyre and Dawson, 1976). Mic = micaceous Barren Dyke, L. mic = less micaceous Barren Dyke; M = macrocrystic, LM = less macrocrystic. Subscripts: m = measured, i = initial, o = present calculated. Best (smallest uncertainty) analyses are reported, repeat analyses are reported in Appendix 3; 2σ uncertainties include error on standards, standard reproducibility reported in Appendix 3.

Dyke	Clewer Dyke	Wynandsfontein Dyke			East Star Dyke		Byrnes Dyke		Barren Dyke	
									mic	l. mic
Sample	JJG 2833	JJG 6389	NC 050	JJG 6362	JJG 4570	SJH 30	SJH 79	SJH 78	NC 051	NC 054
Macro	M	LM	LM	M	M	LM	LM	M	M	M
Rb	82.4	115	139	137	109	160	178	123	150	96.3
Sr	967	1673	2133	2383	1266	1532	2771	1924	872	724
$^{87}Rb/^{86}Sr$	0.240861	0.193594	0.184049	0.162939	0.243604	0.295670	0.181161	0.181202	0.485361	0.375890
$^{87}Sr/^{86}Sr_m$	0.707792	0.708318	0.707701	0.707773	0.707734	0.708711	0.709043	0.708277	0.708263	0.707846
2σ uncertainty	0.000013	0.000016	0.000014	0.000013	0.000014	0.000013	0.000014	0.000015	0.000014	0.000016
$^{87}Sr/^{86}Sr_i$	0.707367	0.707976	0.707376	0.707485	0.707304	0.708189	0.708724	0.707957	0.707407	0.707183
Sm	11.4	17.0	15.6	-	12.4	16.6	16.1	15.5	12.4	9.25
Nd	107	153	143	-	113	156	150	137	117	87.5
$^{147}Sm/^{144}Nd$	0.064550	0.067319	0.066461	-	0.066508	0.064589	0.065266	0.068574	0.064051	0.064172
$^{143}Nd/^{144}Nd_m$	0.512050	0.512091	0.512094	-	0.512066	0.512091	0.512079	0.512091	0.512125	0.512129
2σ uncertainty	0.000018	0.000009	0.000010	-	0.000022	0.000011	0.000014	0.000009	0.000009	0.000015
$^{143}Nd/^{144}Nd_i$	0.511997	0.512036	0.512040	-	0.512012	0.512038	0.512026	0.512035	0.512073	0.512077
ε_{Nd0}	-11.48	-10.68	-10.62	-	-11.16	-10.68	-10.91	-10.68	-10.01	-9.93
ε_{Ndi}	-9.39	-8.63	-8.56	-	-9.11	-8.59	-8.83	-8.65	-7.92	-7.84
ε2σ uncertainty	0.35	0.17	0.19	-	0.44	0.22	0.26	0.18	0.18	0.29
Lu	0.09	0.08	0.08	-	0.06	0.06	0.13	-	0.07	0.06
Hf	1.19	8.21	6.08	-	5.55	6.46	4.02	-	3.63	2.62
$^{176}Lu/^{177}Hf$	0.010905	0.001469	0.001801	-	0.001575	0.001397	0.004456	-	0.00289	0.003502
$^{176}Hf/^{177}Hf_m$	0.282500	0.282489	0.282484	-	0.282475	0.282488	0.282487	-	0.282570	0.282568
2σ uncertainty	0.000008	0.000005	0.000008	-	0.000005	0.000005	0.000006	-	0.000007	0.000008
$^{176}Hf/^{177}Hf_i$	0.282475	0.282486	0.282480	-	0.282472	0.282485	0.282477	-	0.282564	0.282560
ε_{Hf0}	-9.60	-10.01	-10.17	-	-10.49	-10.04	-10.08	-	-7.13	-7.20
ε_{Hfi}	-7.77	-7.40	-7.59	-	-7.88	-7.43	-7.71	-	-4.63	-4.75
ε2σ uncertainty	0.28	0.17	0.29	-	0.19	0.18	0.22	-	0.24	0.28
$\Delta\varepsilon_{Hfi}$	0.83	0.89	0.61	-	1.04	0.81	0.84	-	2.71	2.48

Decay constants used: Rb-Sr = 1.42 x 10^{-11}; Sm-Nd = 6.54 x 10^{-12}; Lu-Hf = 1.876 x 10^{-11};
CHUR: $^{143}Nd/^{144}Nd$ = 0.512638; $^{147}Sm/^{144}Nd$ = 0.1967; $^{176}Hf/^{177}Hf$ = 0.282772; $^{176}Lu/^{177}Hf$ = 0.0332

macrocrystic) samples, and the less macrocrystic sample (SJH 30) from the East Star Dyke, have Nd isotope compositions that show no variation greater than analytical error ($^{143}Nd/^{144}Nd_i$ = 0.512026 ± 14 to 0.512040 ± 10). These samples define a broad positive correlation which approximates a theoretical 124 Ma reference line (following the K-Ar date obtained for the Star kimberlite by McIntyre and Dawson, 1976) on a Sm-Nd isochron diagram (Figure 6.3a). The macrocrystic sample (JJG 4570) from the East Star Dyke has a slightly lower initial $^{143}Nd/^{144}Nd$ ($^{143}Nd/^{144}Nd_i$ = 0.512012 ± 22), although the analytical error on this sample is relatively large and overlaps the lower end of the range described above for the samples that have similar $^{143}Nd/^{144}Nd_i$. JJG 2833 (from the Clewer Dyke), also macrocrystic, lies outside analytical error of the samples with similar Nd isotopic compositions described above, with the lower $^{143}Nd/^{144}Nd_i$ of 0.511997 ± 18 (Table 6.2). There is no correlation between initial $^{143}Nd/^{144}Nd$ and 1/Nd for the Star kimberlite samples, although the two macrocrystic samples with lower $^{143}Nd/^{144}Nd$ have lower Nd concentrations than those with higher $^{143}Nd/^{144}Nd_i$ (Figure 6.3b), suggesting that their deviation in Nd isotope composition may be due in part to contamination by lithospheric mantle. This aspect will be discussed further in Chapter 7.

The Barren Dyke has a considerably higher initial $^{143}Nd/^{144}Nd$ than the diamondiferous dykes, and there is no variation greater than analytical error between the micaceous and less micaceous samples ($^{143}Nd/^{144}Nd_i$ = 0.512073 ± 9 and 0.512077 ± 15 respectively; Table 6.2), despite their different Nd concentrations (Figure 6.3b).

The diamondiferous Star kimberlite dykes show a wide range in Sr isotope compositions, considerably in excess of analytical uncertainty, with initial $^{87}Sr/^{86}Sr$ varying from 0.707304 ± 14 to 0.708724 ± 14 (Table 6.2). The Byrnes and East Star Dykes show wide within-dyke ranges in $^{87}Sr/^{86}Sr_i$ ($^{87}Sr/^{86}Sr_i$ = 0.707957 ± 15 to 0.708724 ± 14 and 0.707304 ± 14 to 0.708189 ± 13 respectively, Table 6.2) and the less macrocrystic samples from each of these dykes have higher $^{87}Sr/^{86}Sr_i$ than the more macrocrystic samples. There is also a wide range in initial $^{87}Sr/^{86}Sr$ within the Wynandsfontein Dyke ($^{87}Sr/^{86}Sr_i$ = 0.707376 ± 14 to 0.707976 ± 16), which encompasses the Clewer Dyke sample, although the macrocrystic Wynandsfontein Dyke sample lies within the range of the less macrocrystic samples from this dyke. The Barren Dyke shows a smaller, but still greater than analytical error, range in initial $^{87}Sr/^{86}Sr$ than the diamondiferous kimberlite dykes. The micaceous sample (with $^{87}Sr/^{86}Sr$ = 0.707407 ± 14; Table 6.2) has the higher ratio and lies within the range of the diamondiferous kimberlite dykes, whereas the less micaceous sample (with $^{87}Sr/^{86}Sr_i$ = 0.707183 ± 16; Table 6.2), has a lower initial $^{87}Sr/^{86}Sr$ than any of the other kimberlite samples.

On a Rb-Sr isochron diagram, the samples with lowest measured $^{87}Sr/^{86}Sr$ (JJG 2833 from the Clewer Dyke, NC 050 and JJG 6362 from the Wynandsfontein Dyke, JJG 4570 from the East Star Dyke) define a broad positive correlation and cluster around a theoretical 124 Ma isochron (following MacIntyre and Dawson, 1976), whereas a group of samples have higher measured $^{87}Sr/^{86}Sr$ (JJG 6369 from the Wynandsfontein Dyke, SJH 30 from the East Star Dyke and the Byrnes Dyke samples) and deviate significantly from this trend (Figure 6.3c). Although the Barren Dyke samples plot close to the reference line illustrated on Figure 6.3c, they have already been noted to be isotopically distinct from the diamondiferous kimberlite dykes with respect to their Nd isotope composition and should be considered to be unrelated to

the diamondiferous dykes. There is no correlation between $^{87}Sr/^{86}Sr_i$ and 1/Sr for the Star kimberlites (Figure 6.3c), and the samples with lower $^{87}Sr/^{86}Sr$ and showing similar initial ratios display a wide range in Sr concentration (Figure 6.3d). However the samples with elevated $^{87}Sr/^{86}Sr$ all have relatively high Sr contents.

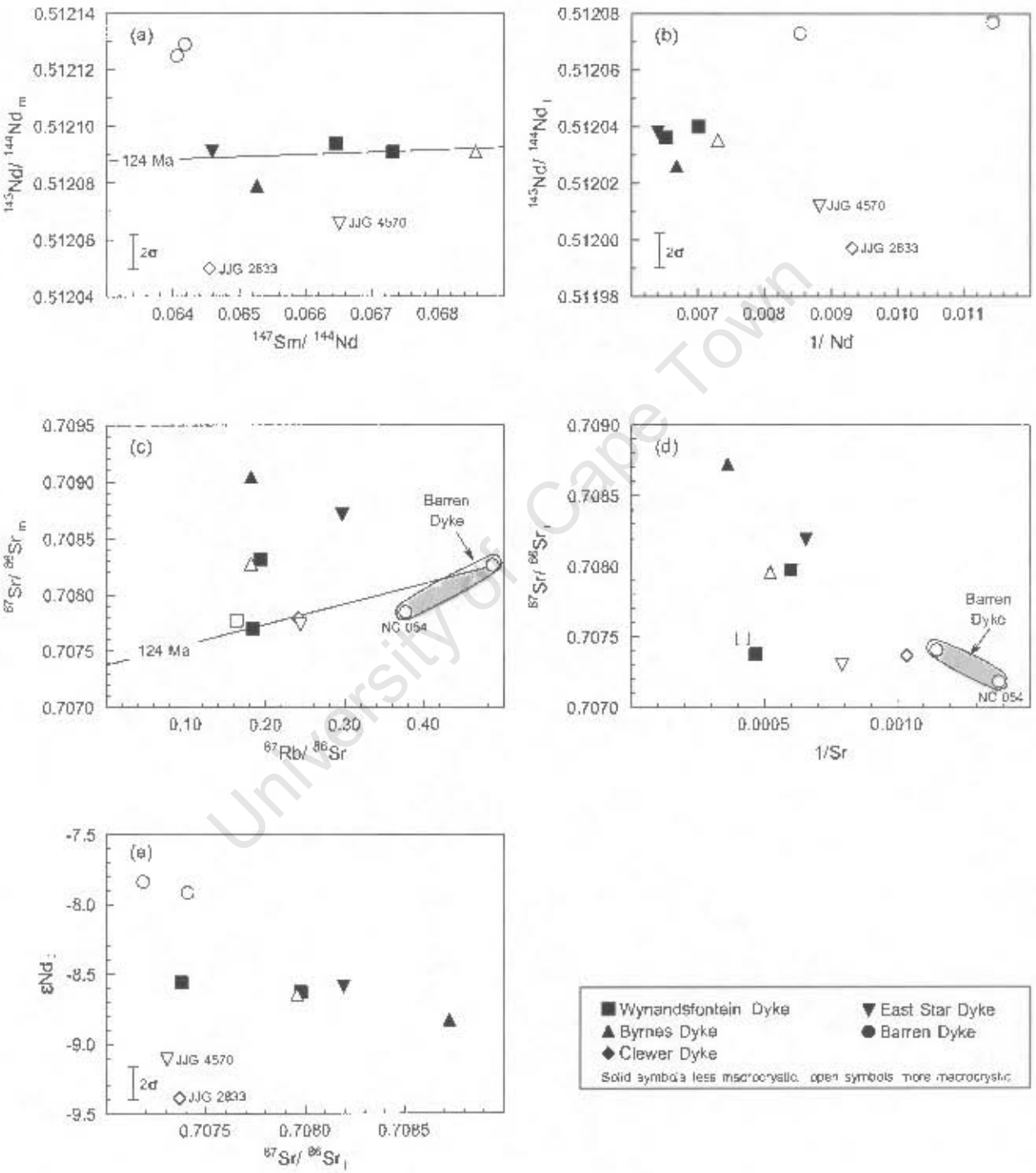

Figure 6.3 Variations in Sr and Nd isotope compositions in the Star kimberlite dykes. Typical Nd analytical 2σ uncertainties shown by error bars, Sr 2σ uncertainties are smaller than symbol size. Regression lines reflect theoretical isochrons calculated at 124 Ma.

There is no apparent correlation between ε_{Nd} and $^{87}Sr/^{86}Sr_i$ for the Star kimberlite dykes (Figure 6.3e). The samples with elevated $^{87}Sr/^{86}Sr_i$ (JJG 6369 from the Wynandsfontein Dyke, SJH 30 from the East Star Dyke and the Byrnes Dyke samples; Table 6.2; Figure 6.3b and c) have similar ε_{Nd}, suggesting that these samples may have been affected by groundwater movement which would affect their Sr, but not disturb their Nd, isotope compositions, as will be discussed further in Chapter 7. The two samples with anomalously low ε_{Nd} (JJG 2833 from the Clewer Dyke and JJG 4570 from the East Star Dyke; Table 6.2, Figure 6.3a and b) have $^{87}Sr/^{86}Sr_i$ within the more restricted range described above. If, as suggested above, the difference in Nd isotope composition of these two samples relative to the other Star diamondiferous dykes is due partly to entrained lithospheric mantle, this process does not appear to have significantly affected their Sr isotope compositions. This aspect will be discussed further in Chapter 7. Despite having significantly higher ε_{Ndi} than the diamondiferous kimberlite dykes, the Star Barren Dyke has $^{87}Sr/^{86}Sr_i$ ratios that overlap those of the diamondiferous dykes.

6.2.2 Hafnium isotopes

The Star diamondiferous kimberlite dykes show very little variation in initial $^{176}Hf/^{177}Hf$, either within or between individual dykes. The Clewer, Byrnes and Wynandsfontein Dyke samples all have compositions within the range of 0.282472 ± 5 to 0.282485 ± 5 defined by the East Star Dyke. The range shown by this dyke is slightly larger than analytical error, and the more macrocrystic sample (JJG 4570) has a lower initial $^{176}Hf/^{177}Hf$ than the less macrocrystic sample. The macrocrystic Clewer Dyke sample (JJG 2833) also has a relatively low $^{176}Hf/^{177}Hf_i$, but the less macrocrystic samples SJH 79 (Byrnes Dyke) and JJG 6369 (Wynandsfontein Dyke) have initial isotopic ratios within analytical error of the macrocrystic samples. On a Lu-Hf isochron diagram, the Star diamondiferous kimberlite dykes show a broad positive correlation, which corresponds well to a theoretical 124 Ma isochron (Figure 6.4a; following MacIntyre and Dawson, 1976). There is no correlation between $^{176}Hf/^{177}Hf_i$ and 1/Hf for the Star diamondiferous kimberlite dykes (Figure 6.4b); the Clewer Dyke has a similar $^{176}Hf/^{177}Hf_i$ despite having a much lower Hf concentration than the East Star, Byrnes and Wynandsfontein dykes.

As with Nd isotopes, the Barren Dyke samples have much higher initial $^{176}Hf/^{177}Hf$ than the other kimberlite dykes at Star ($^{176}Hf/^{177}Hf_i$ = 0.282560 ± 8 to 0.282564 ± 7; Table 6.2) and the variation between the micaceous and less micaceous samples is within analytical error. This dyke does not lie on the well-defined correlation of the other Star kimberlites on a Lu-Hf isochron diagram (Figure 6.4a), and, despite its considerably higher initial isotopic ratio, has absolute Hf concentrations within the range of these dykes (Figure 6.4b).

There is no obvious correlation between ε_{Hfi} and $^{87}Sr/^{86}Sr_i$ for the Star diamondiferous kimberlite dykes, which show a wide range in $^{87}Sr/^{86}Sr_i$ for little change in ε_{Hfi} (Figure 6.4c). However there is a weak positive correlation for these kimberlites between ε_{Hfi} and ε_{Ndi}, with the macrocrystic samples JJG 2833, JJG 4570, which have the lowest ε_{Ndi}, also having low ε_{Hfi} (Figure 6.4d). Although they do not greatly differ from the other Star kimberlites with respect to initial $^{87}Sr/^{86}Sr$, the Barren Dyke samples have much higher initial ε_{Hf}

and ε_{Nd} than the diamondiferous kimberlite dykes and, as discussed further in Chapter 7, are clearly derived from a source with an isotopically distinct composition.

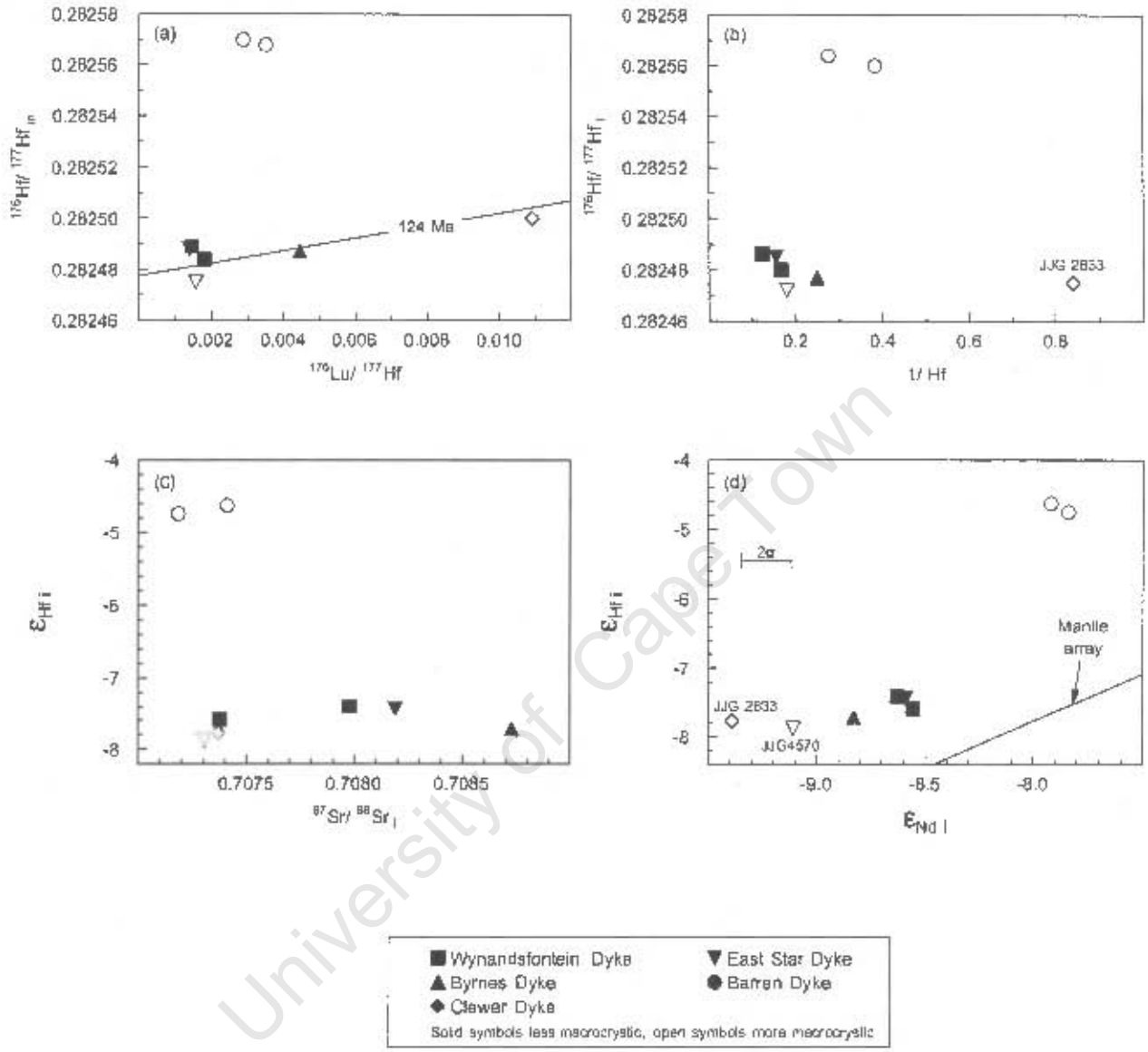

Figure 6.4 Variations in Hf isotope composition in the Star kimberlite dykes. Analytical 2σ uncertainties for Hf are approximately symbol size, 2σ uncertainties for Sr are smaller than symbol size, typical 2σ uncertainties for Nd shown by error bar. Regression line reflects a theoretical isochron calculated at 124 Ma. Mantle array shown in (d) from Vervoort *et al.* (1999).

6.4 Comparison in isotope geochemistry between Swartruggens, Star and other South African kimberlites

Figure 6.5a illustrates the variation of initial ε_{Nd} with $^{87}Sr/^{86}Sr_i$ in the Swartruggens and Star kimberlites, with fields of mid-ocean ridge basalts (MORB), ocean island basalts (OIB) and southern African Group I and Group II kimberlites. It is clear that both the Swartruggens and Star kimberlites fall largely within the field for

other Group II kimberlites, with the Star kimberlites having higher initial ε_{Nd} (ε_{Ndi} = -9.39 ± 0.35 to –7.84 + 0.29; Table 6.2) than the Swartruggens kimberlites (ε_{Ndi} = -11.95 ± 0.34 to -11.37 ± 0.36; Table 6.1). Despite rather restricted initial Nd isotope ratios, both the Swartruggens and Star kimberlites show a wide range in initial Sr isotope ratios (Swartruggens $^{87}Sr/^{86}Sr_i$ = 0.707711 ± 14 to 0.710447 ± 15; Star $^{87}Sr/^{86}Sr_i$ 0.707183 + 16 to 0.708724 ± 14; Tables 6.1 and 6.2) and a number of the Swartruggens samples plot outside the field of Group II kimberlites towards higher initial $^{87}Sr/^{86}Sr$ at lower initial ε_{Nd}.

The Swartruggens and Star kimberlites define sub-parallel, sub-horizontal trends on a plot of ε_{Hfi} versus $^{87}Sr/^{86}Sr_i$, with widely varying $^{87}Sr/^{86}Sr_i$ for little change in ε_{Hfi}, which, with the exception of the high $^{87}Sr/^{86}Sr_i$ Swartruggens samples, lie within the field of other South African Group II kimberlites (Figure 6.5b). The Swartruggens kimberlites (with initial ε_{Hf} = -24.92 + 0.15 to -15.24 ± 0.15; Table 6.1) have lower ε_{Hfi} than the Star kimberlites (with initial ε_{Hf} = -7.8 ± 0.19 to –4.63 ± 0.24; Table 6.2), which also overlap the range in ε_{Hf} of Group I kimberlites.

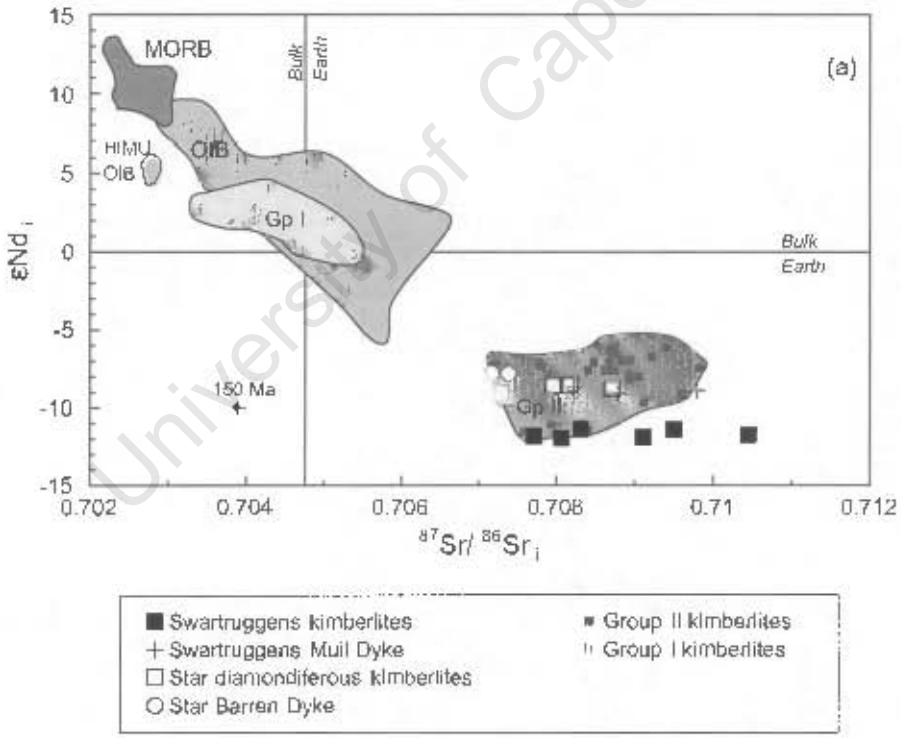

Figure 6.5 Variations in isotopic composition in the Swartruggens and Star kimberlites compared to other South African Group I and Group II kimberlites and other derived mantle rocks. Initial ratios and ε values are calculated assuming ages of 156 Ma for Swartruggens (Smith *et al.*, 1985a), and 124 Ma for Star (MacIntyre and Dawson, 1976). MORB and OIB fields are present day, but the small change in Sr isotopic composition over 150 Ma is illustrated by the vectors for evolution of primitive mantle shown on (a) and (b). The change in Hf and Nd isotopic compositions over 150Ma is too small to be seen. Mantle array shown in (c) from Vervoort *et al.* (1999). Data for MORB and OIB fields from Patchett and Tatsumoto (1980), Patchett (1983), Stille *et al.* (1986), Salters and Hart (1991), Chauval *et al.* (1992), Salters (1996), Salters and White (1998), Nowell *et al.* (1998). Data for Group I and Group II kimberlite fields from Smith (1983a and b), Talnton (1994), Clark (1994), Nowell *et al.* (1999 and 2004).

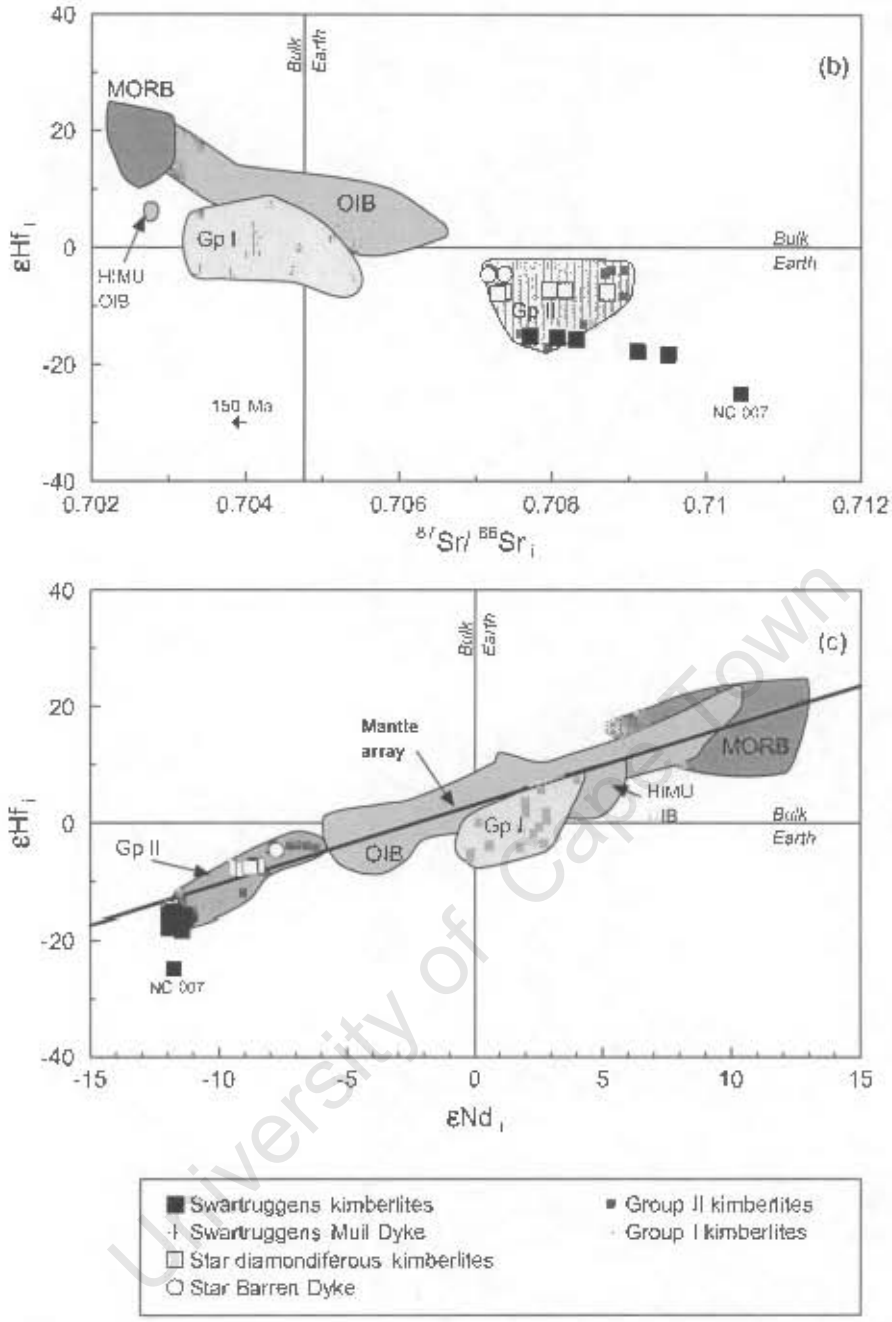

Figure 6.5 Continued.

The variation of ε_{Hf} with ε_{Ndi} for the Swartruggens and Star kimberlites is shown in Figure 6.5c. The Star kimberlites plot within the field of Group II kimberlites, whereas some of the Swartruggens samples trend to slightly lower ε_{Hfi} and ε_{Ndi} compositions than other Group II kimberlites. Group II kimberlites typically plot close to the mantle array defined by MORB and OIB, where $\varepsilon_{Hf} = 1.33\varepsilon_{Nd} + 3.19$ (Vervoort *et al.*, 1999; Nowell *et al.*, 1999); the Star kimberlites plot slightly above this array (with $\Delta\varepsilon_{Hf} = +0.61$ to $+2.71$; Table 6.2) and the Swartruggens kimberlites plot below it (with $\Delta\varepsilon_{Hf} = -12.47$ to -2.72; Table 6.1). Group I kimberlites overlap the OIB field, slightly below the mantle array, with higher ε_{Ndi} and slightly higher ε_{Hfi} than Group II kimberlites.

Chapter 7

Petrogenesis

7.1 Introduction

Kimberlite-like magmas have been produced, by some experimental workers, by small degrees of partial melting of a carbonated garnet lherzolite (e.g. Dalton and Presnall, 1998). The Sr, Nd and Pb isotope systematics of both Group I and Group II kimberlites have been well studied (e.g. Smith, 1983a; Fraser and Hawkesworth, 1992) and the more enriched isotopic ratios of Group II kimberlites have been inferred to reflect their source in the lithospheric mantle, whereas the less radiogenic isotopic ratios of Group I kimberlites have been inferred to reflect their source in the convecting asthenosphere (Smith, 1983a). However, this hypothesis is not undisputed, and le Roex (1986) proposed that the Sr and Nd isotope systematics, combined with the incompatible trace element ratios, of both Group I and Group II kimberlites do not preclude a plume-related origin for both groups in the sub-lithospheric mantle if Group II kimberlites are associated with a plume containing significant recycled lithospheric material. In addition, the negative $\Delta\varepsilon_{Hf}$ signature of Group I kimberlites, and the continuum of Hf isotope compositions between Group I and Group II kimberlites, has been proposed to reflect that the source regions of both kimberlites lie within the sub-lithospheric mantle, with a contribution from a subducted slab component (Nowell *et al.*, 1999, 2003; Dowall *et al.*, 2003a). The most radiogenic Os isotope compositions of both Group I and Group II kimberlites are similar to those of ocean island basalts (Pearson *et al.*, 1995, 2003a), lending further support for an origin of both groups within the convecting asthenosphere.

Due, in part, to the complications caused by post-melting processes, such as lherzolite entrainment, crustal contamination, alteration and crystal fractionation, in ascertaining the nature of primary kimberlite magmas (e.g. Mitchell, 1995), few attempts have been made to quantitatively model the trace element signature of kimberlite source regions. To date only one major study, that of Tainton and McKenzie (1994), has attempted to characterise the source region trace element concentrations of Group II kimberlites. Tainton and McKenzie (1994) constructed a detailed model of trace element behaviour during Group II kimberlite genesis, and calculated a source composition that is strongly enriched in the more incompatible trace elements but depleted in the heavy REE relative to primitive mantle, for the Newlands, Sover-North, Sover-Doornkloof, Bellsbank and Finsch Group II kimberlites. They concluded that such a composition requires a source which had undergone a depletion event, followed by metasomatism, and that the depleted signature of the heavy REE constrains the source of Group II kimberlites to the lithosphere, in agreement with the hypothesis of Smith (1983a) but apparently in conflict with the recent Hf and Os isotope studies of kimberlites (Nowell *et al.*, 1999, 2004; Pearson *et al.*, 1995, 2003a; Dowall *et al.*, 2003a). On the basis of

combined major and trace element and Sr, Nd and Pb isotope data, Fraser and Hawkesworth (1992) reached a similar conclusion to Tainton and McKenzie (1994) for the origin of the Finsch Group II kimberlite, although their hypothesis was based primarily on isotopic constraints, following Smith (1983a). Two recent studies, by le Roex *et al.* (2003) and Harris *et al.* (2004), have attempted to quantify the source region trace element characteristics of Group I kimberlites (from the Kimberley group, and the Uintjiesberg off-craton kimberlite respectively). Based on detailed trace element modelling, both studies illustrated that the source regions of these Group I kimberlites exhibit similar, depleted heavy REE signatures relative to primitive mantle and thus, following the argument of Tainton and McKenzie (1994) described above, may also be located within the lithospheric mantle. However, these authors argued that the source regions of the respective kimberlites have an overprint of strong metasomatism by plume related fluids or melts, and thus this hypothesis is not in conflict with those based on isotopic constraints described above.

Kimberlites are permeable and thus highly susceptible to alteration by percolating groundwater (e.g. Berg, 1994). In addition, due to their rapid ascent, they commonly entrain and partially assimilate mantle and crustal material to variable degrees (e.g. Clement, 1982). These three processes, together with fractional crystallisation, may substantially alter the geochemical composition of the primary kimberlite magma (e.g. Mitchell, 1995). In Section 7.2, the effects of each of these processes on kimberlite geochemistry is considered in detail and applied to the suites of samples from Swartruggens and Star with the intent of isolating close-to-primary kimberlite magma compositions at each locality. Simple partial melting modelling of these close-to-primary kimberlite magmas is then used to place constraints on the trace element geochemistry of the respective source regions. The effects of variables such as the degree of partial melting, the residual source mineralogy and the role played by residual accessory phases are considered in Section 7.4. Evaluation of the trace element signatures of the source regions of the Swartruggens and Star kimberlites, together with their Sr and Nd, and Hf isotope compositions provides, for each locality, a wider perspective than any previous study of the whole-rock geochemistry of a single kimberlite, from which evidence for the contributions made by lithospheric versus asthenospheric mantle can be drawn. This aspect is discussed in Section 7.7.

The principal aims of this chapter are summarised as follows:

1) To assess the effects of late-stage processes such as alteration, crustal assimilation, lherzolite entrainment and crystal fractionation on the major element, trace element and isotopic composition of the Swartruggens and Star kimberlites.
2) To isolate these effects and thus establish the compositions of the close-to-primary kimberlite magma(s) and the origin of geochemical variations between and within the individual dykes at each locality.
3) To use the close-to-primary kimberlite magma compositions to constrain the respective source region geochemistry, mineralogy and location (lithosphere vs. asthenosphere) of the Swartruggens and Star kimberlites.
4) To evaluate the petrogenetic processes giving rise to the Swartruggens Mull lamprophyric dyke and its relationship to the kimberlite dykes.

7.2 Modification of primary kimberlite magmas

7.2.1 Alteration

Petrographically it is evident that some of the samples from both the Swartruggens and Star kimberlites have been affected by low temperature alteration: olivine is commonly altered partially or wholly to serpentine, and sometimes replaced by calcite; in more altered samples phlogopite is altered to chlorite; thin veins of secondary calcite cut through some samples. In identifying the igneous processes that have affected the primary magma compositions of the Swartruggens and Star kimberlites, it is therefore important to consider the effect such alteration may have had on the geochemical composition of the samples studied.

Late-stage, low temperature alteration of kimberlites occurs in two ways:
1 – the high volatile content of kimberlite magmas concentrates into residual fluids during solidification, resulting in pervasive deuteric alteration (le Roex *et al.*, 2003) or "autometasomatic serpentinisation" (Berg and Allsopp, 1972; Berg, 1994) and
2 – post-solidification permeation of groundwater through the kimberlite (e.g. Berg and Allsopp, 1972).

An important consequence of process (1) above is that, in a closed system, the alteration reactions are essentially isochemical and thus extensive serpentinisation of primary minerals, and redistribution of the fluid-mobile elements, may occur without changing the bulk rock composition. For example, Price *et al.* (2000) reported samples from the Jericho kimberlite in Canada with serpentinised groundmass olivine, although O isotope data preclude the involvement of meteoric fluids. In reality, however, some of the primary volatile content of kimberlite magmas is believed to be lost, and thus some of the more fluid mobile elements may be leached, during emplacement. The permeable and porous nature of kimberlites makes them highly susceptible to the percolation of considerable quantities of groundwater (e.g. Berg, 1994). The effect of groundwater movement on the geochemistry of the kimberlites will be similar to that of the loss of magmatic water in leaching mobile elements, but in addition may elevate in the kimberlites the concentrations of mobile elements that are present in high abundance in the host rocks or groundwater.

The alteration of olivine to serpentine by a reaction such as the following:

$$2Mg_2SiO_4 + 3H_2O = Mg_3Si_2O_5(OH)_4 + Mg(OH)_2$$
$$\text{olivine} + \text{water} = \text{serpentine} + \text{brucite}$$

releases Mg, some of which may be leached from the kimberlites (e.g. Clement, 1982). The surrounding shales at Swartruggens and Star are MgO poor (Appendix 4), and so mobility of MgO will result in a net loss from the kimberlites. The abundance of Fe oxides within and around relic olivine macrocrysts suggest that at least some of the Fe released during breakdown of olivine has been retained. Analysis of the country rocks indicate that they contain Fe in similar abundances to the kimberlites (Appendix 4), and thus, even though the Fe concentrations in the kimberlites may be disturbed, the individual kimberlite samples are unlikely to have consistently gained or lost significant Fe. Despite the typically fluid-mobile behaviour of K, as a

stoichiometric component of phlogopite it will be stabilised to some extent by the abundant phlogopite present in both the Swartruggens and Star kimberlites. However, where phlogopite has been altered extensively to chlorite (such as in the Swartruggens Third Lease samples, Appendix 1), K may be more susceptible to leaching. Al_2O_3 and SiO_2 are immobile, but may become enriched in the kimberlites either directly, or relatively as a result of leaching of more mobile elements such as Mg and K (Clement, 1982). Due to the alteration of olivine to serpentine, and chloritisation of phlogopite, samples that have interacted more extensively with groundwater may have elevated LOI. Some authors have used high LOI as an indicator of alteration (e.g. Sweeney and Winter, 1999), although care should be taken with this approach as primary kimberlite magmas are expected to have high volatile contents, which may be lost to variable extents during emplacement (e.g. Dawson, 1980).

The concentrations of the immobile trace elements such as the HFS elements and REE are not susceptible to alteration, whereas the abundances of the more mobile LIL elements may be disturbed. In particular Ba, which is present in high concentrations in the crust (Rudnick and Fountain, 1995), may become elevated in more altered kimberlites by percolating groundwater. This effect is difficult to distinguish from that of assimilation of crustal material discussed in more detain in section 7.2.2.

The Nd and Hf isotope compositions of the kimberlites will remain undisturbed by alteration, as Sm, Nd, Lu and Hf are immobile elements in the weathering environment. However, Sr-bearing groundwater may have a considerable effect on the $^{87}Sr/^{86}Sr$ composition of the kimberlites (e.g. Kramers *et al.*, 1981; Smith, 1983b).

7.2.1.1 The effect of alteration on the Swartruggens kimberlite dykes

All the Swartruggens samples have suffered alteration of the primary minerals to some extent, as described in Chapter 3. The geochemical effect of this alteration is illustrated in Figure 7.1. The majority of the Swartruggens kimberlite samples have MgO/SiO_2 greater than 0.54, and show a limited range of variation both in MgO/SiO_2 and K_2O, which can readily be explained by small degrees of lherzolite entrainment, fractionation of olivine and phlogopite, and possibly assimilation of minor amounts of crust (Figure 7.1a). However, the Third Lease samples, 2 samples from the South Fissure (JJG 3145 and JJG 3150), and 3 samples from the Changehouse Dyke (NC 007, NC 009 and Sr 7) have lower MgO/SiO_2 ratios, and cover a range in MgO/SiO_2 that cannot readily be explained by reasonable amounts of assimilation or fractionation. This range is consistent with some MgO having been leached from the samples due to weathering or groundwater movement, and those samples with lowered MgO/SiO_2 ratios are also depleted in K_2O relative to the least altered samples. Even if the individual dykes forming the Swartruggens kimberlite were formed from separate magmas with different MgO/SiO_2, the observed within-dyke range is too large to be accounted for by any other likely process. The Third Lease samples NC 001 and NC 003 have suffered the most depletion in MgO and K_2O, and this is consistent with the observation that these samples are the most altered petrographically (Appendix 1). The altered samples do not show a consistent trend of increasing LOI with decreasing MgO/SiO_2 (Figure 7.1b). However, it is noteworthy that those samples that are the most altered all have elevated LOI relative to the less altered samples.

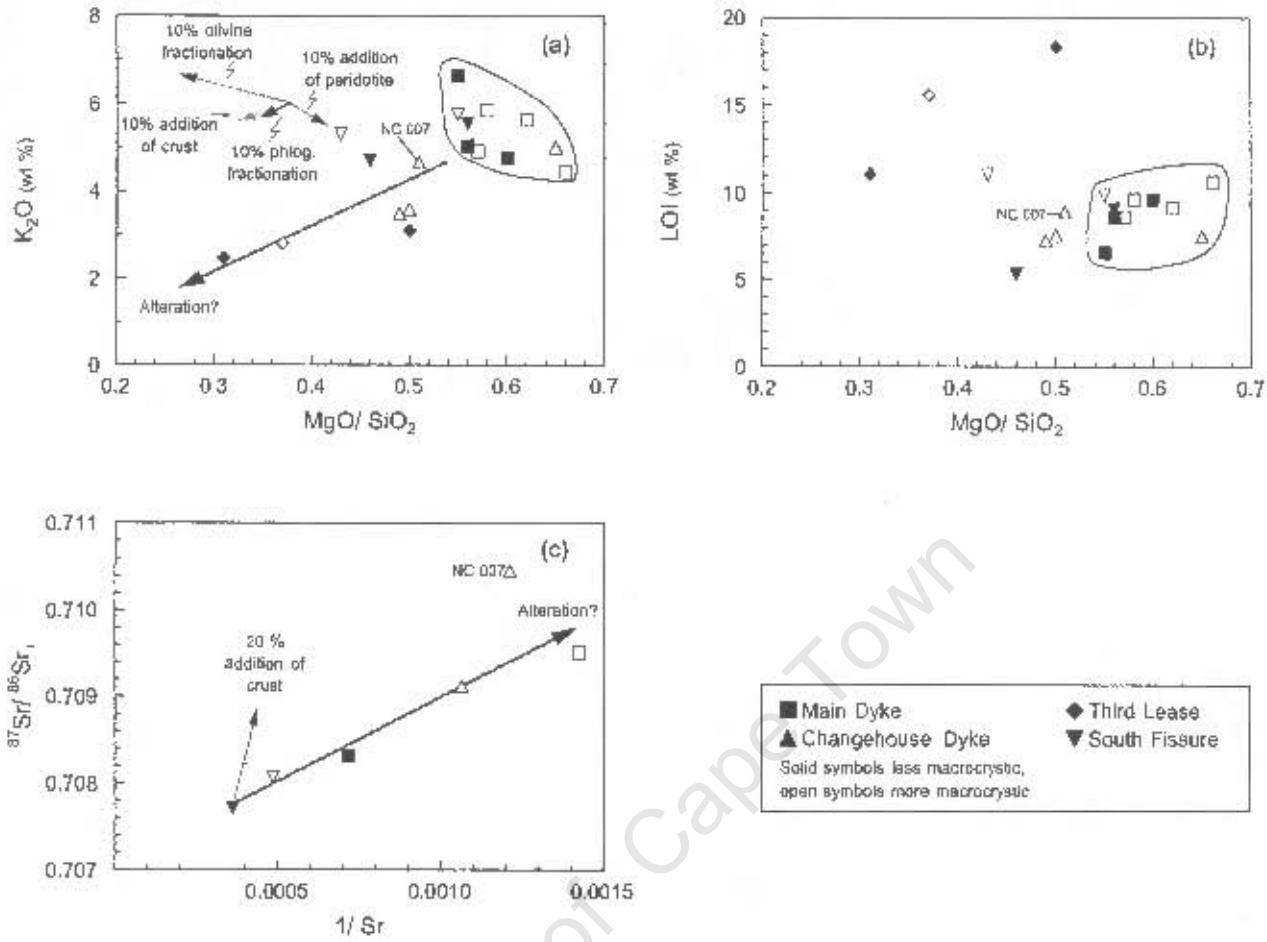

Figure 7.1 The effect of alteration on the K_2O and LOI concentrations relative to MgO/SiO_2, and Sr isotope compositions of the Swartruggens kimberlite dykes. Major element data for typical crust from Rudnick and Fountain (1995); mixing parameters for Sr isotope composition of the crust are given in Table 7.1, after Smith (1983b) and references therein.

The LIL elements are variable in abundance in the Swartruggens kimberlites (Figure 5.4), although there is a well-defined positive correlation between K and Rb, indicating their strong geochemical similarity (Figure 5.4a). The fluid mobility of Ba is reflected in the variable abundance of late-stage barite in the groundmass of some samples (Mitchell, 1995). However, the concentrations of the LIL elements in the Swartruggens kimberlites are high, and although absolute abundances of these elements should be treated with caution in evaluating petrogenetic processes, they may still yield valuable information.

It was noted in Chapter 6 that the Sr isotope compositions of the Swartruggens samples define a positive correlation between $^{87}Sr/^{86}Sr_i$ and 1/Sr, indicative of mixing with a component containing less abundant Sr, with higher $^{87}Sr/^{86}Sr$, than the kimberlite samples. Using the parameters of Smith (1983b), given in Table 7.1, the effect of addition of up to 20% crust is illustrated in Figure 7.1c. This clearly does not account for all the variation in initial $^{87}Sr/^{86}Sr$ even within individual dykes and addition of crust of this composition (300 ppm Sr, $^{87}Sr/^{86}Sr$ = 0.75; Smith, 1983b; Table 7.1) also does not account for the observed variation in absolute Sr concentration within individual dykes. Thus the samples with elevated Sr isotope compositions

are believed to have suffered some interaction with groundwater. However, the broad negative correlation of $^{87}Sr/^{86}Sr_i$ with $^{176}Hf/^{177}Hf_i$ is suggestive that contamination by crust has played some role in creating the observed isotopic variation in the Swartruggens kimberlites, as will be discussed further in Section 7.2.3. Of the samples with most strongly elevated $^{87}Sr/^{86}Sr$ ratios (NC 005 and NC 007 from the Changehouse Dyke, and NC 010 from the Main Dyke), only sample NC 007 appears to have disturbed major element abundances (Figure 7.1a and b).

7.2.1.2 The effects of alteration on the Star kimberlite dykes

Although fresh olivine remains in several of the Star samples, all the samples have been affected to some extent by low temperature alteration as discussed in Chapter 3. The geochemical effect of this alteration is illustrated in Figure 7.2. The majority of aphanitic kimberlite samples from Star have MgO/SiO_2 between approximately 0.5 and 0.8, and show variation in both MgO/SiO_2 and K_2O consistent with small degrees of fractionation of olivine and phlogopite and addition of lherzolite, with possible small amounts of addition of crust (Figure 7.2a). To the high MgO side of this group, the more macrocrystic samples form a trend of increasing MgO/SiO_2 with decreasing K_2O content consistent with entrainment of more substantial quantities of lherzolite, as will be discussed further in section 7.2.4. To the low MgO side of the diagram, a subset of samples (JJG 6361A, SJH 37, JJG 6361C, and JJG 6369 from the Wynandsfontein Dyke; SJH 78 from the Byrnes Dyke) form a trend of decreasing MgO/SiO_2 with decreasing K_2O content. Although a portion of this trend could be attributed to assimilation of small amounts of crust, or small degrees of phlogopite fractionation, these processes cannot account for the entire range in compositions. These samples are therefore interpreted to have suffered leaching of both MgO and K_2O. The Barren Dyke samples also fall on this trend, although, as discussed in earlier chapters, they appear to be geochemically distinct from the other kimberlites at Star (e.g. for Nd and Hf isotopes; Table 6.2) and they should be considered separately. The Barren Dyke samples show no consistent within-dyke trend of alteration.

The most altered Star kimberlite samples all contain high LOI (>15 wt %; Figure 7.2b). However, other samples, such as the aphanitic Byrnes Dyke samples which are considered less altered, also contain high LOI, indicating that high volatile content in kimberlites is not necessarily indicative of highly altered samples.

The LIL elements are variable in abundance in the Star kimberlites, suggesting some redistribution due to the movement of late-stage fluids through the rock. However, they are generally present in high concentrations (Table 5.2) and thus, although their absolute concentrations should be treated with caution in evaluating the petrogenesis of the Star kimberlites, they may still yield valuable information.

As mentioned in Chapter 6, a number of samples from Star (JJG 6369 from the Wynandsfontein Dyke, SJH 30 from the East Star Dyke, and SJH 79 and SJH 78 from the Byrnes Dyke) have elevated initial $^{87}Sr/^{86}Sr$ ratios, compared the to rest of the samples, yet show no variation in Nd or Hf isotope composition. These high $^{87}Sr/^{86}Sr$ samples all have relatively high Sr contents and, with the exception of sample SJH 79 (Byrnes Dyke) form a trend away from the lower $^{87}Sr/^{86}Sr$ samples with high Sr contents towards higher $^{87}Sr/^{86}Sr$ and

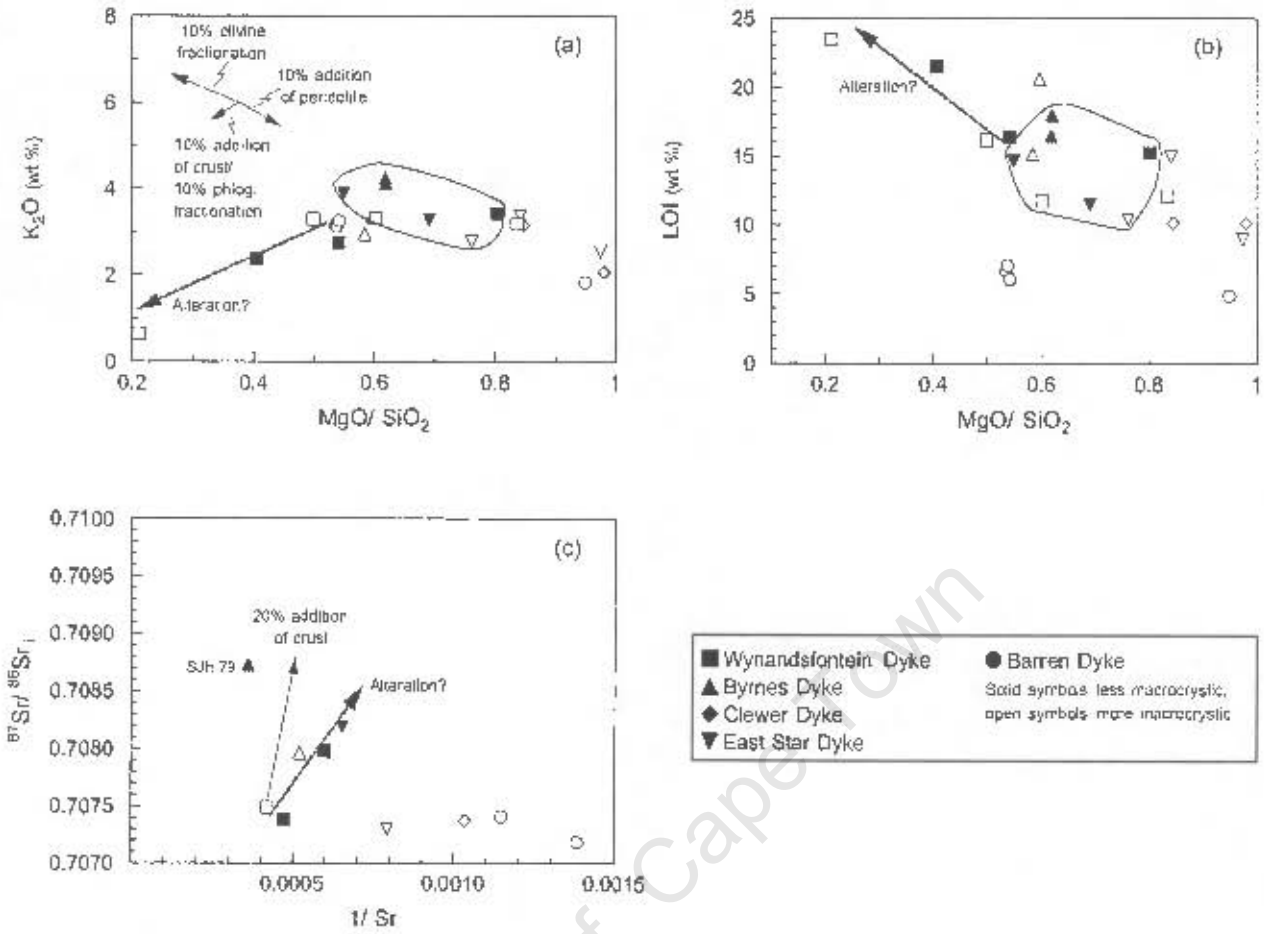

Figure 7.2 The effect of alteration on the K_2O and LOI concentrations relative to MgO/SiO_2, and Sr isotope compositions of the Star kimberlite dykes. Major element data for typical crust from Rudnick and Fountain (1995); mixing parameters for Sr isotope composition of the crust are given in Table 7.1, after Smith (1983b) and references therein.

lower Sr concentrations (Figure 7.2c). Using the mixing parameters of Smith (1983b), given in Table 7.1, the change in Sr abundance in these samples is somewhat too large to be accounted for merely by crustal assimilation (Figure 7.2c) and is better explained by alteration, although of these samples only SJH 78 (Byrnes Dyke) appears to have disturbed major element abundances (Figure 7.2a). In addition, as discussed in Section 7.2.2, the Hf and Nd isotope compositions of these samples do not appear to be affected by crustal contamination. However, absolute Sr abundances, and isotope ratios, are highly variable in the crust (e.g. Barton, 1999), and thus it cannot be concluded that the higher $^{87}Sr/^{86}Sr$ samples have not been contaminated by crust with a lower Sr concentration and higher $^{87}Sr/^{86}Sr$ than given in Table 7.1.

7.2.2 Crustal contamination

Average crustal material is typically enriched in SiO_2, Al_2O_3 and Na_2O, and less enriched in MgO and K relative to kimberlite magmas. On this basis, Clement (1982) proposed the following contamination index (C. I.) for identifying samples that have suffered extensive alteration and crustal assimilation:

$$C.I. = \frac{SiO_2 + Al_2O_3 + Na_2O}{MgO + 2K_2O}$$

Clement (1982) noted that apparently uncontaminated Group II kimberlites have contamination indices up to 1.5. Since low temperature alteration may cause the loss of MgO and K_2O from the kimberlites and relative enrichment of SiO_2 and Al_2O_3, and the index does not distinguish between the two processes. Crustally contaminated kimberlite magmas also commonly have raised abundances of the heavy REE (le Roex *et al.*, 2003), and consequently lower Gd/Yb than uncontaminated kimberlites. le Roex *et al.* (2003) discarded Group I kimberlite samples with large positive Pb anomalies on the basis of crustal contamination, although this approach may not be valid for Group II kimberlites as positive Pb anomalies appear to be ubiquitous and Pb concentrations in the crust (e.g. Rudnick and Fountain, 1995) are similar to, or lower than, those of Group II kimberlites (this study; le Roex, unpublished; Coetzee, unpublished; Fraser and Hawkesworth, 1992; Tainton and McKenzie, 1994).

Assimilation of crust may alter the isotopic ratios of the kimberlites as both $^{143}Nd/^{144}Nd$ and $^{176}Hf/^{177}Hf$ are lower (e.g. Smith, 1983b and references therein; Vervoort and Patchett, 1996), whereas $^{87}Sr/^{86}Sr$ can be considerably higher (Barton, 1999; Smith, 1983b and references therein), in the crust than in kimberlite magmas. Although all these ratios are highly variable in the crust, typical values have been used to illustrate the effects of crustal assimilation on the isotopic compositions of the Swartruggens kimberlites, and are given in Table 7.1. For Sr, these parameters are similar to values reported for crust in the region (Smith, 1983b and references therein; Barton et al., 1999). Hf isotope data for crust in the region do not exist and thus, for illustrative purposes, and average value for Archaean crust has been used (Vervoort and Patchett, 1996).

Table 7.1 Parameters used in crustal assimilation models. Sr parameters after Smith (1983b) and references therein; Hf parameters from Vervoort and Patchett (1996).

	Crust
Sr (ppm)	300
$^{87}Sr/^{86}Sr$	0.75
Hf (ppm)	5
$^{176}Hf/^{177}Hf$	0.2815

7.2.2.1 The effect of crustal assimilation on the Swartruggens kimberlite dykes

Samples NC 001, NC 002, NC 003 (Third Lease), NC 007, NC 009, SR 7 (Changehouse Dyke), JJG 3145, JJG 3150 (South Fissure) have contamination indices of 1.5 or greater (Table 4.1), and all these samples have already been noted to have been affected by alteration (as mentioned in section 7.2.1). However, sample JJG 3150 (South Fissure; Figure 7.3) also shows raised heavy REE abundances and a low Gd/Yb., and may, in addition, be crustally contaminated. Raised heavy REE abundances are also a feature of NC 004 (Main Dyke), despite the lower C.I. of this sample. There is no consistent trend of increasing SiO_2 content with decreasing Gd/Yb_n ratio within the Swartruggens kimberlite dykes. However, this effect may be masked to some extent by lherzolite entrainment or fractional crystallisation (Sections 7.2.3 and 7.2.4). Given the high Zr and Hf concentrations in the continental crust (Zr ~ 100-200ppm; Hf ~ 5ppm; Rudnick and

Fountain, 1995) the positive Zr-Hf anomalies shown by three of the samples with high contamination indices (JJG 3150 from the South Fissure, NC 007 and SR 7 from the Changehouse Dyke), compared to the negative Zr-Hf of uncontaminated samples (e.g. Figure 7.3, Figure 5.5), may also be a feature of crustal contamination. Samples showing any of these features are excluded from further discussion of the petrogenesis of the Swartruggens kimberlite dykes. Nine of the nineteen Swartruggens kimberlite samples are therefore discarded on the basis of crustal contamination/alteration. As discussed in Chapter 5, sample NC 010 (Main Dyke) shows several features on a primitive mantle normalised diagram that are anomalous for the Swartruggens kimberlites (strong negative U and P anomalies; depletion in the heavy REE), and although these features are not readily attributable to crustal contamination, this sample is not believed to be representative of the Swartruggens kimberlite geochemistry and its major and trace element geochemistry are not discussed further.

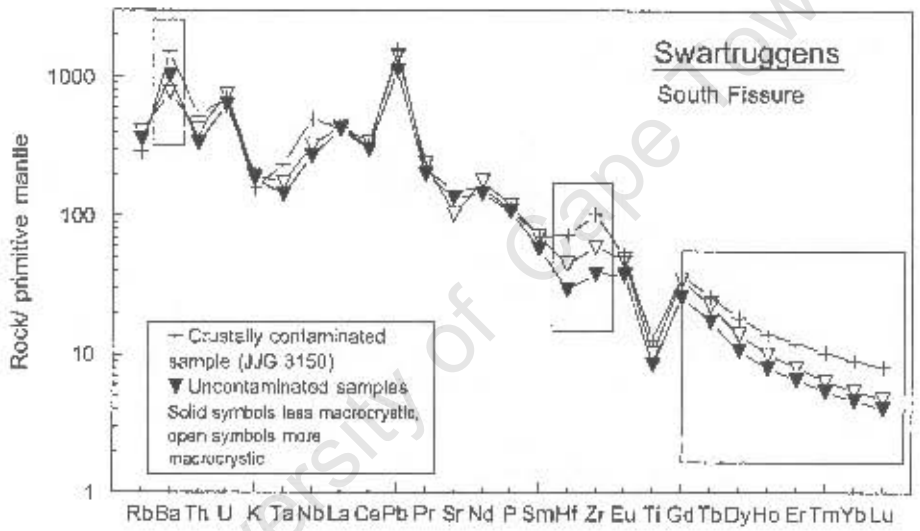

Figure 7.3 Primitive mantle normalised incompatible element patterns for the South Fissure samples (excluding excessively weathered sample JJG 3145), Swartruggens, illustrating the effects of crustal assimilation in terms of raised heavy REE and Zr and Hf abundances. Primitive mantle values from Sun and McDonough (1989).

It was mentioned in section 7.2.1.1, and illustrated in Figure 7.1c, that although some of the range in Sr isotope compositions of the Swartruggens kimberlite samples may be accounted for by alteration, some of the variation present may also be due to contamination by crust. This is supported by the broad negative correlation between the initial Sr and Hf isotope ratios in the Swartruggens kimberlites (Figure 7.4), with samples NC 005, NC 007 (Changehouse Dyke) and NC 010 (Main Dyke) having significantly lower initial $^{178}Hf/^{177}Hf$, combined with higher initial $^{87}Sr/^{86}Sr$, than the other three Swartruggens samples. A mixing curve illustrating the effect of assimilation of crust, using the parameters given in Table 7.1, is illustrated in Figure 7.4, and it is clear that the variation in Sr and Hf isotope composition of samples NC 007, NC 005

(Changehouse Dyke) and NC 010 (Main Dyke) show evidence of severe crustal contamination. Of these samples, NC 010 and NC 007 were noted above to have disturbed major and trace element compositions. However, there is no correlation between Sr or Hf isotope compositions of the Swartruggens kimberlites with Nd isotope composition (Figures 6.1e and 6.2d) and therefore the Nd isotope compositions are believed not to be significantly affected by crustal contamination.

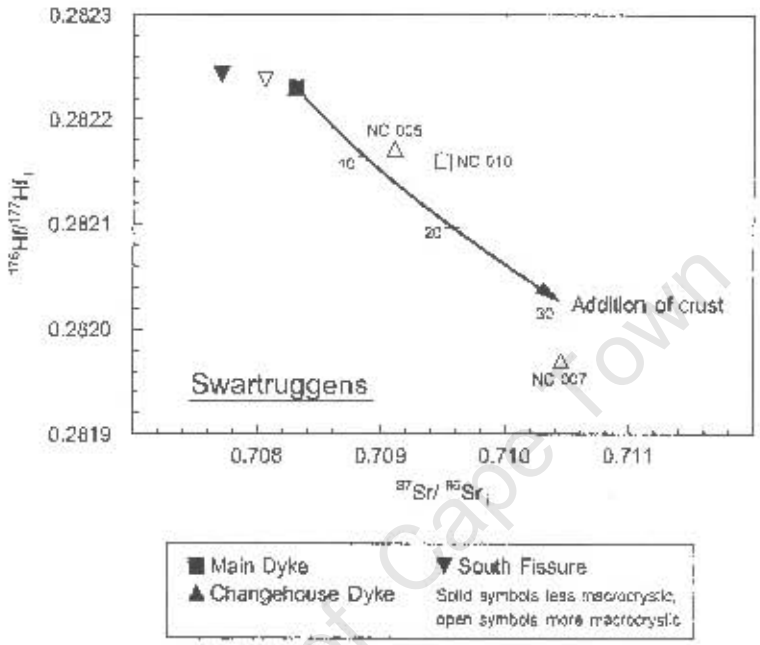

Figure 7.4 $^{176}Hf/^{177}Hf_i$ vs. $^{87}Sr/^{86}Sr_i$ for the Swartruggens kimberlite dykes, illustrating the effect of crustal contamination. Errors are smaller than symbol size. Mixing curve calculated using the parameters for crust given in Table 7.1, after Smith (1983b) and Vervoort and Patchett (1996).

7.2.2.2 The effect of crustal assimilation on the Star kimberlite dykes

Applying Clement's (1982) contamination index, samples SJH 37, JJG 6361A, JJG 6361C and JJG 6369, all from the Wynandsfontein Dyke, are contaminated, i.e. have C. I. > 1.5. All of these samples were noted in section 7.2.1.2 to be altered, and their high contamination indices probably reflect, in large part, their lowered MgO contents due to alteration. However, some of the samples from other dykes (SJH 38 and SJH 101 from the East Star Dyke; SJH 80 from the Byrnes Dyke; Figure 7.5) show elevated heavy REE abundances, and these samples may also be crustally contaminated (following le Roex *et al.*, 2003). Sample SJH 80 from the Byrnes Dyke in addition shows a positive Zr-Hf anomaly when normalised to primitive mantle, compared to the negative anomalies shown by the uncontaminated samples from this dyke (Figure 7.5b). As discussed for the Swartruggens kimberlites, this feature may be due to crustal contamination.

Although there is no consistent correlation between Gd/Yb and SiO_2 for the Star kimberlites as a whole, this effect may be masked by the slightly different Gd/Yb ratios of the individual dykes coupled with variable

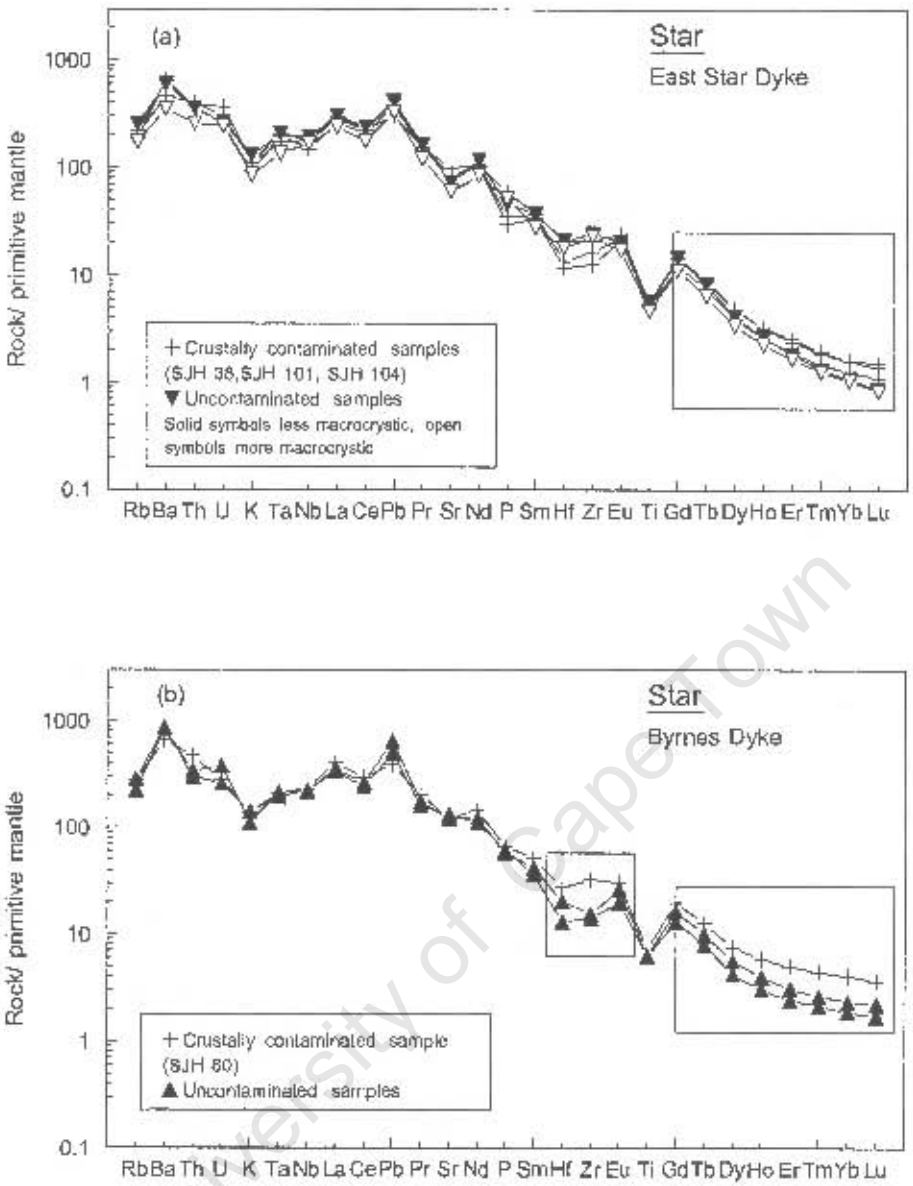

Figure 7.5 Primitive mantle normalised incompatible element patterns for the East Star and Byrnes Dyke samples, Star, illustrating the effects of crustal assimilation in terms of raised heavy REE and Zr and Hf abundances. Primitive mantle values from Sun and McDonough (1989).

degrees of lherzolite entrainment and fractional crystallisation. All samples that may be crustally contaminated using any of the above criteria have been excluded from further discussion of the Star kimberlite petrogenesis. Seven of the Star kimberlite samples (SJH 37, JJG 6361A, JJG 6361C and JJG 6369 from the Wynandsfontein Dyke; SJH 38 and SJH 101 from the East Star Dyke; SJH 80 from the Byrnes Dyke) have been discarded on this basis, in addition to sample SJH 78, noted above to be altered, but without evidence of crustal contamination.

It was concluded in Section 7.2.1.2, and illustrated in Figure 7.2c, that the variation in initial $^{87}Sr/^{86}Sr$ within the Star kimberlite dykes is likely to be due primarily to alteration, although crustal contamination may also

have elevated the $^{87}Sr/^{86}Sr$ of samples JJG 6369 (Wynandsfontein Dyke), SJH 30 (East Star Dyke), SJH 79 and SJH 78 (Byrnes Dyke). However, if these samples have been crustally contaminated, it is not reflected in their Nd or Hf isotope compositions since there is no correlation between Sr isotope composition and Nd or Hf isotope composition (Figures 6.3e and 6.4c).

7.2.3 Peridotite entrainment

Kimberlites frequently contain a suite of macrocryst minerals, which may include olivine, phlogopite, garnet, chromite, clinopyroxene and orthopyroxene (e.g. Clement *et al.*, 1984), which are commonly attributed to disaggregated peridotite entrained by the kimberlite magma *en route* to the surface (e.g. le Roex *et al.*, 2003). In samples of both the Swartruggens and Star kimberlites, macrocrysts of olivine and phlogopite are present, together with rare garnet. These macrocrysts have the typical rounded, strained appearance consistent with a xenocrystic mantle origin and therefore the Swartruggens and Star kimberlites are inferred to have entrained variable quantities of peridotite *en route* to the surface. Macrocryst phases are observed in thin section to be present, in varied proportion, in all the kimberlite samples analysed, and although, as far as possible, macrocrysts were removed prior to analysis, smaller fragments of macrocrysts may have been included. In addition, some minerals (particularly orthopyroxene, which shows a reaction relationship with kimberlite magma; Shee, 1985) may have been assimilated into the kimberlite magma. Thus the effects of lherzolite entrainment on the geochemistry of the analysed samples must be considered in order to isolate close-to-primary magma compositions.

Assimilation of peridotite by the kimberlite magma will increase the Mg# of the kimberlite, and the concentrations of certain compatible trace elements such as Ni, which are high in olivine, orthopyroxene and phlogopite. Incompatible element concentrations are generally low in garnet lherzolites (e.g. Gregoire *et al.*, 2003) compared to kimberlite magmas, and therefore mantle entrainment will simply produce a minor dilution effect on their concentrations in the kimberlite magma.

The Nd and Sr isotope compositions of the continental lithospheric mantle are diverse, with ε_{Nd} ranging from –55 to +40 (although typically between –50 and +10; Pearson and Nowell, 2002; Pearson *et al.*, 2003b) and $^{87}Sr/^{86}Sr$ ranging between 0.702 and 0.78 (although typically between 0.700 and 0.711; Pearson and Nowell, 2002; Pearson *et al.*, 2003b). The Hf isotope compositions are even less constrained, with ε_{Hf} ranging from –15 to +3800 (Ionov and Weiss, 2002; Schmidberger *et al.*, 2002; Simon *et al.*, 2002). Thus the effects of entrainment of peridotite by the kimberlite magmas are difficult to quantify based on isotope compositions alone.

7.2.3.1 Peridotite entrainment in the Swartruggens kimberlite dykes

On a plot of Ce vs. TiO_2, the Main Dyke samples define a positive correlation, with the least macrocrystic sample (NC 006) being the most enriched (Figure 7.6a). The variation within the dyke is consistent with up to 30% dilution by a component such as peridotite, with a very low Ce concentration (<~30 ppm) and approximately 0.4 wt % TiO_2. If the within dyke trends shown by the Main Dyke samples on plots of K_2O vs. Ni, Al_2O_3 vs. Ni and Ni vs. Sc are extrapolated, such that the within dyke variation from NC 006 constitutes

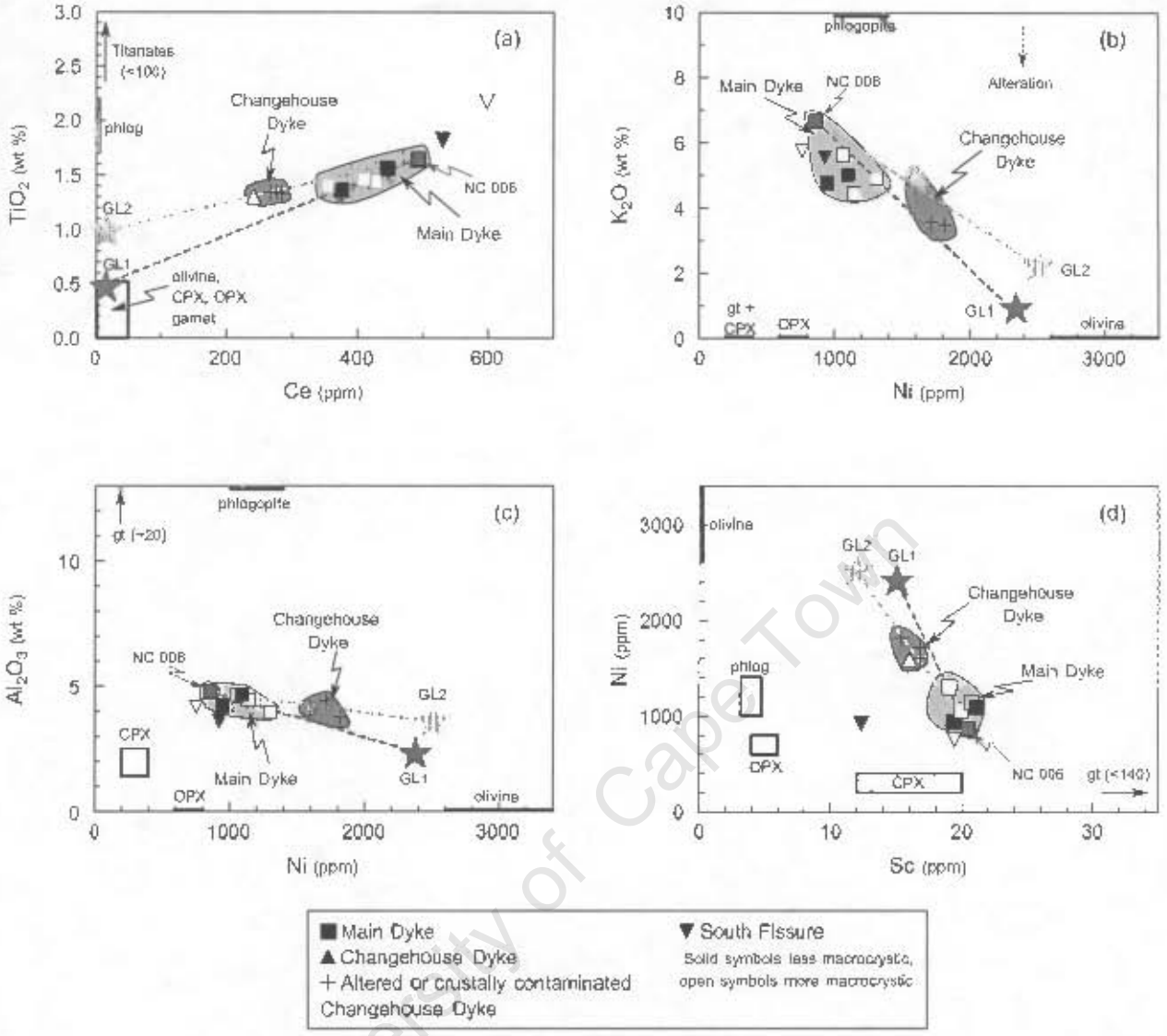

Figure 7.6 Variation diagrams illustrating the effects of peridotite entrainment on the Swartruggens kimberlite dykes. Altered Changehouse Dyke samples are shown as crosses, since, with the exception of K_2O, their abundances of the elements shown do not appear to be disturbed. GL1 is the composition of a hypothetical average peridotite entrained by the Main dyke, GL2 is the composition of a hypothetical average peridotite entrained by the Changehouse Dyke. Mineral composition fields from Gregoire *et al.* (2002 and 2003).

30% of a mixing line, the composition of the other end-member is ~0.4 wt % TiO_2, ~2170 ppm Ni, ~1 wt % K_2O and ~2.5 wt % Al_2O_3 (Figure 7.6). This is consistent with the end-member being a peridotite containing ~10 wt % phlogopite (determined from the K_2O concentration), ~0.5 wt % garnet (determined from the Al_2O_3 concentration) and a maximum of 68 % olivine (determined from the Ni concentration). The REE variation within the Main Dyke can also be accounted for by up to 30% dilution by peridotite (Figure 7.7), and this agrees well with the observed macrocryst proportions in this dyke (Table 3.1).

The Changehouse Dyke composition lies off the inferred mixing trend of the Main Dyke samples (Figure 7.6). On a plot of Ce vs. TiO_2, the composition of this dyke lies on a possible mixing line between the least macrocrystic Main Dyke sample (NC 006) and a component that is Ce poor, but has a higher TiO_2 (~ 1 wt

%) than the average peridotite assimilated by the Main Dyke. The Changehouse Dyke composition could thus be derived from addition of up to 50% of this more TiO_2-rich peridotite to the least macrocrystic Main Dyke composition. If mixing lines are drawn on plots of Al_2O_3 vs. Ni, K_2O vs. Ni and Ni vs. Sc, such that the Changehouse Dyke represents 50% addition of a component to NC 006, then the composition of this component is extrapolated to be ~3.5 wt % K_2O, ~ 2400 ppm Ni, ~ 3.5 wt % Al_2O_3. Assuming that the Changehouse Dyke and the Main Dyke derived from the same parental magma, then the Changehouse Dyke must have assimilated peridotite with an average composition that is higher in K_2O, TiO_2 and Al_2O_3 than that assimilated by the Main Dyke, consistent with a greater proportion of phlogopite in the mineralogy. The REE concentrations in the Changehouse Dyke are also consistent with addition of 50% peridotite to sample NC 006 from the Main Dyke (Figure 7.7). In addition, the Changehouse Dyke has slightly lower initial $^{143}Nd/^{144}Nd$ coupled with lower absolute Nd concentrations than the Main Dyke (Figure 7.8). If this trend represents 50% addition of peridotite, then for 5ppm Nd (Gregoire *et al.*, 2003) the average $^{143}Nd/^{144}Nd$ of the peridotite is ~0.509 (εNd = -33.9), within the range of cratonic lithospheric mantle (Pearson and Nowell, 2002). This argument is also in good agreement with the petrographic observation that the Changehouse Dyke contains up to 50% macrocrysts (Table 3.1). However, it cannot be confirmed that the Main and Changehouse Dykes were not formed from two distinct parental magmas by this approach. This aspect will be discussed in Section 7.5.

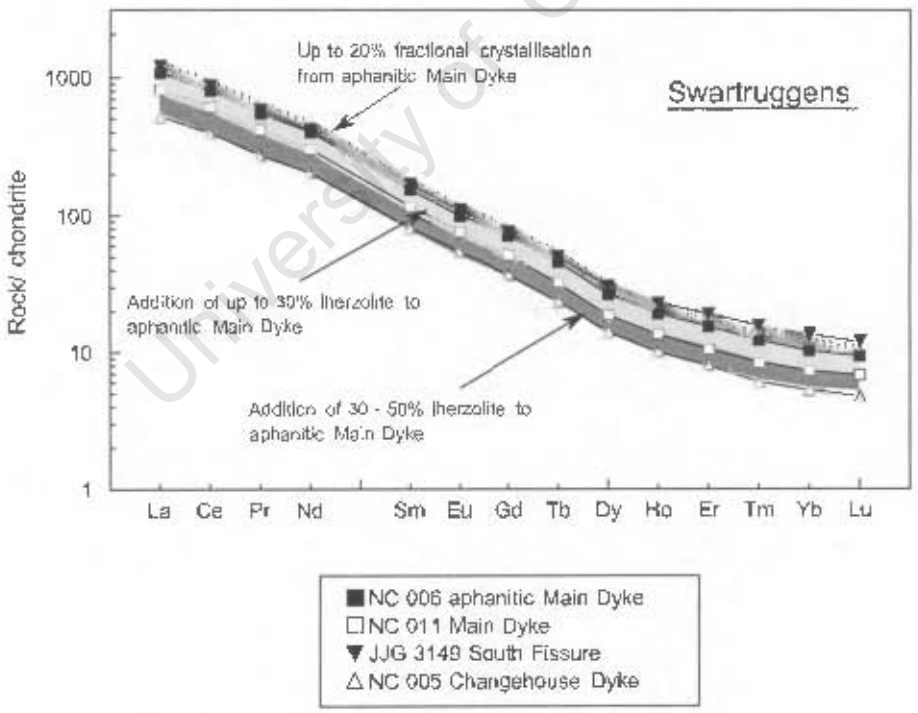

Figure 7.7 Chondrite normalised REE patterns for the Swartruggens kimberlite dykes, relative to calculated fields of up to 30% and 50% peridotite entrainment from, and up to 20% fractional crystallisation of olivine and phlogopite by, the least macrocrystic Main Dyke sample (NC 006). Average Kaapvaal peridotite composition from Gregoire *et al.* (2003); Chondrite values from Sun and McDonough (1989).

The major element concentrations of the South Fissure samples cannot be accounted for simply by entrainment of peridotite by the least macrocrystic Main dyke sample (Figure 7.6) and the South Fissure is more enriched in the REE than the Main Dyke, which is also not consistent with dilution by peridotite (Figure 7.7). However, the South Fissure has initial $^{143}Nd/^{144}Nd$ similar to that of the Changehouse Dyke (Figure 7.8), and the effect of peridotite entrainment on the major and trace element abundances in this dyke may have been masked to some extent by superimposed fractional crystallisation, as will be discussed in more detail in Section 7.2.4. The required degree of addition of peridotite to create the $^{143}Nd/^{144}Nd$ of the South Fissure, illustrated on Figure 7.8, is somewhat too high when compared with petrographic observations (Table 3.1), and the degree of fraction of olivine and phlogopite fractionation (>30%) necessary to create the Nd concentration is too large to be reasonable (e.g. Ni would be completely removed). However the average composition of the peridotite entrained by the South Fissure is unconstrained, and in reality may have higher Nd content and lower $^{143}Nd/^{144}Nd$ than that entrained by the Changehouse Dyke. The cratonic lithosphere typically has ε_{Nd} between from –50 and +10 (Pearson and Nowell, 2002) and so such a hypothesis is not unreasonable.

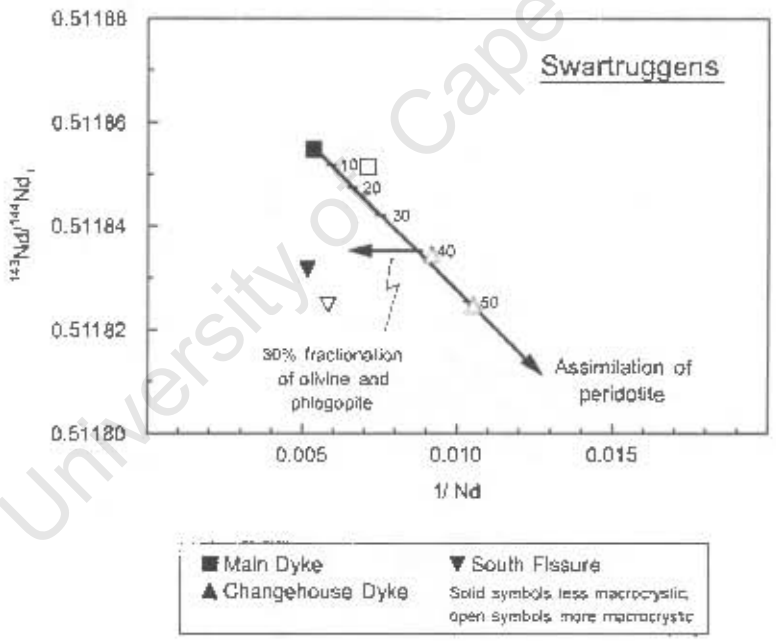

Figure 7.8 The effect of peridotite entrainment on the Swartruggens kimberlite dykes with respect to their Nd isotope compositions. Mixing line assumes a peridotite composition with 5ppm Nd, $^{143}Nd/^{144}Nd$ = 0.509 (Pearson and Nowell, 2002).

7.2.3.2 Peridotite entrainment in the Star kimberlite dykes

If the Barren Dyke is excluded, on a plot of Al_2O_3 vs. Ni the Star kimberlites show a distinct break in slope between the trends of the more aphanitic samples and the more macrocrystic samples at approximately 1400ppm Ni (sample JJG 6362), consistent with addition of peridotite (Figure 7.9a). On a plot of Ce vs. TiO_2 (Figure 7.9b) the magnitude of this dilution can be estimated using the lever rule, as the predominant

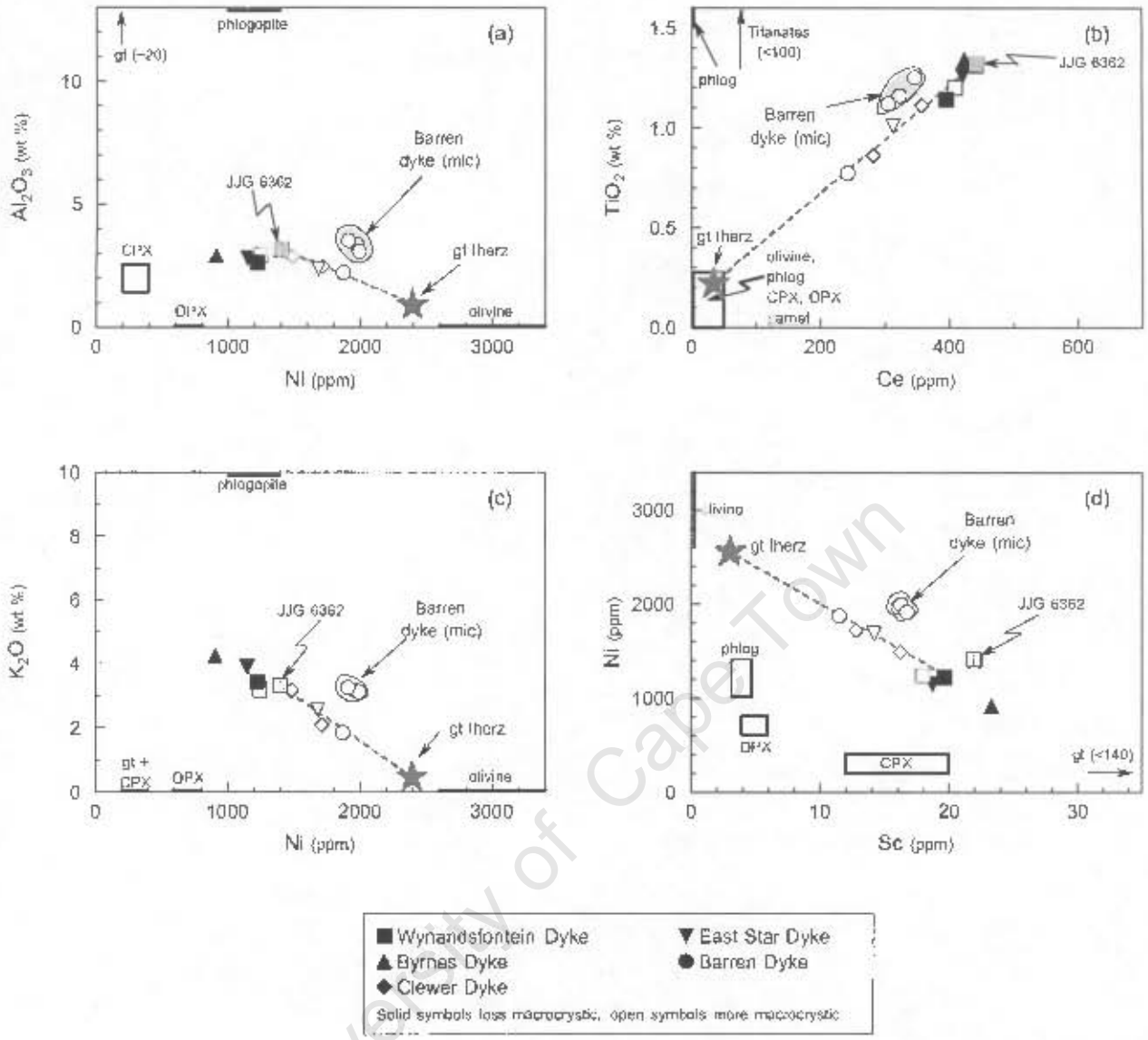

Figure 7.9 Variation diagrams illustrating the effects of peridotite entrainment on the Star kimberlite dykes. Gt. lherz is the composition of a hypothetical average peridotite entrained by the kimberlites consisting dominantly of olivine, and containing approximately 5% phlogopite. Mineral composition fields from Gregoire *et al.* (2002 and 2003).

peridotitic minerals all have very low Ce contents, to be approximately 40%, which is in agreement with the observed proportions of macrocrysts in the Star samples (Table 3.4). Consistent trends within the macrocrystic samples are also observed on plots of K_2O vs. Ni and Sc vs. Ni (Figure 7.9c and d), and if these trends are extrapolated such that the variation within the macrocrystic samples represents up to 40% dilution by peridotite, then the peridotite contains ~2 wt % TiO_2, ~0.7 wt % Al_2O_3, ~0.5 wt % K_2O and ~2400 ppm Ni. The high Ni content of the proposed diluent suggests a dominantly olivine composition, and the Al_2O_3 and K_2O contents imply involvement of approximately 5% phlogopite, broadly in agreement with the observed proportions of olivine and phlogopite in the macrocryst suite of the Star samples (Table 3.4).

As mentioned in Chapter 6, the initial $^{143}Nd/^{144}Nd$ and $^{176}Hf/^{177}Hf$ of the more macrocrystic Star kimberlite samples are lower than those of the less macrocrystic samples. This variation can be accounted for by approximately 40% entrainment of peridotite with a $^{143}Nd/^{144}Nd$ of 0.5105 (ε_{Nd} = -41.7) and $^{176}Hf/^{177}Hf$ of 0.28225 (ε_{Hf} = -18.46), and Nd and Hf concentrations of 6 ppm and 0.5 ppm respectively, by the less macrocrystic samples (Figure 7.10). This Nd isotope composition is within the range of cratonic lithospheric mantle (Pearson and Nowell, 2002), although the Hf isotope composition is slightly lower than previously analysed lithospheric mantle (ε_{Hf} > -15; Ionov and Weiss, 2002; Schmidberger *et al.*, 2002; Simon *et al.*, 2002). However, as discussed above, the cratonic lithospheric mantle is clearly extremely isotopically diverse and the mixing curve shown on Figure 7.10 is only illustrative.

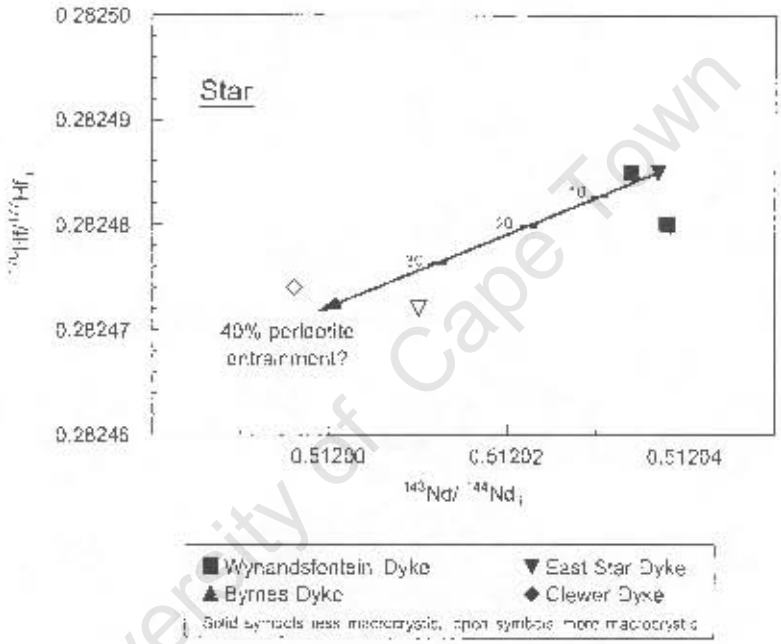

Figure 7.10 Variation of $^{176}Hf/^{177}Hf$ with $^{143}Nd/^{144}Nd$ in the Star kimberlite dykes with respect to their macrocryst content, with a mixing line calculated to represent entrainment of 40% of a theoretical peridotite with $^{176}Hf/^{177}Hf$ = 0.28225, $^{143}Nd/^{144}Nd$ = 0.5105. Numbers refer to % entrainment of peridotite. See text for further discussion.

The absolute concentrations of the REE within the macrocrystic Star kimberlite dykes lie within the range of up to 40% addition of peridotite to the most enriched macrocrystic sample JJG 6362 (Figure 7.11). However, the variation in La/Yb_n between the individual dykes, described in Chapter 5, cannot be accounted for simply by dilution by peridotite and must be explained by another process. This will be discussed further in Section 7.5.2.

The Barren Dyke has been previously identified as different to the other Star kimberlite dykes based on its considerably higher $^{143}Nd/^{144}Nd$ and $^{176}Hf/^{177}Hf$ initial ratios (Table 6.2), which cannot be accounted for by addition of peridotite. It is also clear from Figure 7.9 that the micaceous samples do not lie on the same

trends of peridotite assimilation as the other Star kimberlite samples. However, despite having Nd and Hf isotope compositions within analytical error of the micaceous Barren Dyke, the less-micaceous sample lies on the trend of peridotite assimilation of the diamondiferous kimberlite dykes. This may be due to extreme degrees of peridotite entrainment by this sample, such that its whole rock geochemistry dominantly reflects that of the entrained peridotite.

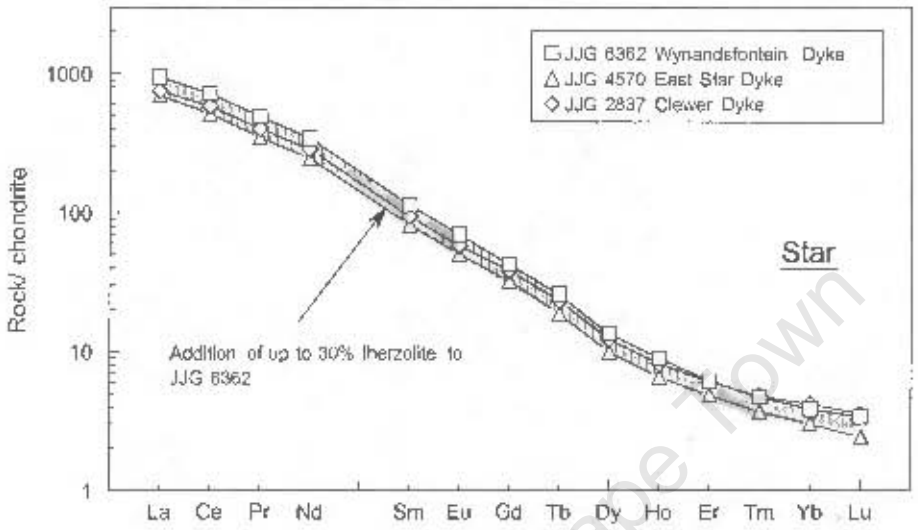

Figure 7.11 Chondrite normalised REE variation of the Wynandsfontein, East Star and Clewer Dykes relative to the calculated field of 30% peridotite entrainment by sample JJG 6362. Typical peridotite composition from Gregoire *et al.* (2003); Chondrite values from Sun and McDonough (1989).

7.2.4 Fractional crystallisation

The effect of olivine fractionation on the major element abundances of the Swartruggens and Star kimberlite magmas will be a decrease in the MgO, FeO and SiO_2 contents of magmas, with consequent enrichment of other major oxides. Certain compatible elements such as Ni and Co, which partition strongly into olivine (Hart and Davis, 1978) will become depleted in the kimberlite magmas, whereas the concentrations of the incompatible elements will become relatively enriched. Since phlogopite is the most abundant phenocryst phase in these kimberlites it is also important to consider the effect of phlogopite fractionation on the kimberlite magmas. This is of particular importance, not only because phlogopite fractionation will decrease the MgO, SiO_2 and Ni concentrations of the primary magma, but also because K is a stoichiometric component of, and Ti substitutes for Al in, phlogopite (Deer *et al.*, 1998) and all the Swartruggens and Star kimberlite samples analysed display strong negative K and Ti anomalies on a primitive mantle normalised incompatible element diagram, as discussed in Chapter 5 (Figures 5.5 and 5.10). The effects of fractional crystallisation within the kimberlite dyke swarms at Swartruggens and Star are discussed separately below, but as both kimberlites display similar negative anomalies on a primitive mantle normalised diagram, the role of fractional crystallisation on these anomalies will be discussed for both localities together in Section 7.2.4.3.

7.2.4.1 Fractional crystallisation in the Swartruggens kimberlite dykes

Although there is no consistent variation between MgO and Ni in the less macrocrystic Main Dyke samples, the South Fissure samples form a trend of decreasing MgO and Ni away from the average less macrocrystic Main Dyke composition, with the less macrocrystic sample (JJG 3149) having a composition consistent with up to 10% fractionation of olivine and phlogopite in the ratio 8:2 (Figure 7.12). The REE concentrations of the South Fissure are also consistent with up to 10% fractional crystallisation from the least macrocrystic Main Dyke sample (Figure 7.7). This is consistent with the observation that the South Fissure is petrographically more evolved than the Main Dyke, as recorded in Chapter 3, containing more abundant diopside both as phenocrysts and a groundmass phase, and the presence of possible sanidine in some South Fissure samples (Allan, 1990). However, as mentioned above, the South Fissure samples do contain a proportion of macrocrysts, and the Nd isotope composition is suggestive of peridotite entrainment to some extent (Figure 7.8). The more macrocrystic Main Dyke samples trend to higher MgO and Ni contents than the average less macrocrystic Main Dyke composition, consistent with peridotite entrainment as discussed above. Sample NC 005, the least altered sample from the Changehouse Dyke, does not have MgO and Ni contents consistent with peridotite entrainment by the less macrocrystic samples, but has lower MgO for a given Ni concentration (Figure 7.12). However, it was noted above that the other three samples from this dyke are significantly altered, and it is therefore likely that this sample has also experienced some loss of MgO, this effect having been masked in Figure 7.1 by the high MgO content of the sample.

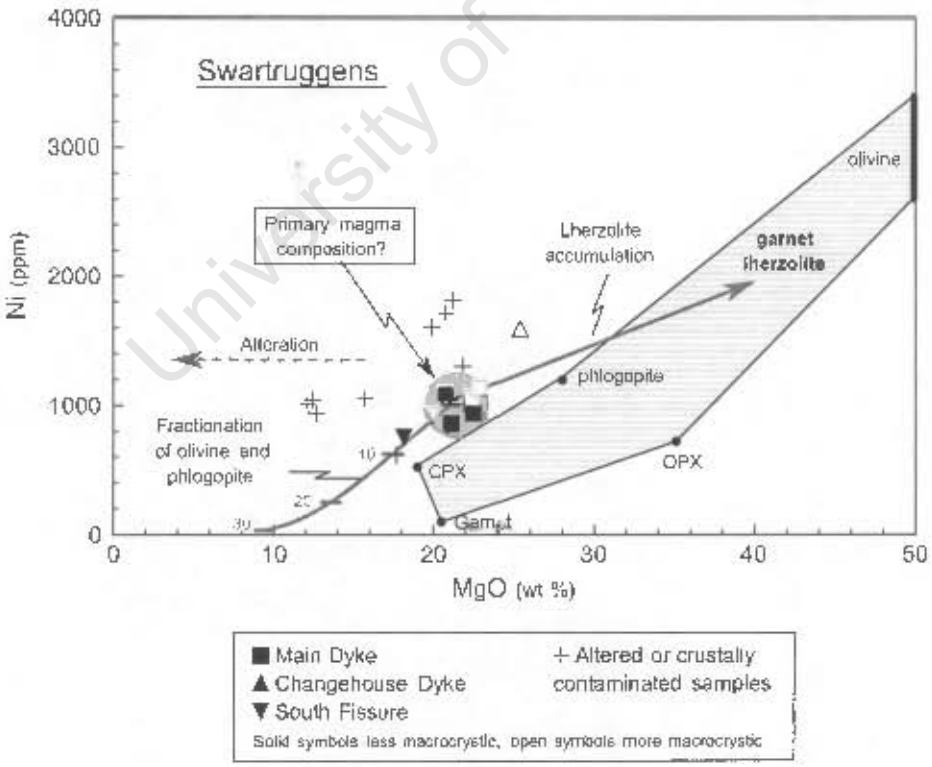

Figure 7.12 The effect of fractionation of olivine and phlogopite in the Swartruggens kimberlite dykes, with respect to their MgO and Ni contents. Numbers along fractionation trajectory refer to the percentage of olivine and phlogopite fractionated in the ratio 8:2. Mineral composition fields from Gregoire *et al.* (2002 and 2003).

7.2.4.2 Fractional crystallisation in the Star kimberlite dykes

The effect of fractional crystallisation of olivine and phlogopite on the MgO and Ni concentrations of the Star kimberlite dykes is illustrated in Figure 7.13. From the macrocrystic sample with the lowest MgO content (JJG 6362; Wynandsfontein Dyke), two trends of peridotite entrainment are evident, with the Wynandsfontein Dyke samples defining a trend towards lower Ni concentrations at given MgO contents than the macrocrystic samples from the other Star diamondiferous kimberlite dykes. The aphanitic Byrnes Dyke samples define a trend consistent with up to approximately 15% fractionation of olivine and phlogopite in the proportions 8:2 from sample JJG 6362. However the REE concentrations of the Byrnes Dyke samples are not consistent with 15% fractionation of olivine and phlogopite from sample JJG 6362, as discussed in Chapter 5, and for similar enrichment in the light REE they are more enriched in the heavy REE than JJG 6362. This feature cannot be attributed to lherzolite entrainment as discussed above, and will be addressed further in Section 7.5.

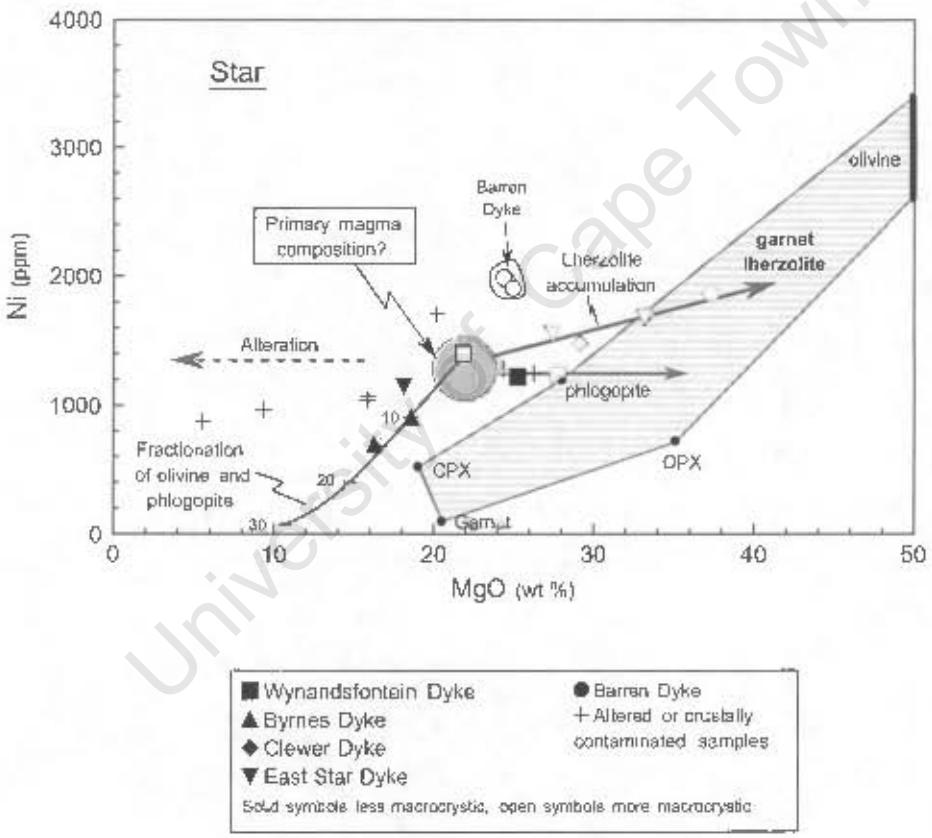

Figure 7.13 The effect of olivine and phlogopite fractionation in the Star kimberlite dykes, with respect to their MgO and Ni contents. Numbers on fractionation trajectory refer to percentage fractionation of olivine and phlogopite in the ratio 8:2. Mineral composition fields from Gregoire *et al.* (2002 and 2003).

7.2.4.3 The effect of fractional crystallisation on primitive mantle normalised incompatible elements.

As phlogopite fractionation appears to have been relatively minor within the Swartruggens and Star kimberlite dykes, it is unlikely to account for the strong negative K anomalies present in all the samples on primitive mantle normalised diagrams (Figures 5.5 and 5.10). Figure 7.14a illustrates the range in size of the

K anomalies (expressed as K/K* as described in Chapter 5), calculated with respect to Th and La (as Nb also partitions into phlogopite; e.g. Gregoire *et al.*, 2003), in the Swartruggens kimberlite samples, and a calculated curve for phlogopite fractionation from a theoretical magma displaying no K anomaly (i.e. K/K* = 1), but with similar La and Th concentrations to those of the Swartruggens and Star kimberlites. It is clear from this diagram that to produce the relative depletion in K observed, 30-40%, and greater than 40%, phlogopite fractionation is required by the Swartruggens and Star kimberlite samples, respectively. The strong negative K anomalies of these samples are therefore concluded to be features of the primary kimberlite magmas at each locality. However, as indicated by the calculated vectors on Figure 7.14a, small degrees (up to 10%) of fractionation and assimilation of phlogopite may account for some of the variability in size of the K anomalies within the kimberlite samples from each locality.

Ti substitutes for Al in phlogopite (Deer *et al.*, 1998) and since all the kimberlite samples from both Swartruggens and Star display strong negative Ti anomalies on primitive mantle normalised incompatible element diagrams (Figures 5.5 and 5.10), it is important to consider the role of phlogopite fractionation may have played in creating these anomalies. The magnitude of the Ti anomaly in the individual samples from Swartruggens and Star, expressed as Ti/Ti* (as described in Chapter 5), is illustrated in Figure 7.14b, together with a fractionation curve illustrating the effect of phlogopite fractionation from a theoretical magma containing no Ti anomaly (i.e. Ti/Ti* = 1), and with Eu and Gd abundances similar to those of the Swartruggens and Star kimberlite samples. For simplicity, Ti has been assumed to be a stoichiometric component, constituting 1.5 wt % (8993 ppm, typical of Swartruggens and Star phlogopite; Tables 3.2 and 3.6), of phlogopite. It is clear from Figure 7.14b that although small degrees of phlogopite fractionation may account for the variation in size of the Ti anomalies at each locality, phlogopite fractionation from a magma where Ti/Ti* = 1 cannot create Ti anomalies of the magnitude of those present in the Swartruggens and Star

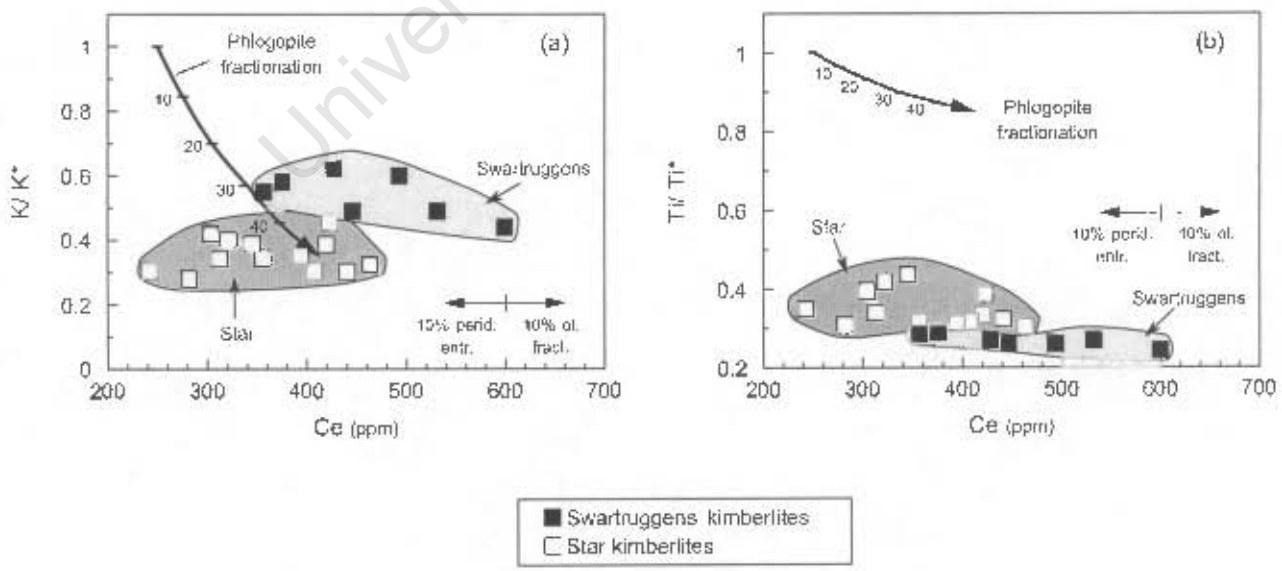

Figure 7.14 The effect of phlogopite fractionation on a theoretical magma displaying no K and Ti anomalies on a primitive mantle normalised incompatible element diagram (K/K* = 1; Ti/Ti* = 1). Numbers on fractionation trajectory refer to percentage phlogopite fractionation. See text for further discussion.

kimberlites. Small degrees of fractionation of a titanate phase such as ilmenite may account for depletion in Ti from some magmas, and in addition would cause relative depletion in Nb and Ta since these elements partition strongly into titanates (e.g. Ryerson and Watson, 1987; Green, 1995; Boudnier *et al.*, 1996; Foley *et al.*, 2000). However, in common with other Group II kimberlites (e.g. Mitchell, 1995), ilmenite was not observed in thin sections of the Swartruggens or Star kimberlite samples and is not considered likely to have fractionated from the respective magmas. Phlogopite is also a host to Nb and Ta, but partition coefficients for Nb into phlogopite are relatively small (of the order of 0.15; calculated from mineral data in Gregoire *et al.* 2002 and 2003) and thus phlogopite fractionation cannot account for these negative anomalies.

7.3 Compositions of the close-to-primary kimberlite magmas

Following the exclusion of all samples believed to have suffered alteration or crustal contamination, the composition of the primary kimberlite magma at each locality should lie between the trends of lherzolite assimilation and fractional crystallisation. This composition is reasonably well defined for the Star kimberlites, as a distinct break in slope on many diagrams (e.g. Figures 7.9, 7.13), with the majority of the macrocrystic samples trending towards a peridotite composition, and the aphanitic samples showing trends consistent with fractionation of olivine and phlogopite (Figure 7.13). The sample that best approximates the close-to-primary magma composition for the Star kimberlites is JJG 6362, from the Wynandsfontein Dyke. Although this sample was observed to be macrocrystic in thin section (Appendix 2), the geochemical effects of peridotite entrainment in this case do not appear to have been severe, perhaps due to heterogeneity of the sample (see discussion in Chapter 3).

The Swartruggens kimberlite dykes behave less coherently as a group than the Star kimberlites, and thus an individual primary kimberlite magma is more difficult to define. However, the Main Dyke samples appear to be the closest in composition to a primary magma, with the Changehouse Dyke being consistent with addition of lherzolite to the least macrocrystic Main Dyke samples (Figure 7.6), and the South Fissure being the most evolved of the dykes, and showing trends of fractionation of olivine and phlogopite away from the average aphanitic Main Dyke composition (Figure 7.12). The Third Lease samples are excluded on the basis of alteration. As there are no coherent trends of fractional crystallisation within the Main Dyke, the least macrocrystic Main Dyke sample NC 006 has been taken to represent the composition of a primary Swartruggens kimberlite magma. The possibility that there may be more than one primary magma composition at Swartruggens will be considered later.

The Swartruggens and Star close-to-primary kimberlite magma compositions are given in Table 7.2 and illustrated in Figure 7.15. The major element compositions of the two magmas are similar (Swartruggens MgO = 21.1 wt %, TiO_2 = 1.64 wt %; SiO_2 = 38.1 wt %; Star MgO = 21.8 wt %, TiO_2 = 1.31 wt %, SiO_2 = 36.2 wt %; Table 7.2), although the Swartruggens close-to-primary kimberlite magma has a significantly higher K_2O and Al_2O_3 contents (K_2O = 6.64 wt %, Al_2O_3 = 4.77 wt %; Table 7.2), and slightly lower CaO

Table 7.2 Close-to-primary magma compositions of the Swartruggens and Star kimberlites. Major oxide data in wt %, trace element data in ppm. Swartruggens major and trace element and Hf and Nd isotope compositions are from sample NC 006 (Main Dyke). Sr composition from JJG3149 (South Fissure). Star major and trace element and Sr isotope compositions from sample JJG 6362 (Wynandsfontein Dyke), Nd and Hf isotope compositions from sample NC 050 (Wynandsfontein Dyke). Ta concentrations may be slightly low, due to incomplete dissolution of certain phases prior to ICP-MS analyses, see Appendix 3 for details; Mg# = atomic $Mg/(Mg + Fe^{2+})$, with $Fe_2O_3/FeO = 0.2$; Initial isotopic ratios calculated using an age of 156 Ma for Swartruggens (Smith *et al.*, 1985a) and 124 Ma for Star (McIntyre and Dawson, 1976); ε values calculated as described in Section 6.1.1; 2σ uncertainties on isotope data are given in brackets.

	Swartruggens	Star
SiO_2	38.1	36.2
TiO_2	1.64	1.31
Al_2O_3	4.77	3.16
Fe_2O_3	8.88	9.23
MnO	0.16	0.29
MgO	21.1	21.8
CaO	8.54	10.5
Na_2O	0.21	0.21
K_2O	6.64	3.32
P_2O_5	1.86	1.09
SO_3	0.34	0.25
NiO	0.1	0.15
Cr_2O_3	0.23	0.31
LOI	6.56	11.76
Total	99.2	99.7
Mg #	0.85	0.85
Sc	20.5	22
V	190	144
Cr	1419	2389
Co	60.4	79
Ni	862	1401
Cu	40.6	36
Zn	95.8	78.5
Rb	273	137
Sr	1422	2383
Cs	6.62	3.75
Ba	3452	5060

	Swartruggens	Star
Pb	40.3	31.8
Y	27.7	12.5
Zr	395	264
Nb	171	152
Hf	8.63	6.14
Ta	5.93	8.08
Th	30.6	33.6
U	7.89	7.39
La	257	223
Ce	493	440
Pr	52.1	46.6
Nd	187	160
Sm	23.6	17.3
Eu	5.77	4.04
Gd	14.7	8.7
Tb	1.74	0.96
Dy	6.85	3.42
Ho	1.1	0.51
Er	2.58	1.01
Tm	0.32	0.12
Yb	1.76	0.66
Lu	0.24	0.09
$^{87}Sr/^{86}Sr_i$	0.707711 (14)	0.707476 (13)
$^{143}Nd/^{144}Nd_i$	0.511855 (19)	0.512036 (10)
ε_{Nd}	-11.37 (0.25)	-8.49 (0.13)
$^{176}Hf/^{177}Hf_i$	0.282230 (4)	0.282480 (8)
ε_{Hf}	-15.74 (0.11)	-7.50 (0.28)

content (CaO = 8.54 wt %; Table 7.1) than the Star close-to-primary magma (K_2O = 3.32 wt %, Al_2O_3 = 3.16 wt %, CaO = 10.5 wt %; Table 7.2).

These two close-to-primary magmas differ from the close-to-primary Kimberley Group I kimberlite magma, as determined by le Roex *et al.* (2003), which has significantly higher MgO (26 - 27 wt %), and higher CaO (CaO = ~12 wt %), content. The Kimberley Group I kimberlite magma also has considerably lower SiO_2 (26-27 wt %), K_2O (~1 – 2 wt %) and slightly lower Al_2O_3 (~2.2 wt %) than, but a similar TiO_2 (1-2 wt %)

27 wt %), K_2O (~1 – 2 wt %) and slightly lower Al_2O_3 (~2.2 wt %) than, but a similar TiO_2 (1-2 wt %) concentration to, the Swartruggens and Star close-to-primary kimberlite magmas (le Roex *et al.*, 2003). The SiO_2, Al_2O_3, and MgO contents of the Swartruggens and Star close-to-primary kimberlite magmas are similar to those determined experimentally by 0.3 to 1% melting of a carbonated garnet lherzolite at 6 GPa (Dalton and Presnall, 1998), although the SiO_2 contents are suggestive of a 1% melt, whereas the MgO contents are considerably lower than those experimentally determined at 1% melting (MgO = ~29 wt %; Dalton and Presnall, 1998), and are more consistent with 0.3% melting. As with the Kimberley Group I close-to-primary magma, both the Swartruggens and Star close-to-primary kimberlite magmas have CaO contents much lower than the experimentally determined melts (CaO = 16 – 18 wt %; Dalton and Presnall, 1998). However, these experiments used starting compositions that are anomalously CaO rich when compared to typical cratonic peridotite. The high Mg#s of the Swartruggens and Star close-to-primary kimberlite magmas (Mg # = 0.85 for both magmas; Table 7.1) suggest equilibration against olivine with $Fo_{\sim 0.95}$ (using an olivine-melt $K^D_{FeO/MgO}$ of 0.36, Herzberg and O'Hara, 2002), slightly higher than that of olivine in garnet lherzolites from the Kaapvaal Craton ($Fo_{.92-94}$; Gregoire *et al.*, 2003).

The close-to-primary Swartruggens and Star kimberlite magmas show several common features on a primitive mantle normalised incompatible element diagram (Figure 7.15). Both magmas are strongly enriched in the more incompatible relative to the less incompatible elements, show similarly-sized negative K, Ti and Sr anomalies (Swartruggens K/K* = 0.59, Ti/Ti* =0.26, Sr/Sr* = 0.41; Star K/K* = 0.30, Ti/Ti* = 0.32, Sr/Sr* = 0.80), and subdued negative Nb, Ta and Hf anomalies. There is some analytical uncertainty on Ta concentrations due to the possible incomplete dissolution of Ta bearing phases prior to ICP-MS analyses (see Appendix 3 for details). A positive Pb anomaly is also present in both close-to-primary magmas (Swartruggens Pb/Pb* = 2.07; Star Pb/Pb* = 2.19). The heavy REE are notably more enriched in the Swartruggens (Gd/Yb_n = 6.9) than the Star (Gd/Yb_n = 11.0) close-to-primary kimberlite magma. For comparison, the composition of the close-to primary Group I kimberlite magma from Kimberley (le Roex *et al*, 2003) is also shown on Figure 7.11. The Kimberley magma also shows strong enrichment in the more incompatible elements relative to the less incompatible elements, although it is less enriched in the former relative to the close-to-primary magmas at Swartruggens and Star. Similar negative Ti and Sr anomalies are displayed by the Kimberley magma, although no negative anomalies are present for Nb or Ta, and a much larger negative K anomaly is present in the Kimberley magma than either the Swartruggens or Star close-to-primary magmas. The Kimberley close-to-primary magma also differs from the Swartruggens and Star close-to-primary magmas in having no positive Pb anomaly.

The Swartruggens close-to-primary kimberlite magma has considerably lower ε_{Nd} and ε_{Hf} than that at Star (Swartruggens close-to-primary ε_{Nd} = -11.37 (± 0.25), ε_{Hf} = -15.74 (± 0.11); Star close-to-primary ε_{Nd} = -11.37(± 0.13); ε_{Hf} = -7.50 (+ 0.28); Table 7.2). The Sr isotope compositions of the Swartruggens kimberlites have clearly been strongly contaminated either by weathering or crustal contamination, as discussed above. The closest to primary initial $^{87}Sr/^{86}Sr$ is inferred to be the lowest (JJG 3149, South Fissure; Table 6.1), as a mixing trend towards higher $^{87}Sr/^{86}Sr$ is clearly evident (Figure 7.1). The initial $^{87}Sr/^{86}Sr$ of the Star close-to-primary kimberlite magma ($^{87}Sr/^{86}Sr_i$ = 0.707476 ± 13; Table 7.2) is slightly lower than that at Swartruggens

$^{87}Sr/^{86}Sr_i$ = 0.707711 ± 14; Table 7.1). However, the Swartruggens ratio cannot be confidently inferred to represent the true primary magma compositions, and the higher initial $^{87}Sr/^{86}Sr$ may in part reflect intrusion through the Chuniespoort dolomite (Kirkley, 1987).

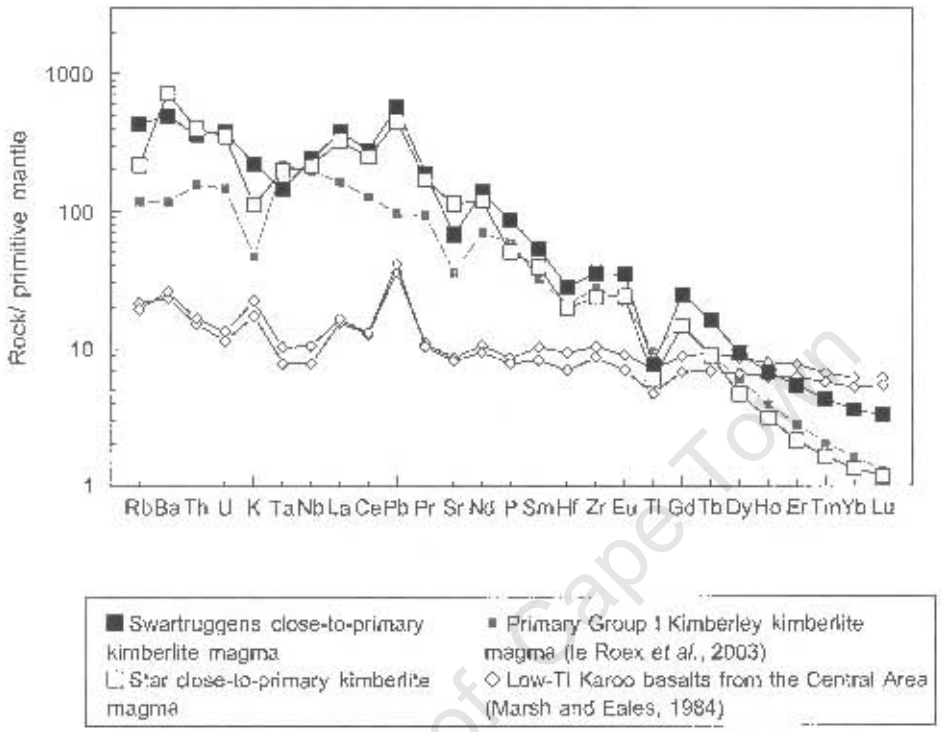

Figure 7.15 Primitive mantle normalised incompatible element abundances in the Swartruggens and Star close-to-primary kimberlite magmas. The close-to-primary magma of the Kimberley Group I kimberlites (le Roex *et al.*, 2003) and low-Ti Karoo basalts from the Central Area (Marsh and Eales, 1984) are shown for comparison.

7.4 Source region characteristics

The source trace element compositions giving rise to the primary kimberlite magmas at Swartruggens and Star can be estimated by using simple partial melting modelling, assuming small degrees of non-modal equilibrium partial melting of a garnet lherzolite source, as suggested by experimental work (e.g. Wyllie, 1980; Dalton and Presnall, 1998; Ulmer and Sweeney, 2002). The calculated trace element concentrations in the source regions are model dependent, and affected by three principal unknowns:

1 – the degree of partial melting giving rise to the kimberlite magmas; although known to be small to account for the enrichment in incompatible elements in the kimberlite magmas, it is uncertain whether the degree of partial melting is of the order 0.5%, or as much as 2% (Dalton and Presnall, 1998). The higher the degrees of partial melting, the more enriched the source region must have been in the more incompatible trace elements.

2 – the assumed presence and proportions of minerals in the source regions; the partition coefficients for the heavy REE are high in garnet (Table 7.4) and thus the amount of residual garnet in the source after melting to a large extent controls the concentration of the heavy REE in the kimberlite magma. The more residual garnet present in the source region, the more enriched the source must have been in the heavy REE. The light and middle REE partition into clinopyroxene, and thus the calculated light REE concentrations in the source region are partly dependent on the assumed amount of residual clinopyroxene.
3 – the presence and role during melting of accessory phases such as phlogopite, and titanates such as ilmenite, lindsleyite and rutile.
These three important variables are addressed below.

7.4.2 The geochemical compositions of the kimberlite source regions at different degrees of partial melting, and the effect of residual mineralogy

The trace element compositions of the respective source regions of the Swartruggens and Star close-to-primary kimberlite magmas, calculated assuming 1% partial melting of a garnet lherzolite source using partition coefficients from a compilation in Späth *et al.* (2001), and given in Table 7.4, are reported in Table 7.5. Mineral proportions (Table 7.3) of the starting source are typical of garnet lherzolite from the Kaapvaal craton (e.g. Gregoire *et al.*, 2003; Pearson and Nowell, 2002) and melt modes (Table 7.3) are those used by le Roex *et al.* (2003) for Group I kimberlites, and are similar to those determined experimentally by Walter (1998) for melting of a dry garnet peridotite at 7 GPa.

Table 7.3 Modal proportions and melt modes of peridotitic minerals (after le Roex *et al.*, 2003) used to model the source region characteristics of the Swartruggens and Star kimberlites.

Phase	Modal proportion (vol. %)	Melting proportion
Olivine	0.57	0.05
Orthopyroxene	0.28	0.05
Clinopyroxene	0.11	0.5
Garnet	0.04	0.4

Chondrite normalised REE patterns for the Swartruggens and Star kimberlite source regions are shown in Figure 7.16. A field of calculated REE abundances in the source region is shown for each locality, to illustrate the effects of varying the degrees of partial melting between 0.5 and 2%, and of varying the proportion of garnet in the source between 2 and 6 volume %. The proportion of clinopyroxene is varied accordingly, such that garnet + clinopyroxene = 15%. In making these calculations, it is evident that the effect on the calculated source composition of varying quantities of clinopyroxene is minimal and is masked by the effect of varying degrees of partial melting (Figure 7.16).

Table 7.4 Partition coefficients for the incompatible elements in peridotitic minerals used in partial melting modelling. From a compilation in Späth *et al.*, (2001).

Phase	Rb	Ba	Th	U	K	Ta	Nb	La	Ce	Pb	Pr	Sr	Nd	P
Olivine	0.001	0.001	0.001	0.001	0.001	0.001	0.001	0.001	0.001	0.001	0.001	0.001	0.001	0.001
Opx	0.001	0.001	0.001	0.001	0.001	0.001	0.001	0.001	0.001	0.001	0.001	0.001	0.001	0.001
Cpx	0.001	0.001	0.001	0.001	0.01	0.01	0.01	0.05	0.08	0.08	0.1	0.12	0.14	0.1
Garnet	0.001	0.001	0.001	0.001	0.001	0.001	0.001	0.01	0.021	0.021	0.054	0.001	0.087	0.05
Spinel	0.001	0.001	0.001	0.001	0.001	0.001	0.001	0.01	0.01	0.01	0.01	0.01	0.01	0.01

Phase	Sm	Hf	Zr	Eu	Ti	Gd	Tb	Dy	Ho	Er	Tm	Yb	Lu
Olivine	0.001	0.001	0.001	0.001	0.001	0.001	0.001	0.001	0.001	0.001	0.001	0.001	0.001
Opx	0.001	0.01	0.01	0.01	0.1	0.016	0.019	0.022	0.022	0.03	0.03	0.1	0.1
Cpx	0.14	0.2	0.2	0.15	0.17	0.2	0.25	0.3	0.3	0.28	0.29	0.3	0.3
Garnet	0.13	0.1	0.1	0.2	0.1	0.3	0.6	0.9	1.4	2	3	4	6
Spinel	0.01	0.01	0.01	0.01	0.01	0.01	0.01	0.01	0.01	0.01	0.01	0.01	0.01

Assuming the primary kimberlite magma was produced by 1% partial melting and the source contained 4 volume % residual garnet, the calculated source for the Swartruggens kimberlite is enriched to approximately 20 times chondrite in La and has heavy REE abundances approximately 3 times chondrite, with $La/Yb_n = 7.4$ (Figure 7.16a). However, higher and lower degrees of melting require a source which is more and less enriched in the light REE respectively, with source region La = 32 times chondrite for 2% partial melting, and La = 13 times chondrite for 0.5% partial melting (Figure 7.16a). The heavy REE abundances in the calculated source vary with assumed mode of residual garnet, and the calculated source containing 6 volume % garnet is more enriched (Yb = 4 times chondrite), and 2 volume % garnet is less enriched (Yb = 1.5 times chondrite), in the heavy REE (Figure 7.16a). By varying the degrees of partial

Table 7.5 Calculated trace element abundances (in ppm) of the Swartruggens and Star kimberlite source regions assuming 1% non-modal partial melting of a garnet lherzolite source, with source mineralogy and melt modes given in Table 7.3 and partition coefficients given in Table 7.4.

	Swartruggens	Star
Rb	3	1.51
Ba	37.9	55.6
Th	0.34	0.37
U	0.09	0.08
K	658	329
Ta	0.07	0.1
Nb	2.04	1.81
La	4.31	3.74
Ce	9.86	8.81
Pb	0.81	0.64
Pr	1.21	1.08
Sr	33.4	56
Nd	5.37	4.59
P	168	110

	Swartruggens	Star
Sm	0.71	0.52
Hf	0.33	0.23
Zr	15	10
Eu	0.21	0.15
Ti	590	471
Gd	0.69	0.41
Tb	0.11	0.06
Dy	0.55	0.28
Ho	0.11	0.05
Er	0.31	0.12
Tm	0.05	0.02
Yb	0.38	0.14
Lu	0.07	0.02

melting and the amount of garnet in the source a range in La/Yb_n from 4.5 to 23 for the source region of the Swartruggens kimberlites is established. It is of interest that the estimated source region for the Swartruggens kimberlites lies within the compositional range of garnet lherzolites from the Kaapvaal craton, as determined by Gregoire *et al.*, (2003), lying at more enriched end of the spectrum.

The REE content, normalised to chondrite, of the mantle source region calculated to give rise to the Star primary kimberlite magma is illustrated in Figure 7.16b, assuming 1% melting and 4% residual garnet. The calculated source is enriched to approximately 17 times chondrite in La, and has approximately chondritic abundances of the heavy REE (Figure 7.16b). The range of possible source region compositions depending

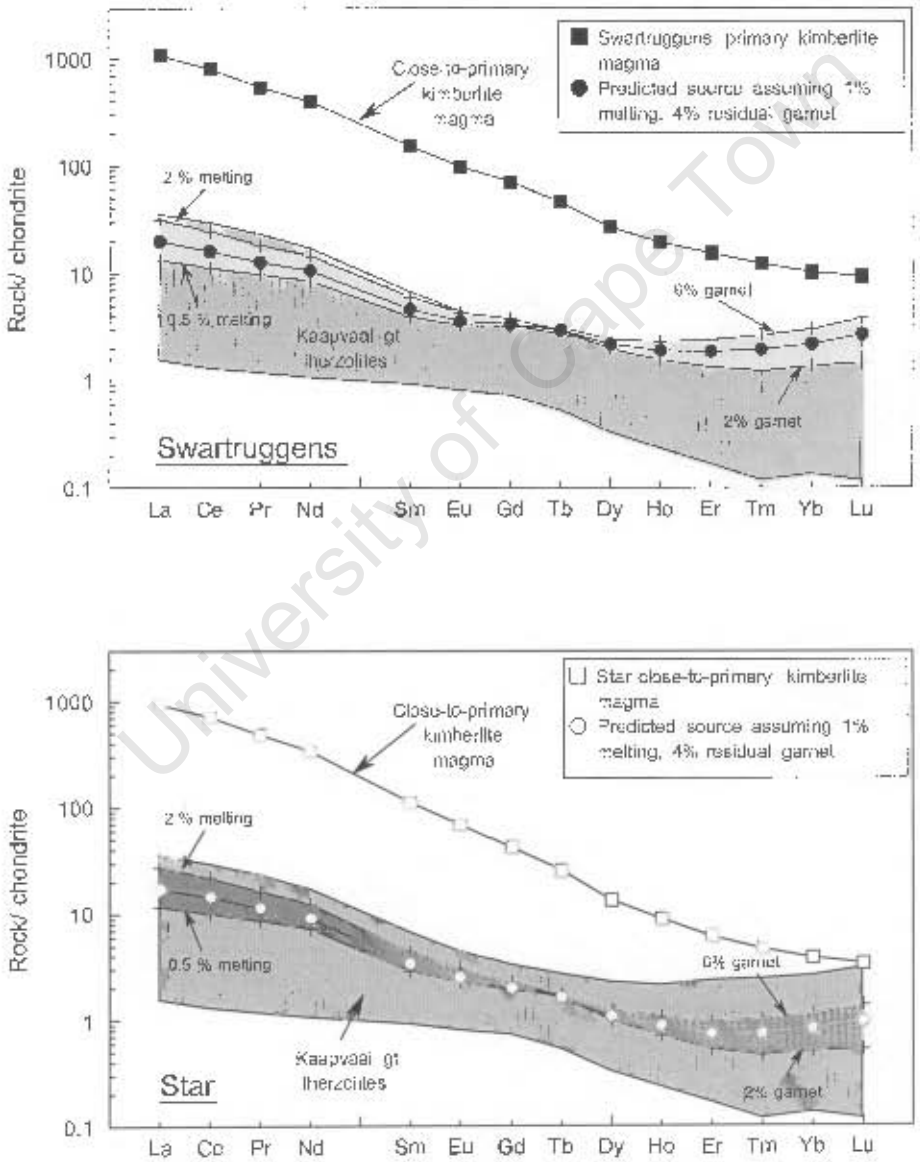

Figure 7.16 Chondrite normalised REE abundances in the calculated source regions of the Swartruggens (a) and Star (b) kimberlites. The effect of variable degrees of partial melting from 0.5 to 2%, and variable volume of residual garnet in the source between 2% and 6% is shown by the light grey and dark grey fields for Swartruggens and Star respectively. Fields for Kaapvaal lherzolites from Gregoire *et al.*, (2003); chondrite values from Sun and McDonough (1989).

on the degree of partial melting and the abundance of garnet in the source is also illustrated in Fig 7.16b; the light REE range from 12 to 27 times chondrite as degree of partial melting varies from 0.5% to 2%, and the heavy REE range from 0.5 to 1.4 times chondrite as residual garnet varies from 2 to 6 volume %. Taking these two variables together, the La/Yb_n ratio of the possible Star source region varies from 10 to 54, with La/Yb_n = 21 for 1% melting of a source containing 4 volume % residual garnet. The calculated REE range for the Star source region lies within the field of garnet lherzolites from the Kaapvaal craton (Gregoire *et al.*, 2003; Figure 7.16b).

The calculated source regions of the Swartruggens and Star kimberlites show several features in common

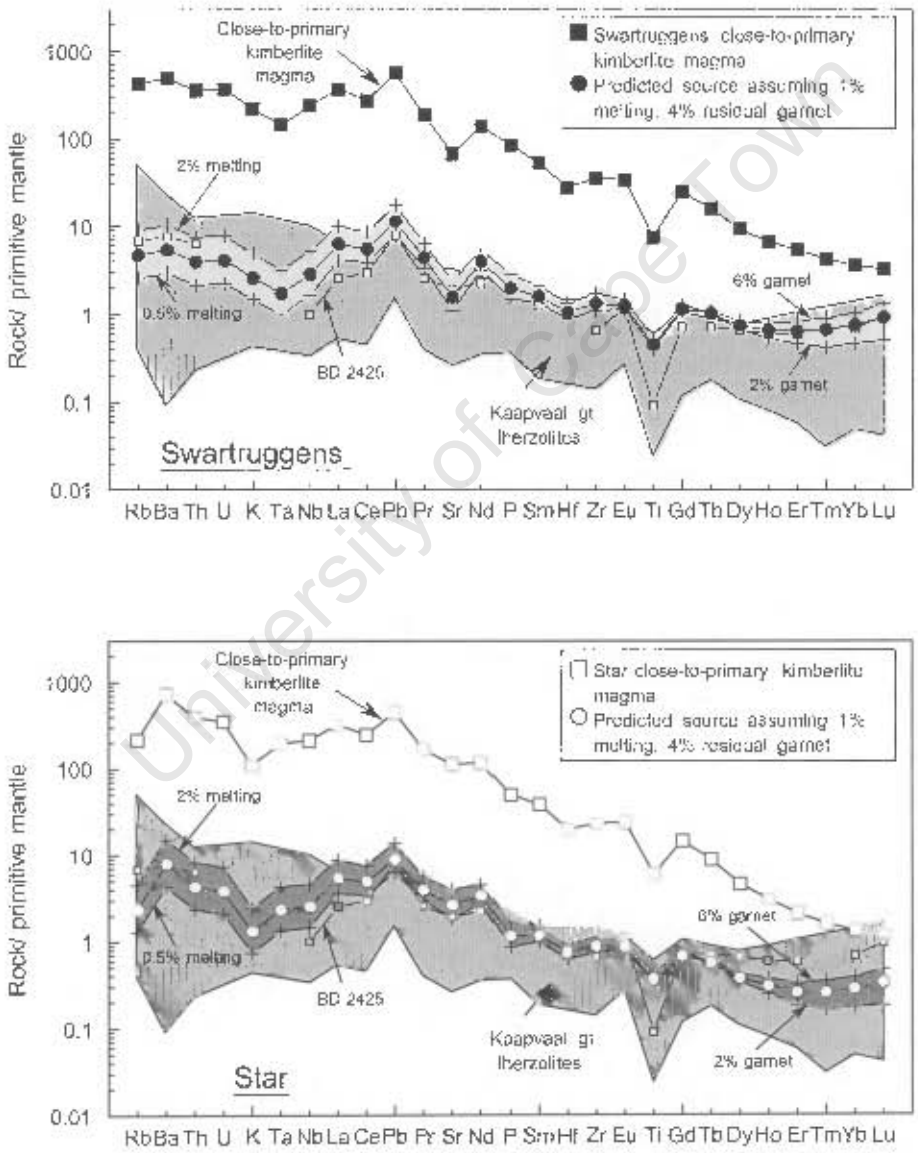

Figure 7.17 Primitive mantle normalised incompatible element abundances in the calculated source regions of the Swartruggens (a) and Star (b) kimberlites. The effect of variable degrees of partial melting from 0.5 to 2%, and variable volume of residual garnet in the source between 2% and 6% is shown by the light grey and dark grey fields for Swartruggens and Star respectively. Fields for Kaapvaal lherzolites from Gregoire *et al.*, (2003); primitive mantle values from Sun and McDonough (1989).

with respect to their incompatible trace element abundances (Figure 7.17). Using the same parameters as for the REE modelling (Tables 7.3 and 7.4), it is evident from Figure 7.17 that both source regions show enrichment in the more incompatible elements compared to the less incompatible elements, with the heavy REE being depleted, relative to primitive mantle (Swartruggens Yb = 0.8 times primitive mantle; Star Yb = 0.4 times primitive mantle, assuming 4 volume % residual garnet). Moderately sized negative Ti and K anomalies (Swartruggens $Ti/Ti^* = 0.4$, $K/K^* = 0.6$; Star $Ti/Ti^* = 0.5$, $K/K^* = 0.3$), and subdued negative Sr anomalies are features of both source regions. The negative Sr anomaly is slightly larger for the Swartruggens source ($Sr/Sr^* = 0.4$ than the Star source ($Sr/Sr^* = 0.7$), although Sr is a moderately mobile element and its analysed abundance should be treated with caution. The Star source region has suppressed Rb, Th and U relative to Ba, and this pattern is also evident, although less pronounced, in the Swartruggens source (Figure 7.17). Both source regions show subdued negative Nb-Ta anomalies (Swartruggens $La/Nb_n = 2.20$, Star $La/Nb_n = 39$) and less pronounced negative Hf anomalies. The Swartruggens and Star kimberlite source regions also both show strong positive Pb anomalies of similar size (Swartruggens $Pb/Pb^* = 2.3$; Star $Pb/Pb^* = 2.0$). The calculated source compositions for both the Swartruggens and Star kimberlites lie within the field of analysed garnet lherzolites from the Kaapvaal craton (Gregoire *et al.*, 2003, Figure 7.17).

7.4.3 Residual accessory phases

The above discussion assumes that the source regions of the Swartruggens and Star kimberlites consisted only of the minerals olivine, orthopyroxene, clinopyroxene and garnet. Since none of these minerals have very high partition coefficients for Ti, K, Nb or Ta (Table 7.4) the relative depletion in these elements on a primitive mantle normalised diagram in the primary kimberlite magmas (Figure 7.15) at both localities are automatically transferred to their respective source regions. However, it is possible that minor residual accessory phases could cause the observed anomalies. For example, phlogopite is present in many garnet lherzolite xenoliths from the Kaapvaal craton (e.g. Gregoire *et al.*, 2002, 2003) and, if residual after melting, could give rise to a magma with a negative K anomaly. Since the partition coefficients for Rb and Ba in phlogopite are also higher than any of the other primary silicate phases (e.g. Gregoire *et al.*, 2002), residual phlogopite could also account for the relative depletion in Rb present in the primary magma at Star, and, to a lesser extent, Swartruggens. A residual phase such as rutile or some other titanate, which are also present in some xenoliths from the Kaapvaal craton (e.g. Haggerty, 1983, Gregoire *et al.*, 2002), could similarly cause relative depletion in Ti, Nb and Ta in a derivative melt.

K is a stoichiometric component of phlogopite, with mantle phlogopites containing approximately 9 wt % K_2O (e.g. Gregoire *et al.*, 2002). The K contents of melts in equilibrium with residual phlogopite are therefore buffered by the phlogopite, and will remain at a constant concentration which is dependent only on the relative proportion of phlogopite entering the melt (Späth *et al.*, 2001). If phlogopite has a melt mode of between 50 and 70% (Wass and Rogers, 1980; Greenough, 1988), the melt in equilibrium with residual phlogopite should contain in excess of 4.5 wt. %, or 36 000 ppm K (le Roex *et al.*, 2003). The Swartruggens and Star kimberlites contain variable K abundances, which may partly reflect the mobility of this element. However, although the Swartruggens kimberlites generally fall within the field for possible equilibration

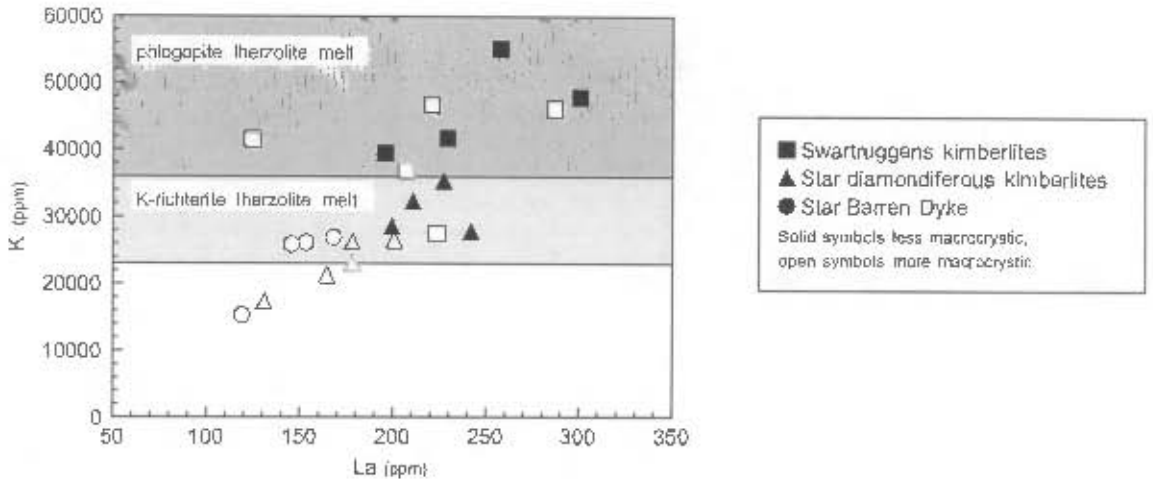

Figure 7.18 K concentrations in the Swartruggens and Star kimberlites relative to the fields of melts in equilibrium with residual phlogopite and K-richterite, after Späth *et al.* (2001).

against residual phlogopite, the Star kimberlites do not contain sufficient K (Figure 7.18). Although the possibility remains that there was residual phlogopite in the source after the Swartruggens kimberlite melt was extracted, some other process must be responsible for the K and Rb depletion in the Star kimberlites.

In addition, whereas early experimental evidence suggests that phlogopite may be stable during melting at pressures in excess of 40 Kb depending on the relative abundances of CO_2 and H_2O (e.g. Wendlandt and Eggler, 1980), more recent evidence suggests it is not stable during melting of garnet peridotite at pressures of greater than 4 - 5 GPa in the presence of CO_2 (Ulmer and Sweeney, 2002), rendering it unlikely that either the Swartruggens or Star kimberlites equilibrated against residual phlogopite. The Star kimberlite dykes contain enough K for K-richterite to be a residual K-bearing phase in the source (Figure 7.18). However, K-richterite does not usually coexist with garnet (Erlank *et al.*, 1987), and in addition, like phlogopite, is believed to be unstable on the peridotite solidus at pressures of greater than 4 - 5 GPa in the presence of CO_2 (Ulmer and Sweeney, 2002). The observed relative depletion in K and Rb in the primary kimberlite magmas from both localities are therefore believed to be features of their respective mantle source regions. A similar argument was put forward by le Roex *et al.* (2003), who attributed the much more pronounced negative K and Rb anomalies in Group I kimberlites to intrinsic features of their mantle source region.

Residual rutile in the source of island arc magmas has been proposed to explain the negative Nb and Ta anomalies observed in such magmas (e.g. Foley and Wheller, 1990; Foley *et al.*, 1999). Since rutile is a common phase in metasomatised mantle xenoliths from the Kaapvaal craton (e.g. Haggerty, 1983; Gregoire *et al.*, 2002), it is conceivable that it may have given rise to the negative Ti and coupled Nb and Ta anomalies observed in the Swartruggens and Star kimberlites. By extrapolation of adjacent elements on a primitive mantle normalised diagram it is estimated that for the source regions of the Swartruggens and Star kimberlites to show no Ti anomaly they must contain approximately 1600 ppm Ti. Rutile consists of almost

100% TiO_2, i.e. 599,500 ppm Ti, and thus the maximum amount of rutile that could be present in the source regions is approximately 0.2%, assuming the entire Ti budget is accommodated by rutile.

Partition coefficients for Nb in rutile in the literature are extremely variable (e.g. 16 to 30, Ryerson and Watson, 1987; 160, Boudinier *et al.*, 1996), although they are always high, with D_{Nb}/D_{Ta} ranging from 0.5 to 0.8 (Green, 1995). The effect of small amounts (<0.2 %) residual rutile on melts of a source where both Eu/Ti_n and $La/Nb_n = 1$, and Eu and La contents are similar to those of the calculated source regions of the Swatruggens and Star kimberlites (Table 7.5), are illustrated in Figure 7.19. A partition coefficient of Nb into rutile of 15 has been used, estimated from mineral data in Gregoire *et al.* (2002) and Gregoire *et al.* (2003), at the lower end of the range of published values. It is clear that small degree (~1%) melts which have equilibrated against 0.1 to 0.2% residual rutile develop Eu/Ti_n and La/Nb_n similar to those of the Swartruggens and Star kimberlites. Melts that have not equilibrated against residual rutile have much lower La/Nb_n and Eu/Ti_n than the kimberlites. Thus, from a geochemical perspective, it is possible that the negative Ti, Nb and Ta anomalies in the Swartruggens and Star kimberlite magmas were created by melting in the presence of residual rutile and are not features intrinsic to their respective source regions. However, there are three strong arguments against this scenario:

1 – As mentioned above, the maximum rutile in the source before melting is 0.2%, if the source regions are to have no Ti anomaly. Therefore an extremely small melt mode (of the order 1.2%) for rutile would be required to leave even 0.1% rutile in residual following a 1% melt extraction. This seems unreasonable considering the metasomatic nature of rutile or other titanate phases, and their likely low melting temperatures compared to other peridotitic minerals.

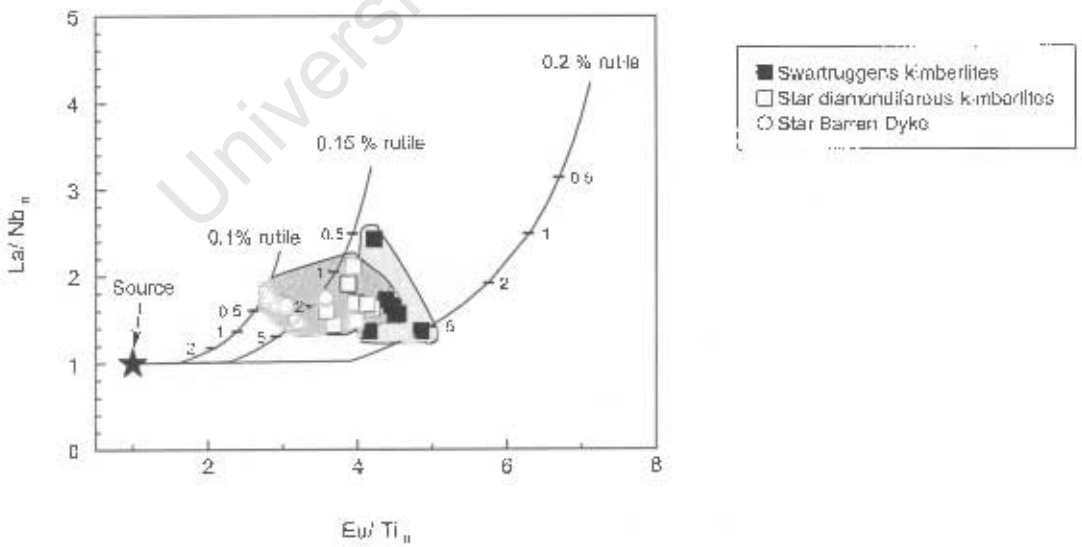

Figure 7.19 Calculated melting curves from a source which dispays no Nb or Ti anomalies relative to primitive mantle ($La/Nb_n = 1$; $Eu/Ti_n = 1$), containing 0.1%, 0.15% and 0.2% residual rutile, relative to the fields of the Swartruggens and Star kimberlites. D_{Nb} rutile/melt is assumed to be 15 (calculated from mineral data in Gregoire *et al.*, 2002, 2003). Numbers on melting trajectories represent percent of partial melting. See text for further discussion.

2 – Not only are the relative depletions in Nb, Ta and Ti of similar magnitudes in the Swartruggens and Star kimberlites, but in many other southern African Group II kimberlites as well (e.g. Tainton and McKenzie, 1994; le Roex, unpublished; Coetzee, unpublished). Given the heterogeneous distribution of metasomatic phases in the lithospheric mantle, as determined from xenoliths in kimberlites (e.g. Gregoire *et al.*, 2002) it seems unlikely that all Group II kimberlites originate from a source containing no less than 0.1%, and no more than 0.2%, rutile.

3 – Relative depletion in Ti, Nb and Ta is also observed in the Karoo and Etendeka flood basalts (e.g. Marsh and Eales, 1984; Figure 7.15). As these are clearly large volume melts, argued by some to be of lithospheric origin (e.g. Hawkesworth *et al.*, 1984), these are even more unlikely to have equilibrated against residual rutile.

The partition coefficient for Ti in clinopyroxene increases considerably with the carbonate content of the melt (Blundy and Dalton, 2000), and also increases with increasing ^{IV}Al content (Hill *et al.*, 2000). Although it also decreases with increasing pressure (Adam and Green, 1994), as kimberlite magmas have high carbonate contents it is important to note that it may be substantially higher than that used in the above model (Table 7.4). Thus it is possible that, with a higher partition coefficient for Ti, residual clinopyroxene could generate a negative Ti anomaly in kimberlite melts. Although a residual oxide phase therefore seem unlikely to be responsible for the negative Ti anomalies relative to primitive mantle in the Swartruggens and Star kimberlites, the coupled negative Nb and Ta are suggestive that such a phase may have played a role in the evolution of the source regions of the kimberlites. It is therefore concluded that the negative Ti, Nb and Ta anomalies present in the Swartruggens and Star, and other Group II, kimberlites are likely to be features intrinsic to their respective source regions. This theory is supported by the presence of strong negative Ti, and more subdued negative Nb-Ta anomalies in many of peridotite xenoliths from the Kaapvaal craton (e.g. BD 2421, Figure 7.17; Gregoire *et al.*, 2003).

7.5 The origins of geochemical variation between the individual kimberlite dykes at Swartruggens and Star

In the subsequent discussion and modelling, the assumption has been made that the compositions of individual dykes can be represented by the samples analysed from the respective dykes. It is recognised that some might represent multiple intrusions, but most show fairly restricted ranges in composition (as reported in Chapters 4, 5 and 6).

7.5.2 Swartruggens kimberlite dykes

It was illustrated in Section 7.2 that the geochemical variation within the Swartruggens kimberlite dykes could be produced by reasonable amounts of peridotite entrainment and fractional crystallisation from the least macrocrystic Main Dyke sample. However, the possibility that the individual dykes were formed from separate magmas should be considered. The isotopic compositions of the individual dykes are similar, suggesting derivation from the same source region, and thus the only other possible source of variation

within the dykes is the degree of partial melting giving rise to the magmas. The REE variation produced by variable degrees of partial melting of the calculated source region for the Swartruggens close-to-primary kimberlite magma (Table 7.5) is illustrated in Figure 7.20. For higher degrees of partial melting the resultant magmas become less enriched in the light REE, whereas lower degrees of partial melting result in a magma which is more enriched in the light REE, relative to chondrite (Figure 7.20). The heavy REE abundances are buffered by the residual garnet in the source and remain fairly constant for different degrees of partial melting.

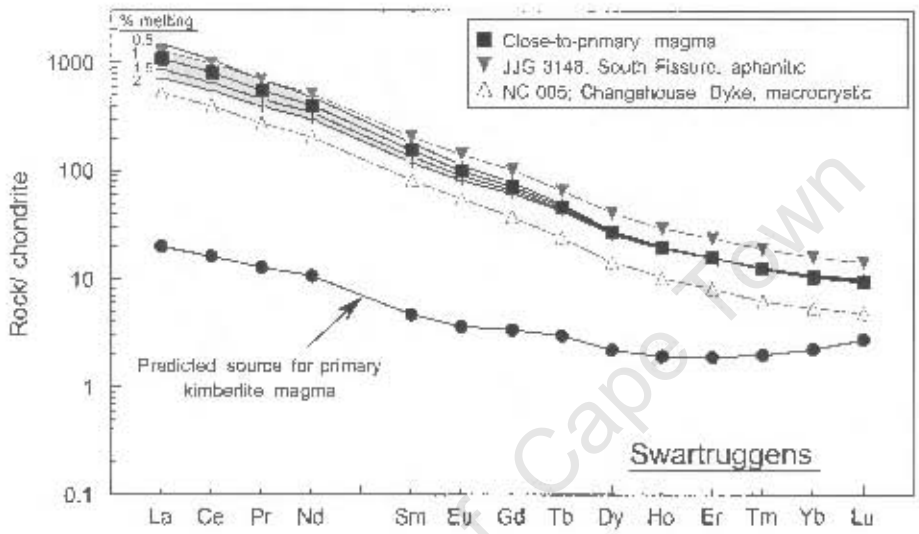

Figure 7.20 The range of chondrite normalised REE abundances, shown by shaded field, produced by variable degrees of partial melting, between 0.5 and 2%, of the source region calculated to give rise to the Swartruggens close-to-primary kimberlite magma by 1% melting, relative to the compositions of the Swartruggens kimberlite dykes. Chondrite values from Sun and McDonough (1989).

Since the Swartruggens kimberlite dykes show sub-parallel chondrite normalised REE patterns with similar La/Yb_n, variable degrees of partial melting cannot account for the variation observed between the individual dykes (Figure 7.20). Therefore, as discussed in Section 7.2, the Main Dyke is inferred to be the closest to the primary kimberlite magma, and the geochemical variation within this dyke is consistent with entrainment of up to 30% peridotite. The geochemical variation between the Main and Changehouse Dykes is concluded to be due to up to 50% peridotite entrainment by the latter, of a different average composition to that entrained by the Main Dyke, as discussed in Section 7.2.1.3. The South Fissure has a composition consistent with up to 10 % fractionation of olivine and phlogopite from the Main Dyke, although the Nd isotope systematics also suggest some degree of peridotite entrainment by the former. The Third Lease samples are all altered to a considerable degree, and were discarded in Section 7.2. However, these samples have similar concentrations of the immobile REE to the Main Dyke (Figure 5.2a and b), and at the time of emplacement they may have represented close-to-primary magma compositions.

7.5.3 Star kimberlite dykes

The diamondiferous Star kimberlite dykes have similar isotopic signatures (Table 6.2), and are therefore believed to originate from the same source region. However, although the variations in absolute major and trace element abundances of the samples from the diamondiferous Star kimberlite dykes are consistent with reasonable degrees of lherzolite entrainment or crystal fractionation, as discussed in Section 7.2, the difference in La/Yb_n of the different dykes, described in Chapter 5, is not accounted for by these processes. Increased degrees of partial melting lowers the La/Yb_n of the magma, as the light REE become less enriched in resultant melts, whereas the heavy REE abundances are buffered by the residual garnet (Figure 7.21a). A range of possible La/Yb_n of ~155 to ~245 is produced in melts of the calculated source of the Star close-to-primary kimberlite magma (reported in Table 7.5) by varying the degrees of partial melting between 0.5% and 2% (Figure 7.21). A melting curve showing the change in La/Yb_n with Ce for partial melts of the source giving rise to the close-to-primary Star kimberlite magma is illustrated in Fig 7.21b, and it is evident that the Star kimberlite samples plot close to this curve, with deviations in Ce content either side consistent with small degrees of peridotite entrainment and fractional crystallisation as discussed in Section 7.2. Whereas the Wynandsfontein and East Star Dyke samples have La/Yb_n consistent with approximately 0.8 - 1.3% melting of this source, the Byrnes and Clewer Dyke samples have lower La/Yb_n consistent with slightly higher degrees (1.5 - 2.2%) partial melting of this source (Figure 7.21b).

The diamondiferous Star kimberlite dykes are therefore believed to originate from the same source region and to represent a continuum of small degrees of partial melting, from the lower degree melts of the Wynandsfontein and East Star Dykes to the slightly higher degree melts of the Byrnes and Clewer Dykes. Further variation between the dykes is established by entrainment of peridotite (dominant within the East Star Dyke) and fractional crystallisation of olivine and phlogopite (dominant within the Byrnes Dyke), with samples from the Wynandsfontein and Clewer Dykes representing closest-to-primary magma compositions (Figure 7.21b).

It was illustrated in section 7.2 that the composition of the Barren Dyke cannot be produced by addition of peridotite or fractional crystallisation from the other kimberlite dykes at Star. In addition, the Nd and Hf isotope compositions of this dyke are significantly more radiogenic than the other kimberlite dykes, confirming derivation from a geochemically distinct source region.

Following the experimental work of Herzberg (1992) which illustrated the pressure sensitivity of the relative proportions of garnet and clinopyroxene entering the melt during partial melting of garnet peridotite, and the consequent change in $CaO/(CaO + Al_2O_3)$ of melts produced at different pressures, Sweeney and Winter (1999) suggested that the depth of origin of kimberlites can be estimated from their whole-rock $CaO/(CaO + Al_2O_3)$. Applying this method to the Star kimberlites, the diamond bearing dykes are calculated to originate at a pressure of approximately 13 GPa (Figure 7.22). The Barren Dyke samples have a much lower $CaO/(CaO + Al_2O_3)$ than the other Star kimberlites, and are calculated to originate at lower pressures of approximately 4-7 GPa (Figure 7.22). Although there is a considerable range in $CaO/(CaO + Al_2O_3)$ within the diamondiferous and the barren kimberlite dykes (Figure 7.22), and thus these pressure estimates are

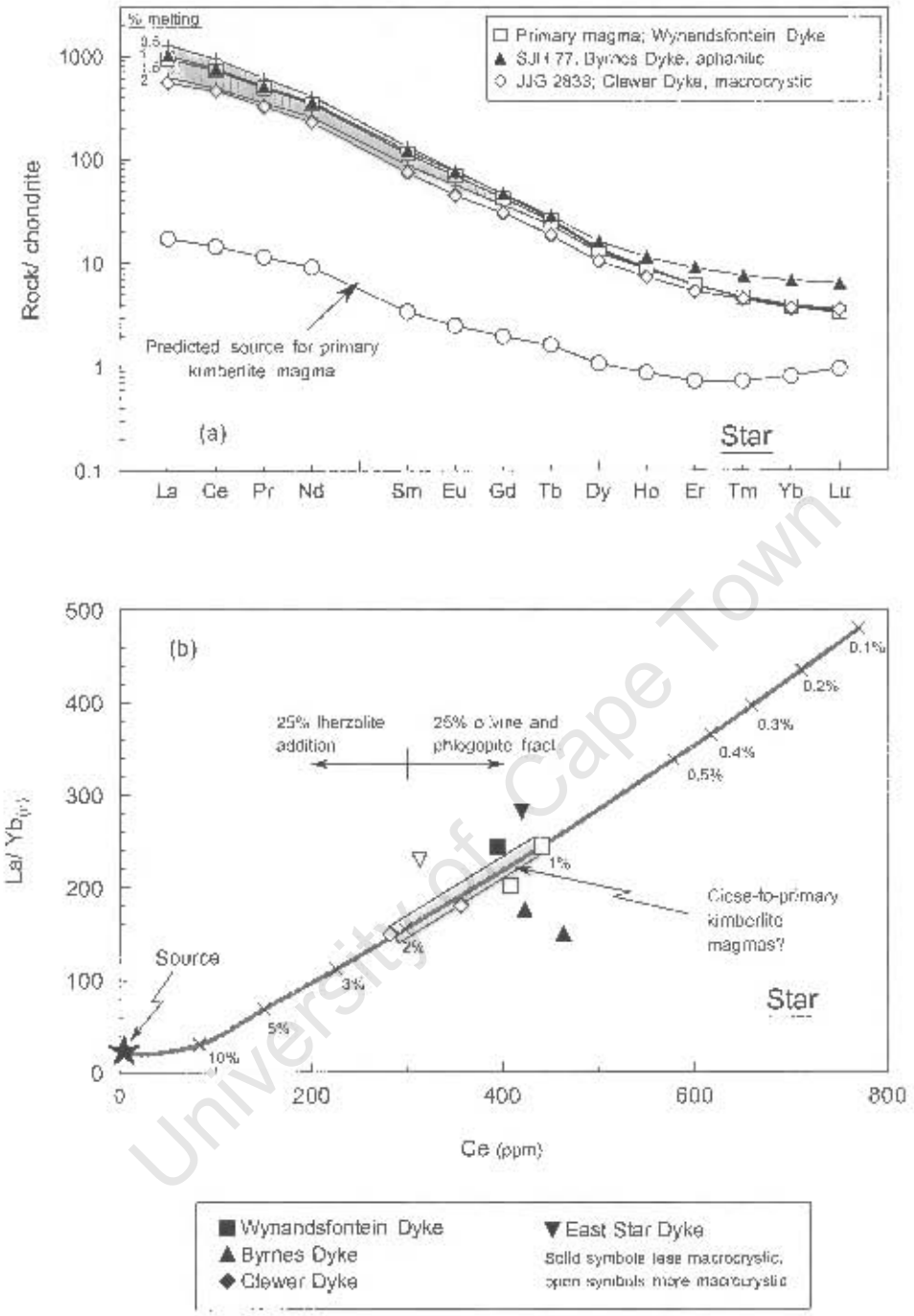

Figure 7.21 (a) The range of chondrite normalised REE abundances, shown by shaded field, produced by variable degrees of partial melting, between 0.5 and 2%, of the source region calculated to give rise to the Star close-to-primary kimberlite magma by 1% melting, relative to the compositions of the Star kimberlite dykes. Chondrite values from Sun and McDonough (1989).

(b) Melting curve illustrating the change in La/Yb_n with Ce for different degree melts from the source region calculated to give rise top the Star close-to-primary kimberlite magma by 1% melting, relative to the compositions of the Star kimberlite dykes. The shaded field shows an array of possible primary melts produced by 1 – 2% melting of this source.

not well constrained, this observation is interesting because it illustrates that not only does the Barren Dyke have a different source region to the other kimberlite dykes at Star, but also that it originated from pressures outside the diamond stability field. The relatively shallow origin of the Barren Dyke thus offers a plausible explanation for the absence of diamonds in this kimberlite dyke.

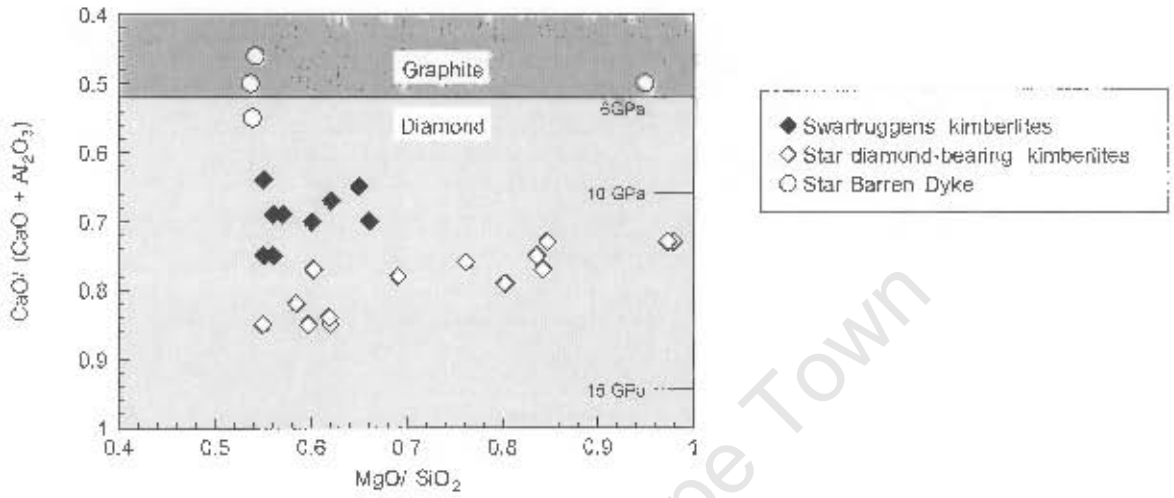

Figure 7.22 $CaO/(CaO + Al_2O_3)$ ratios of the Swartruggens and Star diamondiferous kimberlites and the Star Barren Dyke illustrated as an indicator of melt segregation depth, after Sweeney and Winter (1999). The low $CaO/(CaO + Al_2O_3)$ of the Barren Dyke suggests an origin outside the diamond stability field.

7.6 The origin of the Swartruggens Muil Dyke

Several lines of evidence, summarised below, suggest that the Swartruggens Muil Dyke is unrelated to the kimberlite dykes:

- Petrographically, the Muil Dyke is very different to the kimberlite dykes and is classified as a lamprophyre. Although macrocrystic in places, the macrocrysts are all olivine, and these olivines are euhedral, unlike the rounded macrocrysts in the kimberlite dykes.
- The Muil Dyke has different major and trace element composition, with considerably higher SiO_2, Al_2O_3 and Na_2O, and lower K_2O and CO_2 than the kimberlite dykes, for a similar MgO content (Table 4.1). Despite the higher SiO_2 content, incompatible element concentrations are much lower in the Muil Dyke than the kimberlite dykes, and thus this dyke cannot have evolved from the primary kimberlite magma. The differences in major element composition cannot either be explained by peridotite entrainment by, or crustal contamination of, the primary kimberlite magma, and the Muil Dyke displays strong within dyke trends towards of olivine accumulation that are unrelated to the trends of the kimberlite dykes (Figure 7.23).

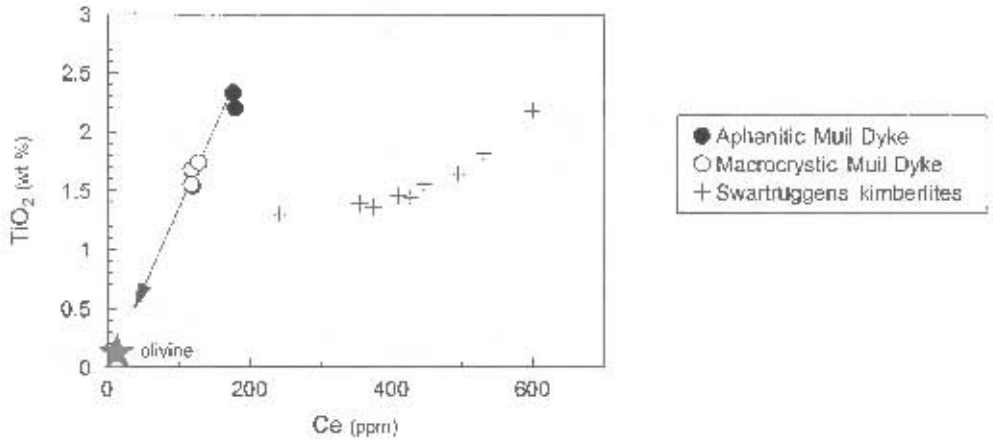

Figure 7.23 TiO_2 vs. Ce in the Mull Dyke compared to the Swartruggens kimberlites, illustrating that this dyke is unrelated to the kimberlite dykes.

- Although La/Yb_n are slightly lower in the Mull Dyke (La/Yb_n = 72.5 ± 3.0) than in the Swartruggens close-to-primary kimberlite magma (La/Yb_n = 105; Table 7.2), the Mull Dyke composition cannot be produced by higher degrees of melting of the source region of the Swartruggens kimberlite magmas. To produce a melt with La concentrations similar to those of the Mull Dyke requires approximately 10% partial melting of the calculated source for the kimberlite dykes, and as the heavy REE abundances in the melt are buffered by residual garnet, such a melt would have a very low La/Yb_n of 12.5.
- The chondrite normalised REE pattern of the Mull Dyke cannot be produced by a second batch of melting of the kimberlite source region after a 1% melt has been extracted. Although a 1 to 2% melt of the depleted source could account for the light REE abundances, as mentioned above the heavy REE abundances in the melt are buffered by the residual garnet and remain a factor of two times chondrite too high (Figure 7.24).

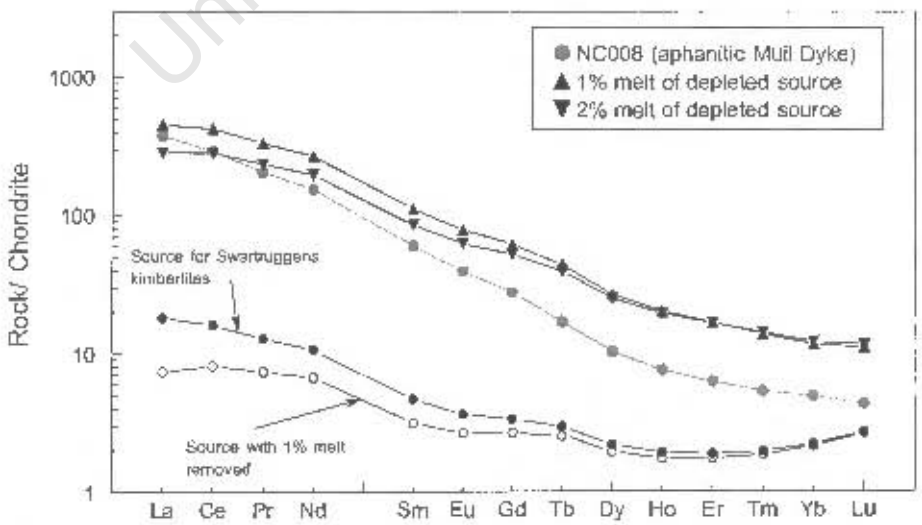

Figure 7.24 Chondrite normalised REE abundances of the source for the Swartruggens kimberlites after a 1% melt has been removed, and the compositions of subsequent 1% and 2% melts of this source relative to the composition of the Swartruggens Mull Dyke. Chondrite values from Sun and McDonough (1989).

- In addition to being less enriched in the incompatible trace elements than the Swartruggens kimberlite dykes, the primitive mantle normalised signature of the Muil Dyke also differs from those of the kimberlite dykes in having no Ti anomaly (Figure 5.5). Since this anomaly is believed to be a source region feature of the kimberlite dykes (see above) the Muil Dyke must originate from a source that is geochemically distinct from the kimberlite source regions.
- The Muil Dyke has a considerably higher initial $^{143}Nd/^{144}Nd$ ratio (with minimum $^{143}Nd/^{144}Nd_i$ = 0.511971 ± 15 to 0.511990 ± 11; Table 6.1) than the Swartruggens close-to-primary kimberlite magma ($^{143}Nd/^{144}Nd$ = 0.511855 ± 19; Table 6.1), and therefore must have an isotopically distinct source region. The difference in Nd isotope composition is unlikely to be due to peridotite entrainment, as this process appears to have lowered, rather than raised, the $^{143}Nd/^{144}Nd_i$ ratios in the more macrocrystic kimberlite samples (Figure 7.8).

Since the Muil Dyke is not a kimberlite, the high contamination indices (following Clement, 1982) of the Muil Dyke samples reported in Table 4.1 are irrelevant, and it is considered that crustal contamination is unlikely to have severely affected the whole-rock geochemistry of the Muil Dyke to the same extent as the kimberlite samples. Major and trace elements within the dyke form coherent trends (Figures 7.23, 7.25, 4.1 and 5.1-5), with the more macrocrystic samples having compositions consistent with up to 30% olivine addition to the most MgO and Ni rich aphanitic sample (NC 008), and sample JJG 3141 having a composition consistent with 20% olivine fractionation from NC 008 (Figure 7.25). On a plot of MgO vs. Ni, the trend of olivine accumulation within the macrocrystic samples is slightly displaced from that of olivine fractionation within the aphanitic samples, possibly due to the loss of some MgO subsequent to the serpentinisation of the olivine macrocrysts. The trend of olivine, rather than peridotite, entrainment is consistent with the petrographic observation that olivine is the only macrocryst phase in the Muil Dyke samples (Table 2.1). Together with the apparently unstrained, euhedral nature of the olivine macrocrysts, this suggests that the Muil Dyke represents a partial olivine cumulate, rather than having entrained peridotite *en route* to the surface in a similar manner to the kimberlite dykes.

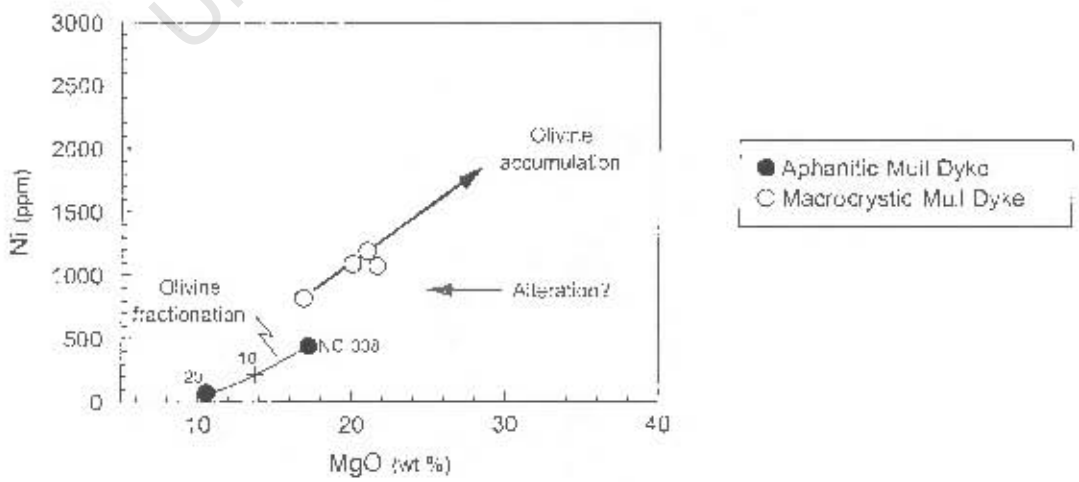

Figure 7.25 The variation in MgO and Ni concentrations in the Muil Dyke relative to trends of olivine accumulation and fractionation. Numbers refer to percentage olivine fractionation.

The strong enrichment in the more incompatible elements relative to the less incompatible elements in the Muil Dyke (Figure 5.5), suggests that it is a low degree partial melt. However, due to its barren nature, there is no reason to conclude that it originated in the garnet stability field. Figure 7.26 shows, for illustration, calculated source region compositions assuming for the 3% partial melting in the garnet and spinel stability fields. The source mineral proportions and melt modes used are the same as for calculating the kimberlite source region characteristics, (Tables 7.3 and 7.4) but with spinel substituted for garnet for melting in the spinel stability field. The two calculated source compositions have essentially the same abundances of all elements except the heavy REEs; a source located in the spinel stability field would be more depleted in the heavy REE (Lu = ~0.12 times primitive mantle), whereas a source located within the garnet stability field would be less depleted in the heavy REE (Lu = ~0.4 times primitive mantle; Figure 7.26).

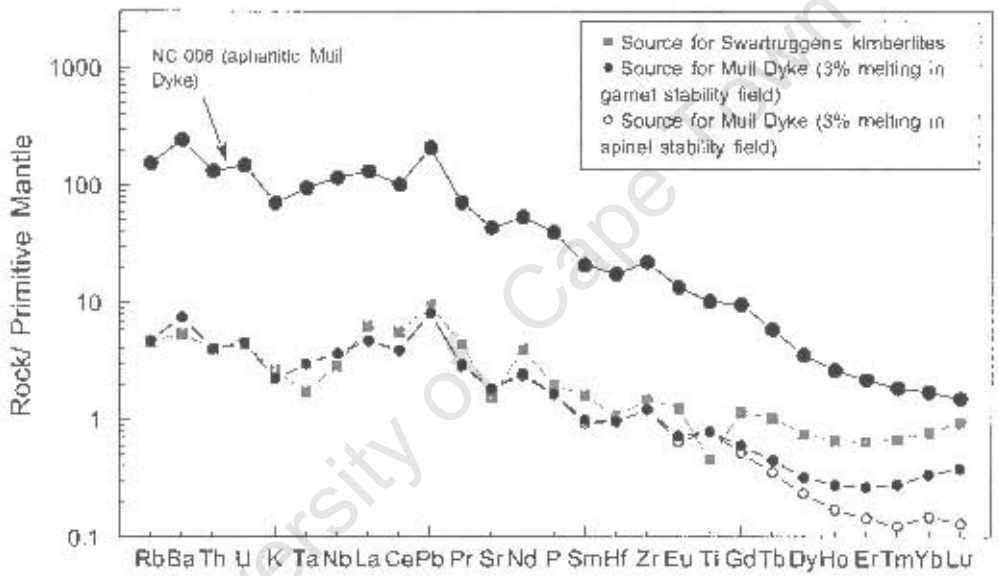

Figure 7.26 Calculated abundances of the incompatible elements, relative to primitive mantle, in the possible source regions of the Swartruggens Muil Dyke assuming 3% melting in the garnet and spinel stability fields. See text for further discussion. Partition coefficients given in Table 7.4; primitive mantle values from Sun and McDonough (1989).

Both calculated source regions are enriched in the more incompatible elements relative to the less incompatible elements relative to primitive mantle (Rb = ~4.5 time primitive mantle) and show rather similar primitive mantle normalised patterns to the Swartruggens kimberlite dykes, with moderate negative K anomalies and Ba being slightly enriched relative to Rb. The calculated Muil Dyke source region also shows a negative Sr anomaly and slight relative depletion in Nb and Ta, although these features are not so strongly defined as in the kimberlite source region. Two marked differences between the Muil Dyke source and the kimberlite source region are evident from Figure 7.26: the absence of a negative Ti anomaly in the Muil

Dyke source region and the relative enrichment of the heavy REE in the kimberlite source region relative to the Muil Dyke source region, whether the latter is located within the spinel or garnet stability fields.

7.7 Location of the source regions: lithospheric vs. asthenospheric contributions

Detailed petrogenetic modelling of trace element behaviour during kimberlite petrogenesis has revealed that the source regions of both Group I and Group II kimberlites are likely to be located within the lithosphere (e.g. Tainton and McKenzie, 1994; le Roex *et al.*, 2003). Tainton and McKenzie (1994) calculated a source for Group II kimberlites that is depleted in the heavy REE relative to primitive mantle, despite being strongly enriched in the more incompatible elements. They proposed that such a signature required a depletion event and subsequent metasomatism, and that the source for these kimberlites must be located within the lithospheric, rather than convecting asthenospheric, mantle for the depleted signature to be preserved. le Roex *et al.*, (2003) and Harris *et al.* (2004) reached a similar conclusion following detailed trace element modelling of the petrogenesis of the Kimberley group, and the Uintjiesberg Group I kimberlites, respectively. The incompatible trace element ratios of the Group I kimberlites (e.g. Nb/U, Ce/Pb) are similar to those of ocean island basalts (OIB), and on this basis these authors concluded that the source regions of Group I kimberlites had been strongly metasomatised by plume related melts or fluids. The hypotheses of Tainton and McKenzie (1994), and le Roex *et al.* (2003) and Harris *et al.* (2004) are in good agreement with Sr, Nd and Pb isotope data, which suggest an ancient enriched source for Group II kimberlites and a slightly depleted source for Group I kimberlites, implying a major contribution from the underlying, convecting mantle to the latter.

Hf isotope systematics provide an alternative approach to determining the location of kimberlite source regions. Nowell *et al.* (1999) proposed a sub-lithospheric origin for both groups, based on their negative $\Delta\varepsilon_{Hf}$ signatures, which they interpreted to reflect a subducted slab component to the source region at depths greater than the lithospheric mantle. Although this was later revised on the basis of more data to apply only to Group I kimberlites (Nowell *et al.*, 2004) and Dowall *et al.* (2003a) consider that the continuum in Hf isotope compositions between Group I and Group II kimberlites is not supportive of completely separate source regions for the two groups. The same conclusion was drawn by Pearson *et al.* (1995, 2003a) based on Os isotope data, which support an asthenospheric origin for both Group I and Group II kimberlites.

After careful selection of the close-to-primary kimberlite magmas at Swartruggens and Star, the calculated incompatible trace element compositions of their respective source compositions are reported in Table 7.5. The dichotomy of source enrichment relative to primitive mantle, discussed below, (Figure 7.17) requires at least a two-stage evolution of the source region. Together with the close-to-primary Sr, Nd and Hf isotope ratios of these kimberlites a number of lines of evidence are provided, discussed below, that both the Swartruggens and Star kimberlites have origins within metasomatised continental lithospheric mantle. The

geochemical compositions of the respective source regions do not require a contribution from the sub-lithospheric mantle.

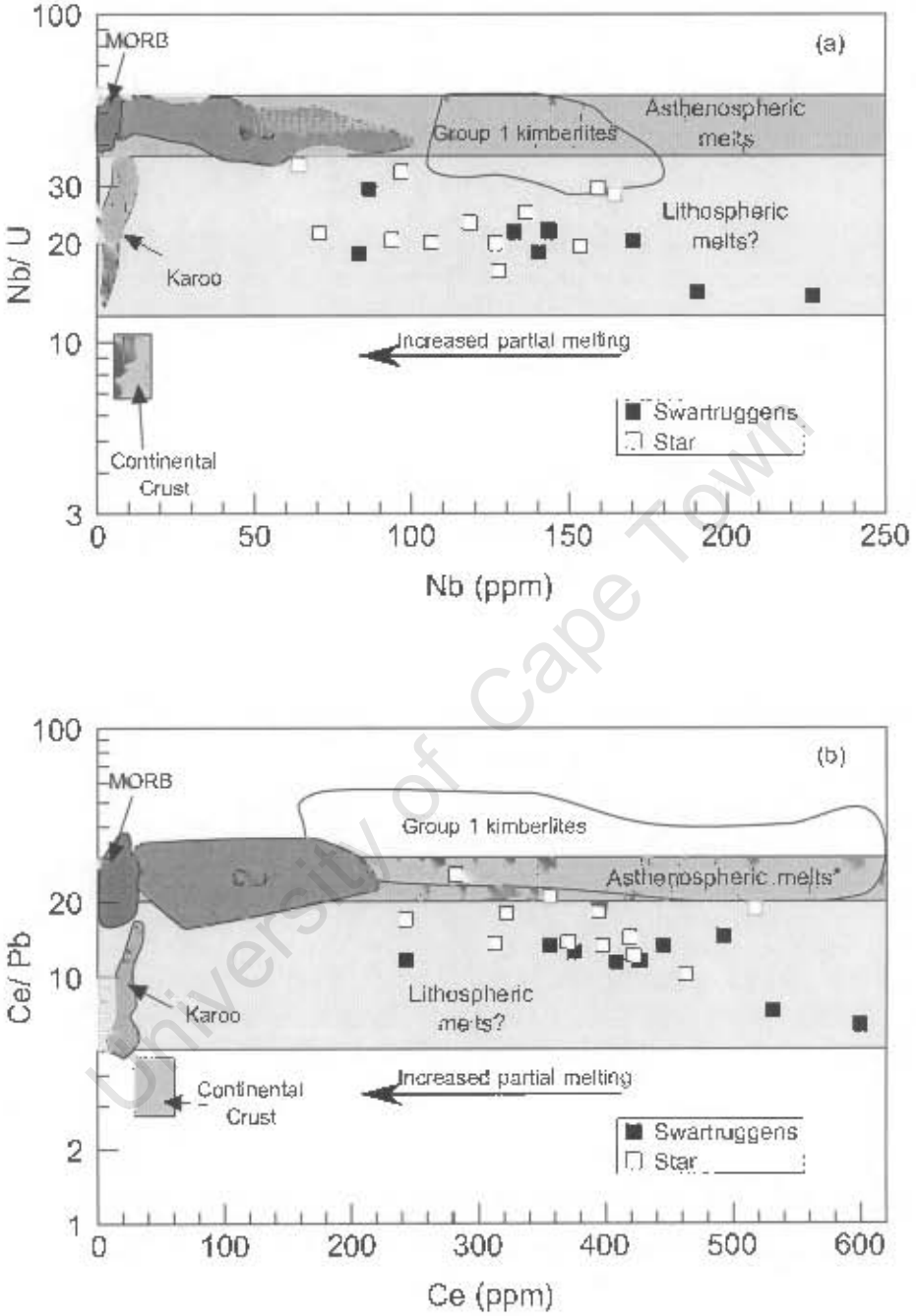

Figure 7.27 Selected incompatible trace element ratios in the Swartruggens and Star kimberlites relative to the field of asthenospheric melts. Data for MORB and OIB from Hofmann *et al.* (1986); Group I kimberlites from le Roex *et al.* (2003); Karoo basalts from Marsh and Eales (1984); continental crust from Rudnick and Fountain (1995).

The heavy REE in the calculated source regions of both the Star and Swartruggens kimberlites are depleted relative to primitive mantle, with maximum depletion of 0.7 and 0.5 times primitive mantle for Star and Swartruggens, respectively, in the presence of 4 volume % residual garnet (Figure 7.17). This inferred depletion suggests that the source regions of both localities had previously undergone melt extraction, in

agreement with the conclusions drawn by Tainton and McKenzie (1994) for the source regions of other southern African Group II kimberlites. The high Mg# of the Swartruggens and Star close-to-primary kimberlite magmas (Mg # = 0.85 for both magmas; Table 7.2) require equilibration against highly magnesian residual olivine, with $Fo_{\sim 90}$ (using an olivine-melt K^{D}_{Fe-Mg} of 0.36, Herzberg and O'Hara, 2002), consistent with derivation from a refractory, previously depleted, mantle source.

Sub-lithospheric melts (mid-ocean ridge basalts and OIB) have a limited range of Nb/U of 37 ± 10, and Ce/Pb of 25 ± 10 (Hofmann *et al.*, 1986). Whereas Group I kimberlites, thought to carry a plume signature, have Nb/U and Ce/Pb which fall within this range (le Roex *et al.*, 2003), both the Swartruggens (average Nb/U = 18.63 ± 2.1; Ce/Pb = 9.8 ± 2.3) and Star (average Nb/U = 24.8 ± 5.91; Ce/Pb = 15.9 ± 4.09) kimberlites have considerably lower ratios for these elements (Figure 7.27). Samples suspected to have suffered crustal contamination or alteration have already been discarded (Sections 7.2.1 and 7.2.2), and addition of minor amounts of typical continental crust (Nb/U = 7-10, Ce/Pb = 3-4.5; Rudnick and Fountain, 1995) could not account for the deviation of the Swartruggens and Star kimberlites from those of asthenospheric melts; addition of the order of 50% crust would be required and such a large quantity would have a noticeable effect on the major and trace element abundances of the kimberlites. The Swartruggens and Star kimberlites are therefore inferred to have source regions that are geochemically distinct from the source of mid-ocean ridge basalts (MORB), OIB and Group I kimberlites. It is of significance that Nb/U and Ce/Pb in the Karoo flood basalts, argued by some to have a source in the sub-continental lithospheric mantle (e.g. Hawkesworth *et al.*, 1984), show a similar range to the Swartruggens and Star kimberlites (Figure 7.27; Marsh and Eales, 1984).

Both the Swartruggens and Star have enriched initial Sr and Nd isotope ratios (Figure 7.28a), requiring a source that has been isolated from the convecting mantle for some time. The Hf isotope compositions of both these kimberlites lie close to the mantle array and thus do not provide any further constraints.

The simplest concept model is that the source regions of these kimberlites are located within the sub-continental lithospheric mantle, with no contribution from the sub-lithospheric mantle. An alternative hypothesis is that the kimberlites are related to plume upwelling, where the source of plume material is recycled or delaminated sub continental lithospheric mantle (e.g. McKenzie and O'Nions, 1983; le Roex, 1986). It is not possible to unequivocally rule out this latter alternative, but it is noteworthy that such extreme Sr and Nd isotope and trace element ratios as those present in the kimberlite magmas have not yet been recognised in the ocean basins surrounding southern Africa. Consequently, a model whereby these two Group II kimberlites are derived from within the sub-continental lithospheric mantle is favoured.

However, whereas the Mg# of the kimberlite magmas and REE of the calculated source regions require a previously depleted source, the incompatible element enrichment of the calculated source regions (Figure 7.17) requires a subsequent metasomatic event. Model Nd enrichment ages, calculated relative to depleted mantle and using the Sm/Nd of the estimated source regions (Table 7.4) suggest that this enrichment occurred at a minimum of 1Ga, and is thus unlikely to be related to Mesozoic plume upwelling. Therefore it

is believed that the trace element and isotopic characteristics of the Swartruggens and Star kimberlites reflect those of the sub-Gondwana lithospheric mantle, metasomatised prior to the Mesozoic break-up of the super-continent. However, the superposition of Mesozoic plume-related metasomatism on a more ancient metasomatic signature is not precluded.

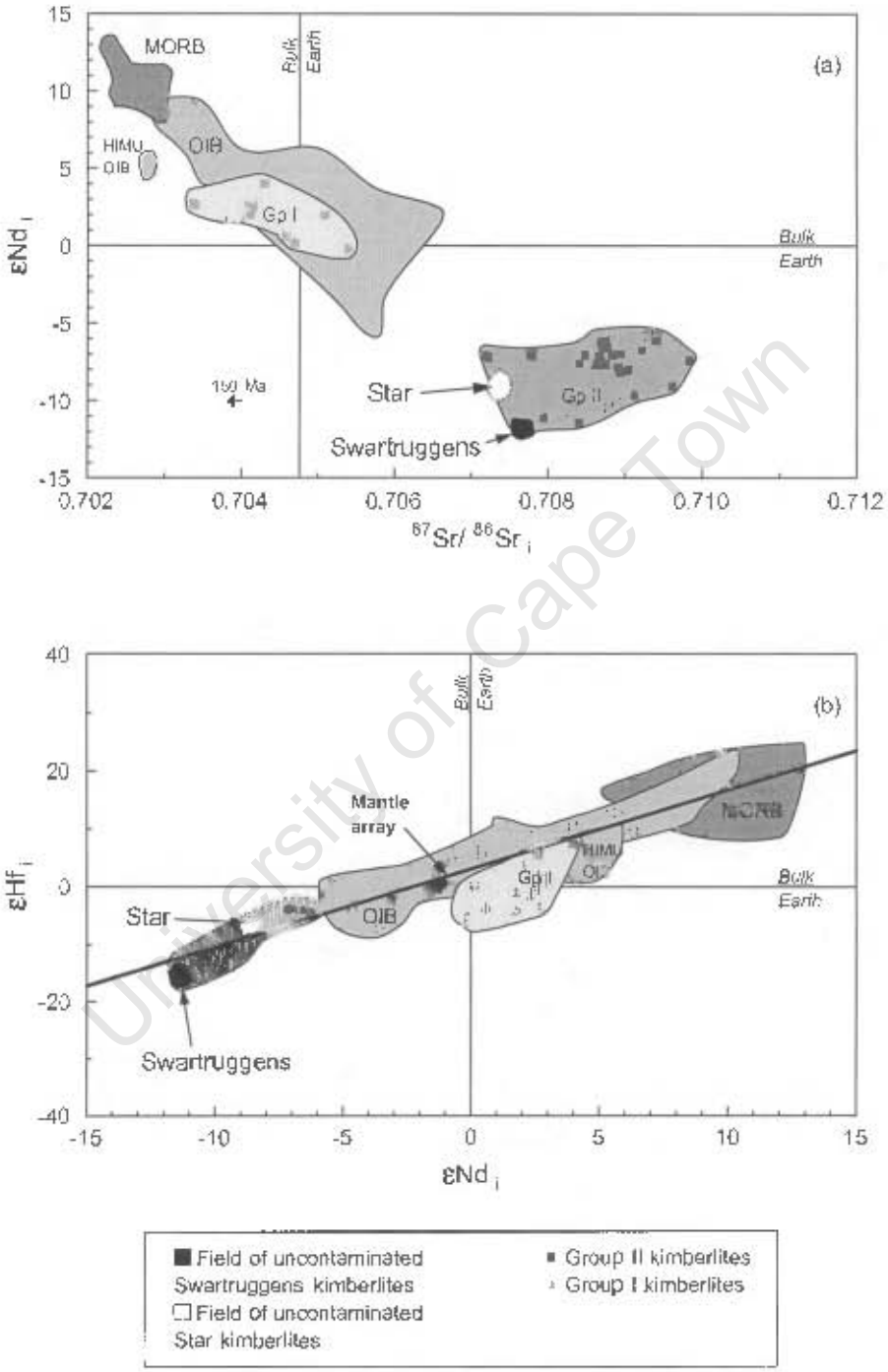

Figure 7.28 Variations in isotopic composition of the uncontaminated Swartruggens and Star kimberlites. Initial ratios and ε values for Swartruggens are calculated assuming an age of 156 Ma, and for Star assuming an age of 128 Ma. MORB and OIB fields are present day, but the small change produced by the evolution of primitive mantle over 150 Ma is shown by a vector on (a), vector is too small to see on (b). Mantle array shown in (c) from Vervoort *et al.* (1999). Data for MORB and OIB fields from Patchett and Tatsumoto (1980), Patchett (1983), Stile *et al.* (1986), Salters and Hart (1991), Chauval *et al.* (1992), Salters and White (1998), Nowell *et al.* (1998), Salters (1996). Data for Group I and Group II kimberlites fields from Smith (1983a and b), Tainton (1994), Clark (1994), Nowell *et al.* (1999 and 2004).

Chapter 8

Summary and Conclusions

8.1 Introduction

Swartruggens and Star are Group II kimberlite dyke swarms, located in the Northwest Province and the Free State, respectively, South Africa. The major and trace element and isotopic compositions, together with detailed petrographic descriptions, for a suite of samples from each of the kimberlite dykes exposed in the mining operations at Swartruggens (Main Dyke, Changehouse Dyke, South Fissure and Third Lease) and Star (Clewer, Wynandsfontein, East Star, Byrnes and Barren Dykes), and the Swartruggens Muil lamprophyric dyke have been used to describe the petrographic and geochemical variation present within and between individual dykes at each locality. Geochemical trends within each locality have been used to assess the extent of the effects of post-melting processes such as peridotite entrainment, crustal assimilation, fractional crystallisation and alteration on the geochemistry of the samples studied. Close-to-primary magma compositions at each locality have thus been isolated, and the origin of the geochemical variation present within and between individual dykes has been assessed. Using simple non-modal equilibrium partial melting modelling of garnet lherzolite source, constraints have been placed on the source region trace element characteristics of the Swartruggens and Star kimberlites, taking into account the effects of variables such as the degree of partial melting, source mineralogy and the role of accessory residual phases. Combined with Sr, Hf and Nd isotopic data, the source region trace element characteristics have then been used to constrain the source region location and evolution, and the likely contributions made by lithospheric and asthenospheric mantle.

8.2 Petrography

The petrography of the Swartruggens and Star kimberlite dykes and the Muil lamprophyre has been described in detail from thin sections of each sample. Both kimberlites are micaceous, and are broadly petrographically similar. They contain variable proportions of rounded, anhedral and fractured olivine and phlogopite macrocrysts, attributed to be disaggregated mantle peridotite, in a groundmass consisting predominantly of phlogopite with lesser calcite and sometimes diopside. The olivine macrocrysts are commonly altered to serpentine and are often replaced by calcite or partially replaced by phlogopite, with associated opaque oxides. The majority of phenocrysts in both kimberlites are phlogopite, with minor diopside present in some dykes. The rarity of olivine as phenocrysts and a groundmass phase in both kimberlites may in part reflect the degree of alteration, such that it is now difficult to distinguish from

groundmass calcite and serpentine. Phlogopite macrocrysts, phenocrysts and in the groundmass is commonly rimmed by tetraferriphlogopite. Groundmass calcite occurs as discrete euhedral crystals, as an interstitial phase, and as secondary calcite veins. In addition to phlogopite and calcite, serpentine, apatite and opaque oxides occur as minor groundmass phases. Distinctive feature so the individual dykes at each locality are summarised below.

- The Swartruggens Main Dyke contains between 10 and 30 volume % macrocrysts, dominantly of serpentinised olivine with lesser phlogopite, with up to 20 volume % phenocrysts of phlogopite, in a groundmass consisting almost entirely of phlogopite with minor calcite. It differs from the other Swartruggens kimberlite dykes in that phenocrysts and groundmass diopside are extremely rare.
- The most macrocrystic of the Swartruggens kimberlite dykes is the Changehouse Dyke, which contains up to 50% macrocrysts, predominantly of olivine, either serpentinised or replaced by calcite, and lesser phlogopite. It is also distinct from the Main Dyke in having phenocrysts of, and groundmass, diopside. The Changehouse Dyke is also distinct from the other Swartruggens kimberlite dykes in having rare olivine phenocrysts, which were not identified in samples from the other dykes.
- The South Fissure is the most evolved of the Swartruggens kimberlite dykes and has been noted to contain groundmass sanidine (Allan, 1990). It contains up to 35 volume % macrocrysts of olivine and phlogopite, with up to 20% phenocrysts dominantly of phlogopite with lesser diopside. Similarly to the other Swartruggens kimberlite dykes the groundmass of the South Fissure consists primarily of phlogopite, with up to 10 volume % calcite and minor diopside.
- Extreme alteration has affected all the samples taken from the Third Lease at Swartruggens; olivine macrocrysts are completely replaced by calcite, and in places phlogopite is partially altered to chlorite. These samples contain up to 25 volume % macrocrysts, the majority of which are relic olivine with subordinate phlogopite. Phenocrysts of phlogopite and minor diopside constitute up to 30 volume % of the Third Lease samples, in a groundmass of phlogopite with up to ~30% calcite.
- Petrographically, the Swartruggens Muil Dyke is different from the kimberlite dykes. It has previously been correctly classified as a lamprophyre, and consists of euhedral serpentinised olivine macrocrysts in a matrix of phlogopite and diopside needles with abundant groundmass sanidine.

- The least macrocrystic Star kimberlite dyke is the Byrnes Dyke. This contains 15 to 30 volume % macrocrysts, dominantly of olivine with subordinate phlogopite, may of which are disaggregated into small (~1mm) rounded fragments. All the phenocrysts in the Byrnes Dyke are phlogopite, and these constitute up to 20 volume % of the dyke, in a groundmass composed primarily of phlogopite with less abundant calcite and minor interstitial serpentine.
- The East Star and Wynandsfontein Dykes are similar petrographically, containing between 20 and 40 volume % macrocrysts, which are predominantly olivine with lesser phlogopite, and up to 10 volume % phlogopite phenocrysts. However, rare olivine phenocrysts were identified in the Wynandsfontein Dyke but olivine phenocrysts are absent from the East Star Dyke samples. The majority of the groundmass of these two dykes is equigranular subhedral phlogopite with abundant, but subordinate, calcite.

- A distinguishing feature of the Clewer Dyke relative to the other Star kimberlite dykes, is the presence of minor diopside, both as a phenocryst phase (up to 2 volume %) and in the groundmass (up to 6 volume %). Groundmass calcite is also less abundant in this dyke, constituting up to 15 volume % of the dyke compared to up to 37 volume % of the Wynandsfontein Dyke. In other respects the Clewer Dyke is similar to the other Star kimberlite dykes with up to 30 volume % macrocrysts, dominantly of olivine with subordinate phlogopite, with up to ~20 volume % phlogopite phenocrysts. Rare olivine phenocrysts are also present in this dyke. Similarly to the other Star kimberlite dykes, the groundmass consists predominantly of phlogopite.
- Petrographically, the Star Barren Dyke can be divided into two categories: three of the samples contain abundant phlogopite, whereas the fourth sample is considerable less micaceous. The micaceous samples are petrographically similar to the other Star kimberlite dykes, containing approximately 30 volume % macrocrysts, the majority of which are olivine with lesser phlogopite. Phlogopite phenocrysts constitute approximately 5 volume % of the dyke, and reside in a groundmass that consists predominantly of phlogopite with lesser calcite. The less micaceous sample is more macrocrystic (40 volume % macrocrysts) and contains no phenocrysts. The groundmass of this dyke also contains abundant phlogopite, but calcite is minor and constitutes only 5 volume % of the sample, and the remainder of the groundmass is primarily serpentine and chlorite.

8.3 Close-to-primary magmas

Kimberlites are hybrid rocks, containing xenoliths and xenocrysts of both mantle and crustal material entrained *en route* to the surface (e.g. Clement, 1983). They also have high volatile contents, and are permeable and porous, making them susceptible to alteration both by deuteric fluids and percolating groundwater (e.g. Berg, 1994). Together with fractional crystallisation, these processes may substantial affect the bulk rock geochemistry of a kimberlite (e.g. Mitchell, 1995). Both the Swartruggens and Star kimberlites have widely varying whole-rock geochemistry, both within and between individual dykes (e.g. Swartruggens MgO = 12.0 – 25.4 wt %, SiO_2 = 25.1 – 41.6 wt %, La = 124 – 300 ppm Ni = 617 – 1814 ppm; Star MgO = 5.50 – 36.7 wt %, SiO_2 = 22.7 – 43.7 wt %, La = 131 – 285 ppm, Ni = 684 – 1988 ppm; Tables 4.1, 4.2, 5.1 and 5.2). However, much of this variation is considered to be due to the post-melting processes described above. Using trends in major and trace element geochemistry between samples from each locality, the geochemical effects of these processes have been established, and samples believed to have suffered extensive alteration or crustal contamination have been discarded. The close-to-primary kimberlite magmas at each locality are inferred to have compositions between the trends of crystal fractionation and peridotite entrainment within the unaltered or uncontaminated samples. Key geochemical characteristics of these close-to-primary magmas are described below.

- The Swartruggens close-to-primary kimberlite magma contains ~38.1 wt %SiO_2, ~21.1 wt % MgO, ~8.54 wt % CaO and ~6.64 wt % K_2O, and is best represented by the Main Dyke.

- For a similar MgO content (~21.8 wt %), the Star close-to-primary kimberlite magma is less enriched in SiO_2 (~36.2 wt %) and K_2O (3.32 wt %) and more enriched in CaO (~10.5 wt %) than that at Swartruggens, and is best represented by the Wynandsfontein Dyke.
- The close-to-primary magmas at both Swartruggens and Star are strongly enriched in both the compatible and incompatible trace elements, with greater enrichment in the more, relative to the less, incompatible trace elements relative to primitive mantle.
- Superimposed on relatively smooth enrichment patterns, both close-to-primary kimberlite magmas display strong negative K, Ti and Sr anomalies, subdued negative Nb, Ta and Hf, and strong positive Pb anomalies, when normalised to primitive mantle.
- The primary magmas at both localities have steep chondrite normalised REE patterns, with greater enrichment in the light REE than the heavy REE. The Swartruggens close-to-primary kimberlite magma is more enriched in the heavy REE (Gd/Ybn = 6.9) than that at Star (Gd/Yb_n = 11.0).
- With respect to their isotope geochemistry, the close-to-primary kimberlite magmas at Swartruggens and Star are slightly different. The Swartruggens close-to-primary magma has $^{87}Sr/^{86}Sr_i$ = 0.707711 ± 14, ε_{Ndi} = -11.37 ± 0.25 and ε_{Hfi} = -15.74 ± 0.11, whereas the close-to-primary kimberlite magma at Star has slightly less radiogenic ratios, with $^{87}Sr/^{86}Sr_i$ = 0.707476 ± 13, ε_{Ndi} = -8.49 ± 0.13, ε_{Hfi} = -7.50 ± 0.28. The age difference of approximately 30 Ma between these two kimberlites is not sufficient to account for the difference in their initial isotopic ratios.

8.4 The origin of geochemical variation at Swartruggens

With respect to their major and trace element geochemistry, the individual dykes at Swartruggens have wide ranges in composition (Table 4.1). However, the individual dykes at Swartruggens also have compositions that are distinct from each other with respect to some elements. The Changehouse Dyke has higher SiO_2 concentrations and is less enriched in the incompatible trace elements than the other kimberlite dykes (Figures 4.1 and 5.5c). The South Fissure is the most enriched in the incompatible elements and is also enriched in TiO_2 compared to the other dykes (Figures 5.5d and 4.1e). Despite having similar abundances of the incompatible elements to the Main Dyke (Figure 5.5), the Third Lease samples have lower MgO and higher CaO and CO_2 abundances than the other Swartruggens kimberlite dykes. Post-melting processes such as alteration, crustal contamination, peridotite entrainment and fractional crystallisation can account all of the variation within and between the kimberlite dykes as described below, but the Muil lamprophyric dyke cannot be related to the kimberlite dykes by these processes.

- The variation within the Swartruggens Main dyke can be accounted for by up to 30% entrainment of peridotite, followed by small amounts of crustal contamination of some samples.
- The composition of the Changehouse Dyke is consistent with up to 50% peridotite entrainment by the close-to-primary kimberlite magma, although the average composition of the peridotite is different to that entrained by the Main Dyke. Thus the magma must have separated at depth. Many of the Changehouse Dyke samples have also suffered extensive alteration.

- The South Fissure samples have more evolved compositions than the close-to-primary kimberlite magma, and this dyke is concluded to have first entrained small quantities of peridotite and subsequently fractionally crystallised olivine and phlogopite.
- The samples taken from the Third Lease have suffered extensive alteration, but have concentrations of the immobile elements similar to those of the close-to-primary kimberlite magma.
- The Swartruggens Muil Dyke is unrelated to the Swartruggens kimberlites and originates from a source that has a distinct isotopic, with much higher $^{143}Nd/^{144}Nd$, and trace element signature from the source of the kimberlites.

8.5 The origins of the geochemical variation at Star

Individual dykes at Star show wide, but overlapping, variations in major and trace element geochemistry. Much of the variation within the diamondiferous dykes can be accounted for by variable degrees of peridotite entrainment, crustal assimilation, fractional crystallisation and alteration. However the different La/Yb_n of the individual dykes cannot be explained by these processes. In addition, these processes cannot account for the difference in geochemical and isotopic composition of the Barren Dyke relative to the diamondiferous kimberlite dykes. The individual dykes are therefore believed to be related as summarised below:

- The difference in La/Yb_n of the Star kimberlite dykes is interpreted to represent a continuum of small degree melts of the same source region, with the Wynandsfontein and East Star Dykes being slightly lower degree melts than the Clewer and East Star Dykes.
- The Byrnes Dyke has a composition consistent with approximately 20% fractional crystallisation of olivine and phlogopite from the close-to-primary kimberlite magma.
- Further geochemical variation is introduced by variable degree of peridotite entrainment and fractional crystallisation within individual dykes, with peridotite entrainment being dominant within the East Star dyke.
- The Star Barren Dyke is unrelated to the diamondiferous kimberlite dykes and originated from a source region with and isotopically distinct signature, with higher ε_{Hf} and ε_{Nd} than that of the other kimberlite dykes. This dyke probably originated from shallower depths, outside the diamond stability field.

8.6 Source region characteristics and location

The trace element compositions of the source regions giving rise to the Swartruggens and Star kimberlites has been estimated using simple partial melting modelling, assuming small degrees of non-modal equilibrium partial melting of a garnet lherzolite source as suggested by experimental work (e.g. Dalton and Presnall, 1998). As the exact degree of partial melting is unknown, the effects of varying the degrees of partial melting between 0.5 and 2% was illustrated in Figures 7.16 and 7.17. It is evident that for higher degrees of melting the source region must have been more enriched in the more incompatible elements. Since the heavy REE partition strongly into garnet, the volume of residual garnet in the source region is also

an important variable to consider. For larger volumes of residual garnet the source regions must have been more enriched in the heavy REE, as illustrated in Figures 7.16 and 7.17. Assuming the close-to-primary kimberlite magmas at Swartruggens and Star represent 1% melting in the presence of 4 volume % residual garnet, the geochemical characteristics of the respective source regions are summarised below:

- On a chondrite normalised REE diagram, the source regions of the Swartruggens and Star kimberlites show greater enrichment in the light REE than the heavy REE (Swartruggens source La/Yb_n = 7.4; Star source La/Yb_n = 21).
- Both source regions are characterised by enrichment in the more incompatible elements relative to the less incompatible elements, and are depleted in the heavy REE, relative to primitive mantle, with greater depletion in the heavy REE at Swartruggens than at Star.
- Superimposed on relatively smooth enrichment patterns, the calculated source regions of the Swartruggens and Star kimberlites show similarly sized strong negative Ti, K and Sr anomalies when normalised to primitive mantle. Although the negative Ti and K anomalies present in the kimberlite magmas could be created by residual accessory phases such as phlogopite, K-richterite and titanates, these phases are not believed to have been residual after the partial melting events giving rise to these two kimberlites.

Combining the source region trace element characteristics with the initial Sr, Nd and Hf isotopic compositions of the primary kimberlite magmas, a number of lines of evidence, summarised below, suggest that the respective source regions of the Swartruggens and Star kimberlites are located within the lithospheric, with no contribution from the asthenospheric, mantle.

- The enriched Sr, Nd and Hf isotopic compositions of the close-to-primary kimberlite magmas require an isotopically enriched mantle source region, which has been separated from the convecting mantle for some time (following Smith, 1983; Figure 7.28).
- The depletion in heavy REE, and enrichment in the more incompatible elements relative to primitive mantle requires that the source region underwent a melt extraction event and subsequent metasomatism. For the depleted signature to be preserved, the source region must be located within the lithospheric, rather than the convecting asthenospheric mantle.
- Nb/U and Ce/Pb ratios of the Swartruggens and Star kimberlites are similar to those of Karoo and Etendeka flood basalts, considered by some authors to be of lithospheric origin (e.g. Hawkesworth *et al.*, 1984), but are much lower than those of asthenosphere derived MORB and OIB (Hofmann *et al.*, 1986). Group I kimberlites, which are believed to originate from a source which has been metasomatised by Mesozoic plume related fluids or melts, have incompatible trace element ratios similar to MORB, and therefore the Swartruggens and Star kimberlites are believed to originate from a source which has not been metasomatised by a mantle plume.

The source regions of the Swartruggens and Star kimberlites are therefore inferred to represent the sub-Gondwana lithospheric mantle. Their geochemical signature does not require a contribution from Mesozoic plumes during the break-up of the supercontinent.

References

Allan, P. (1990). Petrographic description of samples 5 collected at Helam mine, Swartruggens, 21/02/90. Internal Report.

Allsopp, H. L. & Barrett, D. R. (1975). Rb-Sr age determinations on South African kimberlite pipes, *Physics and Chemistry of the Earth* **9**, 605-617.

Allsopp, H. L. & Kramers, J. D. (1977). Rb-Sr and U-Pb age determinations on southern African kimberlite pipes. *Second International Kimberlite Conference Extended Abstracts*, Carnegie institute, Washington D. C.

Barrett, D. R. & Berg, G. W. (1975). Complementary petrographic and Strontium isotope ratio studies of South African kimberlite. *Physics and Chemistry of the Earth* **9**, 619-635.

Barton, J. M., Barton, E. S & Kröner, A. (1999). Age and isotopic evidence for the origin of the Archaean granitoid intrusives of the Johannesburg Dome, South Africa. *Journal of African Earth Sciences* **28**, 693-702.

Berg, G. W. (1994).Alteration reactions which affect the geochemistry of kimberlites and xenoliths and the search for unaltered mantle minerals. PhD. Thesis, University of Cape Town.

Berg, G. W. & Allsopp, H. L. (1972). Low $^{87}Sr/^{86}Sr$ ratios in fresh South African kimberlites. *Earth and Planetary Sciences Letters* **16**, 27-30.

Birch, G. F. (1981). The karbonat-bombe; a precise, rapid and cheap instrument to determine calcium carbonate in sediments and rocks. *Transactions of the Geological Society of South Africa* **84**, 199-203.

Boudinier, J.-L., Merlet, C., Bedini, R. M., Simien, F., Remaidi, M & Garrido, C. J. (1996). Distribution of niobium, tantalum, and other highly incompatible trace elements in the lithospheric mantle: the spinel paradox. *Geochimica et Cosmochimica Acta* **60**, 545-550.

Boyd, F. R. (1987). High- and low- temperature garnet peridotites xenoliths and their possible relation to the lithosphere-asthenosphere boundary beneath southern Africa. In: Nixon, P. H. (Ed.), *Mantle xenoliths*. J. Wiley and sons, New York, pp.403-412.

Canil, D. & Scarfe, C. M. (1990). Phase Relations in Peridotite + CO_2 Systems to 12 GPa: Implications for the Origin of Kimberlite and Carbonate Stability in the Earth's Upper Mantle. *Journal of Geophysical Research* **95** (B10), 15805-15816.

Carlson, R. W. (1995). Isotopic inferences on the chemical structure of the mantle. *Journal of Geodynamics* **20**, 365-386.

Chauval, C. Hofmann, A.W., and Vidal, P. (1992). HIMU-EM: The French Polynesian connection. *Earth and Planetary Science Letters* **110**, pp.99-119.

Chazey III, W. J., Neal, C. R., Jain, J. C. & Kinman, W. S. (2003). A reappraisal of Rb, Y, Zr, Pb and Th value in geochemical reference material BHVO-1. *Geostandards Newsletter* **27**, 181-192.

Clark, T. C. (1994). An integrated geochemical and isotopic study of the Prieska Province kimberlites from the Republic of South Africa. MSc. Thesis, Bernard Price Institute of Geophysics, University of the Witwatersrand.

Clement, C. R. (1982). A comparative geological study of some major kimberlite pipes in the Northern Cape and Orange Free State. PhD. Thesis, University of Cape Town.

Clement, C. R., Skinner, E. M. W. & B. H. Scott Smith (1984). Kimberlite Redefined. *Journal of Geology* **92**, 223-228.

Clifford, T. N. (1966). Tectono-metallogenic unitsand metallogenic provinces of Africa. *Earth and Planetary Science Letters* **1**, 241-434.

Crough, S. T., Morgan, W. J., & Hargraves, R. B. (1980). Kimberlites: their relation to mantle hotspots. *Earth and Planetary Science Letters* **50**, 260-274.

Dalton, J. A. & Presnall, C. (1998). The continuum of primary carbonatitic-kimberlitic melt compositions in equilibrium with lherzolite: data from the system CaO-MgO-Al_2O_3-SiO_2-CO_2 at 6 Gpa. *Journal of Petrology* **39**, 1953-1964.

Dawson, J. B. (1971). Advances in kimberlite geology. Earth Sciences Review **7**, 187-214.

Dawson, J. B. (1980). *Kimberlites and their xenoliths*. Springer-Verlag, Berlin, Heidleberg, New York.

DePaolo, D. J. & Wasserberg, G. J. (1976). Nd isotopic variation and petrogenetic models. *Geophysical Research Letters* **3**, 249-252.

de Wit, M. J., Roering, C., Hart, R. J., Armstrong, R. A., de Ronde, C. E. J., Green, R. W. E., Tredoux, M., Peberdy, E. & Hart, R. A. (1992). Formation of an Archaean continent. *Nature* **357**, 553-562.

Deer, W. A., Howie, R. A. & Zussman, J. (1998). *An introduction to the rock-forming minerals*. Longman.

Dowall, D. P., Pearson, D. G., Nowell, G. M., Kjarsgaard, B. A., Armstrong, J. and Horstwood, M. S. A. (2003a). Comparative geochemistry of kimberlites from the Lac de Gras field, NWT – an integrated isotopic and elemental study. *Extended abstracts, Eighth International Kimberlite Conference*, Victoria.

Dowall, D. P., Pearson, D. G. & Nowell, G. M. (2003b). Chemical pre-concentration procedures for high-precision analysis of Hf-Nd-Sr isotopes in geological materials by plasma ionisation multi-collector mass smectrometry (PIMMS) techniques. In: Holland, J. G. & Tanner, S. D. (Eds.) *Plasma Source Mass Spectrometry: Applications and Emerging Technologies*. The Royal Society of Chemistry, Cambridge, 321-337.

Edgar, A. D., Arima, M., Baldwin, D. K., Bell, D. R., Shee, S. R., Skinner, E. M. W. & Walker, E. C. (1988). High-pressure-high-temperature melting experiments on a SiO_2-poor aphanitic kimberlite from the Wesselton mine, Kimberley, South Africa. *American Mineralogist* **73**, 524-533.

Edgar, A. D. & Charbonneau, H. E. (1993. Melting experiments on a SiO_2-poor, CaO-rich aphanitic kimberlites from 5-10 GPa and their bearing on sources of kimberlite magmas. *American Mineralogist* **78**, 132-142.

Eggler, D. H. & Wendlandt, R. F. (1979). Experimental studies on the relationship between kimberlite magmas and partial melting of peridotite. In: Boyd, F. R. & Meyer, H. O. A. (Eds.) *Kimberlites, Diatremes and Diamonds: their Geology, Petrology and Geochemistry. Proceedings of the Second International Kimberlite Conference, Vol. 1*. Washington, DC: American Geophysical Union, pp. 330-338.

Erlank, A. J., Waters, F. G., Hawkesworth, C. J., Haggerty, S. E., Allsopp, H. L., Rickard, R. S. and Menzies, M. (1987). Evidence for Mantle Metasomatism in Peridotite Nodules from the Kimberley Pipes, South Africa. In: Menzies, M. A. & Hawkesworth, C. J. (Eds.) *Mantle Metasomatism*. Academic Press Geology Series, Harcourt Brace Jovanovich, pp221-309.

Fesq, H. W., Kable, E. J. D. & Gurney, J. J. (1975). Aspects of the geochemistry of kimberlites from the Premier Mine and other South African occurrences, with particular reference to the rare earth elements. *Physics and Chemistry of the Earth* **9**, 686-707.

Finnerty, A. A. & Boyd, F. R. (1987). Thermobarometry for garnet peridotite xenoliths: a basis for mantle stratigraphy. In: Nixon, P. H. (Ed.), Mantle xenoliths, J. Wiley and sons, New York, pp.381-402.

Foley S. F. & Wheller, G. E. (1990). Parallels in the origin of the geochemical signatures of island arc volcanics and continental potassic igneous rocks: The role of residual titanates. *Chemical Geology* **85**, 1-18.

Foley, S. F., Barth, M. G. & Jenner, G. A. (2000). Rutile/melt partition coefficients for trace elements and an assessment of the influence of rutile on the trace element characteristics of subduction zone magmas. *Geochimica et Cosmochimica Acta* **64**, 933-938.

Fraser, K. J. & Hawkesworth, C. J. (1992). The petrogenesis of group 2 ultrapotassic kimberlite from the Finsch mine, South Africa. *Lithos* **28**, 327-345.

Girnis, A. V., Brey, G. P. & Ryabchikov, I. D. (1995). Origin of Group IA kimberlites: fluid saturated melting experiments at 45-55 kbar. *Earth and Planetary Science Letters* **134**, 283-296.

Govindaraju, K. (1989). Compilation of working values and sample description for 272 geostandards. *Geostandards Newsletter* **13** (special issue),1-113.

Govindaraju, K. (1994). Compilation of working values and sample description for 383 geostandards. *Geostandards Newsletter* **18** (special issue), pp.158.

Green, T. H. (1995). Significance of Nb/Ta as an indicator of geochemical processes in the crust-mantle system. *Chemical Geology* **120**, 347-359.

Gregoire, M., Bell, D. R. & le Roex, A. P. (2002). Trace element geochemistry of glimmerite and MARID xenoliths: their relationship to kimberlite and to phlogopite-bearing peridotite revisited. *Contributions to Mineralogy and Petrology* **142**, 603-625.

Gregoire, M., Bell, D. R. & le Roex, A. P. (2003). Garnet lherzolites from the Kaapvaal craton (South Africa): trace element evidence for a metasomatic history. *Journal of Petrology* **44**, 629-657.

Greenough, J. D. (1988). Minor phases in the Earth's mantle: evidence from trace- and minor-element patterns in primitive alkaline magmas. *Chemical Geology* **69**, 177-192.

Gurney, J. J., & Hatton, C. J. (1989). Diamondiferous minerals from the Star mine, South Africa. In: Ross, J. (Ed.), *Kimberlites and Related Rocks, Vol. 2. Their Mantle/Crust Setting, Diamonds and Diamond Exploration, Geological Society of Australia Special Publication* **14**, Blackwell Scientific, pp. 1022-1028.

Gurney, J. J. & Kirkley, M. B. (1996). Kimberlite dyke mining in South Africa. *Africa Geoscience Review* **3** (2), 191–201.

Haggerty, S. E. (1983). The mineral chemistry of new titanates from the Jagersfontein kimberlite, South Africa: implications for metasomatism in the upper mantle. *Geochimica et Cosmochimica Acta* **42**, 1833-1854.

Haggerty, S. E. (1994). Superkimberlites: A geodynamic window to the Earth's core. *Earth and Planetary Science Letters*, **122**, 57-69.

Hammond, A. L. & Mitchell, R. H. (2002). Accessory mineralogy of orangeite from Swartruggens, South Africa. *Mineralogy and Petrology* **76**, 1-19.

Harris, M., le Roex, A. & Class, C. (2004). Geochemistry of the Uintjiesberg kimberlite, South Africa: petrogenesis of an off-craton, group I kimberlite. *Lithos* (In press).

Hart, S. R. & Davis, K. E. (1978). Nickel partitioning between olivine and silicate melt. *Earth and Planetary Science Letters* **40**, 203-219.

Hart, S. R. & Brookes, C. (1977). The Geochemistry and Evolution of Early Precambrian Mantle. *Contributions to Mineralogy and Petrology* **61**, 109-128.

Harte, B., & Harris, J. W. (1994). Lower mantle mineral associations preserved in diamonds. *Mineralogical magazine* **58A**, 284-385.

Hawkesworth, C. J., Marsh, J. S., Duncan, A. R., Erlank, A. J. & Norry, M. J. (1984). The role of continental lithosphere in the generation of the Karoo volcanic rocks: evidence from combined Nd- and Sr-isotope studies. In: *Petrogenesis of the volcanic rocks of the Karoo province.* Erlank, A. J. (Ed.) The Geological Society of South Africa special publication no. **13**, 341-354.

Helmstaedt, H. H. & Gurney, J. J. (1984). Kimberlites of southern Africa – are they related to subduction processes? In: Kornprobst, J. (ed.) *Kimberlites and related rocks*, Elsevier, Netherlands, pp. 425-438.

Helmstaedt, H. H. & Gurney, J. J. (1997). Geodynamic controls of kimberlites – what are the roles of hotspots and plate tectonics? In: Soboloev, N. V. & Mitchell, R. H. (Eds.) *Sixth International Kimberlite Conference volume 2, Diamonds: Characterisation, Genesis and Exploration, Russian Geology and Geophysics* **38**, Allerton Press, New York, pp. 121-132.

Herzberg, C. (1992). Depth and degree of melting of komatiites. *Journal of Geophysical Research* **97** (B4), 4521-4540.

Herzberg, C. & O'Hara, M. J. (2002). Plume-associated ultramafic magmas of Phanerozoic age. *Journal of Petrology* **43**, 1857-1883.

Hill, S. J. (1989). A study of the diamonds and xenoliths from the Star kimberlite, Orange Free State, South Africa. MSc. thesis, University of Cape Town.

Hofmann, A. W. Joachum, K. P., Seufert, M. & White, W. M. (1986). Nb and Pb in oceanic basalts: new constraints on mantle evolution. *Earth and Planetary Science Letters* **79**, 33-45.

Ionov, D. A. & Weiss, D. (2002). Hf isotope compositions of mantle peridotites: first results and inferences for the age and evolution of the lithospheric mantle. *Abstracts, 4th International Conference on Orogenic Lherzolites and mantle processes*. Semani, Japan, pp 56-57.

Johnson, C. M. & Beard, B. L. (1993). Evidence from hafnium isotopes for ancient sub-oceanic mantle beneath the Rio Grande rift. *Nature* 362, 441-444.

Kable, E. J. D., Fesq, H. W. & Gurney, J. J. (1975). The significance of interelement relationships of some minor and trace elements in South African kimberlites. *Physics and Chemistry of the Earth* **9**, 709-734.

Kennedy, C. S., & Kennedy, G. C. (1976). The equilibrium boundary between graphite and diamond. *Journal of Geophysical Research* **81**, 2467-2470.

Kesson, S. E., Ringwood, A. E. & Hibberson, W. O. (1994). Kimberlite melting relations revisited. *Earth and Planetary Science Letters* **121**, 261-262.

Kirkley, M. B. (1987). Aspects of the geochemistry of kimberlite carbonates. Ph.D. thesis, University of Cape Town.

Klump, J. (1995). A pilot study of the Swartruggens kimberlite dyke swarm. Unpubl. Honours thesis, University of Cape Town.

Kramers, J. D. (1977). Lead and strontium isotopes in Cretaceous kimberlites and mantle derived xenoliths from southern Africa. *Earth and Planetary Science Letters* **42**, 58-70.

Kramers, J. D., Smith, C. B., Lock, N. P. Harmon, R. S. & Boyd, F. R. (1981). Can kimberlites be generated from an ordinary mantle? *Nature* **291**, 53-56.

Le Maitre, R. W. (Ed.), Streckheisen, A., Zanettin, B., LeBas, M. J., Bonin, B.,Baternen, P., Bellieni, G., Dudek, A., Etremova, S., Keller, J., Lameyer, J., Sabine, P. A., Schmid, R., Sørensen, H., Woolley, A. R. (2002). *Igneous Rocks A Classification and Glossary of Terms*, 2nd Edition. Recommendations of the

International Union of Geological Sciences Sub commission on the systematics of igneous rocks. Cambridge University Press, 13-15.

le Roex, A. P., Erlank, A. J. & Needham, H. D. (1981). Geochemical and mineralogical evidence for the occurrence of at least three distinct magma types in the "Famous" region. *Contributions to Mineralogy and Petrology* **77**, 24-37.

le Roex, A. P. (1986) Geochemical correlation between southern African kimberlites and South Atlantic hotspots. *Nature* **324**, 243-245.

le Roex, A. P., Bell, D. R., & Davis, P. (2003). Petrogenesis of Group I Kimberlites from Kimberley, South Africa: Evidence from Bulk-rock Geochemistry. *Journal of Petrology* **44**, 2261-2286.

Lorenz, V., Zimanowski, B., Brüttner, R. & Kurszlaukis, S. (1999). Formation of Kimberlite Diatremes by Explosive Interactions of Kimberlite Magma with Groundwater: Field and Experimental Aspects. In: Gurney, J. J., Gurney, J. L., Pascoe, M. D. & Richardson, S. H. (Eds.) *Proceedings of the VIIth International Kimberlite Conference*. Cape Town: Red Roof Design, pp. 522–528.

Marsh, J. S. & Eales, H. V. (1984). The Chemistry and Petrogenesis of igneous rocks of the Karoo central area, southern Africa. In: *Petrogenesis of the volcanic rocks of the Karoo province.* Erlank, A. J. (Ed.) The Geological Society of South Africa special publication no. **13**.

McCandless, T. E. (1999). Kimberlites: Mantle expressions of deep-seated subduction. In: Gurney, J. J., Gurney, J. L., Pascoe, M. D. & Richardson, S. H. (Eds.) *Proceedings of the VIIth International Kimberlite Conference*. Cape Town: Red Roof Design, pp. 545-549.

McIntyre, R. M. & Dawson, J. B. (1976). Age and significance of some South African kimberlites. Abstracts of the 4th Europ Coll Geochron, Cosmochron Isotope geol, Amsterdam, Abstract 66.

McKenna, N. (2001). A study of the diamonds, diamond inclusion minerals and other mantle minerals from the Swartruggens kimberlite, South Africa. MSc. thesis, University of Cape Town.

McKenzie, D. and O'Nions, R.K. (1983). Mantle reservoirs and ocean island basalts. *Nature* **301**, 229-231.

Mitchell, R. H. (1970). Kimberlites and related rocks – A critical reappraisal. *Journal of Geology* **78**, 686-704.

Mitchell, R. H. (1994). Suggestions for revisions to the terminology of kimberlites and lamprophyres from a genetic viewpoint. In: Meyer, H. O. A. & Leonardos, O. H. (Eds.), Proceedings of the Fifth International Kimberlite Conference Volume 1: *Kimberlites and Related Rocks and Mantle Xenoliths*. Companhia de Pesquisa de Recursos Minerais, Brasilia, Special Publication pp. 15-26.

Mitchell, R. H. (1995). *Kimberlites, orangeites and related rocks.* New York: Plenum.

Moore, R. O. & Gurney, J. J. (1985). Pyroxene solid solution in garnets included in diamond. *Nature* **318**, 553-555.

Moore, R. O. & Gurney, J. J. (1989). Mineral inclusions in diamonds from the Monastery kimberlite, South Africa. In; Ross, J. (Ed.), *Kimberlites and Related Rocks, Vol. 2. Their Mantle/Crust Setting, Diamonds and Diamond Exploration, Geological Society of Australia Special Publication* **14**, Blackwell Scientific, pp. 1029-1041

Nowell, G.M., Kempton, P.D., Noble, S.R., Fitton, J.G., Saunders, A.D., Mahoney, J.J., and Taylor, R.N. (1998). High precision Hf isotope measurements of MORB and OIB by thermal ionisation mass spectrometry: Insights into the depleted mantle. *Chemical Geology* **149**, pp. 211-233.

Nowell, G. M., Pearson, D. G., Kempton, P. D., Noble, S. R. & Smith, C. B. (1999). Origins of kimberlites: A Hf isotope perspective. In: Gurney, J. J., Gurney, J. L., Pascoe, M. D. & Richardson, S. H. (Eds.) *Proceedings of the VIIth International Kimberlite Conference*. Cape Town: Red Roof Design, pp 616-624.

Nowell, G. M. & Parrish, R. (2001). Simultaneous acquisition of isotope compositions and parent/daughter ratios by non-isotope dilution solution-mode plasma ionisation multi-collector mass spectrometry (PIMMS) (2001). In: Holland, J. G. & Tanner, S. D. (Eds.), *Plasma Source Mass Spectrometry: The new millenium*, Special Publication of the Royal Society of Chemistry **267**, pp298-310.

Nowell, G. M., Pearson, D. G., Ottley, C. J., Schweiters, J. and Dowall, D. (2003). Long-term performance characteristics of a plasma ionisation multi-collector mass spectrometer (PIMMS): the ThernoFinnigan Neptune. Plasma Source Mass Spectrometry. In: Holland, J. G. and Tanner, S. D. (Eds.) *Plasma Source Mass Spectrometry: Applications and Emerging Technologies*, the Royal Society of Chemistry, Cambridge, 307-320.

Nowell, G. M., Pearson, D. G., Bell, D. R., Carlson, R. W., Smith, C. B., Kempton, P. D. & Noble, S. R. (2004). Hf isotope systematics of kimberlites and their megacrysts: New constraints on their source regions. *Journal of Petrology* **45**, 1583-1612.

O'Nions, R. K., Carter, S., Evensen, N. H. & Hamilton, P. J. (1979). Geochemical and cosmochemical applications of Nd isotope analysis. *Ann. Rev. Earth. Planet. Sci.* **7**, 11-38.

Patchett, P.J. (1983). Hafnium isotope results from mid-ocean ridges and Kerguelen. *Lithos* **16**, pp. 47-51.

Patchett, P.J., and Tatsumoto, M. (1980). Hafnium isotope variations in oceanic basalts. *Geophysical Research Letters* **7**, pp.1077-1080.

Pearson, D. G., Rogers, N. W., Irving, A. J., Smith, C. B. & Hawkesworth, C. J. (1995). Source regions of kimberlites and lamproites: constraints from Re-Os isotopes. *Extended Abstracts, Sixth International Kimberlites Conference*, Novosibirsk 430-432.

Pearson, D. G. &Nowell, G. M. (2002). The continental lithospheric mantle: characteristics and significance as a mantle reservoir. *Philosophical Transactions of the Royal Society of London* A **360**, 2383-2410.

Pearson, D. G., Nowell, G. M., Dowall, D. P., Kjarsgaard, B. A., Kopylova, M. G. & Armstrong, J. A. (2003a). The relative roles of lithosphere and convecting mantle in kimberlites from the Slave province, NWT: constraints from Re-Os isotopes and olivine population studies. *Extended abstracts, Eighth International Kimberlite Conference,* Victoria.

Pearson, D. G., Canil, D. & Shirey, S. B. (2003). Mantle samples included in volcanic rocks: xenoliths and diamonds. In Turekian, K. K. & Holland, H. D. (Eds.) *Treatise on Geochemistry* **volume 2**: The mantle and Core, Chapter 6, Elsevier, Amsterdam.

Pollack, H. N., & Chapman, D. S. (1977). On the regional variation of heat flow, geotherms and lithospheric thickness. *Tectonophysics* **38**, 279–296.

Price, S. E., Russell, J. K. & Kopylova, M. G. (2000). Primitive magma from the Jericho Pipe, N. W. T., Canada: constraints on primary kimberlite melt chemistry. *Journal of Petrology* **41**, 789-808.

Richardson, S. H., Gurney, J. J., Erlank, A. J. & Harris, J. W. (1984). Origin of diamonds in old enriched mantle. *Nature* **346**, 54-56.

Ringwood, A. E., Kesson, S. E., Hibberson, W. & Ware, N. (1992). Origin of kimberlites and related magmas. *Earth and Planetary Sciences Letters* **113**, 521-538.

Rock, N. M. S. (1991). *Lamprophyres*. Glasgow: Blackie.

Rudnick, R. L. & Fountain, D. M. (1995). Nature and composition of the continental crust: a lower crustal perspective. *Reviews of Geophysics* **33**, 267-309.

Ryerson, F. J. & Watson, E. B. (1987). Rutile saturation in magmas: implications for Ti-Nb-Ta depletion in island-arc basalts. *Earth and Planetary Science Letters* **86**, 225-239.

Salters, V.J.M. (1996). The generation of mid-ocean ridge basalts from the Hf and Nd isotope perspective. *Earth and Planetary Science Letters* **141**, pp.109-123.

Salters, V.J.M., and Hart, S.R. (1991). The mantle sources of ocean ridges, islands and arcs : The Hf-isotope connection. *Earth and Planetary Science Letters* **104**, pp.364-380.

Salters, V. J. M. & White, W. M. (1998). Hafnium isotope constraints on mantle evolution. *Chemical Geology* **145**, 447-460.

Scherstén, A., Elliott, T., Hawkesworth, C. & Norman, M. (2004). Tungsten isotope evidence that mantle plumes contain no contribution from the Earth's core. *Nature* **427**, 234-237.

Schmidberger, S. S., Simonetti, A. & Francis, D. (2002). Probing Archaean lithosphere using the Lu-Hf systematics of peridotite xenoliths from Somerset Island kimberlites, Canada. *Earth and Planetary Science Letters* **197**, 245-259.

Shee, S. R. (1985). The petrogenesis of the Wesselton Mine Kimberlite, Kimberley, Cape Province, R. S. A. Ph.D. thesis, University of Cape Town.

Sharp, W. E. (1974). A plate-tectonic origin for diamond-bearing kimberlites. *Earth and Planetary Science Letters* **21**, 42-44.

Simon, N. S. C., Carlson, R. W., Pearson, D. G. & Davies, G. R. (2002). The Lu-Hf isotope composition of cratonic lithosphere: disequilibrium between garnet and clinopyroxene in kimberlite xenoliths. *Geochimica et Cosmochimica Acta* **66**, S1, A717.

Skinner, M. (1976). Star Mine kimberlites. Internal Report, 7p.

Skinner, E. M. W. (1989) Contrasting Group I and Group II kimberlite petrology: towards a genetic model for kimberlites. In*: Kimberlites and Related Rocks*, Volume 1. Geol. Soc. Of Australia, Special Publication No. **14**, Blackwell, Carlton, pp. 528 – 544.

Skinner, E. M. W. & Clement, C. R. (1979). Mineralogical classification of southern African kimberlites. In Boyd, F. R. & Meyer, H. O. A. (Eds.) *Proceedings of the 2nd International Kimberlite Conference*. Washington, D. C.: American Geophysical Union, pp. 129-139.

Skinner, E. M. W. & Scott, B. H. (1979). Petrography, mineralogy and geochemistry of kimberlite and associated lamprophyre dykes near Swartruggens, Western Transvaal, R. S. A. *Extended Abstracts, Kimberlite Symposium II, Cambridge.*

Skinner, E. M. W., Smith, C. B., Viljoen, K. S. & Clark, T. C. (1992). The petrography, tectonic setting and emplacement ages of kimberlites in the South western border of the Kaapvaal craton, Prieska area, South Africa. In: Meyer, H. O. A. & Leonardos, O. H. (Eds.) Proceedings of the Fifth International Kimberlite Conference Volume 1: *Kimberlites, Related Rocks and Mantle Xenoliths*. Companhia de Pesquisa de Recursos Minerais, Brasilia Special Publication, pp. 80-95.

Smith, C. B. (1983a). Pb, Sr, and Nd isotopic evidence for sources of southern African Cretaceous kimberlites. *Nature* **304**, 51-54.

Smith, C. B. (1983b). Rubidium - Strontium, Uranium - Lead and Samarium - Neodymium isotopic studies of kimberlite and selected mantle - derived xenoliths. Bernard Price Institute of Geophysics, Johannesburg, University of Witwatersrand.

Smith, C. B., Allsopp, H. L., Kramers, J. D., Hutchinson, G. & Roddick, J. C. (1985a). Emplacement ages of Jurassic-Cretaceous South African kimberlites by the Rb-Sr method on phlogopite and whole rock samples. *Transactions of the Geological Society of South Africa* **88**, 249-266.

Smith, C. B., Gurney, J. J., Skinner, E. M. W., Clement, C. R. & Ebrahim, N. (1985b). Geochemical character of southern African kimberlites: a new approach based on isotopic constraints. *Transactions of the Geological Society of South Africa* **88**, 267-280.

Späth, A., le Roex, A. P. & Opiyo-Akech, N. (2001). Plume-lithosphere interaction and the origin of continental rift-related alkaline volcanism – the Chyulu Hills Volcanic Province, southern Kenya. *Journal of Petrology* **42**, 765-787.

Stille, P., Unruh, D.M., and Tatsumoto, M. (1986). Pb, Sr, Nd and Hf isotopic constraints on the origin of hawaiian basalts and evidence for a unique mantle source. *Geochimica et Cosmochimica Acta* **50**, pp. 2303-2319.

Sun, S.-s. & McDonough, W. F. (1989). Chemical and isotopic systematics of oceanic basalts: implications for mantle composition and processes. In: Saunders, A. D. & Norry, M. J. (Eds.) *Magmatism in the Ocean Basins. Geological Society, London, Special Publications* **42**, 313-345.

Sweeney, R. J. & Winter, F. (1999). Kimberlite as high-pressure melts; the determination of segregation depths from major element chemistry. In: Gurney, J. J., Gurney, J. L., Pascoe, M. D. & Richardson, S. H. (Eds.) *Proceedings of the VIIth International Kimberlite Conference*. Cape Town: Red Roof Design, pp. 846-851.

Tainton, K. M. (1992). The petrogenesis of Group 2 kimberlites and lamproites from the northern Cape Province, South Africa. Ph. D. thesis, University of Cambridge.

Tainton, K. M. & McKenzie, D. (1994). The generation of kimberlites, lamproites, and their source rocks. *Journal of Petrology* **35**, 787-817.

Ulmer, P. & Sweeney, R. J. (2002). Generation and differentiation of group II kimberlites: constraints from a high-pressure experimental study to 10 Gpa. *Geochimica et Cosmochimica Acta* **66**, 2139-2153.

Vervoort, J. D. & Patchett, J. P. (1996). Behaviour of hafnium and neodymium isotopes in the crust: Constraints from Precambrian crustally derived granites. *Geochimica et Cosmochimica Acta* **60**, 3717-3733.

Vervoort, J., Patchett, P. J., Blichert-Toft, J. & Albarède, F. (1999). Relationships between Lu-Hf and Sm-Nd isotopic systems in the global sedimentary system. *Earth and Planetary Science Letters* **168**, 79-99.

Wagner, P. A. (1914). The Diamond Fields of South Africa. Cape Town: Struik.

Walter, M. J. (1998). Melting of garnet peridotite and the origin of komatiite and depleted lithosphere. *Journal of Petrology* **39**, 29-60.

Wass, S. Y. & Rogers, N. W. (1980). Mantle metasomatism – precursor to continental alkaline volcanism. *Geochimica et Cosmochimica Acta* **44**, 1811-1823.

Wendlandt, R. F. & Eggler, D. H. (1980). The origins of potassic magmas:2, stability of phlogopite in natural spinel lherzolite and the system $KAlSiO_4$-MgO-SiO_2-H_2O-CO_2 at high pressures and high temperatures. *American Journal of Science* **280**, 421-458.

Willis, J. P. (1999). Instrumental parameters and data quality for routine major and trace element determinations by WDXRFS, University of Cape Town, Cape Town.

Wyllie, P. J. (1980). The origin of kimberlite. *Journal of Geophysical Research* **85**, 6902 – 6910.

Appendix 1

Swartruggens sample localities and individual petrographic descriptions

A1.1 Sample localities

The localities of the Swartruggens samples used in this project are reported in Table A1.1. Samples NC 001 – 014 were collected for this project during a visit to Helam mine in January 2002. All other samples are from the mantle room collection at the University of Cape Town.

Table A1.1 Localities of the Swartruggens samples

Sample no.	Dyke	Sample locality
NC 001	Third Lease	Third Lease processing dump
NC 002	Third Lease	Third Lease processing dump
NC 003	Third Lease	Third Lease processing dump
NC 004	Main Dyke	18 level West, cross-cut 39
NC 006	Main Dyke	19 level West, cross-cut 39
NC 010	Main Dyke	21 level West, cross-cut 32
NC 011	Main Dyke	21 level Station: cross-cut 0
SR 6	Main Dyke	16 level East, cross-cut 20 (S), Edward shaft main sub
JJG 3143	Main Dyke	3 level, Edward Shaft
Hons 95-4	Main Dyke	14 level, Edward shaft
NC 005	Changehouse Dyke	19 level, far West
NC 007	Changehouse Dyke	19 level, far East, cross-cut 57
NC 009	Changehouse Dyke	21 level West, cross-cut 32
SR 7	Changehouse Dyke	16 level East, cross-cut 20 (N), Edward shaft main sub
JJG 3149	South Fissure	13-14 level East, Zone 2
JJG 3145	South Fissure	6 level West, cross-cut 11
JJG 3150	South Fissure	13-14 level East, Zone 3
JJG 3148	South Fissure	13-14 level East, Zone 1
NC 008	Muil Dyke	21 level West, cross-cut 32
NC 012	Muil Dyke	Processing dump
NC 014	Muil Dyke	Processing dump
NC 015	Muil Dyke	Unknown
JJG 3141	Muil Dyke	Edward shaft centre
SR 9	Muil Dyke	16 level West, cross-cut 9 (N), Edward shaft main sub

A1.2 Sample descriptions

The petrography of each of the Swartruggens kimberlite and Muil lamprophyre samples analysed in this study has been determined from thin sections using an optical microscope, and is described below. Crystals that are larger than 2mm in size are termed *macrocrysts*, after Mitchell (1995). The rounded, anhedral and fractured nature of many macrocrysts in kimberlites suggests that they are disaggregated mantle peridotite and not genetically related to the kimberlite magma (e.g. le Roex *et al.*, 2003, Shee, 1985). However, in accordance with previous studies the term macrocryst is preferred to xenocryst as it is free from genetic inferences (e.g. Mitchell, 1995). Since many of the macrocrysts are fragmented, anhedral, strained fragments smaller than 2mm are also classed with the macrocryst suite, with the term *phenocryst* being reserved for euhedral or subhedral crystals 0.5 to 2mm in size that are believed to have crystallised from the kimberlite magma. *Microphenocryst* is used to describe subhedral to euhedral crystals less than 0.5mm in size, set in a finer grained or interstitial groundmass. Modal proportions of the mineral phases reported in these descriptions are based on visual estimates.

NC 001 – Third Lease

Texture: Macrocrystic, containing ~25 volume % macrocrysts, with ~30 volume % phenocrysts in a fine-grained (<0.2mm) groundmass.

Macrocryst phases (25%):
Rounded, anhedral relic olivine macrocrysts, ranging in size from 1mm to 7mm, constitute ~90% of the macrocryst suite. No fresh olivine remains; the macrocrysts are almost entirely replaced by calcite, with minor serpentine occurring along fractures and the rims of some macrocrysts. Several smaller, aligned calcite crystals frequently replace one macrocryst. Phlogopite macrocrysts constitute ~10% of the macrocryst suite, occurring as rounded, anhedral, elongate crystals ranging up to 5mm in size. The phlogopite macrocrysts are commonly strained, showing kink banding, and are partially altered to chlorite in parts of the sample.

Phenocryst phases (30%):
The vast majority of the phenocrysts in this sample are phlogopite, which occurs as subhedral crystals up to 1.5mm in length. Some of the phlogopite phenocrysts show distinct optical zoning, most commonly with darker cores than rims, and many are rimmed by tetraferriphlogopite. In places the phlogopite phenocrysts are much more severely chloritised than the macrocrysts. Diopside phenocrysts constitute ~5% of the phenocryst suite. These are subhedral to euhedral lath-shaped crystals up to 1mm in length.

Groundmass (45%):
Approximately 60% of the groundmass consists of highly chloritised phlogopite, in stubby lath shaped crystals up to 0.2mm in size. Calcite occurs both as subhedral crystals and also as interstitial material, and constitutes ~20 to 30% of the groundmass. Serpentine is also present as a subordinate interstitial phase.

Fresh, euhedral to subhedral diopside up to 0.2mm in size constitutes ~5% of the groundmass, and apatite, perovskite and opaque oxides up to ~0.1mm in size are present as accessory phases.

NC002 – Third Lease

Texture: Sparsely macrocrystic, with ~10 volume % macrocrysts set in a fine to medium grained groundmass (crystals 0.3 to 0.5mm) containing ~10 volume % phenocrysts.

Macrocryst phases (10%):
Relic olivine macrocrysts constitute the majority (~70%) of the macrocryst suite of this sample. They are anhedral and rounded, ranging up to 6mm in size, and are completely replaced by calcite. All the olivine macrocrysts have with thick reaction rims. Phlogopite macrocrysts constitute the remaining ~30% of the macrocryst suite, occurring as rounded anhedral, sometimes elongate, crystals up to 4mm in size. The phlogopite macrocrysts are strained, with kink banding, and show undulose extinction. They are commonly severely chloritised, particularly along cleavage planes, although this is not pervasive throughout the sample.

Phenocryst phases (10%):
The vast majority of phenocrysts in this sample are phlogopite, which occurs as euhedral or lath-shaped crystals up to 1.5mm in size. Many of the phlogopite phenocrysts are optically zoned, with darker cores than rims, and some have thin rims of tetraferriphlogopite. Many crystals are altered partially or completely to chlorite. Diopside constitutes approximately 10 % of the phenocryst suite, occurring as subhedral to euhedral elongate crystals up to 2mm in length.

Groundmass (80%):
The fine-medium grained groundmass consists of approximately 50% phlogopite, in subhedral equant crystals up to 0.5mm in size, much of which has been altered to chlorite. Calcite constitutes ~30-40% of the groundmass, and is present both as discrete euhedral crystals up to 0.2mm in size and as an interstitial phase. Euhedral diopside up to 0.3mm in size constitutes ~10% of the groundmass, and accessory opaque oxides up to 0.1mm in size are scattered throughout the groundmass of the sample.

NC003 – Third lease

Texture: Macrocrystic, with ~20 volume % macrocrysts in a fine-grained groundmass (crystal size 0.1-0.2mm), which contains ~20 volume % phenocrysts. Calcite veins up to 1mm thick cut through the sample. The macrocrysts, phenocrysts and groundmass minerals are sub-parallel, giving a weak fabric to the sample.

Macrocryst phases (20%):

Relic olivine macrocrysts constitute ~60% of the macrocryst suite of this sample. These are rounded and anhedral crystals ranging up to 5mm in size. The smaller (<1mm) fragments of olivine macrocrysts are completely altered to serpentine, whereas the larger macrocrysts are all further replaced by calcite. Thick reaction rims and very small (~0.05mm) opaque oxides are common around the edges of the relic olivine macrocrysts. The remaining 40% of the macrocrysts suite comprises anhedral or subhedral rounded phlogopite, which commonly occurs as elongate crystals ranging up to 4mm in length. Many of the phlogopite macrocrysts have slightly distorted crystal shapes, kink banding is common and most show undulose extinction. Optical zoning, from darker cores to paler rims, is common in the phlogopite macrocrysts. Alteration of the phlogopite macrocrysts to chlorite, particularly around the crystal edges, is common but not pervasive throughout the sample.

Phenocryst phases (20%):

The vast majority of phenocrysts in this sample are euhedral to subhedral, lath shaped or equant phlogopite. Some of the phlogopite phenocrysts show weak optical zoning, and many are partially or wholly replaced by chlorite. Diopside phenocrysts are less common, constituting only ~5% of the phenocryst suite of this sample. They occur as subhedral elongate crystals, ranging up to 2mm in length.

Groundmass (60%):

The groundmass of this sample consists of ~60% phlogopite, which occurs most commonly as subhedral stubby laths up to 0.2mm in size. In patches the phlogopite has been severely chloritised, although this is not pervasive and in parts of the sample the groundmass phlogopite is still relatively fresh. The interstitial material (10-15% of the groundmass) is dominantly serpentine with subordinate calcite. Calcite also occurs as discrete euhedral crystals, and in total constitutes ~20% of the groundmass of this sample. Approximately 5% of the groundmass is subhedral or euhedral diopside, up to 0.2mm in size. Opaque oxides (up to 0.1mm in size) are associated with relic olivine macrocrysts and scattered throughout the groundmass of this sample.

NC004 – Main Dyke

Texture: Macrocrystic, with approximately 30 volume % macrocrysts in a medium-fine grained matrix (grain size 0.1-0.2mm) containing 20% phenocrysts.

Macrocryst phases (30%):

Olivine macrocrysts are rounded, anhedral crystals ranging in size from less than 1mm to 8mm and comprise approximately 70% of the macrocryst suite. Although small patches of fresh olivine remain in some of the macrocrysts, the majority are completely altered to serpentine and partly replaced by calcite. Thick dark brown reaction rims surround all the olivine macrocrysts. Phlogopite constitutes approximately 30% of the macrocryst suite, and occurs as subhedral or anhedral, rounded elongate crystals up to 3mm in

size. Although chemically fresh, the phlogopite macrocrysts are strained, showing undulose extinction and some are partlally recrystalised.

Phenocryst phases (20%):

The vast majority of phenocrysts (>95%) are phlogopite, which occurs as euhedral to subhedral lath-shaped crystals up to 1.5mm in size. Many of the phlogopite phenocrysts are optically zoned, and thin rims of tetraferriphlogopite are common. Only one diopside phenocryst was observed in this sample. It is subhedral, approximately 2mm long and slightly altered around the rim.

Groundmass (50%):

The groundmass is fine grained (grain size <0.2mm) and consists of approximately 90% phlogopite in euhedral or subhedral stubby laths up to 0.2mm in size. These are commonly thickly rimmed by, or completely altered to, tetraferriphlogopite. No alteration to chlorite is seen. Small veins (less than 1mm thick) of calcite and serpentine cut through the sample but interstitial or other groundmass calcite is rare. Accessory opaque oxides are scattered throughout the sample. Diopside is rare and constitutes less than 5 volume % of the groundmass.

NC006 – Main Dyke

Texture: Macrocryst poor, containing ~10 volume % macrocrysts, with ~10 volume % phenocrysts, in a fine-grained (<0.2mm) matrix.

Macrocryst phases (10%):

Olivine macrocrysts are rounded and anhedral, ranging from less than 1mm to 7mm in size, and comprise approximately 60% of the macrocryst suite. The majority of the olivine macrocrysts are completely replaced by calcite, although some are altered to serpentine and partially replaced by phlogopite. Many of the relic olivine macrocrysts are rimmed by phlogopite. The remaining 40% of the macrocrysts are phlogopite, which occurs as subhedral to anhedral rounded crystals up to 6mm in size, many of which are partially altered to chlorite. The majority of the phlogopite macrocrysts are optically zoned, with cores that are slightly darker than the rims. Thin rims of tetraferriphlogopite are common. All the phlogopite macrocrysts show undulose extinction, and kink banding is common.

Phenocryst phases (10%):

The vast majority (~95%) of the phenocrysts in this sample are phlogopite. The phlogopite phenocrysts are usually subhedral, although occasional crystals are anhedral and fewer are euhedral, and they range from 0.5mm to 2mm in size. Although slight alteration to chlorite is seen in a few crystals, the phlogopite phenocrysts appear to be fresher than the macrocrysts. Many are rimmed by tetraferriphlogopite and optical zoning is common. Diopside constitutes approximately 5% of the phenocryst suite, occurring as fresh subhedral crystals up to 1mm in length.

Groundmass (80%):

The groundmass is composed almost entirely of phlogopite (~90%), in euhedral to subhedral crystals that average ~0.2mm in size. Almost all of these are rimmed by tetraferriphlogopite. Diopside is present in minor amounts (<5%). Interstitial serpentine comprises ~5% of the groundmass, whereas calcite occurs both as a subordinate groundmass phase and as discrete euhedral crystals comprising a total of 2-3% of the groundmass. Small (<0.1mm) opaque oxides are scattered throughout the sample. Accessory euhedral apatite crystals, approximately 0.1mm in size constitute less than 1% of the groundmass.

NC010 – Main Dyke

Texture: Macrocrystic, with approximately 30 volume % macrocrysts in a fine-grained equigranular groundmass containing approximately 10 volume % phenocrysts.

Macrocryst phases (30%):

Approximately 70% of the macrocrysts in the sample are rounded anhedral pseudomorphs after olivine, ranging from 1mm to 5mm in size. The larger of these macrocrysts are replaced by polycrystalline phlogopite, with some calcite and serpentine, whereas the smaller (<3mm) are more commonly completely replaced by calcite. The phlogopite crystals replacing the olivine range from 0.2 to 0.5 mm and are commonly show undulose extinction, the crystals being slightly deformed. The remaining 30% of the macrocrysts are subhedral to anhedral phlogopite, 2-5mm in size. All these crystal show undulose extinction and several are kink-banded. Optical zoning is common, and their cores show pleochroism from a much darker brown than the rims, to green. Some of the phlogopite macrocrysts have thin rims of tetraferriphlogopite.

Phenocryst phases (10%):

Phlogopite constitutes the vast majority of the phenocryst suite (~90%), occurring as subhedral crystals that range in size from 0.5mm to 2mm. Some of the phlogopite phenocrysts have thin tetraferriphlogopite rims and many are optically zoned as described for the phlogopite macrocrysts in this sample. The remaining ~10% of the phenocrysts in this sample (<10%) are diopside. Most are ~1mm in length and they form subhedral lath shaped crystals.

Groundmass (60%):

The groundmass is fine-grained and equigranular with crystals approximately 0.2mm in size. It consists of ~70% phlogopite, in subhedral to euhedral stubby or equant crystals, most of which are rimmed by. The alignment of the groundmass phlogopites gives a slight fabric to the rock. Euhedral to subhedral diopside constitutes ~5% of the groundmass. Approximately 5 – 10% of the groundmass is interstitial carbonate. Opaque oxides (<0.1mm in size) are abundant throughout the groundmass. Minor accessory perovskite (<0.1mm in size) is also present.

NC011 – Main Dyke

Texture: Macrocrystic, with approximately 20 volume % macrocrysts and 20 volume % phenocrysts in a fine-medium grained (0.2 - 0.4mm) groundmass.

Macrocryst phases (20%):

Approximately 50% of the macrocrysts are rounded, anhedral relic olivine, ranging up to 7mm in length. These have been altered to serpentine and most have been further replaced partially or totally by calcite. There is also some replacement of the macrocrysts by smaller phlogopite crystals. Dark brown alteration rims surround the olivine macrocrysts, and opaque oxides are commonly closely associated. Phlogopite macrocrysts constitute the remaining half of the macrocryst suite. These are subhedral to anhedral, rounded elongate crystals, which range from 2-4mm in length. Some of the phlogopites have been partially altered to chlorite. Most crystals are highly strained, with kink-banding common, and show undulose extinction. One crystal has been torn open along a cleavage plane and the ~0.5mm wide fracture is infilled by calcite.

Phenocryst phases (20%):

All of the phenocrysts observed in this sample are phlogopite. Most are subhedral and range from 0.5mm to 2mm in size. Some of the phlogopite phenocrysts have been partially altered to chlorite.

Groundmass (60%):

The groundmass is fine grained and fairly equigranular with crystals ranging from 0.2mm to 0.4mm in size. Approximately 90% is comprised of phlogopite, both in subhedral stubby laths, and euhedral equant crystals, which are altered slightly to chlorite in places. Thick rims of tetraferriphlogopite are common around the groundmass phlogopites. Approximately 5% of the groundmass is made up from laths approximately 0.2mm in length of diopside. Fe-Ti oxides (<0.1mm) are common, particularly around relic olivine macrocrysts. There is a minor amount (<5%) of interstitial carbonate.

SR6 – Main dyke

Texture: Macrocrystic, with ~30 volume % macrocrysts and 15 volume % phenocrysts in fine-grained matrix (grain size ~0.2mm).

Macrocryst phases (30%):

Approximately 50% of the macrocryst suite comprises rounded, anhedral olivine, ranging in size from approximately 0.5mm to 4mm, and are anhedral and rounded. These macrocrysts have no relics of original olivine left, but have been completely replaced by calcite with small amounts of alteration to serpentine remaining. There has also been some replacement by phlogopite. The olivine macrocrysts have been resorbed around the edges and have dark red-brown alteration rims. Fe-Ti oxides are common around the edges of the macrocrysts. The remaining 50% of the macrocrysts in the sample are anhedral phlogopite, which range from 2mm to 4mm in size. These are commonly rounded, and have clearly been extensively

strained. The crystal shapes are deformed, some are partially recrystalised, and they show undulose extinction. Some of the crystals appear to have been torn apart along cleavage planes, and infilled with calcite.

Phenocryst phases (15%):
All the phenocrysts in this sample are phlogopite. They are subhedral, and commonly occur as lath shaped crystals that range in size from 0.5mm to 2mm. Many of the phlogopite phenocrysts are optically zoned, and rims of tetraferriphlogopite are common. Some crystals are partially altered to chlorite, although this is not common or pervasive throughout the sample.

Groundmass (55%):
The groundmass is comprised of ~90% phlogopite, most of which forms subhedral, lath-shaped crystals <0.2mm in length. Some of these crystals are slightly deformed. Many of the groundmass phlogopites have tetraferriphlogopite rims. The rest of the groundmass (<10%) is made up from calcite, which forms subhedral crystals <0.1mm, and is also the main interstitial phase in this sample. Fe-Ti oxides <0.1mm are abundant in throughout the groundmass and commonly associate with the rims of relic olivine macrocrysts.

JJG 3143 – Main Dyke

Texture: Macrocrystic, with ~30 volume % macrocrysts and ~20 volume % phenocrysts in a medium grained groundmass (grain-size <0.3mm). The sample has a slight fabric shown by alignment of phlogopite macrocrysts and phenocrysts.

Macrocryst phases (30%):
Approximately 70% of the macrocrysts in this sample are rounded, anhedral olivine, ranging in size from <1mm to approximately 8mm. The macrocrysts are altered to serpentine and further almost completely replaced by calcite, with serpentine only remaining along fractures. There has also been some replacement of the olivine macrocrysts by phlogopite, particularly along fractures and around the rims. Red-brown alterations rims surround some of the macrocrysts. The remaining 30% of the macrocryst suite comprises subhedral phlogopite. These range in size from 2mm to 4mm and many approximate lath shapes that show some alignment with the fabric of the sample. Some of the phlogopite macrocrysts are partially altered to chlorite. All the phlogopite macrocrysts show strain features: deformed crystal shapes and slightly undulose extinction. Some of the smaller crystals are also kink-banded.

Phenocryst phases (20%):
All the phenocrysts observed in this sample are phlogopite. They range in size from 0.5mm to 2mm, and are generally subhedral to anhedral. They show varying degrees of alteration to chlorite, with some crystals being unaffected and others completely altered. Tetraferriphlogopite partially rims some of the phlogopite phenocrysts, but this is not common.

Groundmass (50%):

The groundmass of this sample consists almost entirely of phlogopite, most of which occurs as euhedral to subhedral stubby lath-shape crystals <0.3mm in size. Many of the groundmass phlogopites have thin rims of tetraferriphlogopite, and some have been altered partially to chlorite. Calcite comprises the majority of the remainder of the groundmass (<5%) predominantly as discrete euhedral crystals, up to 0.2mm in size, but also as a minor interstitial phase. Opaque oxides <0.1mm in size are common throughout the groundmass of the sample.

Hons 95-4 – Main Dyke

Texture: Approximately 15 volume % of this sample is made up from macrocrysts. These are concentrated into two parallel bands ~75mm thick, and the majority of the sample is relatively aphanitic. The groundmass is fine-grained and fairly equigranular (grain size approx. 0.1mm). The long axes of the macrocrysts are aligned parallel to the bands giving the sample a strong fabric.

Macrocryst phases (15%):

Approximately 80% of the macrocryst suite is comprised of rounded, anhedral olivine, ranging in size from <1mm to ~8mm. These are completely altered to serpentine and partially further replaced by calcite, particularly along cracks. Some crystals have also been partial replaced by phlogopite although this is not common. Red-brown alteration rims surround all the relic olivine macrocrysts. Phlogopite constitutes the remaining 20% of the macrocrysts are phlogopite. This occurs in subhedral laths or rounded anhedral crystals up to 3mm in size, many of which have been partially altered to chlorite. Some of the macrocrysts are optically zoned, with cores much darker than rims, and all the phlogopite crystals have thin rims of tetraferriphlogopite. All the phlogopite macrocrysts display undulose extinction and many are distorted and kink-banded.

Phenocryst phases (10%):

All the phenocrysts observed in this sample are phlogopite. It occurs most commonly in subhedral laths up to 1.5mm in length. Some of the phenocrysts have been partially altered to chlorite. All the phlogopite phenocrysts have thin rims of tetraferriphlogopite.

Groundmass (75%):

Subhedral, stubby laths of phlogopite up to 0.2mm in length constitute ~90% of the groundmass. These all have relatively thick rims of tetraferriphlogopite and show some alignment parallel to the macrocrysts. The remaining 10% of the groundmass is comprised primarily of interstitial calcite, with Fe-Ti opaque oxides less than ~0.1mm in size being common throughout the sample. Accessory perovskite <0.2mm in size is also present.

NC005 – Changehouse Dyke

Texture: Macrocrystic, with approximately 25 volume % macrocrysts in a medium grained (<0.5mm) groundmass. This sample has a relatively strong fabric due to alignment both of the macrocrysts and the groundmass minerals.

Macrocryst phases (25%):

Approximately 70% of the macrocryst suite comprises rounded, anhedral relic olivine, ranging in size up to 8mm. All the olivine has been altered to serpentine or replaced by calcite. Some crystals also show the beginnings of replacement by phlogopite. Groundmass phlogopites are commonly distorted and bent around the relic olivine macrocrysts. Phlogopite constitutes approximately 30% of the macrocryst suite. It occurs most commonly as subhedral lath-shaped crystals up to 3mm in size. Some of the crystals are clearly zoned, with the cores being slightly darker than the rims. All the phlogopite macrocrysts are strained and show undulose extinction. Thin rims of tetraferriphlogopite are common.

Phenocryst phases (40%):

Phlogopite phenocrysts occur as euhedral or subhedral lath-shaped crystals, ranging in size from 0.5mm to 2mm, and constitute approximately 70% of the phenocryst suite. Most of the crystals are fully or partially rimmed by tetraferriphlogopite, although the rims are generally quite thin. The long axes of these crystals show some alignment, parallel to that shown by the macrocrysts. Diopside constitutes the remaining 30% of the phenocryst suite, occurring as subhedral or euhedral elongate crystals that are aligned with the phlogopite phenocrysts. They are 1-2mm in size and relatively fresh, although many are slightly fractured.

Groundmass: (35%)

Approximately 80% of the groundmass is composed of phlogopite, up to 0.5mm in size. The majority of the groundmass phlogopite occurs as subhedral stubby laths, with more rare euhedral equant crystals. Tetraferriphlogopite mantles almost all the groundmass phlogopite, commonly thickly, and some crystals are entirely altered to tetraferriphlogopite. Flow features are evident in the groundmass phlogopite: the laths are aligned parallel to the fabric of the sample and bend around the olivine macrocrysts. Diopside constitutes approximately 20% of the groundmass, occurring as subhedral, elongate crystals reaching approximately 0.5mm in length. Approximately 5% of the groundmass comprises the interstitial phases calcite and serpentine. Minor opaque oxides are scattered throughout the groundmass but are commonly associated with the relic olivine macrocrysts. Accessory perovskite and apatite (~0.2 - 0.3mm) constitute approximately 1% of the groundmass.

NC007 – Changehouse Dyke

Texture: Coarsely macrocrystic, with approximately 40 volume % macrocrysts in a medium-fine grained matrix that contains approximately 30 volume % phenocrysts.

Macrocryst phases (40%):

Rounded, anhedral relic olivine macrocrysts, ranging in size from 1mm to 5mm, constitute 90% of the macrocryst assemblage. These are altered to serpentine and partly further replaced by calcite, and some have been partially replaced by phlogopite. Several of the relic olivine macrocrysts contain small (approx. 0.2mm) inclusions, the majority of which are diopside, and a few fresh olivine fragments that may be remnants of the original crystal. Phlogopite, tetraferriphlogopite and opaque oxides <0.2mm form rims around most of the relic olivine macrocrysts. Opaque oxides are also common within the relic olivines, particularly along fractures. Approximately 10% of the macrocryst assemblage is comprised of subhedral phlogopite, ranging in size from 2mm to 4mm. These commonly have large cores, which are darker in colour than the rims and are often then rimmed by tetraferriphlogopite. Some crystals show slight alteration to chlorite, particularly around the rims. Opaque oxides are often associated with the more altered rims of the phlogopite macrocrysts. Strain features such as undulose extinction and kink banding are common.

Phenocryst phases (30%):

Phlogopite constitutes ~70% of the phenocryst suite, and occurs as euhedral to subhedral crystals ranging up to 2mm in size. The phlogopite phenocrysts tend to be fresher than the macrocrysts, and chlorite is not seen. Thick mantles of tetraferriphlogopite are common around the phlogopite phenocrysts, although, unlike the macrocrysts, there is no alteration of the phlogopite phenocrysts to chlorite. Diopside occurs as euhedral elongate laths up to 1.5mm in size, and comprises ~30% of the phenocryst suite. Only one olivine phenocryst is present in this section. It is subhedral and approximately 1mm in size. Although fractured and slightly recrystalised along one side it is fresh and has not been serpentinised.

Groundmass (30%):

Approximately 80% of the groundmass of this sample is composed of subhedral phlogopite, which ranges up to 0.4mm in size. The groundmass phlogopite is commonly rimmed by, and sometimes completely altered to, tetraferriphlogopite. Diopside constitutes a further 10% of the groundmass, usually as subhedral elongate laths <0.5mm in size. Rare, small (0.1-0.2mm) crystals of fresh euhedral olivine remain in the groundmass. Calcite fills a vein 1mm thick through the sample but primary groundmass carbonate is rare and constitutes less than 5% of the sample. Rare apatite, up to 0.1mm in size, is present, and opaque oxides (<0.2mm in size) are scattered throughout the groundmass.

NC009 – Changehouse Dyke

Texture: Macrocrystic, with ~50 volume % macrocrysts in a fine-grained porphyritic groundmass containing ~25 volume % phenocrysts.

Macrocryst phases: (25%)

Approximately 90% of the macrocrysts in this sample are rounded, anhedral olivine which have been altered to serpentine and further almost completely replaced by calcite. Some of the macrocrysts show partial replacement by phlogopite. They range in size from 1mm up to 9mm. The olivine macrocrysts commonly

have thin rims of dark brown microcrystalline phlogopite. Opaque oxides and euhedral perovskite (approximately 0.1mm long) are closely associated with some of the relic olivines. The remaining 10% of the macrocryst suite comprises subhedral to anhedral, rounded phlogopite crystals that range from 2 to 6mm in length. These tend to be fresh and unaltered, although they are commonly slightly fractured and show undulose extinction. The rims are slightly more Fe rich than the cores, and small (<0.1mm) opaque oxides often cluster around the rims.

Phenocryst phases: (25%)

Approximately 85% of the phenocrysts in this sample are phlogopite. Most of the crystals are subhedral and form laths which are 1-2mm in length and approximately 0.5mm wide. Subordinate numbers of the phlogopite phenocrysts are euhedral or anhedral. No alteration to chlorite is visible in the phlogopite phenocrysts, but some crystals have thin rims of tetraferriphlogopite. One euhedral olivine phenocryst, 1mm in length is present in the section. Diopside constitutes the remaining 15% of the phenocryst suite in this sample. As with the phlogopite phenocrysts they tend to form subhedral to euhedral laths approximately 1-2mm in length. The diopside laths are generally thinner (0.25mm wide) than the phlogopite laths.

Groundmass:

The groundmass of this sample is inequigranular, with coarser (<0.4mm) crystals of phlogopite (80%), diopside (15%) and olivine (5%) in a very fine-grained matrix consisting also of these three minerals together with abundant opaque oxides and accessory apatite (<0.1mm) and perovskite. Most of the phlogopite in this matrix is very thickly rimmed by, or altered completely to, tetraferriphlogopite. The groundmass contains minimal (<5%) interstitial calcite and serpentine.

SR 7 – Changehouse Dyke

Texture: Macrocrystic, consisting of ~40 volume % macrocrysts, with ~20 volume % phenocrysts. The groundmass consists of 50% microphenocrysts (0.1-0.4mm) in an extremely fine-grained (<0.1mm) matrix.

Macrocryst phases (40%):

Rounded anhedral olivine comprises approximately 95% of the macrocryst suite, ranging in size up from <1mm to ~7mm. These have been completely altered to serpentine with minor further replacement by calcite. Phlogopite constitutes the remaining 5% of the macrocryst suite, occurring as rounded subhedral to anhedral elongate crystals that range in size from ~2mm to 4mm. The phlogopite macrocrysts show slightly undulose extinction and have been extensively strained. One macrocryst has been torn along the cleavage planes and infilled with calcite. Partial alteration to chlorite has occurred in some of the phlogopite macrocrysts.

Phenocryst phases (20%):

Approximately 75% of the phenocryst suite is comprised of subhedral to euhedral phlogopite, which ranges from 0.5mm to ~1mm in size. Unlike the phlogopite macrocrysts, the phenocrysts are fresh and show no

alteration to chlorite. Rare euhedral or subhedral olivine phenocrysts, up to 1mm in size, constitute approximately 10% of the phenocryst suite. These are completely altered to serpentine. Diopside constitutes the remaining 15% of the phenocryst suite, and occurs as subhedral or euhedral, commonly elongate lath-shaped crystals up to 1.5mm in length.

Groundmass (40%):

The groundmass of this sample consists of an extremely fine-grained matrix containing approximately 50% microphenocrysts 0.1mm to 0.3mm in size. Approximately 70% of the microphenocrysts are euhedral to subhedral phlogopite, usually in lath- or stubby lath-shaped crystals. The remaining ~30% of the microphenocrysts are subhedral diopside. The matrix is comprised of ~80% phlogopite (<0.1mm in size), with tetraferriphlogopite, diopside, apatite, opaque Fe-Ti oxides, and interstitial serpentine as lesser constituents.

JJG 3149 – South Fissure

Texture: Macrocrystic, with macrocrysts constituting ~35 volume % of the sample, in a medium-grained matrix (crystals <0.5mm), which contains ~20 volume % phenocrysts.

Macrocryst phases (35%):

Approximately 80% of the macrocrysts in this sample are rounded, anhedral olivine, all of which has been completely replaced predominantly by calcite and sometimes partially by subordinate phlogopite. The relic olivine macrocrysts range in size from ~1mm to 5mm. Phlogopite comprises ~20% of the macrocryst suite, occurring as rounded, subhedral or anhedral crystals ranging in size from ~2mm to 4mm, some of which are extensively altered to chlorite. Thin rims of tetraferriphlogopite are common. Strain features are evident in all the phlogopite macrocrysts: they show undulose extinction and are commonly kink-banded. Some macrocrysts are partially recrystalised.

Phenocryst phases (20%):

All the phenocrysts observed in this sample are phlogopite. They are subhedral to euhedral in habit, and range in size from 0.5mm to 1.5mm. The phenocrysts are rimmed to varying extents by tetraferriphlogopite, and some show slight alteration to chlorite.

Groundmass (40%):

Approximately 80% of the groundmass is made up from phlogopite, predominantly occurring as subhedral stubby laths approximately 0.4mm in length. These all have thick rims of, or are completely altered to, tetraferriphlogopite. Approximately 10% of the groundmass is calcite, which occurs both as discrete crystals up to 0.2mm in size, and as interstitial material. Opaque oxides less than 0.1mm in size are abundant throughout the sample, and apatite (<0.1mm) is also present as an accessory phase.

JJG 3145 – South fissure

Texture: Macrocrystic, containing ~20 volume % macrocrysts and ~10 volume % phenocrysts, in a medium grained (<0.4mm) equigranular groundmass. The macrocrysts occur in two distinct bands in the sample, with the long axes of the macrocrysts aligned parallel to the bands.

Macrocryst phases (20%):

Approximately 80% of the macrocrysts in this sample are anhedral, rounded relic olivine, ranging in size from <1mm to 5mm. These have been almost completely replaced, predominantly by calcite, although small (<0.1mm) relics of fresh olivine remain in some macrocrysts. Some of the olivine macrocrysts have also been partially replaced by phlogopite, particularly around the rims. The remaining 20% of the macrocrysts are anhedral to subhedral phlogopite, with some of the macrocrysts being very rounded. Their size ranges from 2mm to 4mm. All the phlogopite macrocrysts are rimmed by tetraferriphlogopite, and some are slightly altered to chlorite. Strain features such as undulose extinction and kink banding are common, and some of the phlogopite macrocrysts are recrystalised.

Phenocryst phases (10%):

Approximately 90% of the phenocrysts are subhedral phlogopite, which ranges from 0.5 to 2mm in size. All the phlogopite phenocrysts are rimmed by tetraferriphlogopite and some are partially altered to chlorite. One phenocryst of diopside is present in this sample. It is subhedral and approximately 1mm in length.

Groundmass (70%):

The groundmass of this sample consists of ~90% phlogopite, which occurs predominantly in subhedral stubby laths ~0.1 to 0.4mm in size. All the groundmass phlogopite has thick rims of, or is sometimes completely altered to, tetraferriphlogopite. The remaining 10% of the groundmass is composed primarily from interstitial carbonate, with minor amounts of subhedral diopside (<0.3mm in length). Opaque oxides (<0.1mm in size) are scattered throughout the groundmass of the sample.

JJG 3150 – South Fissure

Texture: Sparsely macrocrystic, containing ~15 volume % macrocrysts with ~10 volume % phenocrysts in a fine-grained (<0.3mm in size) groundmass.

Macrocryst phases (15%):

Rounded anhedral olivine constitutes ~90% of the macrocryst suite of this sample, ranging up to 6mm in size. These are all completely replaced by calcite, with replacement by phlogopite particularly around the rims. Disseminated opaque oxides are commonly associated with the relic olivine macrocrysts, occurring both within the macrocrysts and around the rims. The relic olivine macrocrysts have preserved strain features and some were clearly recrystalised before being replaced by calcite. Phlogopite constitutes the remaining 10% of the macrocryst suite, and occurs as rounded anhedral crystals up to ~3.5mm in length. They are commonly strained and all display undulose extinction.

Phenocryst phases (10%):

Approximately 90% of the phenocryst suite of this sample is comprised of phlogopite, which occurs as euhedral to subhedral laths up to 1.5mm in length. Subordinate diopside constitutes approximately 5% of the phenocryst suite, most commonly occurring as subhedral elongate laths up to 1mm in length.

Groundmass (75%):

Calcite and phlogopite are the most abundant minerals in the groundmass. Calcite occurs primarily as an interstitial phase and constitutes ~40% of the groundmass. Phlogopite occurs most commonly as subhedral, or occasionally euhedral, stubby lath-shaped crystals up to 0.3mm in size. A further ~5% of the groundmass comprises euhedral to subhedral diopside, which ranges up to 0.3mm in length. Disseminated opaque oxides up to 0.2mm in size are abundant throughout the groundmass, in addition to being commonly closely associated with the relic olivine macrocrysts.

JJG 3148 – South fissure

Texture: This sample was taken from close to the dyke margin. It contains approximately 40 volume % macrocrysts in one half, but becomes almost completely aphanitic towards the contact. The macrocrysts are aligned sub-parallel to the dyke margin, giving a weak fabric to the sample. The grain size of the groundmass ranges from <0.1mm close to the dyke margin to ~0.2mm away from the dyke margin.

Macrocryst phases:

Approximately 60% of the macrocrysts in this sample are rounded anhedral olivine, ranging from 0.5 to 5mm in size, which have been altered to serpentine and in most cases completely further replaced by calcite. Partial replacement or rims of phlogopite around the relic olivine macrocrysts are common. Phlogopite comprises ~40% of the macrocryst suite. This occurs as subhedral to anhedral, commonly elongate, crystals that range from 2mm to 4mm in size. Tetraferriphlogopite rims are common around the phlogopite macrocrysts, which are also sometimes partially altered to chlorite. Strain features such as undulose extinction and kink banding are present in all the phlogopite macrocrysts, and some are partially recrystalised.

Phenocryst phases (15%):

All the phenocrysts present in this sample are phlogopite. They are generally subhedral and range in size from 0.5mm to 2mm. These phenocrysts commonly have thin rims of tetraferriphlogopite, and some have been partly altered to chlorite.

Groundmass:

The grain size of the groundmass in this sample varies from between ~0.1 and 0.2mm on the coarse, macrocrystic side of the sample, to ~0.05mm on the fine-grained side towards the margin of the dyke. Approximately 80% of the groundmass is comprised of phlogopite, which exists in euhedral to subhedral lath shaped or stubby laths. All the groundmass phlogopite has thick rims of tetraferriphlogopite in the

coarser groundmass, all though tetraferriphlogopite is rare towards the dyke margin. Partial alteration of the groundmass phlogopite to chlorite occurs in <5% of the groundmass. The remainder of the groundmass is predominantly calcite, both as interstitial material and discrete, subhedral crystals 0.1-0.2mm in size. Diopside is rare (<5% of the groundmass) and occurs as small, subhedral crystals <0.1mm in length. Fe-Ti oxides up to 0.1mm in size occur throughout the sample.

NC008 – Muil Dyke

Texture: Macrocryst poor, containing ~10 volume % macrocrysts, with ~10 volume % phenocrysts in a fine-medium (0.2-0.3mm in size) grained acicular groundmass.

Macrocryst Phases (10%):
All the macrocrysts in this sample are olivine, which has been altered completely to serpentine, and partially replaced by calcite and subordinate phlogopite. Replacement by phlogopite is particularly common around the edges of the macrocrysts. The relic olivines are euhedral or subhedral, but sometimes show complex crystal shapes, and range up to 4mm in size. Some of the olivine macrocrysts are slightly strained and deformed.

Phenocryst phases (10%):
Olivine constitutes approximately 60% of the phenocryst suite of this sample, occurring as euhedral crystals that range from 0.5 to 1mm in size. All of the olivine has been completely altered to serpentine. The remaining 40% of the phenocryst suite is comprised of needle-like phlogopite, ranging up to 1mm in length. Some of the phlogopite phenocrysts are rimmed by tetraferriphlogopite.

Groundmass (80%):
The groundmass consists of aligned acicular, needle-like crystals of phlogopite and sanidine, up to 0.3mm in length, in approximately equal proportions. Subordinate euhedral sanidine is also present. Euhedral diopside up to 0.3mm is size forms less than 5% of the groundmass. Minor amounts of opaque oxides, <0.1mm in size are scattered throughout the groundmass.

NC012 – Muil dyke

Texture: Macrocrystic, containing ~20 volume % macrocrysts and ~15 volume % phenocrysts in a fine-grained groundmass of aligned needle-like lath shaped crystals. Several small calcite veins cut through the sample.

Macrocryst phases (20%):
All of the macrocrysts in this sample are euhedral to subhedral olivine. They range in size from 2mm to 4mm, and are all completely altered to serpentine with some partial replacement by phlogopite. Some of the

crystal shapes are very well preserved, and twinning can also be seen.

Phenocryst phases (15%):

Approximately 65% of the phenocryst suite is comprised of euhedral olivine, up to 2mm in size, all of which have been completely altered to serpentine. Long thin needles of phlogopite reaching 1.5mm in length comprise approximately 30% of the phenocryst suite. The phlogopite phenocrysts commonly have thin rims of tetraferriphlogopite. The remaining 5% of phenocrysts are euhedral diopside, which also occurs as acicular, needle-like crystals up to 1mm in length.

Groundmass (65%):

The groundmass is fine-grained (0.1mm), and is predominantly comprised of phlogopite (~40%), sanidine (~35%), diopside (~15%) and olivine (~10%). Much of the groundmass phlogopite and diopside, and some sanidine occurs in aligned acicular crystals, although subordinate euhedral diopside and sanidine are also present. Serpentine occurs as a minor interstitial phase, and all the groundmass olivine is also altered to serpentine.

NC014 – Mull Dyke

Texture: Macrocrystic, containing ~30 volume % macrocrysts, in a fine-grained groundmass with ~10 volume % phenocrysts. The groundmass minerals are aligned and flow around the macrocrysts.

Macrocryst phases (20%):

All the macrocrysts in this sample are olivine, which has been completely altered to serpentine and partially replaced by phlogopite. The range up to 4mm in size and are euhedral or sometimes subhedral in habit. Phlogopite replacement is particularly common around the rims of the macrocrysts. Opaque oxides up to 0.1 mm in size commonly occur within, or around the rims of, the relic olivine macrocrysts.

Phenocryst phases (10%):

The phenocryst suite comprises olivine and phlogopite in approximately equal proportions. The olivine phenocrysts are euhedral or subhedral, and range from 0.5 to 2mm in size. All the olivine phenocrysts are completely altered to serpentine. The euhedral or subhedral phlogopite phenocrysts occur as laths up to 1.5mm in length. They are deep red-brown in colour and strongly pleochroic.

Groundmass (70%):

The majority of the groundmass minerals occur in acicular, needle-like crystals up to 0.5mm in length. Phlogopite constitutes ~40% of the groundmass, and diopside a further 25%. Olivine, constituting ~10 % of the groundmass, occurs as euhedral serpentinised crystals up to 0.3mm in size. Diopside also occurs in much smaller euhedral crystals up to 0.1mm in size. The remainder of the groundmass is predominantly euhedral or subhedral sanidine, up to 0.2mm in size, with minor amounts of interstitial serpentine.

NC015 – Muil dyke

Texture: Macrocrystic, with macrocrysts constituting ~30 volume % of the sample. The groundmass is medium-fine grained and contains ~20 volume % phenocrysts.

Macrocryst phases (30%):
All of the macrocrysts are subhedral olivine, ranging up to 5mm in size, which have been completely altered to serpentine. Some of the macrocrysts have further been partially replaced by phlogopite around the rims.

Phenocryst phases (20%):
Approximately 60% of the phenocryst suite is comprised of euhedral to subhedral olivine, ranging up to 2mm in size, all of which is completely altered to serpentine. Phlogopite phenocrysts occur predominantly as subhedral lath-shaped or needle-like crystals up to 1.5mm in size, and constitute approximately 30% of the phenocryst suite. The remaining 10% of the phenocryst suite is composed of acicular, needle-like diopside, ranging in size up to 1mm.

Groundmass (50%):
The groundmass is medium-fine grained and is predominantly composed of lath-shaped or acicular crystals up to 0.5mm in size. Phlogopite constitutes ~50% of the groundmass, and is commonly rimmed by tetraferriphlogopite. Approximately 10% of the groundmass consists of diopside, both as needle-like laths up to 0.4mm in length, and as euhedral crystals up to ~0.3mm in size. Acicular and euhedral to subhedral sanidine comprises approximately 25% of the groundmass, and euhedral or subhedral olivine, completely altered to serpentine, ranging up to 0.3mm in size comprises ~10%.

JJG 3141 – Muil Dyke

Texture: Macrocryst poor, with ~5 volume % macrocrysts and ~10 volume % phenocrysts in fine-medium grained groundmass (grain size <0.3mm).

Macrocryst Phases (5%):
Olivine constitutes the entire macrocryst suite, occurring predominantly as subhedral crystals up to 3mm in size, all of which are completely replaced by calcite, with minor phlogopite around the rims.

Phenocryst Phases (10%):
Approximately 60% of the phenocryst suite is comprised of subhedral phlogopite, up to 2mm in size. The phlogopite phenocrysts are deep red-brown in colour and strongly pleochroic. Olivine phenocrysts constitute ~30% of the phenocryst suite, and have all been altered completely to serpentine with the majority being further replaced by calcite. Subhedral or euhedral diopside up to 1.5mm in length constitutes ~20% of the phenocryst suite.

Groundmass (80%):

Sanidine constitutes ~40% of the groundmass, in euhedral to subhedral crystals up to 0.2mm in size. Microphenocrysts of diopside (~20% of the groundmass) and phlogopite (~5% of the groundmass), commonly occurring as aligned acicular needles up to 0.4mm in size, reside in a matrix of interstitial calcite (~25% of the groundmass). Opaque oxides up to 0.2mm in size are abundant throughout the sample, constituting ~10% of the groundmass.

SR9 – Muil Dyke

Texture: Coarsely macrocrystic, containing ~25 volume % macrocrysts and ~10 volume % phenocrysts in a medium grained acicular groundmass.

Macrocryst phases (25%):

Olivine is the only macrocryst phase in this sample, occurring as subhedral to euhedral crystals up to 8mm in size. These are completely altered to serpentine and further almost entirely replaced by calcite, with serpentine remaining along fractures. Opaque oxides commonly occur within and around the relic olivine macrocrysts.

Phenocryst phases (10%):

Approximately 60% of the phenocryst suite is comprised of euhedral to subhedral olivine, ranging up to 2mm in size. The olivine phenocrysts are altered to serpentine and partially further replaced by calcite. Phlogopite and diopside phenocrysts each constitute approximately 20% of the phenocryst suite. The phlogopite occurs primarily in subhedral lath-shaped crystals but also as acicular needles, up to 1.5mm in size. The diopside phenocrysts are most commonly needle-like crystals ~1mm in size.

Groundmass (35%):

The groundmass consists of ~40% sanidine, as euhedral crystals up to 0.2mm in size. Diopside constitutes approximately 30% of the groundmass, occurring predominantly as aligned acicular needles up to 0.3mm in size. Phlogopite also occurs as acicular needles up to 0.3mm in length, which constitute approximately 20% of the groundmass. Disseminated opaque oxides up to 0.1mm in length are abundant throughout the groundmass. Minor euhedral apatite (<0.1mm in size) is also present.

A1.3 Mineral analyses

Representative major element analyses of phlogopite in the Swartruggens kimberlite dykes and the Muil lamprophyre are reported in Table A1.2.

Table A1.2 Representative major element analyses of phlogopites from the Swartruggens kimberlite dykes and the Muil lamprophyre, as reported in Chapter 3. Mac = macrocryst; g'mass = groundmass; FeO* = total iron as FeO; Mg# = atomic Mg/(Mg + Fe^{2+}) with Fe_2O_3 /FeO = 0.2. Atomic proportions have been calculated on the basis of 22O.

Dyke	Main dyke							
Sample	NC 006	NC 006	NC 006	NC 006	NC 006	NC 010	NC 010	NC 010
Description	Phlog mac	Phlog mac	Phlog mac	Phlog g'mass	Phlog g'mass	Phlog mac	Phlog mac	Phlog mac rim
SiO_2	42.3	42.3	41.2	43.1	42.4	42.2	41.8	41.0
TiO_2	1.65	1.64	1.57	1.76	1.54	1.43	1.88	2.06
Al_2O_3	13.0	12.0	12.4	11.1	7.97	12.6	12.4	8.19
FeO*	4.76	5.19	4.94	4.80	9.24	4.90	4.46	10.5
MnO	0.02	0.02	0.05	0.02	0.07	0.04	0.06	0.08
MgO	24.7	23.9	25.1	24.8	24.2	24.4	23.9	24.6
CaO	0.02	0.01	0.02	0.03	0.09	0.01	0.02	0.12
Na_2O	0.23	0.30	0.19	0.20	0.12	0.19	0.24	0.25
K_2O	10.8	10.2	10.2	9.81	9.06	10.4	10.1	10.2
Total	97.5	95.6	95.8	95.6	94.7	96.2	94.8	96.9
Mg#	0.91	0.90	0.91	0.91	0.84	0.91	0.91	0.82
Atomic proportions calculated on the basis of 22O								
Si	5.889	6.000	5.845	6.079	6.179	5.939	5.954	5.936
Ti	0.173	0.175	0.168	0.187	0.168	0.152	0.202	0.224
Al	2.133	2.013	2.079	1.851	1.368	2.096	2.080	1.400
Fe	0.554	0.616	0.586	0.566	1.125	0.577	0.532	1.270
Mn	0.002	0.003	0.006	0.003	0.008	0.004	0.007	0.010
Mg	5.129	5.044	5.309	5.209	5.249	5.129	5.078	5.306
Ca	0.003	0.002	0.003	0.004	0.013	0.001	0.003	0.019
Na	0.063	0.083	0.051	0.055	0.033	0.051	0.067	0.069
K	1.915	1.846	1.852	1.765	1.682	1.874	1.828	1.881
Sum	15.86	15.78	15.90	15.72	15.83	15.82	15.75	16.11

Dyke	Main Dyke					Changehouse Dyke		
Sample	NC 010	NC 010	NC 010	NC 010	NC 010	NC 009	NC 009	NC 009
Description	Phlog mac rim	Phlog g'mass	Phlog g'mass	Phlog g'mass	Phlog g'mass	Phlog mac	Phlog g'mass	Phlog g'mass
SiO_2	38.2	42.2	42.1	41.5	41.6	40.1	42.5	40.5
TiO_2	1.88	1.60	1.79	1.65	1.69	1.63	2.05	1.82
Al_2O_3	11.5	12.2	12.5	12.3	11.3	14.4	10.2	12.1
FeO*	8.13	4.95	4.33	5.53	6.57	4.27	5.58	4.57
MnO	0.06	0.01	0.03	0.06	0.04	0.02	0.08	0.00
MgO	24.1	25.1	24.2	25.3	25.5	25.3	24.5	24.5
CaO	0.00	0.08	0.03	0.03	0.03	0.08	0.14	0.05
Na_2O	0.21	0.18	0.12	0.13	0.13	0.25	0.24	0.15
K_2O	11.8	10.7	10.5	10.8	10.5	11.1	8.72	9.62
Total	95.9	97.1	95.6	97.3	97.4	97.2	94.0	93.3
Mg#	0.86	0.91	0.92	0.90	0.89	0.92	0.90	0.91
Atomic proportions calculated on the basis of 22O								
Si	5.595	5.908	5.951	5.823	5.863	5.627	6.096	5.873
Ti	0.207	0.168	0.191	0.174	0.179	0.172	0.221	0.199
Al	1.990	2.019	2.087	2.042	1.877	2.378	1.730	2.060
Fe	0.996	0.579	0.512	0.649	0.774	0.501	0.670	0.554
Mn	0.007	0.001	0.003	0.007	0.005	0.002	0.010	0.000
Mg	5.276	5.242	5.103	5.295	5.352	5.290	5.240	5.293
Ca	0.001	0.011	0.005	0.005	0.005	0.012	0.022	0.007
Na	0.060	0.049	0.033	0.036	0.035	0.069	0.066	0.042
K	2.202	1.919	1.894	1.935	1.892	1.990	1.596	1.780
Sum	16.33	15.90	15.78	15.97	15.98	16.04	15.65	15.81

Table A1.2 Continued.

Dyke	Changehouse Dyke		Mull Dyke					
Sample	NC 009	NC 005	NC 012	NC 012	NC 012	NC 012	NC 012	NC 012
Description	Phlog g'mass	Phlog g'mass	Phlog g'mass	Phlog g'mass	Phlog g'mass	Phlog g'mass	Phlog g'mass	Phlog g'mass
SiO_2	41.0	39.4	38.3	37.8	39.8	39.6	39.3	40.1
TiO_2	1.92	1.47	3.87	3.74	3.33	3.75	3.41	3.05
Al_2O_3	12.9	11.8	11.9	12.0	11.9	12.7	11.3	10.2
FeO*	4.45	5.65	7.42	8.25	7.76	7.06	7.14	9.67
MnO	0.06	0.04	0.05	0.07	0.04	0.05	0.09	0.09
MgO	24.6	23.0	22.0	21.5	23.6	22.6	23.9	21.6
CaO	0.02	0.09	0.10	0.04	0.02	0.12	0.10	4.06
Na_2O	0.24	0.11	0.15	0.14	0.21	0.16	0.16	0.66
K_2O	9.94	10.9	8.96	9.06	8.59	9.57	8.55	5.85
Total	95.1	92.5	92.7	92.6	95.2	95.6	93.9	95.3
Mg#	0.92	0.89	0.85	0.84	0.86	0.86	0.87	0.82
Atomic proportions calculated on the basis of 22O								
Si	5.830	5.853	5.681	5.640	5.728	5.679	5.724	5.807
Ti	0.206	0.164	0.432	0.419	0.360	0.405	0.373	0.332
Al	2.159	2.059	2.072	2.107	2.011	2.147	1.935	1.748
Fe	0.529	0.702	0.920	1.030	0.933	0.847	0.870	1.171
Mn	0.007	0.005	0.007	0.009	0.005	0.006	0.011	0.011
Mg	5.217	5.103	4.855	4.791	5.047	4.843	5.191	4.654
Ca	0.002	0.015	0.015	0.006	0.003	0.018	0.015	0.629
Na	0.066	0.031	0.044	0.041	0.058	0.044	0.045	0.186
K	1.803	2.072	1.696	1.725	1.575	1.752	1.588	1.082
Sum	15.82	16.00	15.72	15.77	15.72	15.74	15.75	15.62

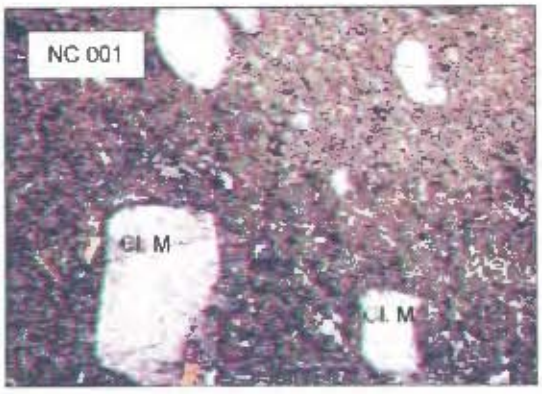

NC 001; Third Lease. FOV ~20mm.
Olivine macrocrysts are completely replaced by calcite. Groundmass is predominantly phlogopite (severely chloritised) and calcite.

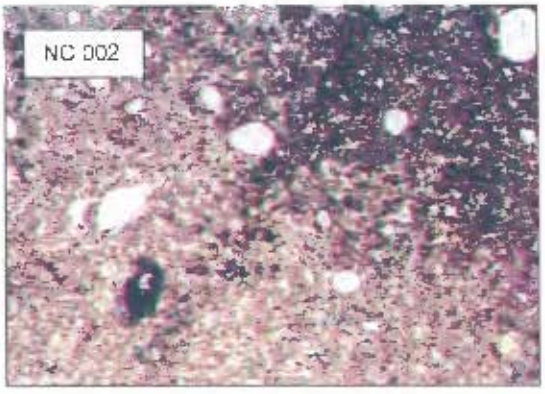

NC 002; Third Lease FOV ~20mm.
Olivine macrocrysts are completely replaced by calcite. Groundmass consists predominantly of partially chloritised phlogopite, and calcite.

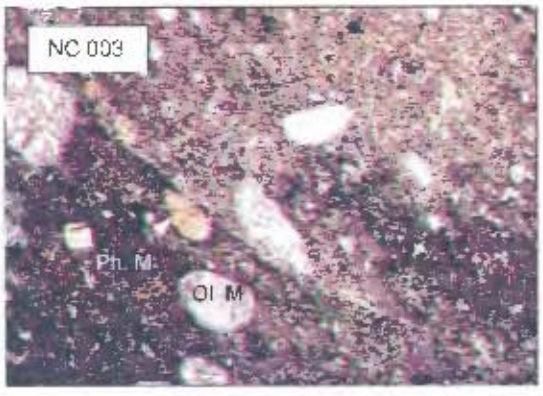

NC 003; Third Lease. FOV ~20mm.
Olivine macrocrysts are completely replaced by calcite. Groundmass is predominantly phlogopite (severely chloritised) and interstitial calcite.

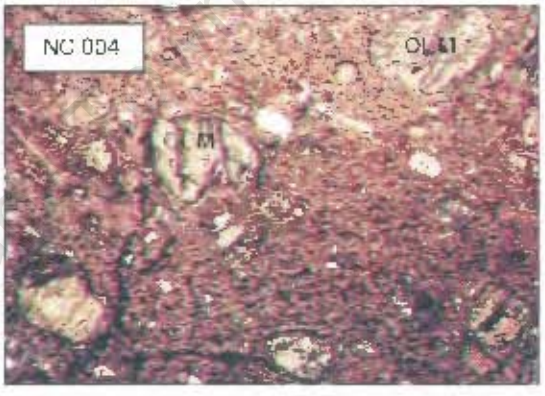

NC 004; Main Dyke. FOV ~15mm.
All the olivine macrocrysts are completely serpentinised and smaller fragments are replaced by calcite. Groundmass predominantly comprised of phlogopite.

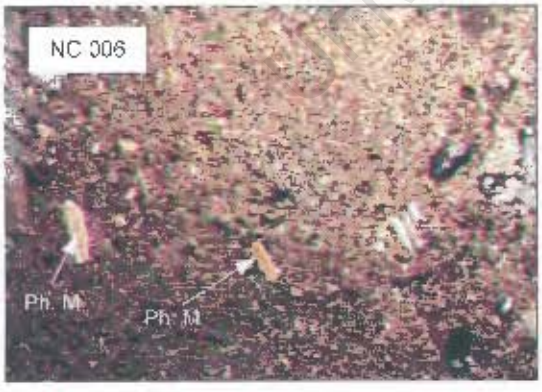

NC 006; Main Dyke. FOV ~20mm.
Small fragments of olivine macrocrysts are replaced by calcite. Phlogopite macrocrysts are optically zoned, with darker cores than rims. Groundmass is precominantly phlogopite.

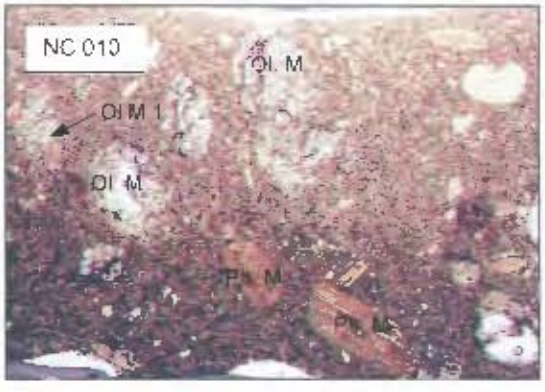

NC 010; Main Dyke. FOV ~20mm.
Olivine macrocrysts are completely replaced by calcite, with some replacement by phlogopite of Ol. M 1. Phlogopite macrocrysts are highly strained. Groundmass is predominantly phlogopite.

Plate A1.1 Photomicrographs of the Swartruggens kimberlite and Muil lamprophyre samples. FOV = field of view. Ol M = olivine macrocryst; Ph. M = phlogopite macrocryst.

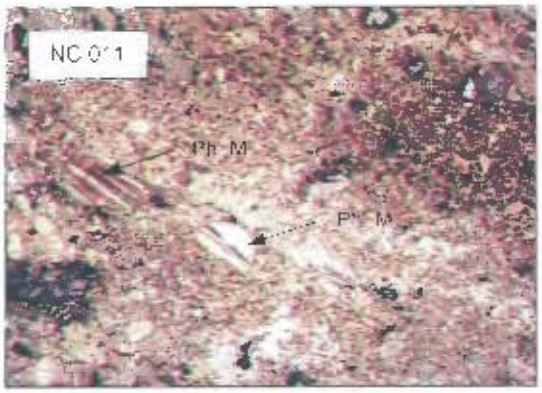

NC 011; Main Dyke. FOV ~15mm.
Fragments of olivine macrocrysts are completely replaced by calcite. Phlogopite macrocrysts are fractured along cleavage planes and infilled by calcite. Groundmass is predominantly phlogopite.

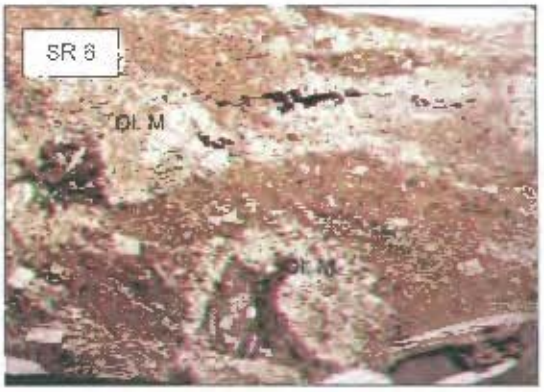

SR 6; Main Dyke. FOV ~10mm.
The olivine macrocrysts are completely replaced by calcite with associated opaque oxides. Groundmass is predominantly phlogopite and calcite.

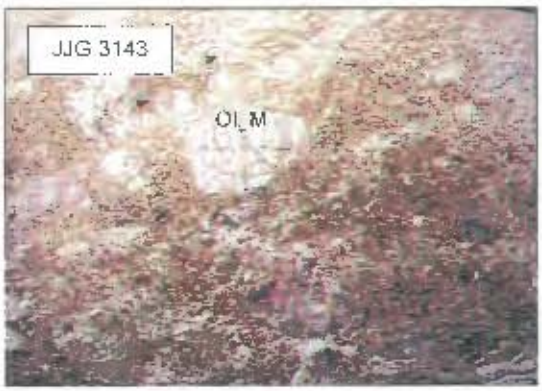

JJG 3143; Main Dyke. FOV ~15mm.
Olivine macrocrysts are completely replaced by calcite. Groundmass phlogopite aligned, and abundant interstitial calcite occurs in sub-parallel bands.

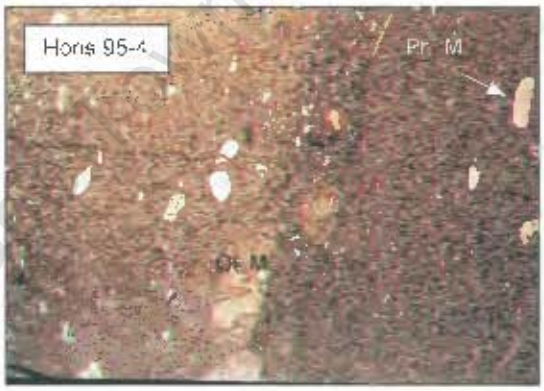

Hons 95-4; Main Dyke. FOV ~20mm.
Olivine macrocrysts, altered to serpentine and partially replaced by calcite, reside in a predominantly phlogopite groundmass. Sample has a strong fabric.

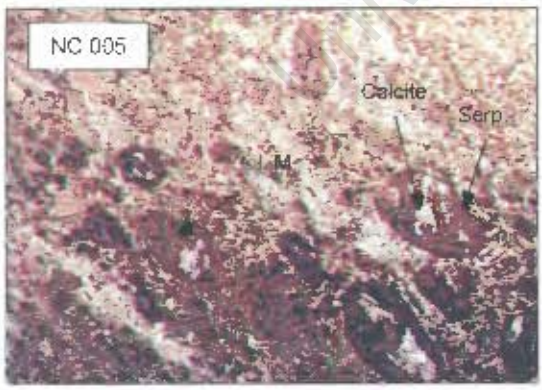

NC 005; Changehouse Dyke. FOV ~15mm.
Olivine macrocrysts are altered to serpentine and partially replaced by calcite. Groundmass consists predominantly of aligned phlogopite and interstitial calcite.

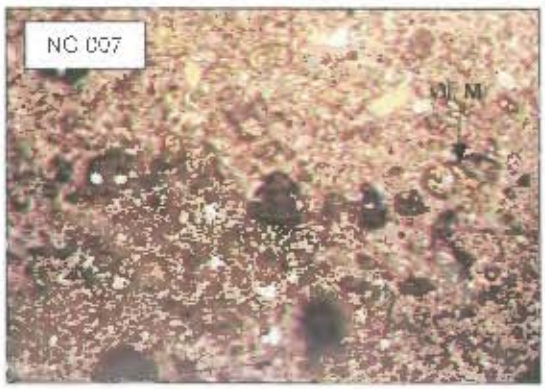

NC 007; Changehouse Dyke. FOV ~20mm.
The abundant olivine macrocrysts are all altered to serpentine, with minor partial replacement by calcite. Many of the macrocrysts are disaggregated into anhedral fragments <1mm in size.

Plate A1.1 Continued. FOV = field of view. Ol. M = olivine macrocryst. Ph. M = phlogopite macrocryst. Serp = serpentine.

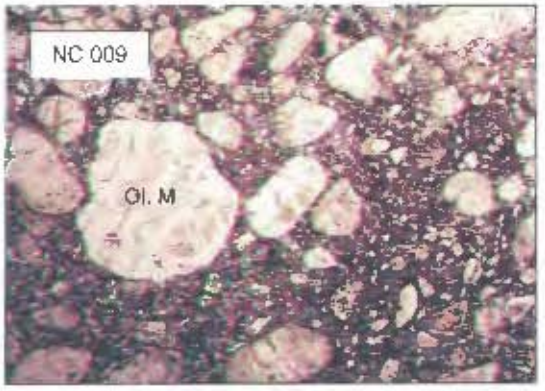

NC 009; Changehouse Dyke. FOV ~15mm.
The abundant olivine macrocrysts are completely altered to serpentine or replaced by calcite. Groundmass contains abundant phlogopite, with subordinate calcite and diopside.

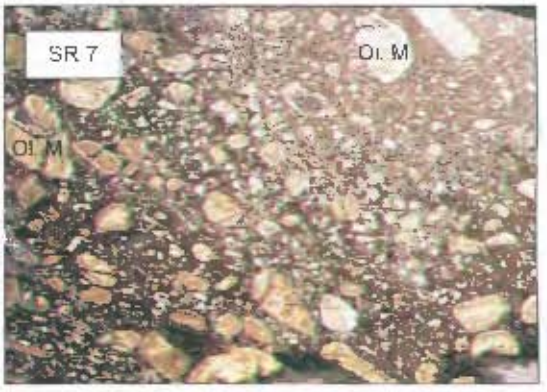

SR 7; Changehouse Dyke. FOV ~15mm.
Rounded olivine macrocrysts, showing a wide range in size, are abundant and are completely altered to serpentine. Groundmass is predominantly phlogopite, with subordinate calcite and minor diopside.

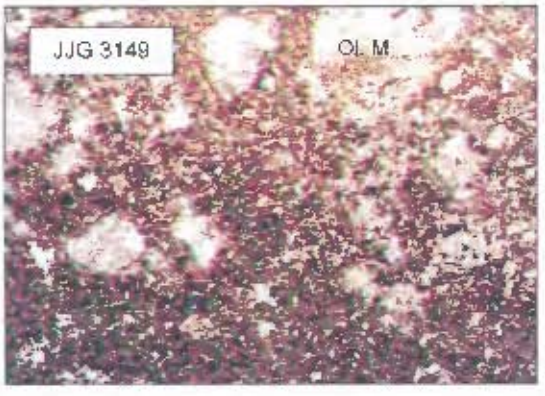

JJG 3149; South Fissure. FOV ~15mm.
Olivine macrocrysts are completely replaced by calcite. The groundmass is predominantly phlogopite, with opaque oxides abundant throughout the sample.

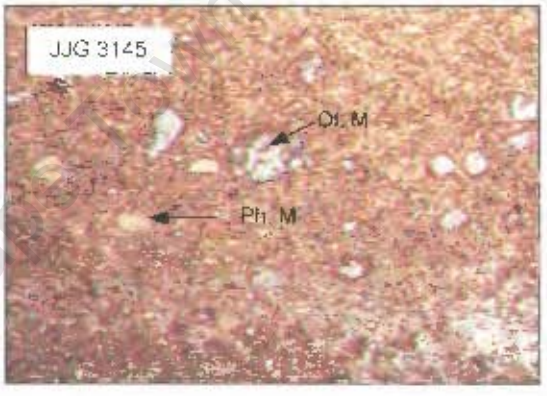

JJG 3145; South Fissure. FOV ~20mm.
Macrocryst poor. Olivine macrocrysts are completely replaced by calcite and commonly fragmented. The groundmass is dominated by phlogopite and tetraferriphlogopite.

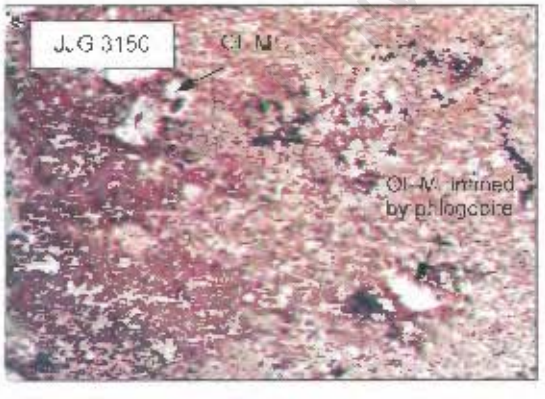

JJG 3150; South Fissure. FOV ~15mm.
Olivine macrocrysts are completely replaced by calcite and sometimes lesser phlogopite. Groundmass is extremely altered and contains abundant calcite and opaque oxides.

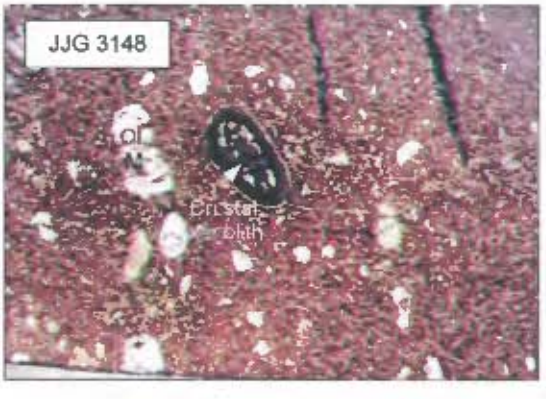

JJG 3148; South Fissure. FOV ~20mm.
Olivine macrocrysts are completely replaced by calcite. The ground mass consists predominantly of phlogopite. A large crustal xenolith is present. The sample becomes more aphanitic towards the top right corner, close to the dyke margin.

Plate A1.1 Continued. FOV = field of view; Ol. M = olivine macrocryst; Ph. M = phlogopite macrocryst, Serp = serpentine.

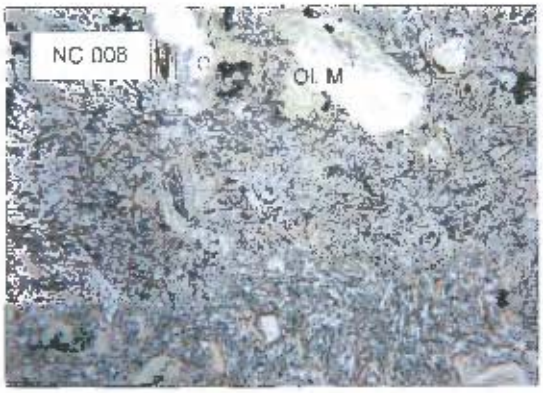

NC 008; Muil Dyke. FOV ~30mm.
Macrocryst poor. Rare olivine macrocrysts are completely altered to serpentine. Abundant phlogopite and diopside phenocrysts in a groundmass of sanidine, diopside and phlogopite.

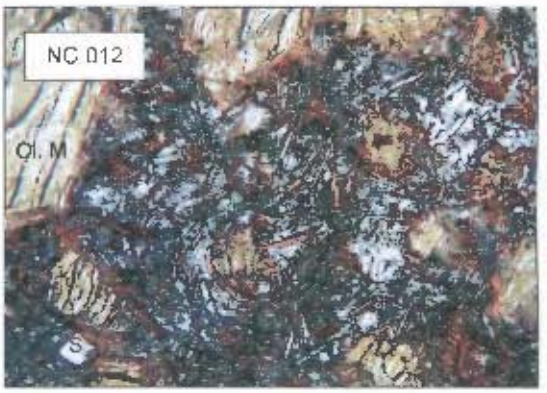

NC 012; Muil Dyke. FOV ~30mm.
Coarsely macrocrystic, with subhedral olivine macrocrysts completely altered to serpentine and partially replaced by phlogopite around the rims. Abundant phlogopite and diopside phenocrysts.

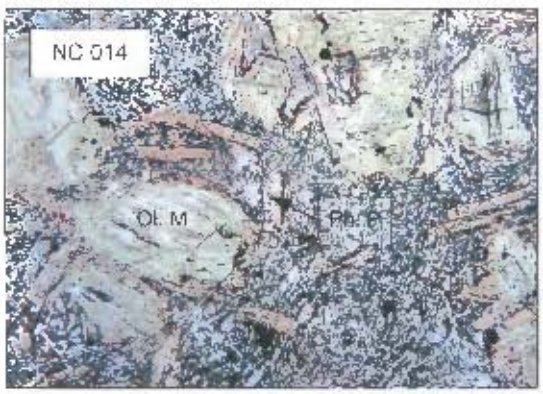

NC 014; Muil Dyke. FOV ~30mm
Subhedral olivine macrocrysts are completely altered to serpentine and partial replaced by phlogopite. Lath-shaped phlogopite phenocrysts reside in a predominantly sanidine groundmass.

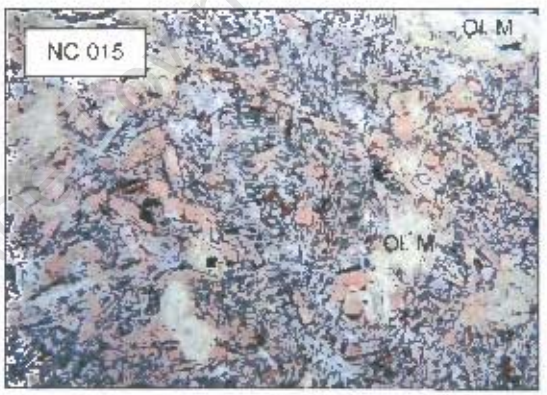

NC 015; Muil Dyke. FOV ~30mm.
Olivine macrocrysts are altered completely serpentine and partially replaced by phlogopite. Lath-shaped phenocrysts of phlogopite and diopside are abundant.

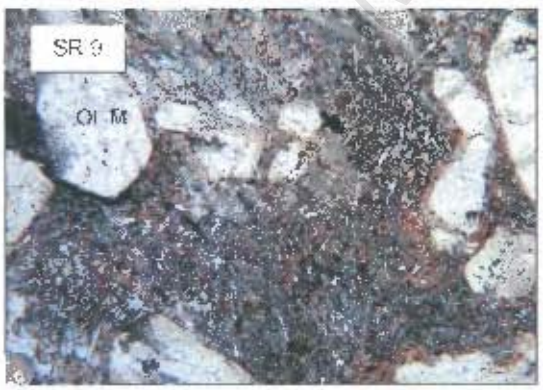

SR 9; Muil Dyke. FOV ~30mm.
Euhedral to subhedral olivine macrocrysts are replaced by calcite, with serpentine along fractures. The groundmass is acicular and fine-grained, with a flow textures which bend around the macrocrysts.

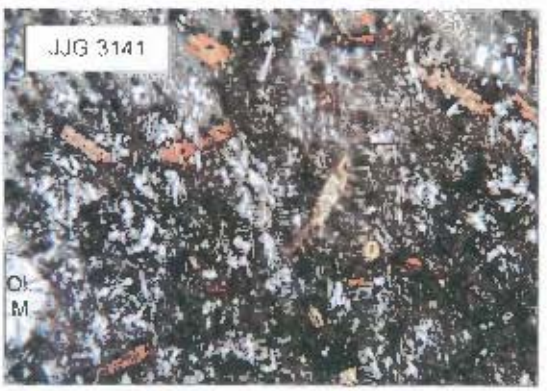

JJG 3141; Muil Dyke. FOV ~30mm.
All olivine is replaced by calcite. Phlogopite phenocrysts are fresh, but groundmass is severely altered and contains abundant calcite and opaque oxides.

Plate A1.1 Continued. FOV = field of view; Ol. M = olivine macrocryst; Ph. M = phlogopite macrocryst; Serp = serpentine; S = sanidine; Ph. P = phlogopite phenocryst.

Appendix 2

Star sample localities and individual petrographic descriptions

A2.1 Sample localities

The localities of the Star samples analysed in this study are reported in Table A2.1. All samples are from the mantle room collection at the University of Cape Town, except samples NC 050 – 054, which were collected for this study during a visit to the Star mine in July 2002. The Barren Dyke samples were collected from mining dumps. Unfortunately, the exact within dyke localities of the other samples are unknown.

Table A2.1 Localities of the Star samples

Sample no.	Dyke
JJG 2833	Clewer Dyke
JJG 2837	Clewer Dyke
SJH 37	Wynandsfontein Dyke
JJG 6361A	Wynandsfontein Dyke
JJG 6361C	Wynandsfontein Dyke
JJG 6369	Wynandsfontein Dyke
JJG 6362	Wynandsfontein Dyke
JJG 6360	Wynandsfontein Dyke
NC 050	Wynandsfontein Dyke
JJG 4570	East Star Dyke
SJH 101	East Star Dyke

Sample no.	Dyke
SJH 30	East Star Dyke
SJH 38	East Star Dyke
SJH 104	East Star Dyke
SJH 80	Byrnes Dyke
SJH 79	Byrnes Dyke
SJH 78	Byrnes Dyke
SJH 77	Byrnes Dyke
NC 051	Barren Dyke
NC 052	Barren Dyke
NC 053	Barren Dyke
NC 054	Barren Dyke

A2.2 Sample descriptions

JJG 2833 – Clewer Dyke

Texture: Macrocrystic, containing ~30 volume % macrocrysts and ~20 volume % phenocrysts in a medium-fine-grained groundmass (grain size <0.5mm).

Macrocryst phases (30%):

By far the most abundant macrocryst phase in this sample is olivine, which forms subhedral to anhedral rounded crystals surrounded by thick reaction rims, and constitutes approximately 90% of the macrocryst

suite. The olivine macrocrysts are typically very fresh in the centre, with only minor replacement by calcite along some fractures. They range from less than 0.5mm to 4mm in size. Phlogopite macrocrysts ranging up to 2mm in size constitute ~10 % of the macrocryst suite. They are anhedral, and show undulose extinction, with slight alteration to chlorite around the edges of some of the crystals. One red-brown anhedral, eclogitic garnet ~0.5mm in size is present in this sample.

Phenocryst phases (20%):

Approximately 95% of the phenocrysts in this sample are phlogopite. They are subhedral and range from approximately 0.5mm to 1.5mm in size. Some of the phenocrysts are clearly zoned, and many show partial alteration to chlorite. Rare subhedral diopside phenocrysts range up to 1mm in length and constitute the remaining 5% of the phenocryst suite. Some are slightly altered.

Groundmass (50%):

The groundmass consists of ~70% phlogopite, in euhedral to subhedral lath-shaped crystals up to 0.5mm in size. In places these are partially altered to chlorite. Interstitial carbonate constitutes ~20% of the groundmass, and euhedral olivine up to 0.4mm in size constitutes ~5%. Opaque oxides (~0.2mm in size) are common throughout the sample, especially around the edges of the macrocrysts

JJG 2837 – Clewer Dyke

Texture: Coarsely macrocrystic, containing ~30 volume % macrocrysts and 5 volume % phenocrysts in a fine-medium grained groundmass (grain size <0.5mm).

Macrocryst phases: (30%)

Approximately 95% of the macrocryst suite comprises olivine, which is altered to serpentine and partially further replaced by calcite, particularly along cracks and around the rims. In places there are small remnants of the original olivine. The olivine macrocrysts are anhedral and rounded, and range up to 5mm in size. The remaining 5% of the macrocrysts are phlogopite. These are no larger than 2mm in length, but are distinguishable from phenocrysts by their distorted crystal shapes and extensive kink-banding.

Phenocryst phases: (5%)

Phenocrysts are rare in this sample, and the majority are phlogopite, ranging from 0.5 to 1mm in size. They are usually subhedral, lath-shaped crystals and commonly have thin rims of tetraferriphlogopite. Approximately 5% of the phenocryst suite is comprised of subhedral olivine, which is altered to serpentine, ranging up to 1mm in size.

Groundmass:

The groundmass consists of ~70% phlogopite, which is subhedral to anhedral, and ranges up to 0.5mm in size. Some of the groundmass phlogopite is rimmed by tetraferriphlogopite. The majority of the remainder of the groundmass is composed of calcite, primarily as an interstitial phase but also as lesser subhedral to

euhedral crystals up to 0.2mm in size. Subordinate interstitial serpentine is also present, and opaque oxides, ranging up to 0.1mm in size, are scattered throughout the sample.

SJH 37 – Wynandsfontein Dyke

Texture: Macrocrystic, containing ~ volume 20% macrocrysts and ~5 volume % phenocrysts in a fine-medium grained groundmass (grain size <0.5mm).

Macrocryst phases (20%):
Olivine constitutes ~90% of the macrocryst suite, occurring as rounded anhedral crystals up to 0.4mm in size. The olivine macrocrysts are completely replaced by calcite, with partial replacement by phlogopite. No relics of original olivine remaining. Phlogopite macrocrysts, ranging up to 2mm in size, constitute ~10% of the macrocryst. These are commonly rounded, anhedral or subhedral crystals, which have been extensively strained and show undulose extinction and kink banding. Some of the phlogopite macrocrysts are partially altered to chlorite. One red-brown garnet is present in this sample, which is anhedral and has disaggregated into several smaller fragments (~0.1mm in size).

Phenocryst phases (5%):
Phlogopite is the only phenocryst phase in this sample. It occurs predominantly as subhedral crystals ranging from ~0.5mm to 1mm in size. Many of the phenocrysts are optically zoned, and some are partially altered to chlorite.

Groundmass (75%):
The groundmass consists predominantly of calcite and phlogopite, in approximately equal proportions. The calcite occurs principally as interstitial material but also as subhedral crystals up to approximately 0.3mm in size. Phlogopite occurs as subhedral to anhedral crystals up to 0.5mm in size, some of which has been partially altered to chlorite. Minor interstitial serpentine is also present and opaque oxides, ranging up to 0.1mm in size, are abundant throughout the groundmass.

JJG 6361A – Wynandsfontein Dyke

Texture: Coarsely macrocrystic, containing ~40% macrocrysts, which range up to 8mm in size, with ~10% phenocrysts in a medium-grained groundmass (grain size <0.5mm).

Macrocryst phases: (40%)
Olivine constitutes ~80% of the macrocryst suite, occurring as anhedral and rounded macrocrysts up to 8mm in size. Most of the olivine macrocrysts are replaced almost completely by calcite, although small relics of original olivine remain. These relics of the original crystals are strained, showing undulose extinction, and are commonly partially recrystalised. Phlogopite macrocrysts range in size up to 2mm and comprise ~20%

of the macrocryst suite. They are anhedral or subhedral, and commonly partially eroded around the rims. The phlogopite macrocrysts are highly strained, with undulose extinction and kink-banding common, and many of the crystals are torn along cleavage planes and infilled by calcite. Some of the phlogopite macrocrysts are partially altered to chlorite. One red-brown anhedral garnet approximately 1mm in size occurs in this sample.

Phenocryst phases (10%):

The majority of the phenocrysts in this sample are subhedral phlogopite up to 1.5mm in size. These are often optically zoned. Some of the phlogopite phenocrysts are partially altered to chlorite. Subhedral olivine phenocrysts, completely altered to serpentine, range up to 1mm in size and comprise approximately 3 volume % of the

Groundmass (50%):

The groundmass consists of approximately equal proportions of phlogopite in subhedral or anhedral crystals up to 0.5mm in size, and calcite. Calcite occurs both as subhedral crystals up to 0.5mm in size and, more commonly, as an interstitial phase. Some of the groundmass phlogopite is altered to chlorite. Subordinate interstitial serpentine is also present (<5% of the groundmass) and opaque oxides (up to 0.1mm in size) are scattered throughout the sample.

JJG 6361C – Wynandsfontein Dyke

Texture: Macrocrystic, containing ~30 volume % macrocrysts, which range up to 8mm in size, with ~10 volume % phenocrysts in a medium-grained groundmass (grain size <0.5mm). This sample contains a large (~15mm diameter) fragment of another kimberlite, which is distinguished by a much finer grain size (<0.2mm) and abundant groundmass diopside.

Macrocryst phases (30%)

Approximately 80% of the macrocryst suite is comprised of rounded, anhedral olivine, ranging up to 5mm in size. All the olivine macrocrysts are completely replaced by calcite. Phlogopite constitutes ~20% of the macrocryst suite, occurring as rounded anhedral or subhedral macrocrysts up to 2mm in size. The phlogopite macrocrysts are highly strained and show undulose extinction and kink banding. Some of the phlogopite macrocrysts are partially altered to chlorite.

Phenocryst phases (10%):

The majority of the phenocrysts in this sample are subhedral phlogopite up to 1.5mm in size. Some of the phlogopite phenocrysts show distinct optical zoning, and some are partially altered to chlorite. A few subhedral serpentinised olivine phenocrysts, ranging up to 1mm in size are also present.

Groundmass (60%):

The groundmass consists of ~50% phlogopite in subhedral crystals up to 0.5mm in size, some of which have been partially altered to chlorite. The remainder of the groundmass is predominantly calcite, which occurs for the most part as interstitial material but also as subordinate subhedral to euhedral crystals up to 0.5mm in size. Minor interstitial serpentine comprises <5% of the groundmass and opaque oxides (up to 0.1mm in size) are abundant throughout the sample.

JJG 6369 – Wynandsfontein Dyke

Texture: Moderately macrocrystic, containing ~20% macrocrysts and ~10% phenocrysts in a fine-medium grained groundmass (grain size <0.5mm).

Macrocryst phases (20%):

Approximately 80% of the macrocryst suite is comprised of relic olivine, all of which is completely altered to serpentine with partial further replacement by calcite particularly along cracks and around the edges of the macrocrysts. Opaque oxides (<0.1mm in size) are common around the rims of, and throughout, the macrocrysts. The olivine macrocrysts are rounded and anhedral, and range up to 7mm in length. Some were clearly extensively strained and partially recrystalised before being altered to serpentine. Phlogopite constitutes ~20% of the macrocryst suite, occurring as subhedral or anhedral crystals up to 2mm in length. The phlogopite macrocrysts are commonly extensively strained, showing undulose extinction and kink banding, and are sometimes torn open along cleavage planes and infilled with calcite.

Phenocryst phases (10%):

The only phenocryst phase in this sample is phlogopite, which most commonly occurs as subhedral lath-shaped crystals up to 1.5mm in length. Some of the phlogopite phenocrysts show weak optical zoning, and thin rims of tetraferriphlogopite are common.

Groundmass (70%):

The groundmass is comprised of ~80% subhedral laths of phlogopite up to 0.5mm in length and ~15% calcite, which occurs predominantly as an interstitial phase but also as subordinate discrete euhedral crystals up to 0.3mm in size. Approximately 5% of the groundmass consists of chlorite and interstitial serpentine. Opaque oxides (<0.1mm in size) are abundant throughout the groundmass, in addition to being closely associated with the relic olivine macrocrysts.

JJG 6362 – Wynandsfontein Dyke

Texture: Macrocrystic, with ~25 volume % macrocrysts and ~5 volume % phenocrysts in a fine-medium grained groundmass (grain size <0.5mm).

Macrocryst phases (25%):

Approximately 90% of the macrocryst suite is comprised of rounded, anhedral olivine, which ranges up to 6mm in size. All the olivine is altered to serpentine with minor further replacement by calcite, particularly along fractures, in some macrocrysts. Phlogopite comprises the remaining ~10% of the macrocryst suite, occurring as anhedral, rounded crystals that range up to 1.5mm in size. The phlogopite macrocrysts are extensively strained and show undulose extinction and kink banding, with some crystals being split along cleavage planes and infilled with calcite.

Phenocryst phases (5%):

All the phenocrysts in this sample are phlogopite, which is most commonly subhedral and ranges up to 1mm in length.

Groundmass:

The groundmass is comprised of ~70% phlogopite, in subhedral crystals up to 0.5mm in length. Approximately 10% of the groundmass is comprised of subhedral calcite, ranging up to 0.2mm in size. The remaining 20% of the groundmass is almost entirely composed interstitial serpentine and calcite. Opaque oxides are abundant, some reaching 0.2mm in size, throughout the groundmass.

JJG 6360 – Wynandsfontein Dyke

Texture: Macrocrystic, containing ~25 volume % macrocrysts and ~10 volume % phenocrysts in a fine-grained groundmass (grain size <0.5mm).

Macrocryst phases (25%):

Olivine constitutes ~80% of the macrocryst suite, occurring as anhedral and rounded crystals that range up to ~5mm in size. They are very fresh and most are almost completely unaltered, with only slight alteration to serpentine and minor replacement by calcite around the rims, and fractures, of a few of the macrocrysts. Serpentinisation occurs more pervasively in one small (<10mm diameter) area of the sample. Approximately 20% of the macrocryst suite is comprised of anhedral or subhedral phlogopite, which ranges up to 2mm in size. The phlogopite macrocrysts are commonly strained and slightly distorted, and show undulose extinction. Some phlogopite macrocrysts are partially altered to chlorite.

Phenocryst phases (10%):

All the phenocrysts in this sample are subhedral to euhedral phlogopite ranging up to ~1mm in size. Some of the phenocrysts are distinctly optically zoned, with darker cores than rims.

Groundmass (65%):

The groundmass is comprised of ~70% phlogopite, in subhedral to euhedral crystals up to 0.5mm in size, some of which are partially altered to chlorite. Approximately 10% of the groundmass is euhedral to subhedral calcite up to 0.2mm in size, and interstitial calcite and subordinate serpentine constitute the

majority of the remaining ~20% of the groundmass. Opaque oxides, up to 0.1mm in size, are abundant throughout the groundmass. Minor subhedral perovskite (<0.1mm in size) is also present.

NC 050 Wynandsfontein Dyke

Texture: Macrocrystic, containing ~20 volume % macrocrysts with ~5 volume % phenocrysts, in a fine-medium grained groundmass (grain size <0.5mm).

Macrocryst phases (20%):
Approximately 90% of the macrocryst suite is comprised of rounded, anhedral olivine, which ranges up to 0.3mm in size. All the olivine macrocrysts are partially altered to serpentine, particularly around the rims and along fractures, although they are largely still fresh. Opaque oxides are commonly associated with particularly the more altered olivine macrocrysts. Phlogopite macrocrysts range in size up to 4mm, and comprise ~10% of the macrocryst suite. They are anhedral and commonly extensively strained, with undulose extinction, and some phlogopite macrocrysts are partially recrystalised.

Phenocryst phases (5%):
The majority of the phenocrysts in this sample are phlogopite, which most commonly occurs as subhedral lath-shaped crystals up to 1mm in length. Some of the phlogopite phenocrysts have thin rims of tetraferriphlogopite. Subhedral olivine, partially or completely altered to serpentine, ranging up to 1mm in size constitutes ~2 volume % of the sample.

Groundmass (75%):
The groundmass consists ~70% phlogopite, occurring as subhedral or euhedral crystals that range from 0.1mm to 0.5mm in size, with ~10% subhedral calcite ranging up to 0.2mm in size. The remaining ~20% of the groundmass is predominantly comprised of interstitial serpentine and subordinate interstitial calcite, with opaque oxides (up to 0.1mm in size) abundant throughout the groundmass and particularly concentrated around the olivine macrocrysts.

JJG 4570 – East Star Dyke

Texture: Coarsely macrocrystic, containing ~30 volume % macrocrysts with ~10 volume % phenocrysts in a medium-fine grained groundmass.

Macrocryst phases (40%):
Approximately 90% of the macrocryst suite is comprised of olivine, in rounded anhedral crystals up to 8mm in size. Some of the larger macrocrysts (>1mm in size) are fresh and unaltered apart from thin rims around the crystal edges, which are altered to serpentine and partially replaced by calcite, and slight alteration to serpentine along fractures. The majority of the smaller or disaggregated macrocrysts are completely

replaced by calcite with some serpentine. Phlogopite macrocrysts are much less abundant than olivine macrocrysts, constituting ~10% of the macrocryst suite, and smaller, reaching up to 1mm in length. They are subhedral and commonly form lath shaped crystals, which are distorted, showing slight kink banding and undulose extinction. The phlogopite macrocrysts are commonly rimmed by tetraferriphlogopite.

Phenocryst phases (10%):
All the phenocrysts in this sample are phlogopite, which occurs as euhedral to subhedral crystals up to 0.7mm in length, commonly rimmed by tetraferriphlogopite. Some of the phlogopite phenocrysts are optically zoned, usually with darker cores than rims.

Groundmass (50%):
The groundmass consists of ~60% phlogopite, which occurs as euhedral to subhedral crystals up to 0.5mm in size, rimmed by tetraferriphlogopite. Approximately 30% of the groundmass consists of calcite, as interstitial material and subhedral crystals up to 0.5mm in size. Opaque oxides and accessory perovskite, up to 0.1mm in size, are scattered throughout the sample.

SJH 101 – East Star Dyke

Texture: Macrocrystic, containing ~20 volume % macrocrysts and ~5 volume % phenocrysts in a fine-grained groundmass. There is a weak fabric due to the alignment of the macrocrysts and the groundmass minerals.

Macrocryst phases (20%):
Rounded, anhedral olivine, ranging up to 4mm in size, constitute ~80% of the macrocryst suite. They are all altered completely to serpentine and partially further replaced by calcite, particularly along fractures. Some of the macrocrysts are also replaced partially by phlogopite and no relics of the original olivine remain. Opaque oxides are commonly associated with the rims of the relic olivine macrocrysts. Phlogopite macrocrysts constitute a further ~20% of the macrocryst suite, and range in size up to approximately 1.5mm, although the majority are ~0.5mm in length. The phlogopite macrocrysts are anhedral or subhedral and commonly extremely strained and distorted. They show kink banding and in places are torn apart along cleavage planes and infilled with calcite. Some of the phlogopite macrocrysts have thin rims of tetraferriphlogopite.

Phenocryst phases (5%):
Phenocrysts are not common in this sample, but where present they are all phlogopite. The phlogopite phenocrysts are typically subhedral to euhedral in habit, and range from 0.5mm up to approximately 0.8mm in length. Some are distinctly optically zoned and they commonly have thin rims of tetraferriphlogopite.

Groundmass (70%):

The groundmass consists of approximately 60% phlogopite, which occurs as subhedral crystals ranging from 0.1mm to 0.5mm in size. Many of the groundmass phlogopites are rimmed by tetraferriphlogopite. Approximately 5 % of the groundmass is comprised of euhedral or subhedral calcite, ~0.1mm to 0.2mm in size. Interstitial carbonate is abundant (~30% of the groundmass) and minor interstitial serpentine constitutes ~10% of the groundmass. Opaque oxides <0.1mm in size are abundant throughout the sample, particularly around the rims of the relic olivine macrocrysts.

SJH 30 – East Star Dyke

Texture: Macrocrystic, containing approximately 20 volume % macrocrysts and 10 volume % phenocrysts in a medium to fine grained groundmass.

Macrocryst phases (20%):

Approximately 80% of the macrocryst suite is comprised of rounded, anhedral olivine, ranging from less than 0.5mm to 4mm in size. The olivine macrocrysts are completely altered to serpentine and partially further replaced by calcite. Phlogopite macrocrysts constitute ~20% of the macrocryst suite and are typically rounded subhedral to anhedral crystals up to 2mm in size. The phlogopite macrocrysts are extensively strained: they show undulose extinction, many are kink banded and some have split along cleavage planes and are infilled by calcite.

Phenocryst phases (10%):

All the phenocrysts in this sample are subhedral to euhedral phlogopite up to 1mm in size. Many are rimmed by tetraferriphlogopite, although there is no alteration to chlorite.

Groundmass:

The groundmass consists of ~70% phlogopite, in euhedral or subhedral laths ranging from less than 0.1mm up to 0.3mm in length. The laths are subparallel, giving a weak fabric to the groundmass that bends around the relic olivine macrocrysts. Some of the groundmass phlogopites have rims of tetraferriphlogopite. Interstitial calcite constitutes ~20% of the groundmass, and calcite also occurs as euhedral to subhedral calcite up to 0.2mm in size. Minor interstitial serpentine is also present and opaque oxides up to 0.1mm in size are common throughout the groundmass.

SJH 38 – East Star Dyke

Texture: Macrocrystic, containing ~25 volume % macrocrysts and ~10 volume % phenocrysts in a fine-grained matrix (grain size 0.1mm).

Macrocryst phases (25%):

Rounded, anhedral olivine macrocrysts constitute ~80% of the macrocryst suite. They range up to 10mm in

size, and are all partially altered to serpentine around the rims and along fractures, although the cores are still fresh. Phlogopite macrocrysts, ranging up to 3mm in length, constitute the remaining ~20% of the macrocrysts. They are subhedral to anhedral and commonly occur as rounded lath-shaped crystals, some of which have rims of tetraferriphlogopite. All the phlogopite macrocrysts are highly strained, with undulose extinction, and some are kink-banded. Alteration to chlorite has occurred around the rims of some of the phlogopite macrocrysts although this is not pervasive. One eclogitic garnet is present, approximately 1mm in size. It is fractured and infilled with calcite.

Phenocryst phases (10%):

Phlogopite constitutes the entire phenocryst suite of this sample, with crystals ranging in size from approximately 0.5mm to 1.5mm. The phlogopite phenocrysts most commonly occur as subhedral or euhedral laths, some of which have thin rims of tetraferriphlogopite.

Groundmass (65%):

The groundmass consists of ~60% phlogopite, which is subhedral to euhedral and forms stubby laths up to 0.2mm in size. Many of the groundmass phlogopites have thin rims of tetraferriphlogopite. Interstitial calcite and serpentine, in approximately equal proportions, constitute the majority of the remaining ~40% of the groundmass. Serpentine has also completely replaced the groundmass olivine. Euhedral calcite, up to 0.2mm in size, is present in minor amounts. Opaque oxides (<0.2mm in size) are common throughout the groundmass.

SJH 104 - East Star Dyke

Texture: Macrocrystic, containing ~25 volume % macrocrysts with ~10 volume % phenocrysts in a medium-grained groundmass (grain size <0.5mm).

Macrocryst phases (25%):

Rounded, anhedral olivine macrocrysts ranging up to 6mm in size comprise ~90% of the macrocryst suite. They are commonly fractured and partially or completely altered to serpentine, with some further replacement by calcite. Approximately 10% of the macrocryst suite is comprised of phlogopite, which occurs as anhedral to subhedral crystals up to ~2mm in size. These are commonly strained, displaying undulose extinction, and are often kink-banded. Some of the phlogopite macrocrysts have thin rims of tetraferriphlogopite.

Phenocryst phases (10%):

All the phenocrysts in this sample are phlogopite. They are euhedral or subhedral and reach 1mm in size. Some of the phlogopite phenocrysts are optically zoned and have darker cores than rims, and thin mantles of tetraferriphlogopite are common.

Groundmass (65%):

The groundmass consists of ~70% phlogopite, which is commonly subhedral and ranges from ~0.1 to 0.5mm in size. The remainder of the groundmass is predominantly calcite, with ~10% occurring as subhedral to euhedral calcite less than 0.1mm in size but the majority occurring as interstitial material. Minor interstitial serpentine is also present, and Fe-Ti opaque oxides, up to 0.1mm in size, are common throughout the sample.

SJH 80 – Byrnes Dyke

Texture: Sparsely macrocrystic, containing ~15 volume % macrocrysts, many of which are fragmented and ~10 volume % phenocrysts in a fine-medium grained groundmass (grain size <0.3mm). The sample has a weak fabric due to the alignment of the phenocrysts and groundmass minerals, particularly the lath-shaped groundmass phlogopites, and the grain size varies in bands parallel to this fabric.

Macrocryst phases (15%):

Olivine constitutes ~80% of the macrocryst suite, occurring as rounded, anhedral crystals that are typically 2-3mm in size, with one macrocrysts reaching 6mm in length. All the olivine macrocrysts are completely altered to serpentine. Phlogopite constitutes ~20% of the macrocryst suite and occurs as rounded subhedral or anhedral crystals that range up to 2mm, but are more commonly less than 1mm, in size. Many of the phlogopite macrocrysts are fractured, particularly along cleavage planes and fractures are infilled by calcite. Kink banding is common and all the phlogopite macrocrysts show undulose extinction.

Phenocryst phases (10%):

Approximately 90% of the phenocryst suite is comprised of phlogopite, which occurs as euhedral to subhedral laths up to 2mm in length. Highly serpentinised euhedral olivine constitutes ~10% of the phenocryst suite.

Groundmass (75%):

The groundmass consists of ~60% phlogopite in euhedral to subhedral stubby laths up to 0.3mm in length. Some of these have thin rims of tetraferriphlogopite, and in parts of the sample the groundmass phlogopite is partially altered to chlorite. Approximately 10% of the groundmass is euhedral to subhedral olivine, up to 0.2mm in size, which is partially or completely serpentinised. The olivine and phlogopite are hosted by an interstitial matrix of calcite and subordinate serpentine. Opaque oxides (<0.1mm in size) are abundant throughout the groundmass.

SJH 79 – Byrnes Dyke

Texture: Macrocrystic, with ~20 volume % macrocrysts and ~10 volume % phenocrysts in a fine-grained groundmass (grain size<0.2mm). The groundmass minerals are sub-parallel, giving a weak fabric to the sample.

Macrocryst phases (20%):

Rounded, anhedral olivine macrocrysts, ranging up to 4mm in length, constitute 80% of the groundmass. They are completely altered to serpentine and some are partially further replaced by calcite. Phlogopite constitutes ~20% of the macrocryst suite, occurring as rounded, anhedral crystals that range up to 3mm in size. All the phlogopite mcrocrysts are extensively strained, with undulose extinction, and show kink banding; some are torn along cleavage planes and infilled with calcite. Some of the phlogopite macrocrysts are partially altered to chlorite but this is not pervasive, and some are rimmed by tetraferriphlogopite.

Phenocryst phases (10%):

The entire phenocryst suite of this sample is comprised of phlogopite, which occurs as euhedral to subhedral laths up to 1.5mm in length. Thin rims of tetraferriphlogopite are common and many of the phenocrysts are optically zoned, displaying darker cores than rims.

Groundmass (60%):

Approximately 80% of the groundmass is comprised of subhedral phlogopite, ~0.1mm to 0.2mm in size, with rims of tetraferriphlogopite. Serpentinised subhedral olivine, up to 0.2mm in size, comprises ~5% of the groundmass. The remainder of the groundmass consists primarily of calcite, both as euhedral crystals up to 0.2mm in size and as interstitial material. Lesser amounts of interstitial serpentine are also present and opaque oxides (<0.1mm in size) are scattered throughout the sample.

SJH 78 – Byrnes Dyke

Texture: Macrocrystic, containing ~30 volume % macrocrysts and ~5 volume % phenocrysts in a fine-medium grained groundmass (grain size <0.3mm).

Macrocryst phases (30%):

Approximately 90% of the macrocryst suite is comprised of rounded anhedral olivine, which ranges up to ~5mm in size. All the olivine macrocrysts are altered to serpentine and partially further replaced by calcite, particularly along cracks and around the edges of the macrocrysts. Most of the smaller (<1mm) fragments are completely replaced by calcite. Phlogopite constitutes ~10% of the macrocryst suite, occurring as rounded subhedral or anhedral, commonly elongate, crystals up to 2mm in length. All the phlogopite macrocrysts are strained and show undulose extinction and kink-banding. Some are fractured, particularly along cleavage planes, and infilled with calcite. Partial alteration to chlorite of some of the phlogopite macrocrysts has occurred.

Phenocryst phases (5%):

Phlogopite constitutes the entire phenocryst suite of this sample. The phlogopite phencorysts are euhedral or subhedral and range up to 1.5mm in length. Some are optically zoned, darker cores than rims. Some of the phlogopite phenocrysts are partially altered to chlorite.

Groundmass (65%):

The groundmass is comprised of ~70% phlogopite, which usually occurs as subhedral stubby laths up to approximately 0.3mm in length. Calcite constitutes much of the remainder (~25%), as interstitial material and discrete euhedral crystals up to 0.2mm in size. Minor groundmass olivine is also completely replaced by calcite. Minor interstitial serpentine constitutes <5% of the groundmass, and Fe- Ti- oxides (<0.1mm in size) occur throughout the sample.

SJH 77 - Byrnes Dyke

Texture: Macrocryst poor, with an aphanitic appearance. Although this sample contains approximately 15 volume % macrocrysts, these are fragmented and range up to only ~1mm in size. The sample has a strong fabric, which is particularly well defined by the alignment of the groundmass minerals. Approximately 20 volume % phenocrysts are hosted by a fine-medium grained matrix (grain size <0.4mm).

Macrocryst phases (15%):

Disaggregated olivine macrocrysts reaching up to 1mm in size comprise ~70% of the macrocryst suite. They are rounded and anhedral in habit, and are altered to entirely to serpentine with some partial further replacement by calcite. Two of the olivine macrocrysts in the sample recrystalised, before being replaced by calcite. Phlogopite macrocrysts range up to approximately 1mm in length and constitute ~30% of the macrocryst suite. They are rounded and subhedral to anhedral in habit. Some of the phlogopite macrocrysts show distinct optical zoning, and many are partially altered to chlorite. Undulose extinction is common.

Phenocryst phases (20%):

All the phenocrysts present in this sample are subhedral to euhedral phlogopite, most of which occurs as lath-shaped crystals up to 1mm in length. Many of the phenocrysts show distinct optical zoning, and they commonly have thin rims of tetraferriphlogopite.

Groundmass (35%):

The groundmass consists of ~50% phlogopite, which occurs as lath shaped euhedral or subhedral crystals up to 0.4mm in length, which are commonly rimmed by tetraferriphlogopite. The remaining 50% of the groundmass is predominantly composed of calcite, for the most part occurring as an interstitial phase but also as discrete subhedral crystals up to 0.2mm in size, with subordinate interstitial serpentine. Opaque Fe-Ti oxides (up to 0.1mm in size) are common throughout the sample.

NC 051 – Barren Dyke

Texture: Macrocrystic, containing ~30 volume % macrocrysts with ~5 volume % phenocrysts, in a fine-medium grained groundmass (grain size <0.5mm).

Macrocryst phases (30%):

Approximately 95% of the macrocrysts in this sample are rounded, anhedral olivine. The olivine macrocrysts range up to 7mm in size, although they are commonly fragmented and many are less than 1mm. All the olivine macrocrysts are altered to variable extents, to serpentine. Rare anhedral phlogopite macrocrysts, ranging up to 3mm in size, constitute ~5% of the macrocryst suite. They are extensively strained and commonly distorted or completely fragmented.

Phenocryst phases (5%):

Phenocrysts are rare in this sample but those present are predominantly phlogopite with lesser olivine. The phlogopite phenocrysts are commonly subhedral, lath-shaped crystals and range from 0.5mm to 1mm in length. Olivine phenocrysts constitute ~2 volume % of the sample, occurring as subhedral serpentinised crystals up to 1mm in size.

Groundmass (65%):

The groundmass consists of approximately 70% phlogopite, which occurs as subhedral microphenocrysts ranging from 0.1 to 0.5mm in size. They are hosted by a matrix of predominantly interstitial serpentine with subordinate interstitial calcite. Minor (~ 5% of the groundmass) calcite is also present in subhedral crystals up to 0.2mm in size. Opaque oxides (<0.1mm in size) are abundant throughout the sample, and accessory euhedral perovskite (<0.1 mm in size) is also present.

NC 052 – Barren Dyke

Texture: Macrocrystic, containing ~30 volume % macrocrysts, with ~5 volume % phenocrysts in a fine-medium grained groundmass (grain size <0.5mm).

Macrocryst phases (30%):

The vast majority (~95%) of the macrocryst suite is comprised of olivine, which occurs as rounded anhedral crystals that range up to 8mm in length. All the olivine macrocrysts are strained, with undulose extinction, and some are partially recrystalised. Partial alteration to serpentine has occurred only around the rims and along fractures of some of the olivine macrocrysts, although more pervasive alteration, particularly of the smaller fragments, is common. Partial replacement by phlogopite is evident along fractures of some of the olivine macrocrysts. Rare, anhedral to subhedral phlogopite macrocrysts constitute ~5% of the macrocryst suite. These range up to 1.5mm in size and are commonly extensively strained, with undulose extinction, distorted crystal shapes and kink banding.

Phenocryst phases (5%):

All the phenocrysts in this sample are phlogopite. They range from 0.5mm to 1.5mm in size and are subhedral to euhedral.

Groundmass (65%):

The groundmass consists of ~70% phlogopite, which occurs as subhedral or euhedral crystals that range from 0.1 to 0.5mm in size, in a matrix of interstitial serpentine with subordinate interstitial calcite. Approximately 5 – 10% of the groundmass is comprised of subhedral calcite, up to 0.2mm in size. Two calcite veins (approximately 0.1mm wide) cut through the sample. Opaque oxides (<0.1mm in size) are abundant throughout the groundmass.

NC 053 – Barren Dyke

Texture: Macrocrystic, containing ~30 volume % macrocrysts with ~5 volume % phenocrysts, in a fine-medium grained groundmass (grain size <0.5mm).

Macrocryst phases (30%):

Approximately 95% of the macrocryst suite is comprised of olivine, which occurs as rounded, anhedral crystals ranging up to 7mm in size. All the olivine macrocrysts are partially altered to serpentine, although the majority of the larger (>1mm) macrocrysts have fresh cores. The remaining ~5% of the macrocryst suite is comprise of rounded, anhedral phlogopite. The phlogopite macrocrysts range up to ~1.5mm in size and are commonly extensively strained and distorted, with undulose extinction.

Phenocryst phases (5%):

Phlogopite comprises the entire phenocryst suite of this sample, occurring as commonly subhedral, lath-shaped crystals that range from 0.5mm to ~1.2mm in length.

Groundmass (65%):

Subhedral laths of microphenocrystal phlogopite ranging up to 0.5mm in size constitute ~70% of the groundmass. The remaining ~30% of the groundmass is comprised predominantly of interstitial serpentine with subordinate interstitial calcite. Calcite also occurs as euhedral crystals (~0.2mm in size), which constitute ~5% of the groundmass. Opaque oxides (<0.1mm in size) are abundant throughout the groundmass, in addition to being closely associated with relic olivine macrocrysts.

NC 054 – Barren Dyke

Texture: Macrocrystic, with ~30 volume % macrocrysts in an interstitial matrix containing microphenocrysts of phlogopite.

Macrocryst phases (30%):

The majority of the macrocryst suite (~95%) is comprised of anhedral, rounded olivine, which ranges in size up to 7mm. All the olivine macrocrysts are extremely fresh, with only very slight alteration along cracks to serpentine, and minor replacement by calcite or phlogopite. Some of the macrocrysts are partially or completely recrystalised and they commonly show undulose extinction. Phlogopite macrocrysts constitute ~5% of the macrocryst suite. They range up to 1.5mm in size and are subhedral or anhedral, with eroded rims that are commonly partially altered to chlorite. The phlogopite macrocrysts are strained and typically display undulose extinction.

Phenocryst phases (3%):

All the phenocrysts observed in this sample are subhedral, serpentinised olivine ranging up to 1mm in size. No phlogopite phenocrysts were observed, although considering the extremely altered nature of the groundmass (see below), phlogopite phenocrysts may have been present but become extensively chloritised.

Groundmass (70%):

Approximately 40% of the groundmass is comprised of microphenocrysts of subhedral phlogopite, which range up to ~0.5mm in size. The groundmass phlogopite is severely chloritised, and commonly eroded around the rims. The majority of the remainder of the groundmass consists of a matrix of interstitial serpentine with subordinate chlorite, most of which is likely to be a product of alteration of phlogopite. Minor amounts of interstitial carbonate are also present. Opaque oxides, ranging up to 0.1mm in size, are scattered throughout the groundmass.

A2.3 Mineral analyses

Representative major element analyses of macocrystic olivine and phlogopite in the Star kimberlite dykes are reported in Tables A2.2 and A2.3 respectively.

Table A2.2 Representative major element analyses of olivine macrocrysts in the Star kimberlite dykes, acquired using the electron microprobe, University of Cape Town. Ol = olivine; mac = macrocryst; co = core; FeO* = total iron as FeO; Fo cont. = Mg/ (Mg + Fe^{2+}). Atomic proportions for these analyses have been calculated on the basis of 4O.

Dyke	Clewer Dyke			East Star Dyke				
Sample	JJG 2833	JJG 2833	JJG 2833	JJG 4570	JJG 4570	JJG 4570	JJG 4570	JJG 4570
Description	Ol mac 1 co	Ol ma 4 co	Ol mac 8 co	Ol mac 1 co	Ol mac 7 co	Ol mac 7 rim	Ol mac 8 co	Ol mac 8 rim
SiO_2	40.5	40.5	41.2	41.3	41.4	40.7	40.6	40.1
TiO_2	0.00	0.00	0.01	0.00	0.00	0.00	0.00	0.00
Al_2O_3	0.00	0.00	0.00	0.00	0.00	0.00	0.00	0.00
Cr_2O_3	0.02	0.06	0.01	0.03	0.01	0.01	0.04	0.03
FeO*	7.15	11.2	8.34	6.16	7.04	7.05	10.4	10.4
MnO	0.09	0.28	0.10	0.07	0.09	0.07	0.12	0.12
MgO	50.9	48.1	49.6	52.2	51.2	51.3	48.0	48.8
CaO	0.01	0.03	0.01	0.01	0.00	0.01	0.02	0.03
NiO	0.42	0.02	0.43	0.40	0.42	0.40	0.49	0.49
Total	99.0	100.2	99.7	100.2	100.2	99.5	99.7	99.9
Fo cont.	0.93	0.90	0.92	0.94	0.94	0.94	0.90	0.90
Atomic proportions based on 4O								
Si	0.992	0.997	1.006	0.994	1.002	0.992	1.003	0.989
Ti	0.000	0.000	0.000	0.000	0.000	0.000	0.000	0.000
Al	0.000	0.000	0.000	0.000	0.000	0.000	0.000	0.000
Cr	0.000	0.001	0.000	0.001	0.000	0.000	0.001	0.001
Fe	0.147	0.231	0.170	0.124	0.142	0.144	0.215	0.215
Mn	0.002	0.006	0.002	0.002	0.002	0.001	0.002	0.003
Mg	1.858	1.767	1.805	1.877	1.844	1.863	1.765	1.794
Ca	0.000	0.001	0.000	0.000	0.000	0.000	0.001	0.001
Ni	0.008	0.000	0.008	0.008	0.008	0.008	0.010	0.010
Sum	3.008	3.003	2.993	3.005	2.998	3.008	2.996	3.011

Dyke	Wynandsfontein Dyke				Barren Dyke (non-micaceous)			
Sample	JJG 6360	JJG 6361	JJG 6362	JJG 6363	NC 054	NC 054	NC 054	NC 054
Description	Ol mac 1 co	Ol mac 1 rim	Ol mac 5 co	Ol mac 5 rim	Ol mac 3 co	Ol mac 3 rim	Ol mac 8 co	Ol mac 8 rim
SiO_2	41.5	40.4	40.7	40.9	40.9	41.0	41.4	41.2
TiO_2	0.00	0.00	0.00	0.00	0.00	0.00	0.00	0.00
Al_2O_3	0.00	0.00	0.00	0.00	0.00	0.00	0.00	0.00
Cr_2O_3	0.06	0.05	0.03	0.02	0.07	0.08	0.05	0.04
FeO*	8.04	7.92	9.38	9.21	7.86	7.97	7.04	7.10
MnO	0.09	0.10	0.10	0.13	0.10	0.11	0.10	0.08
MgO	50.8	50.5	49.5	49.0	50.4	49.8	50.8	51.0
CaO	0.05	0.03	0.02	0.01	0.06	0.07	0.04	0.03
NiO	0.42	0.42	0.39	0.38	0.41	0.39	0.42	0.42
Total	101.0	99.4	100.1	99.7	99.8	99.4	99.8	99.8
Fo cont.	0.93	0.93	0.91	0.91	0.93	0.93	0.93	0.93
Atomic proportions based on 4O								
Si	1.000	0.991	0.996	1.004	0.998	1.004	1.004	1.001
Ti	0.000	0.000	0.000	0.000	0.000	0.000	0.000	0.000
Al	0.000	0.000	0.000	0.000	0.000	0.000	0.000	0.000
Cr	0.001	0.001	0.001	0.000	0.001	0.001	0.001	0.001
Fe	0.162	0.162	0.192	0.189	0.160	0.163	0.143	0.144
Mn	0.002	0.002	0.002	0.003	0.002	0.002	0.002	0.002
Mg	1.825	1.844	1.806	1.792	1.831	1.816	1.836	1.843
Ca	0.001	0.001	0.001	0.000	0.002	0.002	0.001	0.001
Ni	0.008	0.008	0.008	0.008	0.008	0.008	0.008	0.008
Sum	2.999	3.009	3.004	2.996	3.002	2.996	2.995	2.999

Table A2.3 Representative major element analyses of phlogopite macrocrysts in the Star kimberlite dykes acquired using an electron microprobe, University of Cape Town. Phlog = phlogopite; mac = macrocryst; FeO* = total iron as FeO; Mg# = atomic Mg/ (Mg + Fe^{2+}) with Fe_2O_3/ FeO = 0.1. Atomic proportions for these analyses have been calculated on the basis of 22O.

Dyke	Clewer Dyke				East Star Dyke		
Sample	JJG 2833	JJG 2833	SJH 39	SJH 39	JJG 4570	JJG 4570	SJH 30
Description	Phlog mac 1	Phlog mac 2	Phlog mac 3	Phlog mac 4	Phlog mac 5	Phlog mac 6	Phlog mac 7
SiO_2	42.6	39.2	40.6	40.6	41.9	37.7	40.6
TiO_2	1.50	2.08	1.87	2.07	1.66	1.69	1.77
Al_2O_3	12.7	12.6	13.9	13.5	13.5	12.7	14.8
FeO*	4.63	5.16	4.07	5.52	4.65	7.10	4.81
MnO	0.04	0.03	0.05	0.06	0.01	0.05	0.03
MgO	22.8	23.8	21.4	21.2	21.6	21.4	24.8
CaO	0.09	0.02	0.07	0.03	0.03	0.01	0.02
Na_2O	0.27	0.17	0.17	0.09	0.23	0.14	0.23
K_2O	9.88	9.53	10.1	10.5	10.3	10.0	9.64
Total	94.5	92.6	92.1	93.6	93.9	90.8	96.7
Mg#	0.91	0.90	0.91	0.88	0.90	0.86	0.91
Atomic proportions calculated on the basis of 22O							
Si	6.062	5.753	5.933	5.902	6.022	5.720	5.671
Ti	0.161	0.229	0.206	0.226	0.179	0.193	0.186
Al	2.137	2.187	2.389	2.322	2.285	2.282	2.434
Fe	0.552	0.633	0.498	0.671	0.560	0.901	0.562
Mn	0.004	0.003	0.006	0.008	0.002	0.006	0.004
Mg	4.846	5.199	4.655	4.591	4.627	4.850	5.175
Ca	0.013	0.004	0.012	0.005	0.005	0.001	0.004
Na	0.073	0.047	0.049	0.025	0.063	0.042	0.062
K	1.795	1.786	1.886	1.943	1.890	1.939	1.719
Sum	15.64	15.84	15.63	15.69	15.63	15.94	15.82

Dyke	East Star	Byrnes Dyke					
Sample	SJH 30	SJH 79	SJH 79	SJH 79	SJH 79	SJH 79	SJH 79
Description	Phlog mac 8	Phlog mac 9	Phlog mac 10	Phlog mac 11 rim	Phlog mac 12	Phlog mac 13	Phlog mac 14
SiO_2	42.4	41.4	41.2	46.7	39.0	43.1	40.0
TiO_2	1.72	1.57	1.57	0.33	1.94	0.40	1.67
Al_2O_3	13.6	13.3	12.5	0.83	13.1	13.0	11.9
FeO	5.46	5.08	5.58	15.4	4.89	2.81	5.25
MnO	0.03	0.03	0.03	0.15	0.05	0.01	0.05
MgO	24.3	25.0	24.9	23.6	24.8	26.8	25.1
CaO	0.13	0.03	0.03	0.12	0.02	0.01	0.06
Na_2O	0.14	0.19	0.26	0.13	0.15	0.16	0.29
K_2O	9.80	10.4	10.4	8.40	10.2	10.7	10.7
Total	97.6	97.0	96.4	95.7	94.2	96.9	95.0
Mg#	0.90	0.91	0.90	0.75	0.91	0.95	0.90
Atomic proportions calculated on the basis of 22O							
Si	5.873	5.794	5.826	6.887	5.656	5.959	5.765
Ti	0.179	0.165	0.168	0.037	0.212	0.041	0.181
Al	2.226	2.199	2.083	0.145	2.231	2.123	2.027
Fe	0.632	0.595	0.660	1.902	0.593	0.325	0.633
Mn	0.004	0.003	0.004	0.019	0.006	0.001	0.006
Mg	5.017	5.224	5.248	5.184	5.354	5.522	5.398
Ca	0.019	0.005	0.005	0.020	0.003	0.001	0.009
Na	0.038	0.052	0.071	0.039	0.043	0.044	0.081
K	1.733	1.859	1.870	1.582	1.882	1.888	1.964
Sum	15.721	15.897	15.936	15.814	15.979	15.904	16.063

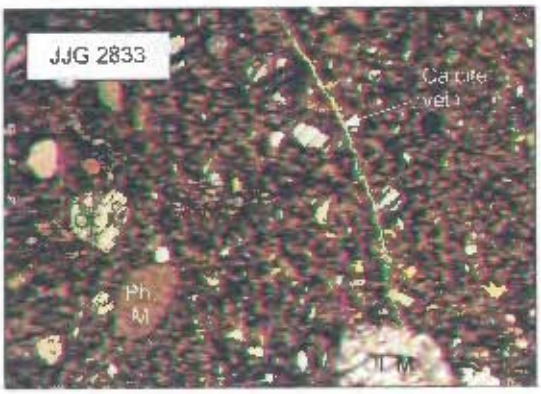

JJG 2833; Clewer Dyke. FOV ~20mm. Macrocrystic. Olivine macrocrysts are fresh, although commonly fragmented. Groundmass is predominantly phlogopite, with subordinate olivine and calcite.

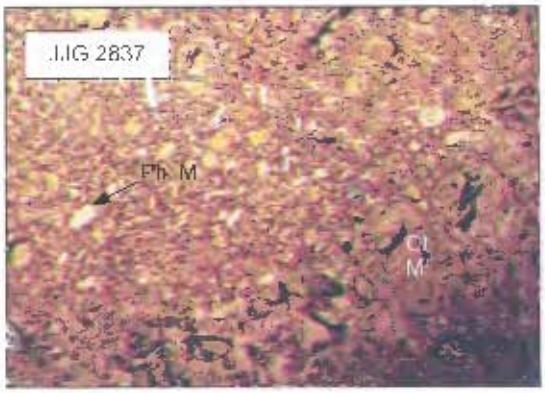

JJG 2837; Clewer Dyke. FOV ~20mm. Macrocrystic. Olivine macrocrysts are completely serpentinised and the majority are concentrated into one band. Groundmass consists primarily of phlogopite with lesser calcite and olivine.

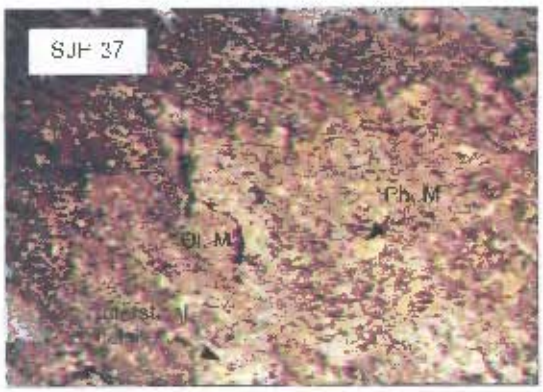

SJH 37; Wynandsfontein Dyke. FOV ~15mm. Sparsely macrocrystic. Olivine macrocrysts are completely replaced by calcite. Groundmass contains ~equal proportions of phlogopite and interstitial calcite, with abundant opaque oxides.

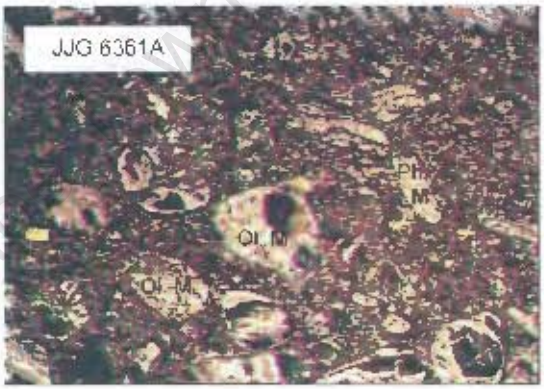

JJG 6361A; Wynandsfontein Dyke. FOV ~20mm. Macrocrystic. Olivine macrocrysts are completely replaced by calcite. Phlogopite macrocrysts are partially altered to chlorite. Groundmass is predominantly phlogopite and calcite.

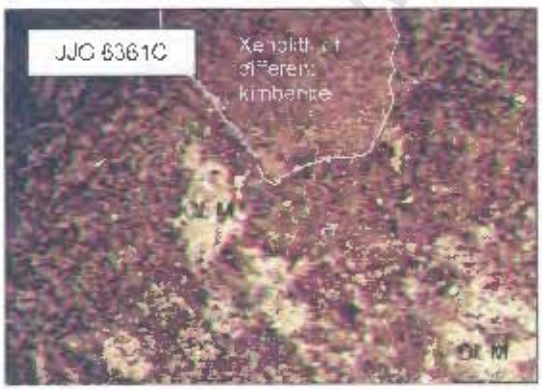

JJG 6361C; Wynandsfontein Dyke. FOV ~20mm. Macrocrystic. Olivine macrocrysts are completely replaced by calcite. Also contains a large xenolith of finer-grained, diopside rich kimberlite (outlined in white). Groundmass dominantly phlogopite and calcite.

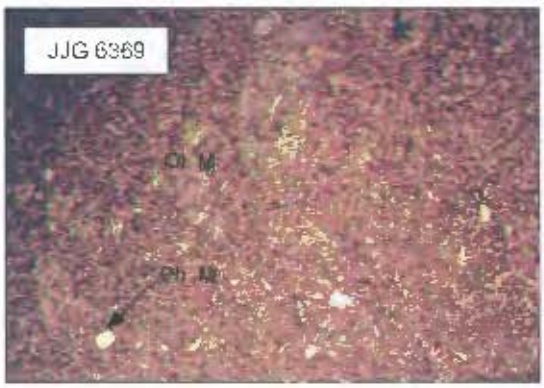

JJG 6369; Wynandsfontein Dyke. FOV ~20mm. Sparsely macrocrystic. All of the olivine macrocrysts are completely altered to serpentine, with partial replacement by calcite. Groundmass dominantly consists of phlogopite with interstitial calcite and serpentine.

Plate A2.1 Photomicrographs of the Star kimberlite samples. FOV = field of view; Ol. M = olivine macrocryst; Ph. M = phlogopite macrocryst.

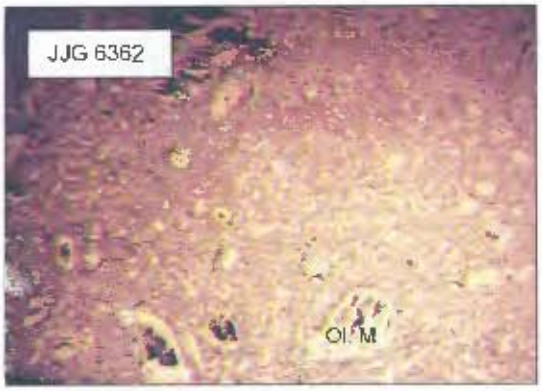

JJG 6362; Wynandsfontein Dyke. FOV ~20mm. Moderately macrocrystic. Olivine macrocrysts are altered to serpentine. And commonly fragmented. Groundmass is predominantly phlogopite. with subordinate interstitial calcite and serpentine.

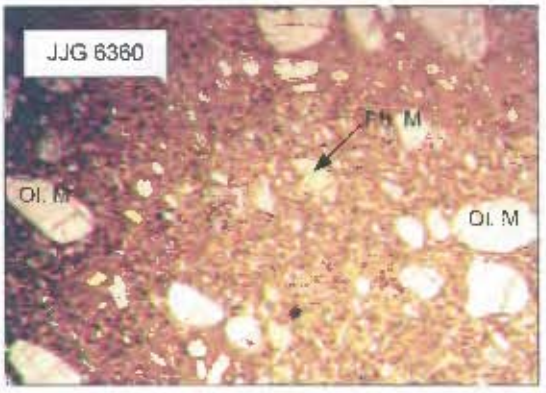

JJG 6360; Wynandsfontein Dyke. FOV ~20mm. Macrocrystic. Olivine macrocrysts are fresh. Groundmass consists primarily of phlogopite with subordinate interstitial calcite and serpentine.

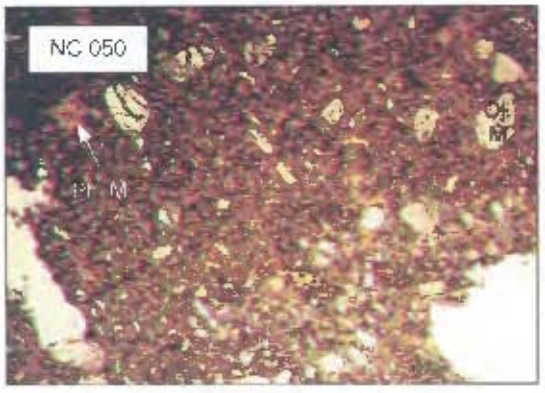

NC 050; Wynandsfontein Dyke. FOV ~20mm. Moderately macrocrystic. Olivine macrocrysts are fresh. with only minor alteration to serpentine. Groundmass consists predominantly of phlogopite, with interstitial carbonate and serpentine.

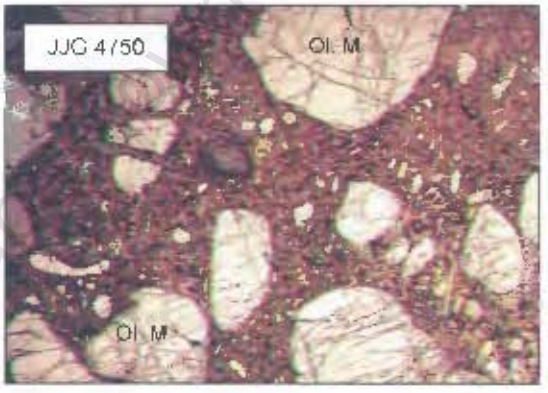

JJG 4750; East Star Dyke. FOV ~20mm. Coarsely macrocrystic. Olivine macrocrysts are fresh. Section contains a small crustal xenolith. Groundmass is predominantly phlogopite with subordinate calcite.

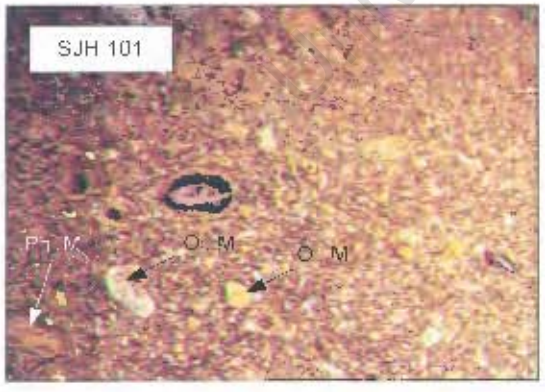

SJH 101; East Star Dyke. FOV ~20mm. Sparsely macrocrystic. Olivine macrocrysts are altered to serpentine and commonly fragmented Groundmass dominantly phlogopite with lesser interstitial calcite and subordinate serpentine.

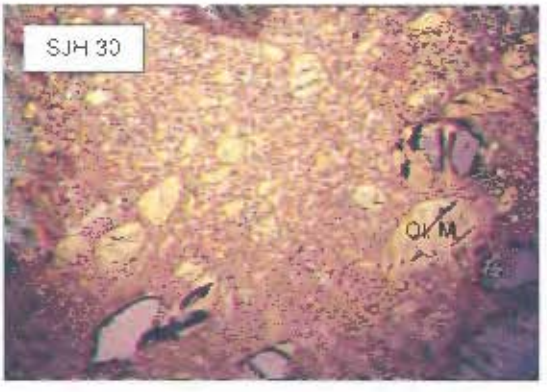

SJH 30; East Star Dyke. FOV ~20mm. Moderately macrocrystic. Olivine macrocrysts are completely altered to serpentine. with partial replacement by calcite. Groundmass dominantly phlogopite with subordinate interstitial calcite and serpentine.

Plate A2.1 Continued. FOV = field of view; Ol. M = olivine macrocryst; Ph. M = phlogopite macrocryst

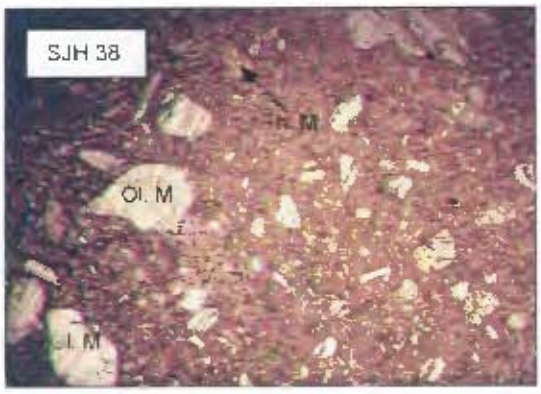

SJH 38; East Star Dyke. FOV ~20mm.
Macrocrystic. Olivine macrocrysts are fresh although commonly fragmented, but with serpentine along fractures. Groundmass is dominantly phlogopite, with interstitial serpentine and calcite.

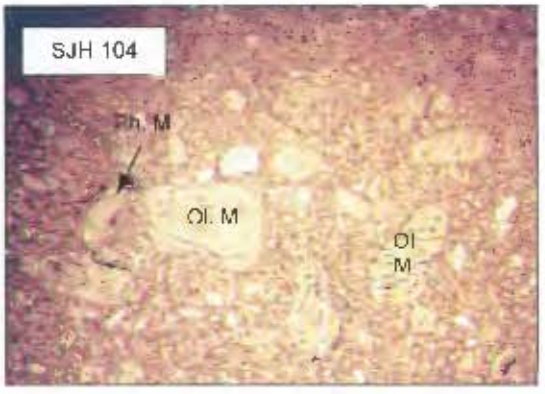

SJH 104; East Star Dyke. FOV ~20mm
Macrocrystic. Olivine macrocrysts are completely serpentinised, with partial further replacement by calcite. Groundmass consists primarily of phlogopite with subordinate calcite

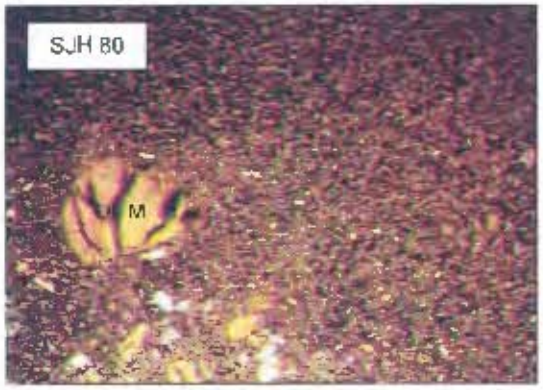

SJH 80; East Star Dyke. FOV ~20mm.
Sparsely macrocrystic. Olivine macrocrysts are completely altered to serpentine. Groundmass consists predominantly of phlogopite, with lesser serpentinised olivine in an interstitial matrix of calcite and serpentine.

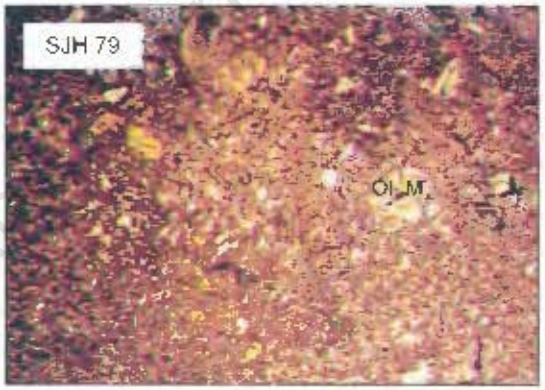

SJH 79; East Star Dyke. FOV ~20mm.
Sparsely macrocrystic. Olivine macrocrysts are entirely altered to serpentine. The majority of the groundmass is phlogopite, with subordinate calcite.

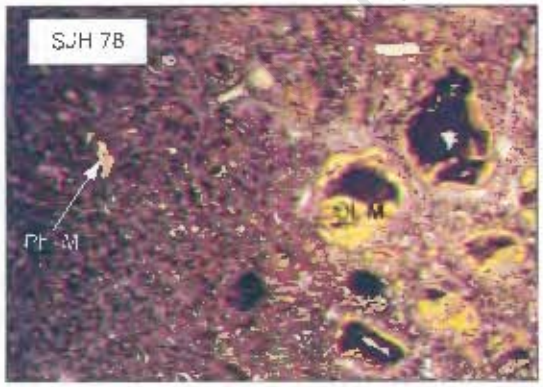

SJH 78; East Star Dyke. FOV ~20mm.
Macrocrystic. Olivine macrocrysts are entirely altered to serpentine. Groundmass consists dominantly of phlogopite with subordinate calcite.

SJH 77; East Star Dyke. FOV ~20mm.
Sparsely macrocrystic. Small fragments of olivine macrocrysts are completely altered to serpentine, with partial replacement by calcite. Groundmass dominantly consists of phlogopite and calcite.

Plate A2.1 Continued. FOV = field of view. Ol. M = olivine macrocryst. Ph. M = phlogopite macrocryst.

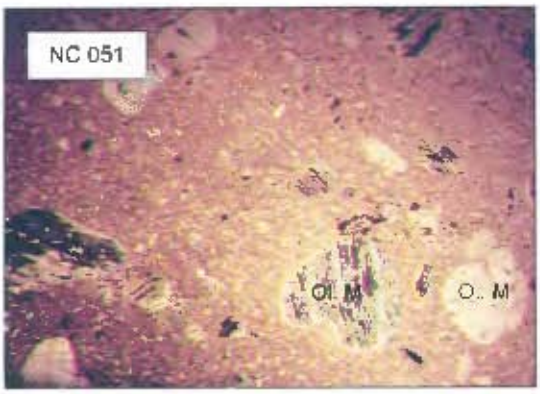

NC 051; Barren Dyke. FOV ~20mm
Macrocrystic. Olivine macrocrysts are partially altered to serpentine. Groundmass consists dominantly of phlogopite with interstitial serpentine and subordinate calcite.

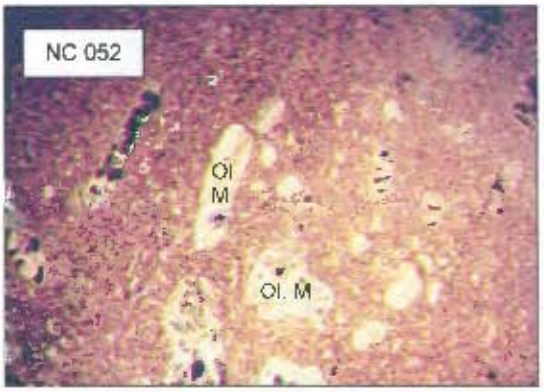

NC 052; Barren Dyke. FOV ~20mm.
Macrocrystic. Olivine macrocrysts are partialiy altered to serpentine. The groundmass consists primarily of phlogopite with subordinate interstitial serpentine and minor calcite

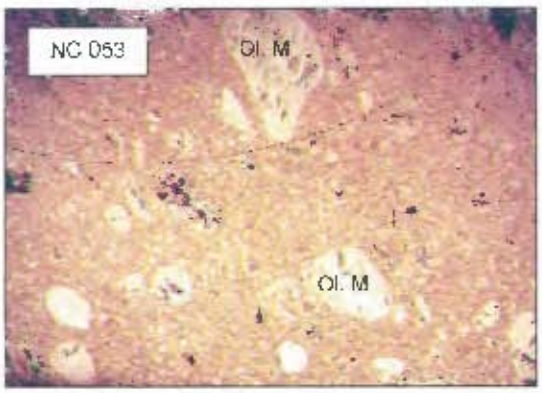

NC 053; Barren Dyke FOV ~20mm.
Macrocrystic. Olivine macrocrysts are fresh, with only minor alteration to serpentine. Groundmass consists predominantly of phlogopite, with interstitial serpentine and subordinate calcite.

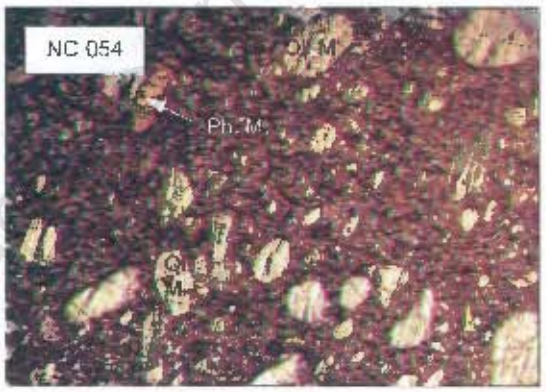

NC 054; Barren Dyke. FOV ~20mm.
Coarsely macrocrystic. Olivine macrocrysts are fresh and commonly fragmented. Groundmass contains ~40% phlogopite in an interstitial matrix of predominantly serpentine and chlorite.

Plate A2.1 Continued. FOV = field of view, Ol. M = olivine macrocryst; Ph. M = phlogopite macrocryst.

Appendix 3

Sample preparation and analytical techniques

A3.1 Electron microprobe analyses

All the mineral compositions reported in Chapter 3 were determined from polished 30 µm thick thin sections on a Cameca Camebax 4 channel electron microprobe at the Department of Geological Sciences, University of Cape Town. An accelerating voltage of 15kV and a beam current of 15nA were used. TLAP (Na, Mg, Si, Al), LiF (200) (Fe, Ni) and PET (Ca, Ti, K, Cr) analysing crystals were used to detect X-ray emissions from analyte elements. Counting times were 10s at peak and background positions, except Ni, for which the counting time was 30s. Online data reduction was carried out according to the PAP procedure.

A3.2 Powdering

- Each sample was split into small (~5cm) pieces and weathered surfaces were removed using a hydraulic splitter, and subsequently jaw-crushed into <1cm chips.
- The jaw-crushed samples were hand picked to avoid mantle and crustal xenoliths and xenocrysts, excessive alteration and secondary veins.
- Only fresh, visibly uncontaminated, sample was then powdered in a carbon steel Sieb swing mill for 1 minute.
- As a test of the repeatability of the picking and subsequent analytical procedures, sample NC 008 was hand-picked twice, to form two batches of visibly uncontaminated sample: NC 008a and NC 008b. These two batches were treated as separate samples throughout all analytical procedures.

A3.3 Major element analyses

The concentrations of a range of major oxides in the Swartruggens and Star samples were determined using X-ray fluorescence spectrometry, and CO_2 concentrations were determined using a Karbonat Bomb as described below.

A3.3.1 X-Ray Fluorescence Spectrometry (XRF)

- Approximately 2g of powdered sample were placed into porcelain crucibles and the exact weight recorded.
- To determine the weight percentage of H_2O^- present in the samples, the crucibles containing sample were left to dry in an oven at 110°C overnight, and subsequently weighed again.
- Overnight the samples were then roasted at 850°C and reweighed to determine the weight percentage lost on ignition (LOI).

- Fusion discs were prepared using precisely 0.7g of roasted sample and 6g of a $Li_2B_4O_7$ and $LiBO_2$ flux, using a Claisse fluxy.
- Prior to analysis, the samples were stored in a dessicator.

The concentrations of the major elements in the samples were determined by XRF spectrometry using a Mo-Sc X-ray tube in a Philips X'Unique wavelength dispersive spectrometer at the University of Cape Town. A low dilution fusion technique was used. Analytical errors and detection limits are similar to those reported by le Roex *et al.* (1981) and Willis (1999). Comparative analyses of the two batches of sample NC 008, prepared and analysed as separate samples are reported in Table A3.1.

Table A3.1 Comparison of the major element data (in wt %) obtained from two separately prepared batches of sample NC 008, from the Swartruggens Muil Dyke. FeO* = total Iron; H_2O^+ = LOI – CO_2; Mg# = atomic Mg/(Mg + Fe^{2+}).

Sample	NC 008a	NC 008b
SiO_2	40.7	41.1
TiO_2	2.10	2.10
Al_2O_3	7.03	7.10
FeO*	10.2	10.3
MnO	0.14	0.14
MgO	16.3	16.3
CaO	8.53	8.32
Na_2O	1.30	1.40
K_2O	2.01	2.07
P_2O_5	0.82	0.82
SO_3	0.29	0.29
NiO	0.04	0.05
Cr_2O_3	0.15	0.14
H_2O^-	4.91	4.68
LOI	4.89	4.90
Total	99.4	99.7
CO_2	0.78	0.59
H_2O^+	4.11	4.31
Mg#	0.79	0.79

A3.3.2 Karbonat bombe

The Karbonat Bombe is a simple instrument used for determining CO_2 concentrations of samples. It consists of a plexiglass cylinder, containing a small plastic bucket, with a manometer attached to the screw-on lid. The instrument and technique are described by Birch (1981).

- To calibrate the instrument, 1g pure $CaCO_3$ was placed in the plexiglass cylinder, and 5ml concentrated HCl was poured into the small bucket. The bucket was then placed into the cylinder and the lid screwed on tightly. The cylinder was subsequently shaken to allow the acid to come into contact with the $CaCO_3$. Once

the entire $CaCO_3$ sample had reacted with the acid (1 to 2 minutes), a reading was taken from the manometer. This was repeated using 0.5g $CaCO_3$, and the resulting calibration is illustrated in Figure A3.1. Separate calibrations were necessary for Swartruggens and Star as the analyses were carried out on different occasions.

- 3-5g of sample powder was then weighed and placed in the cylinder, and concentrated HCl was added as described above. The manometer reading was taken and the calibration lines illustrated in Figure A3.1 were used to determine the $CaCO_3$ concentration of the sample.
- CO_2 contents of the samples were then determined using stoichiometry.
- The instrument was thoroughly cleaned between analyses, and standards of 1g pure $CaCO_3$ were run after every 5 samples.

For samples containing greater than 5% $CaCO_3$, the precision of this technique is approximately 2%, and for samples containing less than 5% $CaCO_3$ precision is lower than 4% (Birch, 1981).

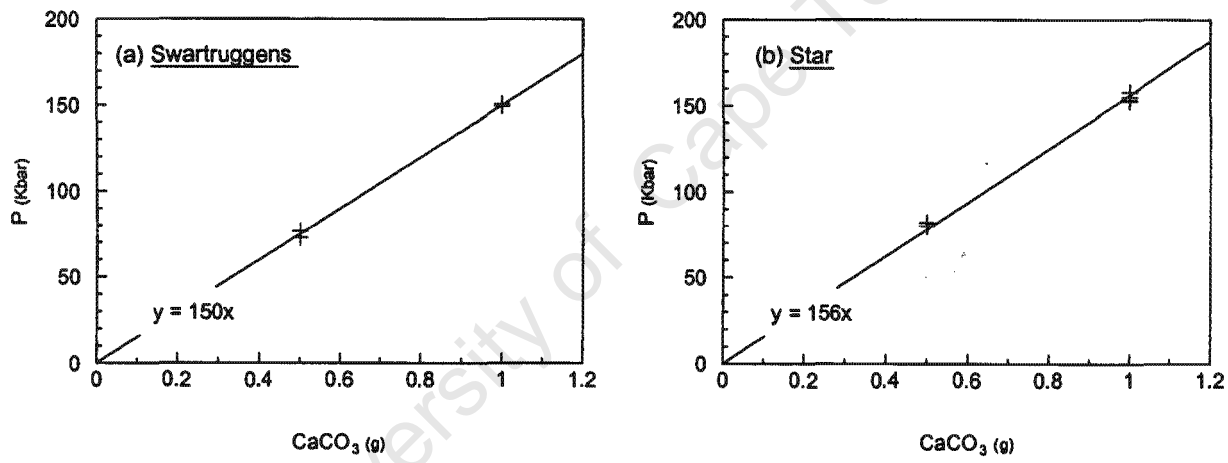

Figure A3.1 Calibration curves, calculated from standard data, for the pressure reading on the manometer relative to the $CaCO_3$ content of the samples for the Karbonat bombe for a) the Swartruggens samples, and b) the Star samples. Two curves are necessary as the samples from the two localities were analysed on different days.

A3.4 Trace element analyses

The concentrations of 32 trace elements in the Swartruggens and Star samples were determined using inductively coupled plasma mass spectrometry (ICP-MS), and of 12 trace elements using XRF spectrometry, at the University of Cape Town.

A3.4.1 X-ray Fluorescence Spectrometry (XRF)

- Using boric acid as a backing, 6g of the powdered samples were pressed into briquettes under a 10-ton press.
- Trace element concentrations were determined using a Philips X' Unique wavelength dispersive spectrometer, at the University of Cape Town. An Au tube was used to determine the concentrations of Zn,

Cu, Ni, Cu, Co, Cr and V, and a Rh tube to determine the concentrations of Nb, Zr, Y, Sr, Rb and U in the samples. Analytical errors and detection limits are similar to those reported by le Roex *et al.* (1981) and Willis (1999). Calculated UCT data for the mafic standard JB-1, from Willis (1999), together with errors and lower limits of detection are reported in Table A3.2. Recommended values from Govindaraju (1989) are reported for comparison.

Table A3.2 Comparison of UCT data for the mafic standard JB-1 (Willis, 1999) with recommended values from Govindaraju (1989) ; Data in ppm. 1σ = 1σ error; LLD = lower limit of detection.

Sample	UCT	1σ	LLD	Recommended
Zn	84	0.4	0.9	83.0
Cu	55	0.5	1.1	56.3
Ni	139	0.7	1	139
Co	37	0.9	2.3	38.7
Cr	406	1.5	2.0	469
V	193	1.4	3.0	212
Nb	28	0.2	0.5	35
Zr	152	0.2	0.4	143
Y	24	0.2	0.6	24.0
Sr	444	0.3	0.5	435
Rb	39	0.2	0.6	41
U	2.3	0.4	1.2	1.7

For comparison, the trace element concentrations, determined by XRF, of the two batches of sample NC 008, prepared and analysed independently are reported in Table A3.3.

Table A3.3 Comparison of the trace element data (in ppm) obtained by XRF from two separately prepared batches of sample NC 008, from the Swartruggens Muil Dyke.

Sample	NC 008a	NC 008b
Zn	92.8	92.5
Cu	86.6	87.8
Ni	451	430
Co	67.7	65.6
Cr	1039	943
V	320	317
Nb	82	82
Zr	247	249
Y	12.2	12.1
Sr	915	904
Rb	97	97
U	3.1	3.6

A3.4.2 Inductively Coupled Plasma Mass Spectrometry (ICP-MS)

- 50 mg of powdered sample were weighed and dissolved in Teflon beakers using the procedure outlined in Table A3.4.

Table A3.4 Outline of the dissolution procedure prior to ICP-MS analyses. *Stock solution contains 5% HNO3 and 10 ppb Re, Rh, In and Bi internal standards.

Reagent	Volume (mls)	Action
4 HF: 1 HNO_3	4	Beakers sealed and placed on hotplate for 2 days to allow sample to digest. Sample dried down.
Conc. HNO_3	2	Samples dissolved and dried down on hotplate.
Conc. HNO_3	2	Samples dissolved and dried down on hotplate. Beakers removed from hotplate.
Stock solution*	4	Samples and stock solution thoroughly mixed in ultrasonic bath for one hour.

- 50ml solutions were prepared by further dilution of the samples to 1000 times with the stock solution (containing 5% HNO3 and 10 ppb Re, Rh, In and Bi internal standards). One drop of HF was added to keep Ta in solution for the duration of the analyses.

ICP-MS analyses of 32 trace element analyses were carried out using a Perkin-Elmer ELAN 6000 ICP-MS using multi element artificial standards. Total procedural blanks (TPB) were run with each batch of

Table A3.5 Average of analyses (in ppm) of total procedural blanks run with each batch of Swartruggens and Star samples.

	TPB		TPB
Sc	0.0139	Nd	0.0012
V	0.0020	Sm	0.0004
Cr	0.0908	Eu	0.0002
Co	0.0036	Gd	0.0004
Ni	0.0139	Tb	0.0001
Cu	0.0245	Dy	0.0003
Rb	0.0022	Ho	0.0001
Sr	0.0177	Er	0.0001
Y	0.0010	Tm	0.0001
Zr	0.0176	Yb	0.0001
Nb	0.0008	Lu	0.0001
Cs	0.0005	Hf	0.0047
Ba	0.0523	Ta	0.0121
La	0.0016	Pb	0.1570
Ce	0.0025	Th	0.0017
Pr	0.0003	U	0.0001

Swartruggens and Star samples, and the average of these is reported in Table A3.5. With the exception of Ta, internal repeat analyses of the international standard BHVO-1 have a relative standard deviation of better than 3% (Table A3.6). The relative standard deviation for Ta is 3.5%. The current in-house UCT average is compared with average BHVO-1 standard data for each batch of Swartruggens and Star sample analyses in Table A3.6. For comparison the recommended BHVO-1 values of Govindaraju (1994) are included.

Table A3.6 Average analyses in ppm of the International standard BHVO-1 obtained during each analytical session. The current UCT in house average and recommended values are reported for comparison. * Recommended values are from Govindaraju (1994); values in brackets are from Chazey III *et al.* (2003). n = number of analyses; RSD = relative standard deviation.

	This work		Current UCT in house		Recommended*
	Average	% RSD	Average	% RSD	
Sc	32	0.01	30.2	3.74	31.8
V	330	0.01	322	3.51	317
Cr	309	0.01	286	6.84	289
Co	45.0	0.01	45.1	2.68	45
Ni	124	0.01	117	4.65	121
Cu	145	0.01	142	2.85	136
Rb	9.33	0.01	9.54	3.40	11 (9.3)
Sr	403	0.01	400	3.10	403
Y	24.0	0.01	24.4	2.58	27.6 (24.4)
Zr	171	0.01	172	3.56	179 (172)
Nb	19.9	0.01	19.0	3.91	19
Cs	0.10	0.29	0.10	7.71	0.13
Ba	128	0.01	130	2.22	139
La	14.8	0.01	15.0	2.21	15.8
Ce	37.5	0.01	37.7	1.68	39
Pr	5.15	0.01	5.23	2.38	5.7
Nd	24.4	0.01	24.5	1.85	25.2
Sm	5.84	0.01	5.90	2.82	6.2
Eu	1.97	0.00	2.00	2.71	2.06
Gd	6.51	0.01	6.02	3.35	6.4
Tb	0.95	0.00	0.88	3.07	0.96
Dy	5.23	0.00	5.01	2.33	5.2
Ho	0.94	0.00	0.92	2.68	0.99
Er	2.41	0.00	2.37	2.51	2.4
Tm	0.32	0.03	0.31	2.97	0.33
Yb	1.89	0.00	1.85	2.51	2.02
Lu	0.27	0.04	0.26	2.96	0.29
Hf	4.06	0.01	4.11	3.99	4.38
Ta	1.53	0.00	1.18	6.81	1.23
Pb	2.19	0.00	2.17	5.92	2.6 (2.2)
Th	1.24	0.00	1.25	2.61	1.08 (1.22)
U	0.44	0.02	0.45	3.52	0.42

The ICP-MS data obtained by two separately prepared batches of sample NC 008 are reported in Table A3.7.

Table A3.7 Comparison of the trace element data in ppm obtained by ICP-MS from two separately prepared batches of sample NC 008, from the Swartruggens Muil Dyke.

Sample	NC-008a	NC-008b
Sc	23.1	22.9
V	272	275
Cr	314	289
Co	52.7	52.3
Ni	341	333
Cu	95.8	97.0
Rb	97.8	99.0
Sr	940	936
Y	10.4	10.3
Zr	222	225
Nb	84.7	86.0
Cs	7.41	8.17
Ba	1690	1759
La	89.2	88.7
Ce	179	179
Pr	19.5	19.4
Nd	72.0	71.8
Sm	9.24	9.24
Eu	2.27	2.28
Gd	5.71	5.75
Tb	0.63	0.65
Dy	2.62	2.58
Ho	0.43	0.43
Er	1.04	1.03
Tm	0.14	0.14
Yb	0.84	0.83
Lu	0.11	0.11
Hf	5.39	5.43
Ta	3.85	3.89
Pb	16.3	15.6
Th	10.8	10.5
U	2.73	2.58

For comparison of the two techniques, certain trace elements (Cu, Ni, Cr, V, Nb, Zr, Y, Sr, Rb, U) were analysed by both ICP-MS and XRF. For most elements the two techniques produce data that are in good agreement with each other. However, although Nb data obtained by XRF and ICP-MS are comparable for the Swartruggens samples (Figure A3.2a), a subset of samples have higher measured Nb concentrations

when analysed by XRF relative to ICP-MS (Figure A3.2b). Samples SJH 37, JJG 6369, JJG 6362 from the Wynandsfontein Dyke and JJG 4570 and SJH 101 from the East Star Dyke are most affected. This is probably due to incomplete dissolution of Nb bearing phases during preparation of the samples for ICP-MS analyses and Nb data obtained by XRF are therefore preferred and are reported in Chapter 5. Since Ta shows similar geochemical behaviour to Nb, it is likely that Ta data obtained by ICP-MS for the above mentioned samples are also low.

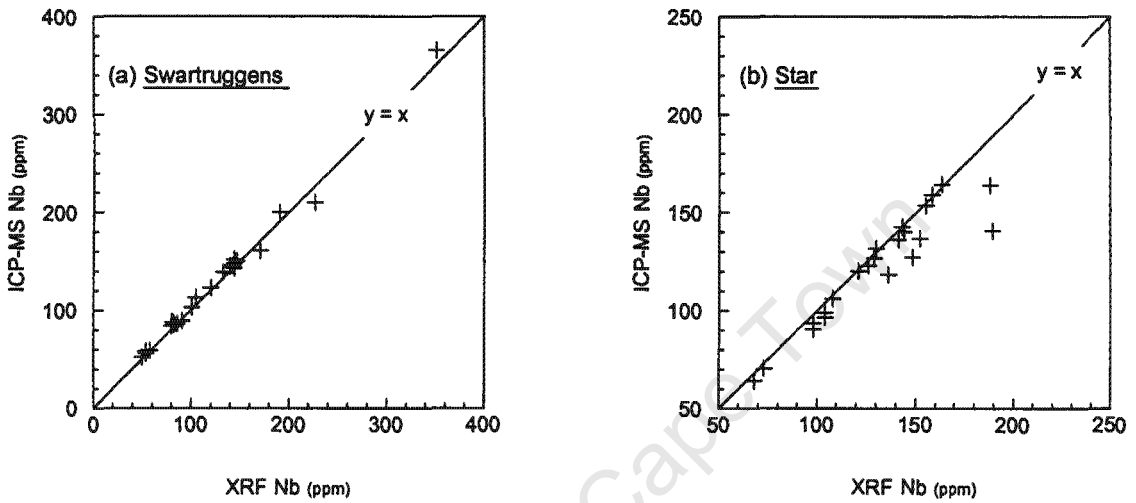

Figure A3.2 Comparison of the Nb data obtained by XRF and ICP-MS in (a) the Swartruggens and (b) the Star samples. A subset of samples from Star have lower measured Nb contents when analysed by ICP-MS relative to XRF.

A3.5 Sr, Nd and Hf isotope determinations

Samples were prepared for Sr isotope analysis in the Department of Geological Sciences, University of Cape Town. Hf and Nd sample preparation and all analyses were carried out at the Arthur Holmes Isotope Geosciences Laboratory, Department of Earth Sciences, University of Durham.

A3.5.1 Sample dissolution

Strontium

100mg of each sample was weighed out and dissolved in Teflon beakers using the procedure outlined in Table A3.8.

Once the samples were dissolved in 1ml 2.5M HCl they were transferred to centrifuge tubes and centrifuged for approximately 15 minutes to separate any undissolved sample prior to loading onto the columns. 0.5ml of the solution was then loaded onto primary cation exchange columns following the method of Hart and

Table A3.8 Dissolution procedure prior to Sr separation.

Reagent	Volume (mls)	Action
4 HF: 1 HNO_3	4	Beaker sealed and placed on hotplate for 2 days to allow sample to digest. Sample dried down.
6.2M HCl	4	Sample dissolved and dried down
6.2M HCl	4	Sample dissolved and dried down
2.5M HCl	1	Sample dissolved.

Brookes (1977) outlined in Table A3.9. The columns are 19cm in height and 0.5cm in diameter, and contain Dowex AG 50WX-8 (200-400 mesh) resin.

Table A3.9 Separation procedure for Sr using primary cation exchange columns.

Reagent	Volume (mls)	Action	Elements Eluted
2.5M HCl (Sample)	0.5	Loaded and eluted	Bulk of sample
2.5M HCl	1	Eluted	
2.5M HCl	1	Eluted	
2.5M HCl	1	Eluted	
2.5M HCl	23	Eluted	
2.5M HCl	8.5	**Collected**	Sr

Hafnium and Neodymium

Full details of the dissolution and chemical separation procedures used at Durham University are reported in Dowall *et al.* (2003b) and only summarised below.

Table A3.10 Procedure for the dissolution of silicate minerals.

Reagent	Volume (mls)	Action
16M HNO_3 29M HF	1 4	Beakers sealed and placed on hotplate at 120°C for 24-48hrs. Sample dried down at <100°C until almost dry.
16M HNO_3	1	Beakers sealed and placed on hotplate at 100C overnight. Sample dried down at <100°C
12M HCl	2	Beakers sealed and placed on hotplate at 100°C overnight. Sample dried down at <100°C
1M HCl	1	Beakers sealed. Samples warmed on hotplate for 30mins.

Approximatley 0.1grams of each sample was dissolved in Teflon beakers for Hf and Nd analyses using the procedure outlined in Table A3.10.

Once samples were dissolved in 1ml of 1M HCl they were transferred to centrifuge tubes and centrifuged at 5000rpm for 15mins to remove any un-dissolved sample residue prior to loading on the 1st stage column.

Separation of Nd and Hf for mass spectrometric analysis was achieved using a two-column procedure as outlined in Tables A3.11 and A3.12.

Table A3.11 Separation procedure for Hf and Nd using the 1st stage cation exchange columns.

Reagent	Volume (mls)	Action	Elements Eluted
1M HCl (Sample)	1	Loaded and **collected**	Hf + other HFSE and 1st period transition elements
1M HCl-1M HF	3	**Collected**	Hf + other HFSE and 1st period transition elements
1M HCl-1M HF	13	Eluted	Rb + bulk of sample
2.5M HCl	14	Eluted	Sr + other alkaline elements
2M HNO_3	10	Eluted	Removes Ba
6M HCl	12	**Collected**	Nd + other REE

The first 4mls collected from the 1st stage column (Table A3.11) were dried down and re-dissolved in 1ml of 0.26M H_2SO_4 – 5% H_2O_2 prior to loading on the 2nd column. The Nd fractions were dried down and dissolved in 1ml 3% HNO_3 ready for mass spectrometric analysis.

Table A3.12 Separation procedure for Hf and Ti on the 2nd stage anion exchange column.

Reagent	Volume (mls)	Action	Elements Eluted
0.26M H_2SO_4 – 5% H_2O_2	1	Loaded and eluted	Ti
0.26M H_2SO_4 – 5% H_2O_2	4	Eluted	Ti
1M HF – 2M HCl	5	**Collected**	Hf + Zr

The Hf fractions collected from the second stage anion exchange column (Table A3.12) were dried down on a hotplate at 100°C until the bulk of the solution had evaporated. The hotplate was then increased to 230°C to evaporate residual concentrated H_2SO_4. The samples were then re-dissolved in 1ml of 3% HNO_3 – 0.04%HF ready for mass spectrometric analysis.

A3.5.2 Mass Spectrometry

All samples were analysed at the Arthur Holmes Isotope Geosciences Laboratory, Department of Earth Sciences, University of Durham, using a ThermoFinnigan Neptune Plasma Ionisation Multi-collector Mass Spectrometer (PIMMS). Details of the Durham Neptune and its long-term performance can be found in Nowell *et al.* (2003). Specific details of the analytical methods for each element are given below.

Strontium:

Sample introduction

Samples, dissolved in 1ml of 3% HNO_3, were naturally aspirated using an Elemental Scientific Inc (ESI) PFA50 microflow nebuliser, operating at an uptake rate of approximately 75µl min^{-1}, coupled to an ESI dual cylonic-Scott Double Pass spraychamber.

Washout

Each analysis was followed by a minimum 5 minute washout with 3% HNO_3 and until ^{88}Sr intensity levels out at <4mV. A 10µl aliquot of Iso-propyl Alcohol (IPA) was used if ^{88}Sr intensity not reduced to <4mVwith 3% HNO_3.

Cup configuraion

Cups were configured for analyses as reported in Table A3.13.

Table A3.13 Cup configurations for Sr isotope analyses. Isotopes in italics were monitored for interference corrections on Sr.

Low 4	Low 3	Low 2	Low 1	Axial	High 1	High 2
^{82}Kr	*^{83}Kr*	^{84}Sr	*^{85}Rb*	^{86}Sr	^{87}Sr	^{88}Sr

Method

1 block of 50 cycles, 4 second integration time per cycle. All cup efficiencies set at 1. Mass bias correction with $^{88}Sr/^{86}Sr$ = 8.375209 (equivalent to $^{86}Sr/^{88}Sr$ = 0.1194), applying an exponential law. ^{82}Kr or ^{83}Kr and ^{85}Rb used for corrections of ^{84}Kr and ^{86}Kr and ^{87}Rb on ^{84}Sr, ^{86}Sr and ^{87}Sr respectively using the method outlined in Nowell *et al.* (2003).

Hafnium

Sample introduction

Samples, dissolved in 1ml of 3% HNO_3 – 0.04%HF, were naturally aspirated using a CETAC Aridus desolvating nebuliser with uptake rate of approximately 80µl min^{-1}.

Washout

Each analysis was followed by a minimum 5 minute washout with 3%HNO_3 – 0.04%HF and until ^{180}Hf intensity levels out at <2mV. 2 minute IPA washout was also used to dry-out the spraychamber and desolvation membrane if ^{180}Hf intensity not reduced to <2mV with 3% HNO_3 – 0.04% HF.

Cup configuration

Cups were configured for analyses as reported in Table A3.14

Table A3.14 Cup configuration for Hf isotope analyses. Isotopes in italics were monitored for interference corrections on Hf.

Low 4	Low 3	Low 2	Low 1	Axial	High 1	High 2	High 3
^{172}Yb	^{173}Yb	^{175}Lu	^{176}Hf	^{177}Hf	^{178}Hf	^{179}Hf	^{180}Hf

Method

1 block of 50 cycles, 4 second integration time per cycle. All cup efficiencies set at 1. Mass bias correction with $^{179}Hf/^{177}Hf$ = 0.7325, applying an exponential law. ^{172}Yb or ^{173}Yb and ^{175}Lu used for the off-line correction of ^{176}Yb and ^{176}Lu on ^{176}Hf respectively using the procedure outlined in Nowell and Parrish (2001)

Neodymium:

Sample introduction

Samples, dissolved in 1ml of 3% HNO_3, were naturally aspirated using an ESI PFA50 microflow nebuliser, operating at an uptake rate of approximately 75µl min^{-1}, coupled to an ESI dual cylonic-Scott Double Pass spraychamber.

Washout

Each analysis followed by a minimum 5min washout with 3% HNO_3.

Cup configuration

Cups were configured for analyses as reported in Table A3.15.

Table A3.15 Cup configuration for Nd isotope analyses. Isotopes in italics were monitored for interference corrections on Nd.

Low 4	Low 3	Low 2	Low 1	Axial	High 1	High 2	High 3	High 4
^{142}Nd	^{143}Nd	^{144}Nd	^{145}Nd	^{146}Nd	^{147}Sm	^{148}Nd	^{149}Sm	^{150}Nd

Method

1 block of 50 cycles, 4 second integration time per cycle. All cup efficiencies set at 1. Mass bias correction with $^{146}Nd/^{145}Nd$ = 2.071943 (equivalent to the more commonly used $^{146}Nd/^{144}Nd$ of 0.7219), applying an exponential law. ^{147}Sm and ^{149}Sm used for the off-line correction of ^{144}Sm, ^{148}Sm and ^{150}Sm on ^{144}Nd, ^{146}Nd and ^{150}Nd respectively using the procedure outlined in Nowell and Parrish (2001)

Standards and Instrument reproducibility

Appropriate isotopic standards were run repeatedly at the beginning of each analytical session, prior to running any samples, and at regular intervals throughout the session to check for instrument reproducibility

and any sample memory effects. Standards used were NBS 987, J&M and JMC 475 for Sr, Nd and Hf respectively. Table A3.16 gives the accepted ratios for each of the isotopic standards.

Table A3.16 Accepted values for isotopic standards. * value equivalent to a La Jolla International Nd standard value of 0.51186.

Standard	Ratio	Accepted value	Reference
NBS 987	$^{87}Sr/^{86}Sr$	0.71024	Thirlwall (1991)
J&M	$^{143}Nd/^{144}Nd$	0.511110*	Nowell *et al.* (in press)
JMC 475	$^{176}Hf/^{177}Hf$	0.28216	Nowell *et al.* (1998)

Since the Nd isotopic composition of the samples was determined from a total REE cut from the 1st column, Ce and Sm, which both have atomic interferences on Nd, are present in the sample. No correction was made for Ce but it was essential to correct for ^{144}Sm, ^{148}Sm and ^{150}Sm on ^{144}Nd, ^{148}Nd and ^{150}Nd, respectively. All atomic interference corrections were done using the method of Nowell and Parrish (2001). To assess the accuracy of the Sm correction algorithm Sm-doped J&M standards were run, in addition to pure J&M standards.

Average values for isotopic standards measured during each analytical session are reported in Table A3.17. All sample isotope data reported in Chapter 6 has been normalised using the accepted standard values and the average values measured during the relevant analytical session.

Table A3.17 Average ratios for isotopic standards analysed during each analytical session. * Includes both pure and Sm-doped standards.

Standard and date	Average	2SE	n
NBS 987 Sr:			
09/07/03	0.710266	0.000009	11
12/08/03	0.710264	0.000010	9
***J&M Nd:**			
03/02/03	0.511095	0.000013	9
22/07/03	0.511103	0.000007	7
JMC 475 Hf:			
02/01/03	0.282144	0.000003	7
23/07/03	0.282145	0.000002	10

Appendix 4

Country rock analyses

Samples of the host shales of the Swartruggens and Star kimberlites were analysed for their major element (by XRF) and trace element (by XRF and ICP-MS) concentrations as described in Appendix 3. Data are reported in Table A4.1.

Table A4.1 Major and trace element abundances of the host shales of the Swartruggens and Star kimberlites. Major oxide data in wt %, trace element data in ppm. ** = trace elements analysed by XRF, all other trace elements analysed by ICP-MS.

	Swartruggens	Star
SiO_2	60.9	57.7
TiO_2	0.60	0.68
Al_2O_3	20.3	15.2
Fe_2O3	7.45	6.57
MnO	0.03	0.11
MgO	2.03	5.36
CaO	0.40	1.69
Na_2O	0.47	1.55
K_2O	3.01	3.94
P_2O_5	0.09	0.18
SO_3	b.d.	0.02
NiO	0.01	0.01
Cr_2O_3	0.01	0.01
H_2O^-	0.27	1.88
LOI	3.92	4.56
Total	99.4	99.4
Sc	12.6	12.6
V	97.5	145
Cr**	119	62.2
Co	14.4	15.0
Ni**	56.6	54.9
Cu	38.5	44.4
Zn**	93.8	111
Rb	166	175.7

	Swartruggens	Star
Sr	153	280
Cs	11.2	14.2
Ba	493	859
Pb	31.1	31.0
Y	21.5	23.0
Zr	172	191
Nb**	17.0	44.6
Hf	4.75	6.14
Ta	1.87	1.44
Th	22.3	13.3
U	4.72	4.22
La	38.6	35.5
Ce	80.4	71.1
Pr	8.48	8.40
Nd	31.1	32.2
Sm	5.35	5.95
Eu	1.02	1.20
Gd	4.50	5.10
Tb	0.67	0.78
Dy	3.99	4.34
Ho	0.81	0.83
Er	2.29	2.14
Tm	0.36	0.29
Yb	2.39	1.77
Lu	0.37	0.27